

Stabilizing metal halide perovskites by computational compositional engineering

Citation for published version (APA):

Jiang, J. (2021). *Stabilizing metal halide perovskites by computational compositional engineering*. [Phd Thesis 1 (Research TU/e / Graduation TU/e), Applied Physics and Science Education]. Eindhoven University of Technology.

Document status and date:

Published: 14/10/2021

Document Version:

Publisher's PDF, also known as Version of Record (includes final page, issue and volume numbers)

Please check the document version of this publication:

- A submitted manuscript is the version of the article upon submission and before peer-review. There can be important differences between the submitted version and the official published version of record. People interested in the research are advised to contact the author for the final version of the publication, or visit the DOI to the publisher's website.
- The final author version and the galley proof are versions of the publication after peer review.
- The final published version features the final layout of the paper including the volume, issue and page numbers.

[Link to publication](#)

General rights

Copyright and moral rights for the publications made accessible in the public portal are retained by the authors and/or other copyright owners and it is a condition of accessing publications that users recognise and abide by the legal requirements associated with these rights.

- Users may download and print one copy of any publication from the public portal for the purpose of private study or research.
- You may not further distribute the material or use it for any profit-making activity or commercial gain
- You may freely distribute the URL identifying the publication in the public portal.

If the publication is distributed under the terms of Article 25fa of the Dutch Copyright Act, indicated by the "Taverne" license above, please follow below link for the End User Agreement:

www.tue.nl/taverne

Take down policy

If you believe that this document breaches copyright please contact us at:

openaccess@tue.nl

providing details and we will investigate your claim.

Stabilizing Metal Halide Perovskites by Computational Compositional Engineering

Junke Jiang

The work presented in this thesis was funded by the Computational Sciences for Energy Research (CSER) tenure track program of Shell and NWO (Project No. 15CST04-2). The research was conducted at Eindhoven University of Technology (TU/e), the Netherlands.

A catalogue record is available from the Eindhoven University of Technology Library.

ISBN: 978-90-386-5370-9

NUR: 925

Cover: compositional engineering of perovskite by hybrid organic and inorganic cations, created with VESTA software (<http://jp-minerals.org/vesta/en/>)

Printed by Gildeprint, the Netherlands

Copyright © 2021 Junke Jiang. All Rights Reserved.

Stabilizing Metal Halide Perovskites by Computational Compositional Engineering

THESIS

ter verkrijging van de graad van doctor aan de Technische Universiteit
Eindhoven, op gezag van de rector magnificus prof.dr.ir. F.P.T. Baaijens,
voor een commissie aangewezen door het College voor Promoties, in
het openbaar te verdedigen op donderdag 14 oktober 2021 om 11:00 uur

door

Junke Jiang

geboren te Hunan, China

Dit proefschrift is goedgekeurd door de promotoren en de samenstelling van de promotiecommissie is als volgt:

Voorzitter:	prof.dr.ir. G.M.W. Kroesen
1 ^e promotor:	prof.dr. P.A. Bobbert
Copromotor:	dr. S. Tao
leden:	dr. L. Pedesseau (INSA Rennes)
	prof.dr. L.J.A. Koster (Rijksuniversiteit Groningen)
	prof.dr. M. Creatore
	prof.dr.ir. R.A.J. Janssen
	prof.dr. G.H.L.A. Brocks

Het onderzoek of ontwerp dat in dit thesis wordt beschreven is uitgevoerd in overeenstemming met de TU/e Gedragscode Wetenschapsbeoefening.

Contents

1. Introduction.....	1
1.1. The position of solar energy	1
1.2. Perovskite solar cells	2
1.3. Metal halide perovskites.....	4
1.4. Stabilizing MHPs by compositional engineering.....	6
1.5. Stabilizing MHPs by tuning the dimension.....	9
1.6. Stabilizing MHPs by precursor solution engineering	11
1.7. This thesis.....	13
2. Computational Methods.....	17
2.1. Electronic Hamiltonian	17
2.1.1. Schrödinger equation	17
2.1.2. Born-Oppenheimer approximation	18
2.2. Density functional theory	19
2.2.1. Hohenberg and Kohn theorems	20
2.2.2. Kohn-Sham equation.....	20
2.3. Exchange and correlation functionals.....	21
2.4. DFT-1/2 method	23
2.5. <i>Ab initio</i> molecular dynamics	24
2.6. Thermodynamic ensembles	25
2.7. AIMD simulation condition	26
3. Atomistic and Electronic Origin of Phase Instability of Metal Halide Perovskites	29
3.1. Introduction.....	30

3.2. Methods.....	32
3.2.1. Computational methods and structural models.....	32
3.2.2. Calculations of formation energy.....	34
3.2.3. Crystal orbital hamilton population analysis.....	34
3.2.4. Chemical bonding in AMX_3 perovskites.....	36
3.2.5. Mixing thermodynamics.....	37
3.2.6. Formation energy calculation of Sn vacancy.....	38
3.2.7. Synthesis of $CsSn_{1-y}Pb_yI_3$ quantum dots.....	38
3.3. Results and discussion.....	39
3.3.1. Suppression of the phase transition by mixing Cs and FA in $Cs_xFA_{1-x}PbI_3$	39
3.3.2. Suppression of the phase transition by mixing Br and I in $CsSn(Br_zI_{1-z})_3$	44
3.3.3. Experimental observation of the phase transition in $CsSn_yPb_{1-y}I_3$	45
3.3.4. Suppression of the phase transition by mixing Sn and Pb in $CsSn_yPb_{1-y}I_3$	47
3.4. Conclusions.....	49
4. Stabilizing Lead-Free All-Inorganic Tin Halide Perovskites by Ion Exchange	51
4.1. Introduction.....	52
4.2. Computational methods and structural models.....	55
4.3. Results and discussion.....	57
4.4. Conclusion.....	65
5. The Role of Sodium in Stabilizing Tin-Lead (Sn-Pb) Alloyed Perovskite Quantum Dots.....	67
5.1. Introduction.....	68
5.2. Methods.....	71
5.2.1. Density functional theory calculation.....	71
5.2.2. <i>Ab Initio</i> molecular dynamics simulation.....	71
5.2.3. Chemical bonding analysis.....	72
5.2.4. Structural models.....	72
5.2.5. Vacancy formation energy.....	73
5.2.6. Ligand binding energy.....	74
5.2.7. Charge displacement curve.....	74

5.2.9. Experiments	75
5.3. Results and discussion	76
5.3.1. Enhancing the surface Sn-I bonding strength	76
5.3.2. Enhancing the ligand passivation effect	80
5.3.3. Interface dynamics on different terminations	85
5.4. Conclusions.....	88
6. The Role of Solvents in the Formation of Methylammonium Lead Triiodide Perovskite	89
6.1. Introduction.....	90
6.2. Methods.....	92
6.2.1. Density functional theory calculations	92
6.2.2. <i>Ab Initio</i> molecular dynamics simulation	93
6.2.3. Structural models	94
6.3. Results and discussion	94
6.3.1. Formation enthalpies of iodoplumbates.....	94
6.3.2. Formation dynamics of MHPs with different solvents	99
6.4. Conclusions.....	102
7. Conclusions and Outlook.....	105
7.1. Conclusions.....	105
7.2. Outlook.....	108
Appendix A: Supplemental Information for Chapter 3	111
Appendix B: Supplemental Information for Chapter 4.....	121
Appendix C: Supplemental Information for Chapter 5	129
Appendix D: Supplemental Information for Chapter 6.....	141
Bibliography.....	149
Summary.....	181
List of Publications	185
List of Presentations	189
Acknowledgement	191
Curriculum Vitae	195

Chapter 1

Introduction

1.1. The position of solar energy

With the rapid growth of the world population, the energy demand continues to increase. Nowadays, most of the energy is provided by fossil fuels by burning coal, oil, or natural gas. These substances are non-renewable, and combustion emits carbon dioxide and other greenhouse gases, leading to climate change. A realistic solution to prevent this situation from getting out of control is to make a transition to renewable energy sources such as solar, wind, or hydropower. These energy sources are sustainable, less polluting, and, more importantly, inexhaustible. Given the abundance of resources and available knowledge to convert it into electricity, solar energy is a promising option. Figure 1.1 provides a brief view of the energy reserves available on the earth, which demonstrates the dominant position of solar energy among all renewable and non-renewable energy sources. The total sum of recoverable energy from all the reserves is around 1% of the solar energy supplied to the earth surface by the sun. Moreover, the solar energy (23,000 TWy/y) supplied to the total surface (land and water) of the earth is more than one thousand times larger than the global energy consumption (18.5 TWy/y in 2015). Evidently, solar energy is much more than enough to meet all energy needs for the lifetime of the solar system, but the challenge lies in the development of economically viable technologies for its harnessing.

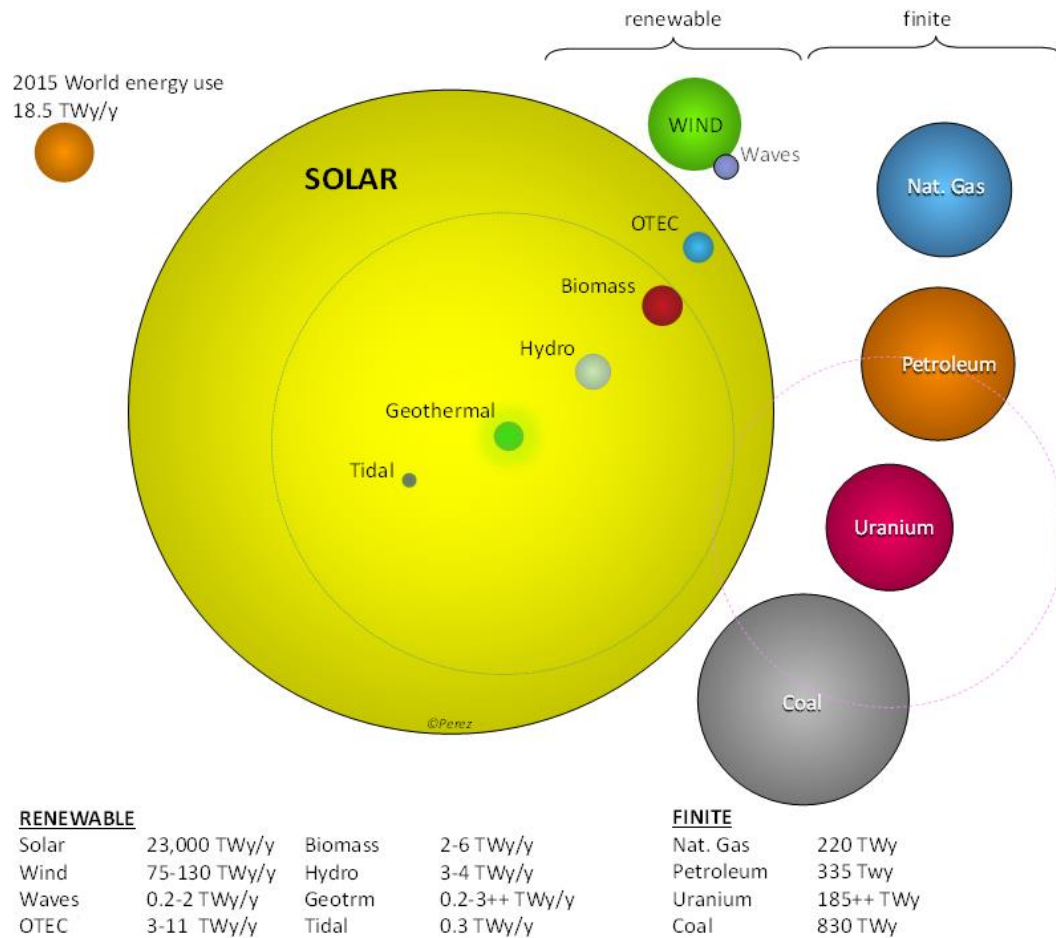


Figure 1.1. Energy reserves on earth (OTEC: Ocean Thermal Energy Conversion). The renewable and non-renewable energy reserves as of the year 2015. Figure reproduced from reference [1].

1.2. Perovskite solar cells

The use of solar irradiance requires photosensitive materials that absorb light and generate excitons or electron-hole pairs. In order to generate electricity, electron-hole pairs need to separate and start to flow. So far, significant efforts have been made to find and adjust materials that can capture solar energy with higher efficiency at a competitive production cost. Some of the most researched ones include crystalline silicon (Si), cadmium telluride (CdTe), copper indium gallium selenide (CIGS), gallium arsenide (GaAs), conductive organic materials, and metal halide perovskites (MHPs). So far, traditional silicon-based solar cells are the market standard. This is mainly due to their long-term stability, relatively high power conversion efficiency (PCE), and

competitive price. Silicon-based solar cells are the most widely solar cells for residential use, and the majority of the solar cells produced at present are crystalline silicon solar cells. However, the production of silicon-based solar cells involves complex energy-intensive processes. This prompted researchers to look for alternative photoactive materials with lower energy costs and easier manufacturing processes. Among various choices, MHPs show great potential to become the next-generation solar cell material. Perovskite solar cells were first manufactured in 2009, with a PCE of 3.8%, showing a significant improvement in efficiency in the last decade, reaching a PCE higher than 25% now (see Figure 1.2).

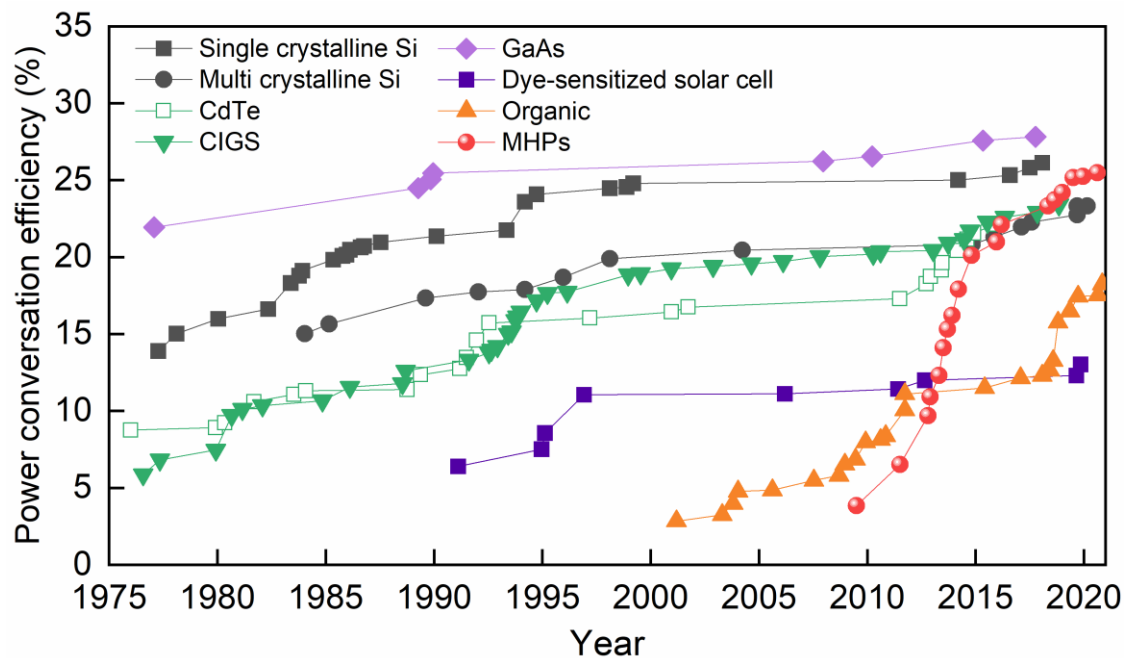


Figure 1.2. Record power conversion efficiencies (PCEs) for different solar cell materials. Data Source: PCEs evolution of MHPs solar cell before 2015 are from Park [2], other data from National Renewable Energy Laboratory (NREL) [3].

MHPs are attractive in photovoltaic applications for many reasons, for example, the low-cost solution manufacturing processes [4], the earth-abundant compositions [5], the adjustable band gap [6, 7], the long carrier diffusion length [6, 8], the high absorption coefficient [6, 9], and the low charge recombination rate [10]. A perovskite solar cell (PSC) is a photovoltaic device where the MHPs is used as the active light-

harvesting layer. Typically, the device consists of selective transport layers for electrons and holes and an absorber layer sandwiched between them. The structure follows a heterojunction concept. Figure 1.3 shows a scheme of a typical perovskite solar cell. However, for the MHPs used in the active light-harvesting layer MHPs, the toxicity of lead and solvents used in the manufacturing process is a problem. In addition, MHPs also encounter various stability problems, which including thermal instability [11, 12], phase instability [13, 14], photoinduced halide segregation [15, 16], photochemical instability [17, 18], and instability towards moisture [19, 20] and oxygen [21, 22]. To tackle these instability issues of MHPs, many methods have been proposed, including tuning the final film/precursor composition [23, 24], reducing the dimensions [25, 26], surface post-treatment [27, 28], and heterojunction control [29, 30]. This thesis will focus on the compositional engineering for both film and precursor, and the dimensional engineering with the overall aim of improving the stability of MHPs and the devices made of them.

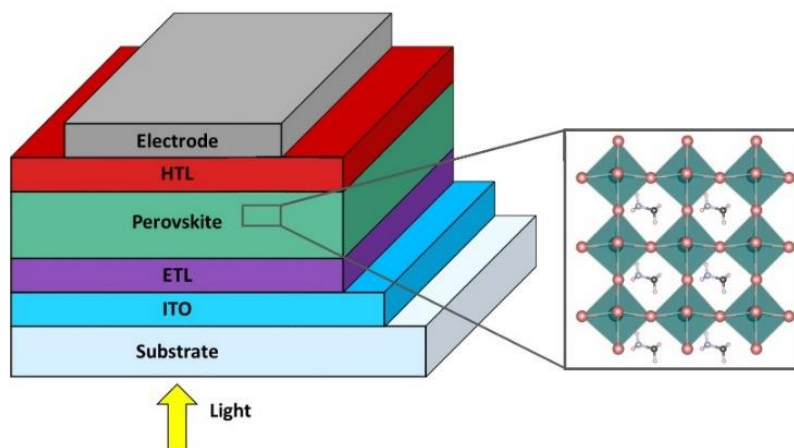


Figure 1.3. A typical structure of a perovskite solar cell. The active halide perovskite absorber layer is sandwiched between the transport layers for electrons (ETL) and holes (HTL).

1.3. Metal halide perovskites

The crystalline perovskite material named after the Russian mineralogist Lev A. Perovski has been known for more than a century. The calcium titanate CaTiO_3 was discovered in the Ural Mountains of Russia in 1839 by Gustav Rose. Perovskites have

a typical structure of AMX_3 , where A and M are cations, and X is an anion (see Figure 1.4a). Within the perovskite structure, materials can be formed in several possible symmetries, such as cubic (α), tetragonal (β), and orthorhombic (γ). In the ideal cubic structure, the materials consist of octahedra formed by $[MX_6]^{4-}$, where M takes a central position, and X is located at the vertices of the octahedra. The A-site cation is located in the cuboctahedral cavity formed by eight $[MX_6]^{4-}$ octahedra.

As a member of the perovskite materials family, MHPs have the same general formula, with several possible choices of the A cation, either organic or inorganic. The metal atom M is usually Pb or Sn, and X is a halide (I, Br, or Cl). The ionic components of MHPs are shown in Figure 1.4a. To predict the compatibility of ions within the perovskite structure, we can analyze the structure with the empirical rule known as Goldschmidt's tolerance factor [31], which quantifies how the ion size affects crystal structure and stability. This applies to all perovskite materials, including MHPs. The tolerance factor t is given by Equation 1.1,

$$t = \frac{r_A + r_X}{\sqrt{2}(r_M + r_X)} \quad (1.1)$$

where r_A , r_M , and r_X are the ionic radii of the ions at the A, M, and X sites. A tolerance factor of 1 indicates an ideal fit that stabilizes the cubic structure. In general, perovskites form in the range of $t = 0.8 - 1.0$. Octahedral tilting can occur if $t < 0.8$ with a small A cation, leading to less symmetric tetragonal or orthorhombic structures. For larger A cations with $t > 1$, the corresponding perovskites are less stable and difficult to be formed (see Figure 1.4b).

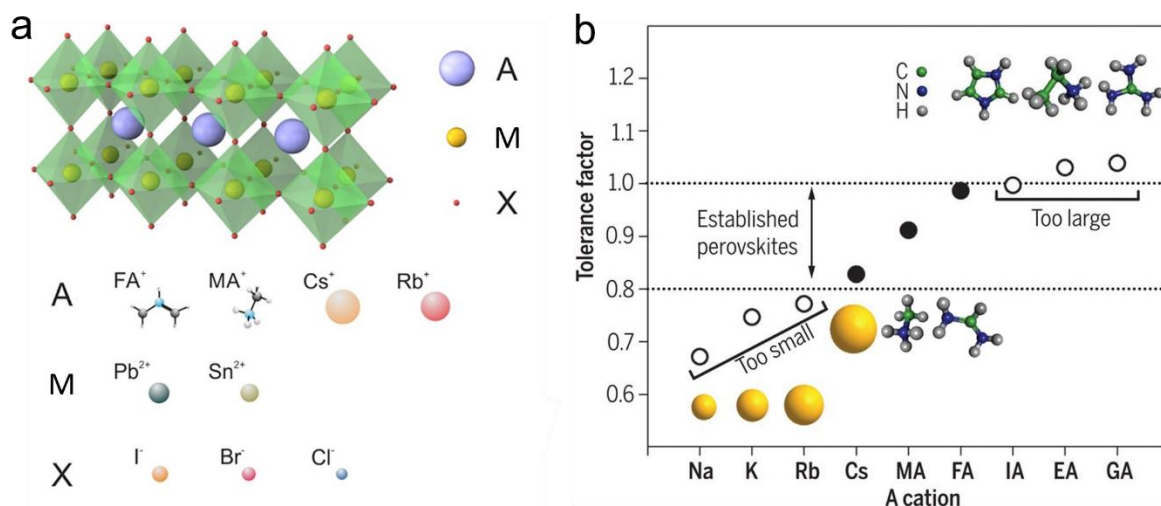


Figure 1.4. (a) Schematic illustration of an AMX₃ perovskite and typical elements occupying the different positions in the structure. Figure reproduced from reference [32]. (b) Tolerance factors of lead iodide perovskite. Site cations with tolerance factors of 0.8-1.0 form stable photoactive perovskites (filled circles). Above or below this range, a photoinactive solid (hollow circle) will be formed. The abbreviations are MA = methylammonium, FA = formamidinium, IA = imidazolium, EA = ethylammonium, GA = guanidinium. Figures reproduced from reference [33, 34].

1.4. Stabilizing MHPs by compositional engineering

In detail, for different ions, the tolerance factors t of FA, MA, and Cs-based lead iodide perovskites are in the range 0.8~1.0. However, the ionic radii mismatch with the cuboctahedral cavity resulting in the different phases for the perovskite. There are several phases (α -, β -, γ -, and δ -phase) of perovskites depending on their exact composition and the temperature. The crystal structures of these phases are shown in Figure 1.5a and the structural phase transitions of different MHPs as a function of temperature are illustrated in Figure 1.5b. For FAPbI₃, X-ray diffraction (XRD) data shows a tetragonal β -phase below 130 K, a cubic phase above 450 K, and a hexagonal δ -phase in between [13]. Thus, FAPbI₃ exists as the photoinactive nonperovskite hexagonal δ -phase at room temperature and will undergo a high-temperature phase transition to the photoactive cubic α -phase. For MAPbI₃, XRD data show a distinct orthorhombic γ -phase below 160 K, a cubic α -phase above 330 K, and a tetragonal β -phase in between [35]. Thus, MAPbI₃ exists in a photoactive tetragonal β -phase at room temperature [36, 37]. Although MAPbI₃ exhibits a photoactive phase at ambient

temperature, it suffers a rapid decomposition when exposed to light and air [21, 22]. For CsPbI₃, a photoinactive orthorhombic δ -phase is stable at room temperature. Upon heating, this transforms into a photoactive cubic α -phase near 645 K, while upon cooling, the perovskite does not return to the δ -phase immediately. The cubic α -phase distorts initially to a tetragonal β -phase followed by a further change to the orthorhombic γ -phase at 510 K, which persists down to 325 K [38]. For the lead-free perovskite CsSnI₃, two higher-symmetry structures are observed at room temperature: a photoinactive orthorhombic δ -phase and a photoactive orthorhombic γ -phase. When heated above 425 K, the δ -phase transforms to a cubic α -phase. It was demonstrated by thermal analysis and XRD that during cooling, the α -phase first deforms to a tetragonal β -phase at 426 K [39, 40]. With further cooling, the β -phase converts back to the γ -phase at 351 K [41, 42].

As shown by the phase variation above, except for MAPbI₃, the perovskites considered in this thesis, including FAPbI₃, CsPbI₃, and CsSnI₃, will be in the photoinactive δ -phase at room temperature. This means that the photoactive phase at room temperature will undergo a structural transition at ambient conditions from a perovskite to a nonperovskite structure. This intrinsic structural instability is regarded as phase instability. The transition from perovskite to nonperovskite structure has been observed in ambient conditions for all these three perovskites. Because of the distinct electronic properties of the nonperovskite structure, i.e. large and indirect band gaps [41, 43-45], the unwanted phase transition is detrimental to the light absorption properties, leading to decreased solar cell efficiency and reduced stability of MHPs solar cells.

Compositional engineering through mixing cations or anions has been widely reported to be effective in suppressing the undesirable phase transition. Several experiments demonstrated that exchanging or mixing A, M, or X ions is an effective way to improve their intrinsic structural stability [46-51]. For instance, mixing organic A-site cation (MA⁺) [48] or/and inorganic cation (Cs⁺) [52] has been reported to improve the stability of the FAPbI₃ perovskite. Partial substitution of I⁻ with Br⁻ (X-site anion) improved the phase stability of the CsPbI₃ perovskite [53, 54], although at the

cost of degrading the light-harvesting capacity due to the increased band gaps. Partial substitution of Pb^{2+} (M-site cation) with other metal ions (Sn^{2+} or Mn^{2+}) has also been suggested as a possible way to improve the stability of CsPbX_3 perovskites [25, 52]. Moreover, crystal size or dimensionality reduction, which help perovskite convert to a more symmetric crystal structure, have been suggested as the reason for these stabilization effects.

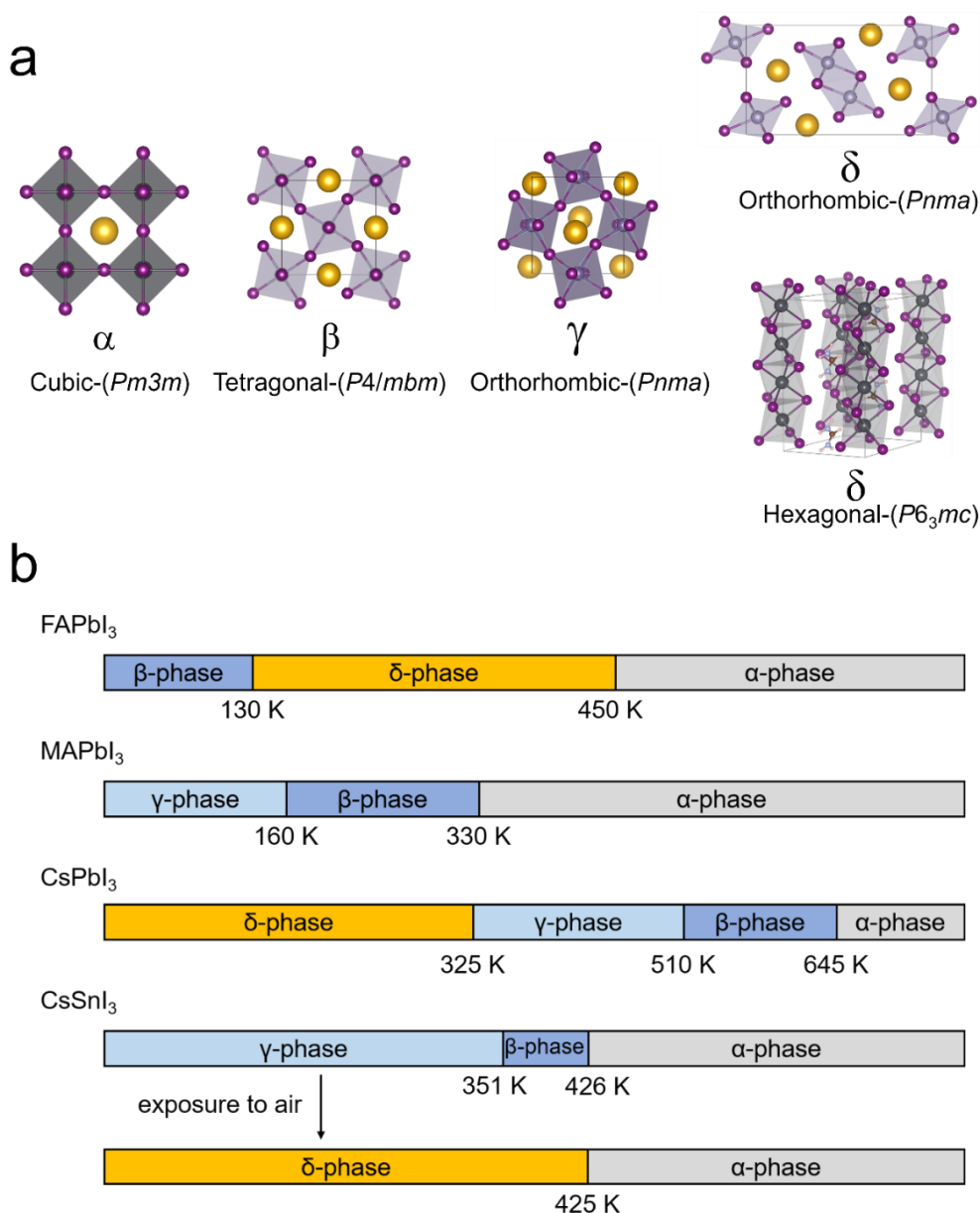


Figure 1.5. (a) Atomic structure of AMX_3 ($A = \text{Cs, FA, MA}$, $M = \text{Pb, Sn}$, and $X = \text{Br, I}$) polymorphs. It should be noted that the nonperovskite δ -phase of FAPbI_3 and CsPbI_3 (or CsSnI_3) are different, with a hexagonal structure for FAPbI_3 . (b) The phase variations of FAPbI_3 , MAPbI_3 , CsPbI_3 , and CsSnI_3 at various temperatures.

1.5. Stabilizing MHPs by tuning the dimension

Larger A site organic cations have been incorporated into perovskite-like structures since the first successful attempt in the year 2015 [55]. This category of perovskites is called 2D perovskites, including the Ruddlesden-Popper phase [56], Hybrid Dion-Jacobson phase [57], and alternating cations in the interlayer space perovskites [58], which have different stoichiometries and superstructures compared to the 3D perovskites. Compared to 3D perovskites, 2D perovskites show greater stability against ambient environments (e.g., heat, light, and humidity), as well as an oriented structure and dense packing [59, 60]. However, the quantum well induced by the insulated large A-cation between layers in 2D perovskites is harmful for the carrier transportation, thus detrimental for the corresponding device performance [61-63].

Apart from tuning the dimension of MHPs from 3D to 2D by incorporating a large A-cation, we next point out another important way to stabilize MHPs. The emergence of all-inorganic perovskite quantum dots (QDs), also called nanocrystals (NCs), provided an implemented solution for this dilemma, reducing crystallite size of MHPs from bulk with large grains to the low dimensional quantum dots (QDs). Importantly, the phase stability of perovskites is largely improved due to the significant contribution from the surface energy and the protection from organic passivation ligands [64-70]. Thus, tuning perovskites from bulk to QDs could benefit the stability of hybrid inorganic perovskite caused by the mismatch of ions. Moreover, compared with the bulk counterpart, the increased exciton binding energy of QDs resulting from geometry and quantum confinement, excitons are more abundant in these nano-sized semiconductor crystals, leading to enhanced radiative recombination and a high theoretical photoluminescence quantum yield (PLQY) [71]. In this thesis, we will investigate the stability of Sn-Pb alloyed perovskite and the effect of doping with alkali cation.

The surface chemistry of perovskite QDs is complex in the presence of capping ligands on the surface [66, 72-75]. To date, most of the perovskite QDs synthesized are primarily based on long-chain ligands. Usually, long-chain amines in combination with a long-chain acid have been used as ligands in the synthesis of perovskite QDs.

In this base-acid pair, the proton is transferred from the acid to the amine, leading to the formation of an ammonium cation ($R-NH_3^+$), which then takes the place of surface A-cation positions on the QDs surface, while the halide or carboxylate attaches on the surface or occupies the halide position, maintaining charge neutrality [76-78]. The prototypical example in the synthesis process of perovskite QDs is the oleylamine-oleic acid pair. With the ionic character of perovskite QDs, the surfaces are typically dynamically stabilized with either an oleylammonium halide or an oleylammonium oleate [76], as shown in Figure 1.6. The surface ligands also have a large diffusion coefficient, which implies highly dynamic ligand binding, with a fast exchange between the bound and free states. Such dynamics is likely the origin of the ease of halide exchange [79, 80] and ligand loss upon purification of perovskite QDs [81-83]. Therefore, a thorough understanding of the surface ligands binding and surface dynamics is essential for further improvement of the stability of perovskite QDs. This thesis will investigate the stability of Sn-Pb alloyed perovskites and the doping effect with alkali cation.

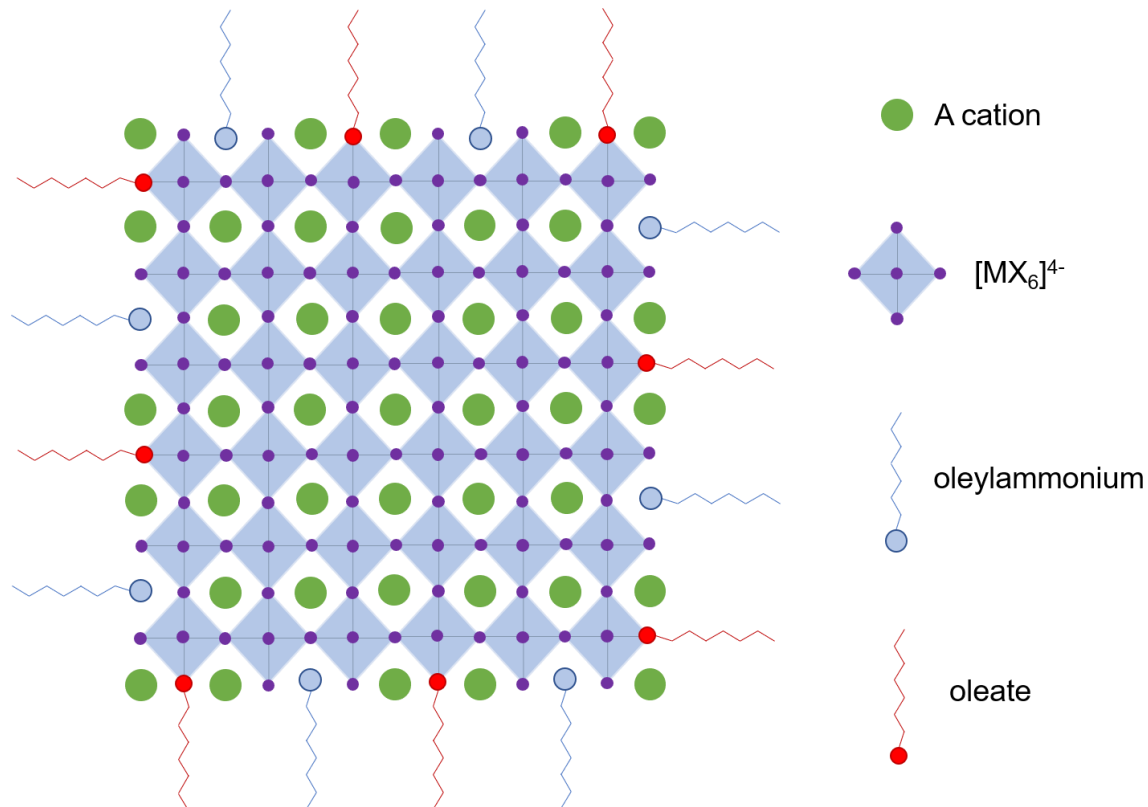


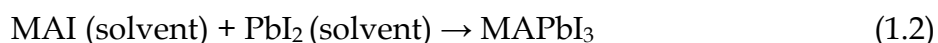
Figure 1.6. Illustration of the typical structure of perovskite QDs capped with organic ligands on the surface.

1.6. Stabilizing MHPs by precursor solution engineering

One of the main advantages of perovskite solar cells is that MHP films can be deposited through a low-cost and energy-saving simple solution process [84-86]. However, the simplicity of the synthesis of MHPs does not mean that the physicochemical processes are also simple. Therefore, understanding the precursor-solution chemistry and the reaction kinetics is essential in controlling the formation of a homogeneous, defect-free photoactive layer for efficient solar cells [87-89].

The synthesis processes of MHPs involve the solvation/de-solvation and complexation equilibria of all participating species as solvated precursors, nucleation, and evolution through various intermediate phases [90-95]. The solvents are acting to dissolve the precursors, forming iodoplumbate complexes, which facilitate perovskite film formation [87, 95, 96]. By changing experimental conditions in the solution deposition, the composition and microstructure of MHPs can be largely tuned. Microstructure control is still a challenge in practice, and a wide range of manufacturing techniques have been explored to meet this challenge. The processing parameters directly affect crystallization processes, which have a significant impact on the microstructure of the MHPs films and will be key for improving the stability of MHPs.

As an example, methylammonium lead iodide (MAPbI₃) can be formed by dissolving two precursor salts, methylammonium iodide (MAI) and lead(II) iodide (PbI₂), in a solvent solution (typically dimethylformamide: DMF [91, 97] and dimethyl sulfoxide: DMSO [90, 97]) and mixing them together, as shown in Equation 1.2,



According to the processing conditions and the category of precursors and solvents, widely used deposition techniques can be divided into two methods, namely "one-step deposition" and "two-step deposition" (sequential deposition) (see Figure 1.7).

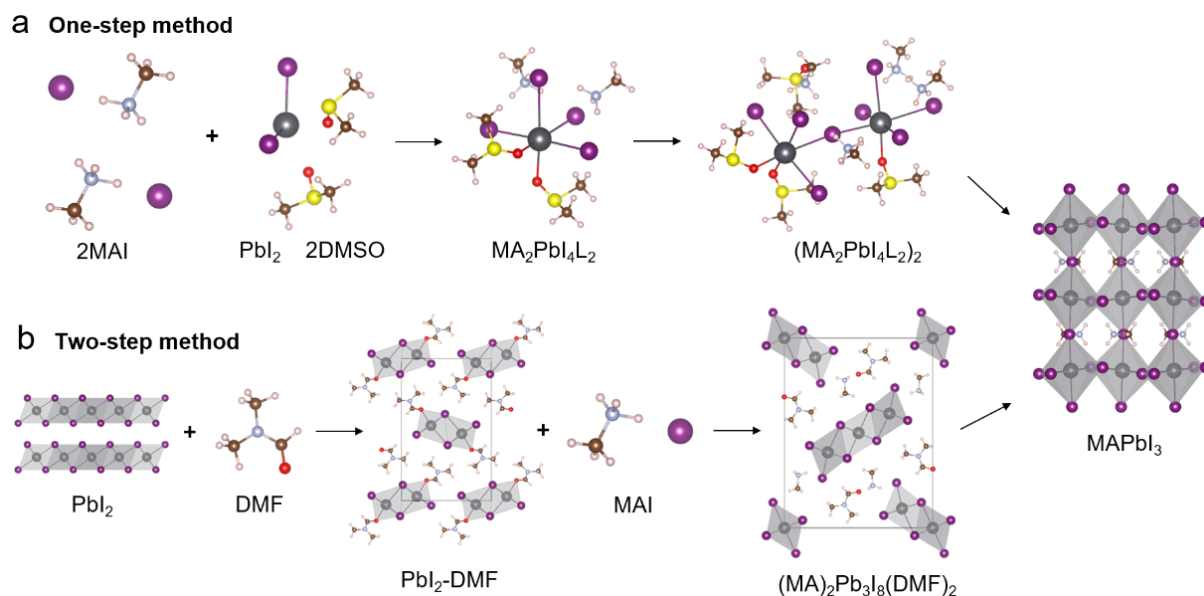


Figure 1.7. Illustration of possible molecular level interactions at the initial and intermediate phases before the onset of nucleation of MAPbI₃ perovskites. (a) One-step method, where the precursors and solvents interact in various molecular complexes, forming iodoplumbate and polynuclear iodoplumbate. L denotes the solvent. (b) Two-step method, where the evolution of Pb-I coordination can be monitored by the conversion from face to edge and to corner-shared PbI_x octahedra.

The one-step deposition starts with loosely dispersed atomic species in the solvent. In the one-step deposition, a precursor solution with a mixture of metal halide PbI₂, organic halide MAI, and solvents is spin-coated on the substrate and followed by thermal annealing to induce nucleation and growth. From an atomistic view, the iodoplumbate $[\text{PbI}_m\text{L}_n]^{2-m}$ (L = solvent, m is the number of iodide anions, and n is the number of solvent molecules) will first form. The number of iodine coordinated with Pb²⁺ increases until Pb²⁺ is fully coordinated. Then, the formation of polynuclear iodoplumbate starting from an iodoplumbate monomer is expected [98] (see Figure 1.7a). In contrast, two-step deposition provides additional control over the process by depositing a thin film of PbI₂ and then exposing it to an organic cation solution to form a perovskite in the second step. The solvation of a PbI₂ layer is followed by several intermediate solvated phases, such as PbI₂L and MA₂Pb₃I₈L₂. Several pathways are expected to compete in both processes due to the rich chemical species involved, as shown in Figure 1.7b. Therefore, determining the energetics of these species during the

evolution of the chemical bonding in iodoplumbates is an important first step in understanding the whole crystallization process of MHPs. This will be the focus of the last chapter of this thesis.

1.7. This thesis

As summarized above, stability issues remain the main obstacle to practical large-scale applications of MHPs. Compositional engineering in both the final films and the precursors has been shown to be an effective way to improve the stability of MHPs. Although much progress has been made to improve the stability of halide perovskites, a comprehensive understanding of the atomistic mechanisms is still lacking. Composition engineering often results in changes in several physical and chemical properties. The complex interplay of several processes and properties is often difficult to study in experiments since common experimental techniques are tailored to investigate a particular process and/or properties of the materials and devices. While experimental studies offer a wide variety of insights into the perovskite films and precursors-solvent interactions at the macro and mesoscopic scales, the atomistic level of detail remains elusive. Computational modelling of materials is complementary to experiments and can be used to obtain atomic-scale insights into the materials. Among all computational methods, Density Functional Theory (DFT) and *ab-initio* Molecular Dynamics (AIMD) simulations are useful tools for looking into the atomistic structural details of materials and investigating dynamical properties under specific conditions that might not be feasible in experiments. This thesis aims to provide insights into the stabilizing effect of compositional engineering on MHPs in both the final film and precursor solutions from a computational perspective.

In Chapter 2, we give a brief physical background of the computational tools, including DFT and AIMD used in this thesis.

In Chapter 3, we start with tackling the challenge of phase instability. We explain the atomistic origins of the phase instability of some primary perovskites, like CsSnI₃, CsPbI₃, and FAPbI₃. Furthermore, we reveal the underlying mechanisms for the improved phase stability of MHPs by computational engineering of either mixing cations or mixing anions. We investigate the electronic properties and relative bond

strengths in the different phases to explain how mixing ions affects phase stability. Four correlated factors, namely, the average metal-halide bond length, the overall bonding strength (including metal halide bonds and hydrogen bonds), the formation energies, and the Sn vacancy formation energy are identified to be responsible for the phase transition.

In Chapter 4, based on the insights on the origin of the phase instability obtained in the Chapter 3, we identify the mixed-cation and mixed-anion $Rb_yCs_{1-y}Sn(Br_xI_{1-x})_3$ perovskites, and suggest them as promising candidates for solar cell applications. In addition, by using binary alloying theory, we predict that mixing both anions and cations is beneficial for a highly homogeneous solid solution and improved film quality.

We then extend our investigation from bulk perovskites to QDs, as the dimensional engineering will further improve the stability of alloyed and Sn-based perovskites. In Chapter 5, we investigate how additives affect the properties of perovskite QDs and improve the performance and stability of Sn-based perovskite QDs. We reveal the role of sodium doping by studying its interaction with surfaces of perovskites and surface ligands. We explain the mechanism for the enhanced photoluminescence of Sn-Pb perovskite QDs and propose future strategies to further enhance their stability.

Next, to understand the effect of the compositional tuning of precursors solutions in affecting the perovskite crystallization process, in Chapter 6 we make a comprehensive investigation to understand the crystallization chemistry. Here, using $MAPbI_3$ as an example, we study the complex evolution of the molecular species from the solution to the initial stage of the nucleation and determine the reaction pathways for the formation of a polynuclear iodoplumbate in different solvents environments. The advantage of the usage of DMF-DMSO binary solvents in the experiment is explained. The results obtained for formation enthalpies indicate that the formation of $[PbI_3L_n]^{1-}$ iodoplumbate and its further coordination should be one of the key steps which determine the final crystallinity of $MAPbI_3$. The DMF-DMSO binary solvent

shows slower formation of high-I coordinated iodoplumbates as compared to DMF, which benefits the crystallization of MAPbI₃ with better crystallinity.

Finally, in Chapter 7 we summarize our main conclusions and discuss directions for future research directions.

Chapter 2

Computational Methods

Several computational methods are used in this chapter, which are the foundation of computational modelling for MHPs. Firstly, the fundamental definitions and expressions valid for many-body systems are reviewed. Secondly, the fundamental principles of density functional theory (DFT) and its derivative DFT-1/2 are reviewed. Thirdly, the basics of *ab initio* molecular dynamics (AIMD), the simulation technique that allows us to investigate the dynamical behaviour of the perovskites, are treated. Finally, the ensemble and thermostat implemented for the AIMD simulations are introduced.

2.1. Electronic Hamiltonian

In this thesis, we are interested in computing the various properties of MHPs via first-principle simulations. The central theory that describes the properties of matter is rooted in the Schrödinger equation, which is the starting point of this section.

2.1.1. Schrödinger equation

The Schrödinger equation is central to quantum mechanics [99], and solving the Schrödinger equation can be viewed as the fundamental problem of quantum mechanics. In quantum mechanics, all possible information about a given system is contained in the system's wave function Ψ . To obtain the wave function, one needs to solve the Schrödinger equation. The most general form is the time-dependent Schrödinger equation, which describes a system evolving with time. For systems in a stationary state, the time-independent Schrödinger equation is sufficient. In a many-body system that contains N electrons and M nuclei, a simple form of the Schrödinger equation could be given as:

$$\hat{H}\Psi(\mathbf{r}_1, \mathbf{r}_2, \dots, \mathbf{r}_N; \mathbf{R}_1, \mathbf{R}_2, \dots, \mathbf{R}_M) = \tilde{E}\Psi(\mathbf{r}_1, \mathbf{r}_2, \dots, \mathbf{r}_N; \mathbf{R}_1, \mathbf{R}_2, \dots, \mathbf{R}_M) \quad (2.1)$$

where \mathbf{r}_i and \mathbf{R}_i are the spatial coordinates of the electrons and nuclei, respectively, \hat{H} is the Hamiltonian operator, and \tilde{E} represents the total energy of the system. Given a system with the electrons of mass m and nuclei of mass M_j , the Hamiltonian operator is then expressed as:

$$\hat{H} = \underbrace{-\frac{\hbar^2}{2m} \sum_{i=1}^N \nabla_i^2}_{\hat{T}_e} - \underbrace{\frac{1}{4\pi\epsilon_0} \sum_{i=1}^N \sum_{j=1}^M \frac{Z_j e^2}{|\mathbf{r}_i - \mathbf{R}_j|}}_{\hat{V}_{en}} + \underbrace{\frac{1}{8\pi\epsilon_0} \sum_{i \neq j}^{N,N} \frac{e^2}{|\mathbf{r}_i - \mathbf{r}_j|}}_{\hat{V}_{ee}} - \underbrace{\frac{\hbar^2}{2} \sum_{j=1}^M \frac{\nabla_j^2}{M_j}}_{\hat{T}_n} + \underbrace{\frac{1}{8\pi\epsilon_0} \sum_{i \neq j}^{M,M} \frac{Z_i Z_j e^2}{|\mathbf{R}_i - \mathbf{R}_j|}}_{\hat{V}_{nn}} \quad (2.2)$$

where the ϵ_0 is the permittivity of the free space, Z_j is the atomic number of the j th nuclei, and e is the elementary charge. The five terms on the right of the equation define, in order, the kinetic energy of electrons \hat{T}_e , the electrostatic potential energy of electron-nucleus attraction \hat{V}_{en} , the potential energy of electron-electron repulsion \hat{V}_{ee} , the kinetic energy of nuclei \hat{T}_n , and the potential energy of nucleus-nucleus repulsion \hat{V}_{nn} .

2.1.2. Born-Oppenheimer approximation

The Born-Oppenheimer approximation [100] could adiabatically decouple the wave function of a many-body system into its electronic and ionic components. The approximation is based on the fact that the motion of the nuclei is much slower than electrons, because atomic nuclei are much heavier than individual electrons. In this approximation method, one can consider the electrons moving in the field produced by the fixed nuclei. Thus for fixed positions of the atomic nuclei, one can solve the Schrödinger equation that describes the electron motion. For a given set of electrons moving in the field formed by a set of nuclei, one can find the lowest energy state (ground-state) of the electrons. As the repulsion between different nucleus is the classical interaction and is not germane to the problem of describing the electrons, one can incorporate the potential energy of nucleus-nucleus repulsion \hat{V}_{nn} into \tilde{E} as:

$$E = \tilde{E} - \underbrace{\frac{1}{8\pi\epsilon_0} \sum_{i \neq j}^{M,M} \frac{Z_i Z_j e^2}{|\mathbf{R}_i - \mathbf{R}_j|}}_{\hat{V}_{nn}} \quad (2.3)$$

By neglecting the kinetic energy of nuclei, the nuclear terms in Equation 2.2 are excluded. One could focus on the electronic part of the wave function and define an electronic Hamiltonian \hat{H}_e as:

$$\hat{H}_e = \underbrace{-\frac{\hbar^2}{2m} \sum_{i=1}^N \nabla_i^2}_{\hat{T}_e} - \underbrace{\frac{1}{4\pi\epsilon_0} \sum_{i=1}^N \sum_{j=1}^M \frac{Z_j e^2}{|\mathbf{r}_i - \mathbf{R}_j|}}_{\hat{V}_{en}} + \underbrace{\frac{1}{8\pi\epsilon_0} \sum_{i \neq j}^{N,N} \frac{e^2}{|\mathbf{r}_i - \mathbf{r}_j|}}_{\hat{V}_{ee}} \quad (2.4)$$

Therefore, the electronic Schrödinger equation is reduced to

$$\hat{H}_e \Phi = E \Phi \quad (2.5)$$

where Φ is the electronic wave function. The electronic wave function is a function of each of the spatial coordinates of all N electrons, could be written as:

$$\Phi = \Phi(\mathbf{r}_1, \mathbf{r}_2, \dots, \mathbf{r}_N) \quad (2.6)$$

Essentially, the Born-Oppenheimer approximation reduces the complexity of electronic structure calculations by reducing the degree of freedom of the Schrodinger equation from $3M + 3N$ to $3N$, directing from the total many-body Schrödinger equation to the electronic Schrödinger equation. However, with this simplification, the task of solving the electronic Schrödinger equation remains challenging.

2.2. Density functional theory

Density functional theory (DFT) is derived from two powerful theorems formulated by P. Hohenberg and W. Kohn [101] in 1964, which provides the theoretical basis for the application of the electron density $\rho(\mathbf{r})$ instead of the many-body wavefunction to solve the Schrödinger equation. The wave function for any particular set of coordinates cannot be directly observed. The quantity that can (in principle) be measured is the probability that the N electrons are at a particular set of coordinates, $\mathbf{r}_1, \mathbf{r}_2, \dots, \mathbf{r}_N$. Then the electron density $\rho(\mathbf{r})$ at a particular position \mathbf{r} can be calculated from the many-electron wave function in an N -electron system,

$$\rho(\mathbf{r}) = N \int \dots \int |\Phi(\mathbf{r}_1, \mathbf{r}_2, \dots, \mathbf{r}_N)|^2 d^3r_2 \dots d^3r_N \quad (2.7)$$

where $|\Phi(\mathbf{r}, \mathbf{r}_2, \dots, \mathbf{r}_N)|^2$ is the probability of finding an electron at position \mathbf{r} and the spin coordinates are not shown explicitly. The electron density is a function of only three coordinates regardless of the number of electrons. Compared with using the many-electron wave function, which depends on the $3N$ spatial coordinates for an N -electron system, the electron density treatment remarkably reduces the complexity of solving the Schrödinger equation [102].

2.2.1. Hohenberg and Kohn theorems

The two powerful theorems put forward by Hohenberg and Kohn (HK) include: i) For any non-relativistic system of N interacting electrons in an external potential $V_{\text{ext}}(\mathbf{r})$, the ground-state density $\rho_0(\mathbf{r})$ uniquely determines the potential $V_{\text{ext}}(\mathbf{r})$ except for a constant shift. ii) For any number of electrons in any external potential, a universal energy functional $E[\rho]$ exists. The density that minimizes the functional $E[\rho]$ is the exact ground-state density $\rho_0(\mathbf{r})$ and the global minimum value of this functional is the exact ground-state energy:

$$E[\rho_0(\mathbf{r})] = \langle \Phi_0 | \hat{H}_e | \Phi_0 \rangle \quad (2.8)$$

A corollary to the first statement is that the ground-state density uniquely determines the non-degenerate ground-state wave function Φ_0 . It means there is a one-to-one relationship between Φ_0 and the ground state density ρ_0 of an N -electron system. Therefore, all properties of the system are completely determined, given only the ground-state density. A corollary to the second statement is that the functional $E[\rho]$ alone is sufficient to determine the exact ground-state energy and density.

The HK theorems enable us to focus on the ground-state density $\rho_0(\mathbf{r})$, rather than on the much more complicated many-particle ground-state wave function. However, besides proving the existence of $E[\rho]$, the HK theorems do not provide any guidance on constructing this energy functional.

2.2.2. Kohn-Sham equation

One year later in 1965, Kohn and Sham proposed a method to calculate $\rho_0(\mathbf{r})$ using the variational properties of DFT [103]. This method provides means for practical calculations. Kohn and Sham proposed that the ground-state density of the many-

particle system is equal to that of some noninteracting system. This leads to independent-particle equations for the noninteracting system, which can be considered exactly solvable with all the difficult many-body terms incorporated into an exchange-correlation functional of the density. For an auxiliary system of noninteracting particles, the single-particle Schrödinger equation is written as:

$$\left[-\frac{\hbar^2}{2m}\nabla^2 + V_S(\mathbf{r}) \right] \phi_i(\mathbf{r}) = \epsilon_i \phi_i(\mathbf{r}) \quad (2.9)$$

where $V_S(\mathbf{r})$ is an effective local potential acting on an electron at point \mathbf{r} , and ϵ_i is the orbital energy of the Kohn-Sham single-electron wave function $\phi_i(\mathbf{r})$ at point \mathbf{r} . The electron density of the non-interacting system is then given by:

$$\rho_S(\mathbf{r}) = \sum_i |\phi_i(\mathbf{r})|^2 \quad (2.10)$$

In fact, it can be shown that $\rho_S(\mathbf{r})$ equals to the ground state density of the real system $\rho_0(\mathbf{r})$ if the effective potential is set in the following way:

$$V_S(\mathbf{r}) = -\sum_j \frac{Z_j}{|\mathbf{r} - \mathbf{R}_j|} + \int d\mathbf{r}' \frac{\rho(\mathbf{r}')}{|\mathbf{r} - \mathbf{r}'|} + \frac{\delta E_{XC}[\rho(\mathbf{r})]}{\delta \rho(\mathbf{r})} \quad (2.11)$$

The first term on the right of the equation is the interaction potential of electron-nucleus pairs. The second term is the Hartree potential, which causes the classical part of the electron-electron interaction energy (the electrostatic repulsion). The last term is the exchange-correlation potential, which is defined as the functional derivative of the exchange-correlation energy $E_{XC}[\rho(\mathbf{r})]$ to the electron density. By putting $V_S(\mathbf{r})$ into Equation 2.9, one can get the so-called Kohn-Sham equation.

2.3. Exchange and correlation functionals

The Kohn-Sham method is a mature quantum theory, based not only on electron density, but also on stringent exchange-correlation (XC) functionals. Therefore, it is difficult to evaluate the reliability of the Kohn-Sham method and its derivative theories without special consideration of the exchange-correlation functionals used. So far, various exchange-correlation functionals have been developed based on different physical models. Local Density Approximation (LDA) is a simple, effective, and

feasible approximation [104]. This approximation assumes the electron density can be treated locally as a uniform electron gas, which could be written in the following way:

$$E_{XC}^{LDA}[\rho(\mathbf{r})] = \int \rho(\mathbf{r})\varepsilon_{XC}[\rho(\mathbf{r})] d^3\mathbf{r} \quad (2.12)$$

where ε_{XC} is the XC energy per electron of the uniform electron gas at point \mathbf{r} . Even though the LDA seems like a coarse approximation, calculations based on LDA have provided quite accurate results for many cases. For example, the LDA gives ionization energies of atoms, dissociation energies of molecules and cohesive energies with a fair accuracy [105]. The LDA also gives bond lengths and the geometries of molecules and solids typically with remarkable accuracy of 1% [106]. However, when predicting band gaps of semiconductors, one has to be careful because the LDA is known to underestimate the band gap [105].

While the LDA is based on an ideal uniform electron gas model, the real problem is often not the case. The electron density of atomic and molecular systems is not uniform, and the LDA no longer meets the needs of computational researchers. In order to solve the problem of LDA and improve the accuracy of these type of calculations, it is necessary to consider the inhomogeneity of the electron density. The best-known class of functional after the LDA is the Generalized Gradient Approximation (GGA), which uses information about the local electron density and the electron density gradient [104]. The GGA functional can be described as:

$$E_{XC}^{GGA}[\rho(\mathbf{r})] = \int \rho(\mathbf{r})\varepsilon_{XC}F_{XC}[\rho(\mathbf{r}), \nabla\rho(\mathbf{r})] d^3\mathbf{r} \quad (2.13)$$

where F_{XC} is known as the enhancement factor, a dimensionless parameter considering the gradient dependency, and ε_{XC} is the exchange-correlation energy density derived from the LDA formalism. In contrast to LDA, the GGA functional does not have a uniquely justifiable form and could be chosen to satisfy various physical constraints. However, it is impossible to simultaneously satisfy every constraint, such that the functional form is usually (but not always) selected according to the nature of the system under consideration. This leads to a variety of parameterizations of GGA grounded on the choice of F_{XC} . Among different choices, the Perdew and Wang (PW91)

[107] and Perdew, Burke and Enzerhof (PBE) [108] are the most used functionals. The PBE functional, which used in this thesis, could be expressed as:

$$E_{XC}^{GGA}[\rho(\mathbf{r})] = \int \rho(\mathbf{r}) \varepsilon_{XC} F_{XC}[r_s, \zeta, s] d^3\mathbf{r} \quad (2.14)$$

where r_s is the local Seitz radius, ζ is the relative spin polarization, and s is defined as the scaled dimensionless reduced density gradient,

$$s = \frac{|\nabla\rho(\mathbf{r})|}{2(3\pi^2)^{\frac{1}{3}}\rho(\mathbf{r})^{\frac{4}{3}}} \quad (2.15)$$

Many variations to the functional form of F_{XC} in Equation 2.15 have been proposed to improve the accuracy of PBE functional for some specific cases. For instance, PBEsol [109] recovers the second-order density gradient expansion for the uniform electron gas limit in the exchange term and better describes geometries for solids and surfaces.

2.4. DFT-1/2 method

The DFT-1/2 method (often also denoted LDA-1/2 or GGA-1/2) is a semi-empirical approach which attempts to correct the DFT self-interaction error in local and semi-local exchange-correlation functionals for extended systems, by defining an atomic self-energy potential that cancels the electron-hole self-interaction energy. This method, introduced by Ferreira *et al.* [110], is based on the much older Slater half-occupation scheme for molecules [111] (also known as the transition state method). Slater's original method consists in carrying out a self-consistent calculation with half an electron removed from the system, and taking the eigenvalue of the half-filled state as an estimate for the ionization energy. The addition of the DFT-1/2 self-energy potential to the DFT Hamiltonian has been found to greatly improve band gaps for a wide range of semiconducting and insulating systems. This approach was formalized in the Janak's theorem:

$$\frac{\partial E(f_\alpha)}{\partial f_\alpha} = \epsilon_\alpha(f_\alpha) \quad (2.16)$$

where $E(f_\alpha)$ is the total energy of the system and f_α is the occupation of state α (between 0 and 1), and ϵ_α is the eigenvalue of the state. The success of the half-occupation

scheme is grounded on the $\epsilon_\alpha(f_\alpha)$ is almost precisely linear for many cases. The introduction of a half-ionization state of individual atoms is done by removing 1/2 electron of occupied levels that contribute to the top of the valence bands. In this method, the atomic self-energy potential V_S is expressed as.

$$V_S \simeq V(f_\alpha = 0) - V(f_\alpha = -1/2) \quad (2.17)$$

where $V(f_\alpha = 0)$ and $V(f_\alpha = -1/2)$ are the all-electron potentials obtained in the neutral and 1/2-ionized states. In order to avoid the Coulomb tail (of 1/2 electron) penetrating into the neighbouring atoms, the self-energy potentials should be trimmed with a cutoff function $\Theta(r)$.

$$\Theta(r) = \begin{cases} (1 - (\frac{r}{r_c})^8)^3 & r \leq r_c \\ 0 & r > r_c \end{cases} \quad (2.18)$$

The cutoff radius r_c is the only parameter introduced in the method and is determined variationally by choosing the value which maximizes the band gap.

2.5. *Ab initio* molecular dynamics

Ab initio molecular dynamics (AIMD) is an important technique for the realistic simulation of complex molecular systems [112]. With AIMD, it is possible to investigate the phenomena that are difficult, expensive, or even currently deemed infeasible for experiments. The molecular dynamics (MD) method is a very powerful computational technique for studying many-body systems. The purpose of MD simulations is to study the time evolution of a number of properties. The properties are calculated by time averages of a certain quantity, which is equivalent to ensemble averages (this is the so-called ergodic hypothesis). The main problem in any molecular dynamics project is how to describe the interactions between atoms. In classical molecular dynamics simulations, the potentials are determined in advance, and the entire interaction is split into many-body contributions, including electrostatic, non-electrostatic, short-range, long-range, bonded, and non-bonded terms. However, using predefined potentials between atoms implies serious drawbacks because the parameterization of the interactions between different atoms in a chemically complex system is a very difficult task. The emergence of AIMD schemes can enable simulations

of complex systems without relying on any adjustable parameters. The main idea of the AIMD method is grounded on the on-the-fly computation of forces through accurate electronic structure calculations. In general, the AIMD concept can be employed in conjunction with any electronic structure method, which leads to various methods including, for example, Ehrenfest Molecular Dynamics [113-115], Born-Oppenheimer molecular dynamics (BOMD) [112], Hartree-Fock Molecular Dynamics [116], and Car-Parrinello Molecular Dynamics (CPMD) [117]. Despite the variety of techniques, this term is nowadays usually used as a synonym of BOMD, and we will use it with this meaning in the rest of the thesis.

In Born-Oppenheimer molecular dynamics (BOMD), the static electronic structure problem is solved in each molecular dynamics step, given a fixed set of classical point-particle nuclear positions at that instant of time. In other words, the time-independent Schrödinger equation is solved for the electrons, concurrently propagating nuclei through classical molecular dynamics.

The resulting BOMD method is defined by:

$$M_I \ddot{\mathbf{R}}_I(t) = -\nabla_{\mathbf{r}_I} \min_{\Psi_0(\mathbf{r}; \mathbf{R})} \{ \langle \Psi_0(\mathbf{r}; \mathbf{R}) | \hat{H}_{el} | \Psi_0(\mathbf{r}; \mathbf{R}) \rangle \} \quad (2.19)$$

From a first glance, solving Equation 2.19 looks like a formidable task. A standard solution for ordinary differential equations in all molecular dynamics methods is the finite difference approach. Given the molecular positions and velocities at time t , the positions and velocities at a later time $t + \Delta t$ are obtained to a sufficient degree of accuracy. The choice of the time interval, Δt , also known as timestep, depends on the propagation algorithm, but usually, it is determined by the fastest motion of the system. Many algorithms apply the finite difference method, and among them, the most widely used one to integrate the equations of motion is the Verlet algorithm, and it is used in the AIMD simulations in this thesis.

2.6. Thermodynamic ensembles

The core of equilibrium statistical mechanics is the theory of equilibrium ensembles. As mentioned above, an ensemble is a set of microscopic states distributed in the phase space according to a certain probability density. The thermodynamic ensembles

usually used in molecular simulations are the microcanonical (NVE), the canonical (NVT), the isothermalisobaric (NPT) ensembles [118]. The N , V , T , and P means the number of particles, volume, temperature, and pressure, respectively. In this thesis, all *ab initio* calculations are performed by using the canonical ensemble, thus I will focus on present it in the next paragraph.

The canonical ensemble offers a statistical microscopic description of a system at constant number of particles, N , volume, V and temperature, T . The probability density in the canonical ensemble is deduced from that of the microcanonical ensemble. The system has a fixed volume and is in contact with a much larger system called bath. As a result of the interaction with bath, the energy E of the system will fluctuate. The probability density of this ensemble is the Boltzmann (canonical) distribution:

$$\rho_{i,NVT} = \frac{1}{Q(N,V,T)} \exp(-\beta E_i) \quad \text{for } i = 0,1,2, \dots \quad (2.20)$$

where $Q(N,V,T) = \sum_i e^{-\beta E_i}$ is the canonical partition function, and $\beta = 1/k_B T$. The classical analogues of Equations 2.21 and 2.22 are:

$$\rho_{NVT}(\{\mathbf{q}_i\}, \{\mathbf{p}_i\}) = \frac{1}{Q(N,V,T)} \frac{1}{h^{3N} N!} e^{-\beta H(\{\mathbf{q}_i\}, \{\mathbf{p}_i\})} \quad (2.21)$$

and

$$Q(N,V,T) = \int_{\Gamma} \frac{e^{-\beta H(\{\mathbf{q}_i\}, \{\mathbf{p}_i\})}}{h^{3N} N!} d^{3N} \mathbf{q}_i d^{3N} \mathbf{p}_i \quad (2.22)$$

Finally, the canonical ensemble is connected with macroscopic thermodynamics via the Helmholtz energy (Equation 2.23).

$$A = -k_B T \ln(Q_{NVT}) \quad (2.23)$$

2.7. AIMD simulation condition

The regulation of the temperature is vital for AIMD simulations in the canonical ensemble, which can be controlled by means of a thermostat. There are many methods for temperature control, including constraint methods, extended system methods, and stochastic methods. All of these methods introduce a thermostat which is an algorithm for simulations at a constant temperature. The thermostat can be considered as the equivalence of the bath in the real system, and the behaviour of the simulated system

should not depend on the details of the bath or thermostat, respectively. In this thesis, the Nosé-Hoover thermostat [119, 120] are employed for temperature control during the equilibration of the systems because it is usually used for simulations that employing the canonical (NVT) ensemble. What follows is a short explanation of the Nosé-Hoover thermostat. The Nosé-Hoover thermostat is a deterministic algorithm that follows the idea of the extended system method. In the beginning, Nosé introduced a bath with the degree of freedom s , with the system under study exchanges energy. Hence, a Hamiltonian is postulated to describe the system (Equation 2.24).

$$H = \sum_i \frac{p_i^2}{2m_i S^2} + \Phi(q) + \frac{p_s^2}{2Q} + gkT \ln s \quad (2.24)$$

where the first term is the kinetic energy and the second term is the potential energy of the system under study. The last two terms correspond to the degree of freedom s , where p_s is a conjugate momentum of s , Q is considered the "mass" for the motion of s , and T is the temperature of the bath. The parameter g is equal to the number of degrees of freedom of the physical system.

Chapter 3

Atomistic and Electronic Origin of Phase Instability of Metal Halide Perovskites

The excellent optoelectronic properties of metal halide perovskites (MHPs) have attracted extensive scientific interests and boosted their application in optoelectronic devices. Despite their attractive optoelectronic properties, their poor stability under ambient conditions remains the major challenge, hindering their large-scale practical applications. In particular, some MHPs undergo spontaneous phase transitions from perovskites to nonperovskites. Compositional engineering via mixing cations or anions has been widely reported to be effective in suppressing such unwanted phase transitions. However, the atomistic and electronic origins of the stabilization effect remain unexplored. Here, by using DFT calculations, we provide insights for the undesired phase transition of pristine perovskites (FAPbI₃, CsPbI₃, and CsSnI₃) and reveal the mechanisms of the improved phase stability of the mixed compounds Cs_xFA_{1-x}PbI₃, CsSn_yPb_{1-y}I₃, and CsSn(Br_zI_{1-z})₃. We identify that the phase transition is correlated with the relative strength of the M-X bonds as well as that of the hydrogen bonds (for hybrid compositions) in perovskite and nonperovskite phases. The phase transition can be suppressed by mixing ions, giving rise to either an increased bond strength for the perovskite or a decreased bond strength in their nonperovskite counterparts, or suppressed vacancy defect formation for Sn-Pb mixed perovskites. Our results present a comprehensive understanding of the mechanisms for the phase instability of MHPs and provide design rules for engineering phase-stable perovskite compositions.

This chapter is based on the publication: J Jiang, F Liu, I Tranca, Q Shen, S Tao, "Atomistic and Electronic Origin of Phase Instability of Metal Halide Perovskites", ACS Applied Energy Materials, 2020, 3, 11548-11558.

3.1. Introduction

Metal halide perovskites (MHPs) are solution-processed semiconducting materials with the general formula AMX_3 , where A is monovalent cations [A = $CH_3NH_3^+$ (methylammonium, MA^+), $CH(NH_2)_2^+$ (formamidinium, FA^+) or Cs^+ ; M = Pb^{2+} or Sn^{2+} ; X = I^- , Br^- or Cl^-] [121, 122]. This class of materials has attracted extensive research interest in the scientific community, owing to their application in efficient and low-cost photovoltaics [43, 123, 124], as well as for light emission [25, 125], photodetectors [126, 127], and lasing [128, 129]. Within only 10 years, the power conversion efficiency (PCE) of perovskite solar cells (PSCs) has drastically increased from 3.8% in 2009 up to 25.5% in 2020 [3, 130]. Although the efficiency of perovskite solar cells is quite high, their instability issues remain the main obstacles to the large-scale applications.

One of the instability issues is the intrinsic structural instability of some pristine perovskites. These include, for example, $FAPbI_3$, $CsPbI_3$, and $CsSnI_3$. They undergo structural transitions at ambient conditions from a perovskite structure to a nonperovskite structure. At room temperature, both $CsSnI_3$ and $CsPbI_3$ have two coexisting polymorphs (γ - and δ -phases) that belong to the $Pnma$ space group and exhibit an orthorhombic structure [14, 131]. For $FAPbI_3$, there are also two existing phases (α - and δ -phases). The α -phase has a cubic symmetry and the δ -phase has a hexagonal structure [132, 133]. The transition from a perovskite to a nonperovskite has been observed in ambient conditions for all these three perovskites; the size of FA^+ is slightly too large, while that of Cs^+ is slightly too small, thus approaching the limits of the tolerance factor of AMI_3 with an optimal range within 0.8-1.0 [134]. Because of the distinct electronic properties of nonperovskites, that is, large and indirect band gaps [41, 43-45], the unwanted phase transition is detrimental to the light absorption properties, therefore leading to a decreased solar cell efficiency and reduced stability of perovskite solar cells.

Several experiments demonstrated that exchanging or mixing A, M, or X ions is an effective way to improve their intrinsic structural stability [46-51]. For instance, mixing the organic A-site cation (MA^+) [48] and/or inorganic cation (Cs^+) [52] has been

reported to improve the stability of the FAPbI₃ perovskite. Partial substitution of I⁻ with Br⁻ (X-site anion) improved the phase stability of the CsPbI₃ perovskite [53, 54], although at the cost of degrading the light-harvesting capacity because of the increased band gaps. Partial substitution of Pb²⁺ (M-site cation) with other metal ions (Sn²⁺ or Mn²⁺) has also been suggested as a possible way to improve the stability of CsPbX₃ perovskites [25, 52]. The crystal size or dimensionality reduction helped perovskites to convert to a more symmetric crystal structure and is suggested as the reason for these stabilization effects. Besides experimental reports, many theoretical studies were also carried out to understand the phase instability issues. Most of the proposed mechanisms focused on the size of the ions [34], and their compatibility with each other (tolerance factors) [13], the mobility of inorganic ions [135], and the effect of the rotation dynamics of the organic cations [136]. However, the underlying atomistic and electronic origin of the phase transition and why mixing of ions can suppress the phase instability is not yet fully understood. Answering these questions is not only fundamentally important but also essential to develop strategies for ultimate stable perovskite materials to meet commercial standards for the long-term stability of perovskite optoelectronic devices.

Here, we provide answers to these questions by using a combination of DFT calculations and experimental stability tests. We study four pristine perovskites (CsPbI₃, CsSnI₃, CsSnBr₃, and FAPbI₃) and their alloys, and demonstrate that alloying A, M, or X ions can suppress the undesired phase transition. We carefully analyze the evolution of their formation energies, atomistic structure, and chemical bonding character and strength for both the perovskite and nonperovskites. Four correlated factors, namely, the average M-X bond length, the overall bonding strength (including M-X bond and hydrogen bonds), the formation energies, and the Sn vacancy formation energy are identified to be responsible for the phase transition. We first explain why mixing Cs and FA or I and Br stabilizes Cs_xFA_{1-x}PbI₃ and CsSn(Br_zI_{1-z})₃ perovskites, respectively. We further discover a new mixed Sn and Pb perovskite composition, CsSn_{0.75}Pb_{0.25}I₃, which is subsequently validated by experiments to be exceptionally stable, maintaining its black phase more than 6 months in ambient conditions.

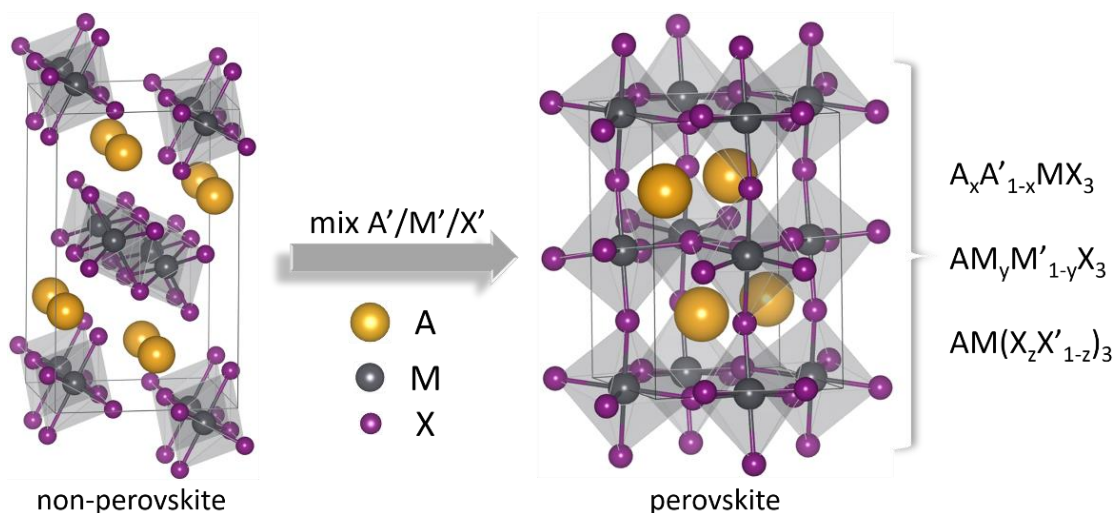


Figure 3.1. Schematic illustration of the suppressed phase transition from perovskites to nonperovskites via mixing ions ($A = \text{Cs}$, FA ; $M = \text{Pb}$, Sn ; $X = \text{I}$, Br). The presented structures here are a $(1 \times 1 \times 2)$ supercell of the δ -phase nonperovskite (left) and a unit cell of the γ -phase perovskite for CsMX_3 (right).

3.2. Methods

3.2.1. Computational methods and structural models

Structure optimizations were performed using DFT as implemented in the Vienna ab-initio simulation package (VASP) [137]. The PBEsol functional [109] was used. The projector-augmented wave (PAW) pseudopotentials [138, 139] were used to treat semi-core electronic states, with the $\text{Cs}[5s^2 5p^6 6s^1]$, $\text{Pb}[6s^2 6p^2 5d^{10}]$, $\text{Sn}[5s^2 5p^2 4d^{10}]$, $\text{I}[5s^2 5p^5]$, $\text{Br}[4s^2 4p^5]$, $\text{C}[2s^2 2p^2]$, $\text{N}[2s^2 2p^3]$ and $\text{H}[1s^1]$ electrons being treated as valence states. For CsMX_3 (CsPbI_3 , CsSnI_3 , and CsSnBr_3) and its alloys, a $2 \times 1 \times 1$ supercell for the γ -phase (perovskite phase for CsMX_3) and a $1 \times 1 \times 2$ supercell for the δ -phase (nonperovskite phase for CsMX_3) were used, respectively (Figure 3.1). For FAPbI_3 and its alloys, the $2 \times 2 \times 2$ (cubic phase) and $1 \times 1 \times 2$ supercells were used for the α -phase (perovskite phase for FAPbI_3) and δ -phase (nonperovskite phase for FAPbI_3), respectively (Figure A.1).

To select a functional used in this work, we tested PBE [108], PBEsol [109], and SCAN-rvv10 [140]. From Table A.1-S3, the PBEsol functional gives the most accurate lattice parameters for all perovskites compared with experiments, while PBE generally

overestimates the lattice parameters and SCAN-rvv10 severely underestimates the lattice parameters of inorganic perovskites and nonperovskites. Therefore, the PBEsol functional was used for all the calculations in this work. During the structural optimization, the positions of all atoms, and the shape and the volume of the unit cell were allowed to relax (ISIF = 3). All space groups of pure perovskites or pure nonperovskites were preserved after geometry optimization. For the alloys, most of the structures maintained their initial space groups except for a few cases. These are the nonperovskite Sn-Pb alloys, which will be further discussed in the Results and discussion section. An energy cutoff of 500 eV and $6 \times 4 \times 6$, $4 \times 10 \times 2$, $4 \times 4 \times 4$, and $8 \times 8 \times 4$ k -point meshes were used for γ -CsMX₃, δ -CsMX₃, α -FAPbI₃, and δ -FAPbI₃ to achieve energy and force convergence of 0.01 meV and 20 meV/Å, respectively.

To study the mixed compounds, we have considered seven [CsSn(Br_zI_{1-z})₃, $z = 0, 1/6, 1/3, 1/2, 2/3, 5/6$ and 1] and five [Cs_xFA_{1-x}PbI₃, $x = 0, 1/4, 1/2, 3/4, 1$; CsSn_yPb_{1-y}I₃, $y = 0, 1/4, 1/2, 3/4, 1$] compositions by interchanging the type and number of X, A, and M ions in the simulation cells, respectively. Owing to a large number of possible configurations of the mixed halide X (22, 139, 252, 139 and 22 possible configurations for $z = 1/6, 1/3, 1/2, 2/3, \text{ and } 5/6$, respectively) and the mixed M cation (5, 10, and 5 possible configurations for $y = 1/4, 1/2, \text{ and } 3/4$, respectively), we have calculated only two possible configurations for each, namely, two extreme cases with maximum and minimum formation energies selected by the strategy illustrated in our previous publication [141]. Previous observations from experiments show that FA cations are disordered at a finite temperature in the α -FAPbI₃ phase [142]. The reported FAPbI₃ perovskite configuration with a tilted FA cation in a $1 \times 1 \times 1$ cell is energetically favourable [143, 144]. To take these two effects into account, we tested eight configurations of the $2 \times 2 \times 2$ α -FAPbI₃ perovskite and four configurations of $1 \times 1 \times 2$ δ -FAPbI₃ nonperovskites (in the order of increasing degree of the FA disorder), respectively (see Figure A.2 and A.3). We used the most stable configuration for the perovskite and nonperovskite FAPbI₃ as a starting point to study the mixed perovskites. For mixing A cation, 3, 6, and 3 possible configurations were calculated for the Cs_xFA_{1-x}PbI₃ perovskite (using a supercell $2 \times 2 \times 2$) for $x = 1/4, 1/2, \text{ and } 3/4$,

respectively; 2, 4, and 2 possible configurations were considered for the $\text{Cs}_x\text{FA}_{1-x}\text{PbI}_3$ nonperovskite for $x = 1/4, 1/2, \text{ and } 3/4$, respectively. The details are shown in Supporting Information in Figures A.4-S9. Overall, when Cs cations occupy positions along the (1 1 1) direction of the $2 \times 2 \times 2$ $\text{Cs}_x\text{FA}_{1-x}\text{PbI}_3$ perovskite supercells, the FA cations tend to be more disordered, leading to a more stable configuration. The energy differences in different configurations of the $\text{Cs}_x\text{FA}_{1-x}\text{PbI}_3$ nonperovskite are relatively small (compared to those of the perovskite phase) and show no clear trends.

3.2.2. Calculations of formation energy

The formation energy of pure perovskite AMX_3 is defined as $\Delta H = E_{\text{AMX}_3} - E_{\text{AX}} - E_{\text{MX}_2}$, where E_{AMX_3} , E_{AX} , and E_{MX_2} are the total energy of AMX_3 , AX , and MX_2 , respectively. For the mixed perovskites, because of different precursors and synthesis routes, the expressions can differ. The formation energy of $\text{Cs}_x\text{FA}_{1-x}\text{PbI}_3$ is defined as $\Delta H = E_{\text{Cs}_x\text{FA}_{1-x}\text{PbI}_3} - xE_{\text{CsI}} - (1-x)E_{\text{FAI}} - E_{\text{PbI}_2}$, where $E_{\text{Cs}_x\text{FA}_{1-x}\text{PbI}_3}$, E_{CsI} , E_{FAI} , and E_{PbI_2} are the total energy of $\text{Cs}_x\text{FA}_{1-x}\text{PbI}_3$, CsI , FAI , and PbI_2 , respectively. The formation energy of $\text{CsSn}_y\text{Pb}_{1-y}\text{I}_3$ is defined as $\Delta H = E_{\text{CsSn}_y\text{Pb}_{1-y}\text{I}_3} - E_{\text{CsI}} - yE_{\text{SnI}_2} - (1-y)E_{\text{PbI}_2}$, where $E_{\text{CsSn}_y\text{Pb}_{1-y}\text{I}_3}$, E_{CsI} , E_{SnI_2} , and E_{PbI_2} are the total energy of $\text{CsSn}_y\text{Pb}_{1-y}\text{I}_3$, CsI , SnI_2 , and PbI_2 , respectively. The formation energy of $\text{CsSn}(\text{Br}_z\text{I}_{1-z})_3$ is defined as $\Delta H = E_{\text{CsSn}(\text{Br}_z\text{I}_{1-z})_3} - zE_{\text{CsBr}} - (1-z)E_{\text{CsI}} - zE_{\text{SnBr}_2} - (1-z)E_{\text{SnI}_2}$, where $E_{\text{CsSn}(\text{Br}_z\text{I}_{1-z})_3}$, E_{CsBr} , E_{CsI} , E_{SnBr_2} , and E_{SnI_2} are the total energy of $\text{CsSn}(\text{Br}_z\text{I}_{1-z})_3$, CsBr , CsI , SnBr_2 , and SnI_2 , respectively. A negative value of ΔH represents the favourable formation of the perovskite compounds: the more negative the ΔH , the easier the formation of the corresponding compound. The configurations of CsI , FAI , PbI_2 , and SnI_2 used for formation energy calculations are listed in Figure A.10.

3.2.3. Crystal orbital hamilton population analysis

The partial density of states (pDOS) and the crystal orbital hamilton population (COHP) [145-147] analysis were computed with the Lobster code [148], *via* transformation of the plane wave functions obtained by VASP into a localized basis set (STO). The pDOS provides information on the probability to find an electron with

energy E in atomic orbitals. Related to the pDOS, the COHP allows partitioning of the electron density distribution into bonding, nonbonding, and antibonding interaction domains. The $-\text{COHP}_{ij}(E)$ is defined as:

$$-\text{COHP}_{ij}(E) = H_{ij} \sum_n c_i^n c_j^{*n} \delta(E - E_n) \quad (3.1)$$

where H_{ij} represents the Hamiltonian matrix element between atomic orbitals φ_i and φ_j , and c_i and c_j are the coefficients of these atomic orbitals in the molecular orbital ψ_n ($\psi_n = \sum_i c_i^n \varphi_i$). A positive value for $-\text{COHP}_{ij}(E)$ symbolizes a bonding electronic interaction between the atomic orbitals i and j , while a negative value describes an antibonding interaction. A value of zero is associated with a nonbonding interaction.

The integrated value of $\text{COHP}_{ij}(E)$, named integrated COHP (ICOHP), is a good indication and usually used to measure the bond strength. The ICOHP was also proven to be very powerful in analyzing the phase stability [149], magnetism [150], and catalytic reactivity [151-153] of solid-state materials. To be consistent with $-\text{COHP}_{ij}(E)$, we use the $-\text{ICOHP}$ thereafter for convenient analysis, that is, a straightforward comparison of the positive values. It is commonly believed that the electronic states near the Fermi level often play an important role in affecting the nature of bonding relevant to the phase transitions [154]. Therefore, in this study, we closely investigate the $-\text{ICOHP}$ from -4.5 eV up to the Fermi level (Figure 3.2), which can be expressed as:

$$-\text{ICOHP}_{ij} = - \int_{-4.5}^{E_F} \text{COHP}_{ij}(E) dE \quad (3.2)$$

The more positive $-\text{ICOHP}$ means the stronger bond strength. It should be noted that $-\text{ICOHP}$ in this work is an average value of all metal-halide bonds per the AMX_3 formula unit; for perovskites containing the organic cation FA, the $\text{NH}\cdots\text{I}$ hydrogen bonding is also included.

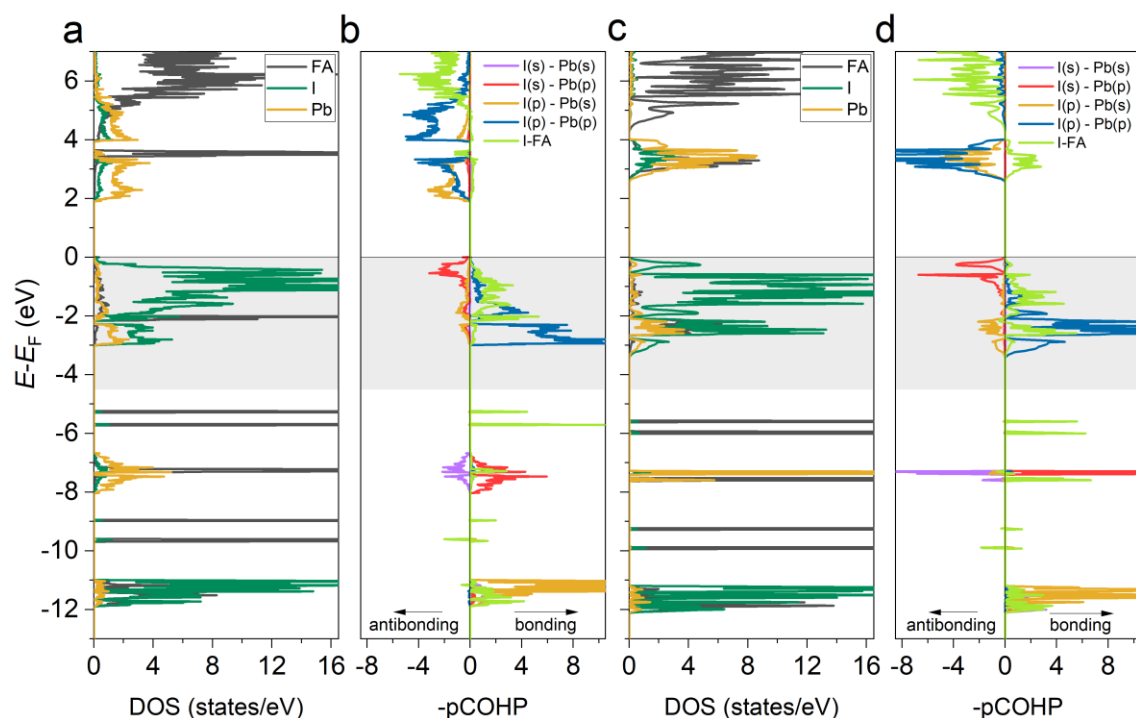


Figure 3.2. Comparison of pDOS and COHP analyses of FAPbI₃ in the form of the perovskite and nonperovskite: (a, c) pDOS and (b, d) orbital resolved COHP (pCOHP). The COHP plots are normalized by each AMX₃ formula unit.

3.2.4. Chemical bonding in AMX₃ perovskites

To investigate the underlying reason for the unwanted phase transition in MHPs, we analyze the nature of the chemical bonding of the typical perovskite and nonperovskite. Figure 3.2 shows a direct comparison of pDOS and COHPs of FAPbI₃ in the forms of the perovskite and nonperovskite, giving the bonding and antibonding characters and indicating which atomic orbitals are involved in the relevant chemical bonding. As frequently reported in the literature [44, 155-158], the metal-halide characters dominate the conduction band and valence band band edges. In both phases, four pairs of bonding and antibonding interactions including I(s)Pb(p), I(s)Pb(s) and I(p)Pb(s), I(p)Pb(p) (shown in Figure 3.2b, d) form as a result of the hybridization of *s* and *p* orbitals of the metal cation and halide anion. It should be noted that, in the case of organic cations, they also form hydrogen bonds with the halide, for example, the FA-I bonding in FAPbI₃ perovskites also contributes to the bonding state. This pattern does not hold for all-inorganic perovskites, where Cs cation characters are almost absent in the orbital-resolved COHP of CsSnI₃ (Figure A.11), implying that the inorganic A-site

cation does not participate in covalent bonding. Therefore, for all-inorganic perovskites, we only focus on the metal-halide interactions. As previous studies [159, 160] show that the phase transition behavior of a particular material can very often find its origin in the electronic levels, in our case we will investigate the relevant bonding from the COHPs near the Fermi level (shaded in Figure 3.2). Usually, a dominant antibonding near a Fermi level associates with the phase instability. However, the COHP characters of both phases are of similar nature, where bonding and antibonding states appear in a similar energy range and originated from the same pairs of orbitals: I(s)Pb(p), I(s)Pb(s) and I(p)Pb(s), I(p)Pb(p). For a more straightforward comparison, we use integrated COHP (ICOHP) as a measure of the strength of overall interactions and we systematically investigate the bond strength differences between perovskites and nonperovskites.

3.2.5. Mixing thermodynamics

To assess the thermodynamic stability of mixed perovskites (solid solution), we evaluated the free energy of mixing (ΔF) [131, 161] for each composition according to the expression:

$$\Delta F = \Delta H - T\Delta S \quad (3.3)$$

where ΔH and ΔS are the enthalpy of mixing and entropy of mixing, respectively, and T is the absolute temperature. According to Schelhas *et al.*, [162] the enthalpy of mixing could be approximately given by the change in the internal energy (ΔU), which is the difference between the total energy of the mixed halide perovskite with respect to the total energy of the constituents. Thus, the enthalpy of mixing of the mixed perovskite could be approximately given as:

$$\Delta H = \Delta U = E_{\text{mixed-perovskite}} - xE_{\text{component 1}} - (1-x)E_{\text{component 2}} \quad (3.4)$$

where $E_{\text{mixed-perovskite}}$, $E_{\text{component 1}}$, and $E_{\text{component 2}}$ are the total energies of mixed perovskite, component 1, and component 2, respectively. The entropy of mixing is calculated in the homogeneous limit according to the formula:

$$\Delta S = -k_B[x \ln x + (1 - x) \ln(1 - x)] \quad (3.5)$$

where k_B is the Boltzmann constant.

3.2.6. Formation energy calculation of Sn vacancy

We calculate the formation energies of Sn vacancy of $\text{CsSn}_y\text{Pb}_{1-y}\text{I}_3$ perovskite ($y = 0.25, 0.5, \text{ and } 0.75$). As references, we also calculate the same formation energy of pristine CsSnI_3 . The details of the computational procedure are as follows. The formation energy of Sn vacancy have been calculated by using a $2 \times 2 \times 1$ supercell, as given in Equation 3.6.

$$\Delta E_{vac} [\text{CsSn}_y\text{Pb}_{1-y}\text{I}_3] = E_{tot} [\text{Sn}_{vac}] - E_{tot} [\text{perovskite}] + \mu[\text{Sn}] + E_f \quad (3.6)$$

where $E_{tot} [\text{Sn}_{vac}]$ and $E_{tot} [\text{perovskite}]$ are the total energies of the perovskite with and without Sn vacancy, respectively, and $\mu[\text{Sn}]$ and E_f are the chemical potential of Sn and Fermi energy, respectively. The $\mu[\text{ion}]$ is assumed to be the same for all perovskites. This approximation is valid because in our experiments the important parameters (e.g., precursor concentration, the source of ions, and synthesis temperature) during synthesis process of these perovskites are kept the same. The E_f is assumed to be similar or with negligible difference for $\text{CsSn}_y\text{Pb}_{1-y}\text{I}_3$ and CsSnI_3 [25].

We define the relative formation energy as Ref [163]. The suppression of Sn vacancy formation by mixing Sn and Pb is quantitatively evaluated by eq 3.7:

$$\Delta \Delta E_{vac} = \Delta E_{vac} [\text{Sn-Pb}] - \Delta E_{vac} [\text{Sn}] \quad (3.7)$$

Where $\Delta E_{vac} [\text{Sn-Pb}]$ is the formation energy of Sn vacancy in Sn and Pb mixed perovskite, and $\Delta E_{vac} [\text{Sn}]$ represents the one of the pure CsSnI_3 perovskite.

3.2.7. Synthesis of $\text{CsSn}_{1-y}\text{Pb}_y\text{I}_3$ quantum dots

All chemicals were used as received without further purification. 0.74 g of SnI_2 (99%, Wako Pure Chemicals, Japan) and 0.2-0.5 g of PbI_2 (99%, Sigma-Aldrich, USA) were mixed into 2.5 mL of tri-*n*-octylphosphine (TOP, 97%, Sigma-Aldrich, USA) to prepare a TOP- SnI_2 - PbI_2 stock solution. The mixture was vigorously stirred on a hot plate at 90 °C for about 3 h. In a 50 mL three-neck flask, 0.12 g of Cs_2CO_3 (99.9%, Sigma-Aldrich,

USA), 0.4 mL of oleic acid ($\geq 65.0\%$, Wako Pure Chemicals, Japan), and 0.4 mL of oleylamine (70%, Sigma-Aldrich, USA) were added into 12 mL of octadecene (90%, Sigma-Aldrich, USA). The mixture was degassed at 100 °C for 3 h with vigorous stirring and then heated to 120 °C under a nitrogen atmosphere until the solution became clear (the temperature was monitored using a Sanyo mercury thermometer, Japan). The temperature was then set at 160 °C followed by the quick injection of the above-prepared TOP-SnI₂-PbI₂ solution. About 5 secs after the injection, the reaction was quenched by the immediate immersion of the flask into an ice bath. QDs were precipitated by adding 25 mL of methyl acetate (MeOAc, anhydrous 99.5%, Sigma-Aldrich, USA), followed by centrifugation at 4000 rpm for 3 min. The supernatant was discarded, and the QD precipitate was dispersed in hexane. The detailed synthetic recipes for obtaining perovskites with various mixed Pb and Sn compounds are summarized in Table A.4.

3.3. Results and discussion

3.3.1. Suppression of the phase transition by mixing Cs and FA in Cs_xFA_{1-x}PbI₃

For both pure FAPbI₃ and pure CsPbI₃ perovskites, the formation energies of the nonperovskite are more negative when compared with those of the perovskite (Figure 3.3a), indicating that the perovskite phase is unfavourable. Upon mixing Cs and FA, the difference in formation energies of the perovskite and nonperovskite become smaller. A critical point appears near $x = 0.25$, where the difference reaches a minimum, which is in agreement with the experimental observation that the better stability of the perovskite Cs_xFA_{1-x}PbI₃ solid-state alloys was observed with x roughly in the range of $0.2 \leq x \leq 0.3$ [13, 164].

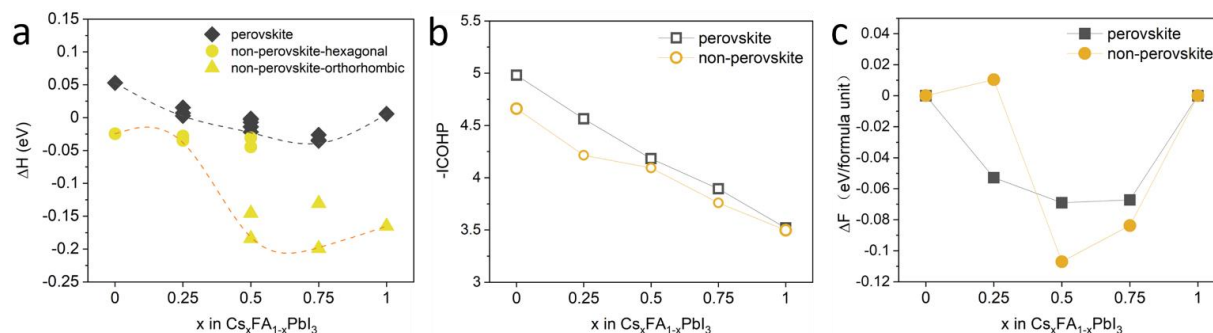


Figure 3.3. (a) Formation energy (ΔH), (b) -ICOHP, and (c) free energy of mixing (ΔF) of perovskite and nonperovskite $\text{Cs}_x\text{FA}_{1-x}\text{PbI}_3$. The lines are included to guide the eye. All these -ICOHP and ΔF are calculated by using the most stable structure, that is, with the most negative ΔH . It should be noted that the cubic phase of CsPbI_3 for the perovskite is used here to compare consistently with the FAPbI_3 perovskite phase.

To understand the changes in formation energy, we study in detail the atomistic structures of both the perovskite and nonperovskite. As shown in Figure 3.4, for FAPbI_3 , the average bond length of the perovskite is equal to the nonperovskite (3.22 Å), which indicates a similar metal-halide bond strength in the perovskite and nonperovskite. With the introduction of 25% Cs, the local geometry within the PbI_6 octahedral and the average bond length of metal-halide bonds in the perovskite become slightly smaller than those in the nonperovskite (3.17 vs 3.20 Å), indicating a slight stabilization effect when a small amount of Cs is introduced in FAPbI_3 . This is in good agreement with the experimental observations, the phase stability of FAPbI_3 is enhanced with 25% Cs doping [13, 164].

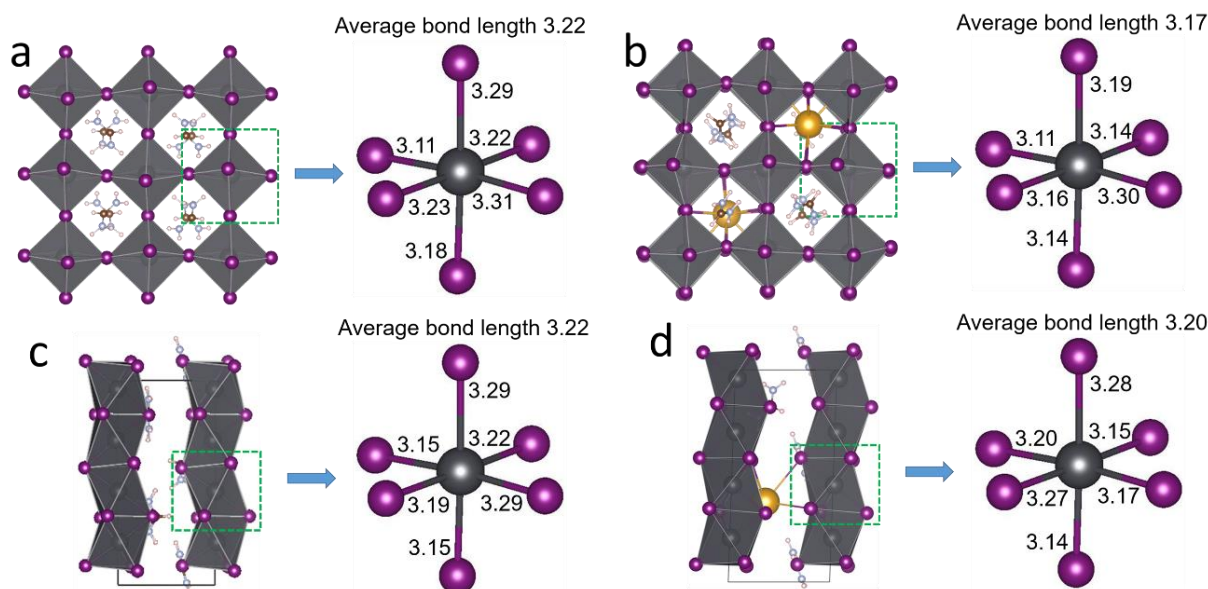


Figure 3.4. Comparison of structures of perovskite and nonperovskite $\text{Cs}_x\text{FA}_{1-x}\text{PbI}_3$. Atomistic structure and bond lengths of corresponding Pb-I bonds in angstroms of (a) perovskite FAPbI_3 , (b) perovskite $\text{Cs}_{0.25}\text{FA}_{0.75}\text{PbI}_3$, (c) nonperovskite FAPbI_3 , and (d) nonperovskite $\text{Cs}_{0.25}\text{FA}_{0.75}\text{PbI}_3$, respectively. The purple, light blue, brown, light pink, dark grey, and dark yellow spheres denote I, N, C, H, Pb, and Cs atoms, respectively.

The trends in the formation energies and the structures could be explained by -ICOHP of the perovskite and nonperovskite in Figure 3.3b and data set in Table A.5. The -ICOHP is a measurement for the strength of a chemical bond between a pair of atoms, with a larger -ICOHP signifying a stronger bond. From Figure 3.3b, we observe that with the increasing concentration of Cs, the -ICOHPs of both phases decrease. This is because the interaction of the FA cation with I anions also contributes significantly to the -ICOHP, which decreases with the increase in the Cs concentration of the alloys. Compared to all the compositions from Figure 3.3b, the smallest difference in -ICOHP of the perovskite and nonperovskite is observed for pure CsPbI_3 , where the -ICOHP of the perovskite is very slightly larger than that of the nonperovskite (3.52 vs 3.50). This agrees with the instability of the perovskite CsPbI_3 structure. The differences become larger upon alloying FA with Cs. The largest differences in -ICOHP between the perovskite and nonperovskite were observed at 75% of FA, that is, 25% Cs (4.56 vs 4.21), indicating that the difference between the overall bonding strength of the perovskite and nonperovskite reaches a maximum.

We note that although the -ICOHP of the pure FAPbI₃ perovskite is larger than that of nonperovskite (4.98 vs 4.67), the difference between the two (0.31) is slightly smaller than that of Cs_{0.25}FA_{0.75}PbI₃ (0.35). We explain this by the stronger FA-I bond (characterized by -ICOHP) in the perovskite phase than that in the nonperovskite phase (0.89 vs 0.87, in Table A.5). This means that the FA-I hydrogen bond plays a vital role in the phase stability of Cs and FA mixed compounds. To better understand the role of the FA-I hydrogen bond in the phase stability of Cs_xFA_{1-x}PbI₃, we summarize the NH...I bond lengths with different Cs concentrations in Figure 3.5. Typically, the length of NH...I hydrogen bonds between -NH₂ groups and the iodide atoms of the [PbI₆] framework fall in the range of <3.00 Å [134]. From Figure 3.5, the average bond length of all hydrogen bonds in perovskite and nonperovskite FAPbI₃ are 2.85 and 2.77 Å, respectively. Upon mixing Cs into FAPbI₃, the change of the average hydrogen bond length follows two distinct trends for 25% Cs and for those of higher percentages, that is, 50 and 75%. Adding 25% Cs into FAPbI₃ leads to the formation of a stronger perovskite phase (average bond length of 2.80 Å) as well as a weaker nonperovskite phase (average bond length of 2.89 Å). This stabilizes the Cs_{0.25}FA_{0.75}PbI₃. However, adding more Cs have the opposite effect (2.85 Å for the perovskite and 2.61 Å for the nonperovskite with 50% Sn; 2.85 Å for the perovskite and 2.73 Å for the nonperovskite with 75% Sn), giving rise to a destabilization effect. This confirms the experimental observation that about 25% Cs is optimum to stabilize the FAPbI₃ perovskite.

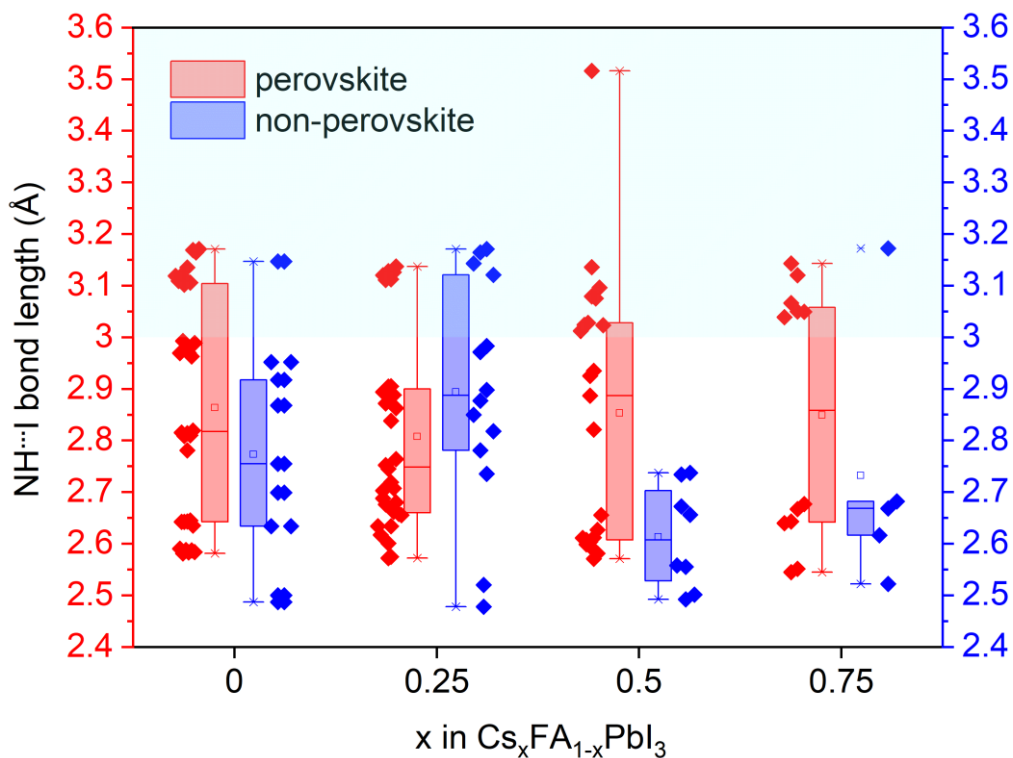


Figure 3.5. NH...I bond lengths in the perovskite and nonperovskite of $\text{Cs}_x\text{FA}_{1-x}\text{PbI}_3$ ($x = 0, 0.25, 0.5,$ and 0.75).

We note that while our DFT calculations indicate the relative stability of the perovskite of the mixed Cs and FA compared to the nonperovskite at 0 K, they cannot account for the temperature effect. To better represent the thermodynamics of these alloys, we also calculated the free energy of mixing (ΔF) to determine the mixing thermodynamics of the involved perovskite alloys. The negative value of ΔF indicates the favour of mixing. In Figure 3.3c, the ΔF are all negative except at the $\text{Cs}_{0.25}\text{FA}_{0.75}\text{PbI}_3$ nonperovskite, indicating more favourable mixing of the perovskite phase than mixing of the nonperovskite phase.

Taking all analyses mentioned above (the energies, the atomic structures and the bonding strength of the M-X bonds, and FA-I hydrogen bonds), we argue that the mixed compositions of $\text{Cs}_x\text{FA}_{1-x}\text{PbI}_3$, in particular with relatively low concentration of Cs (25%), the perovskite structure is more favourable compared with their nonperovskite counterparts; therefore, they are less likely to undergo the phase transition from perovskites to nonperovskites.

3.3.2. Suppression of the phase transition by mixing Br and I in $\text{CsSn}(\text{Br}_z\text{I}_{1-z})_3$

From Figure 3.6a, the formation energies of perovskite and nonperovskite CsSnI_3 are almost the same, while those of perovskite CsSnBr_3 is much negative compared with those of the nonperovskite, indicating that the perovskite phase of CsSnI_3 is metastable and that of CsSnBr_3 is stable. Upon mixing Br and I, the formation energies of $\text{CsSn}(\text{Br}_z\text{I}_{1-z})_3$ show a unique trend with a critical point at $z = 1/3$, which is also shown in our previous work [141]. When $z > 1/3$, all formation energies of the perovskite are more negative than those of the nonperovskite, indicating the perovskite being more stable than the nonperovskite.

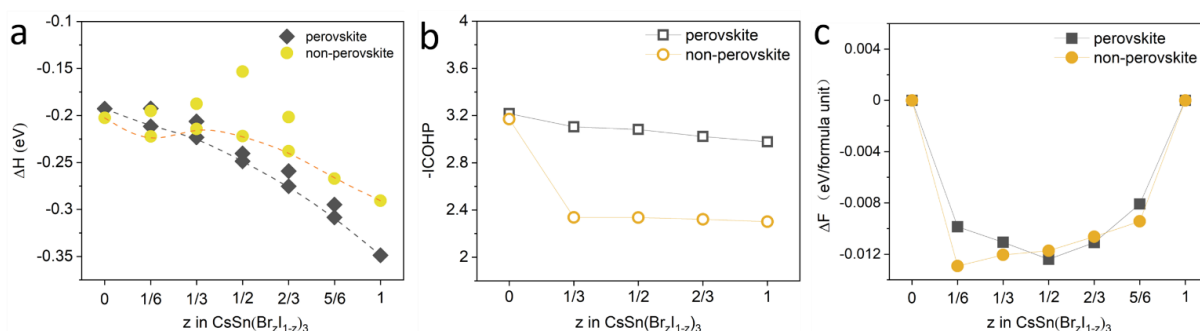


Figure 3.6. (a) Formation energy, (b) $-\text{ICOHP}$, and (c) free energy of mixing of perovskite and nonperovskite $\text{CsSn}(\text{Br}_z\text{I}_{1-z})_3$. The lines are included to guide the eye.

The trends in the energies are also reflected by the trends in the structures in Figure 3.7. Generally, the average Sn-X bond length in the perovskite is shorter than that in the nonperovskite. For CsSnI_3 , the average Sn-X bond length in the perovskite is shorter than that in the nonperovskite (3.11 vs 3.17 Å). With the increasing concentration of Br, the average bond length of the perovskite decreased more obviously than that of the nonperovskite, leading to much stronger bonds in the perovskite than in the nonperovskite (3.04 vs 3.14 Å for CsSnBrI_2). Therefore, the phase transition is less likely to occur. The introduction of more Br to even 100% also makes the Sn-X bonds much stronger in the perovskite than in the nonperovskite.

The bonding analysis shows similar trends to those of the energies and the structures. Figure 3.6b and Table A.6 show that $-\text{ICOHP}_{\text{perovskite}}$ decreases slightly with the increasing percentage of Br, while $-\text{ICOHP}_{\text{nonperovskite}}$ decreases drastically in the range of $z \leq 1/3$ and then remains constant at a higher Br concentration. As a result,

the difference in the -ICOHPs of the perovskite and nonperovskite first increases sharply in the range of $z \leq 1/3$ and then maintains a large difference in the range of $1/3 < z < 1$. Indeed, previous experimental results agree with our theoretical analysis, where the perovskite black phase (γ -phase) becomes more stable and the transition to the nonperovskite is less likely with the increasing Br percentage in $\text{CsSn}(\text{Br}_z\text{I}_{1-z})_3$. The transition point is formed when the concentration of Br is being around $1/3$ [165, 166]. For both the perovskite and nonperovskite, the free energy of mixing (ΔF) is negative (Figure 3.6c) upon mixing Br and I, being favourable for mixing.

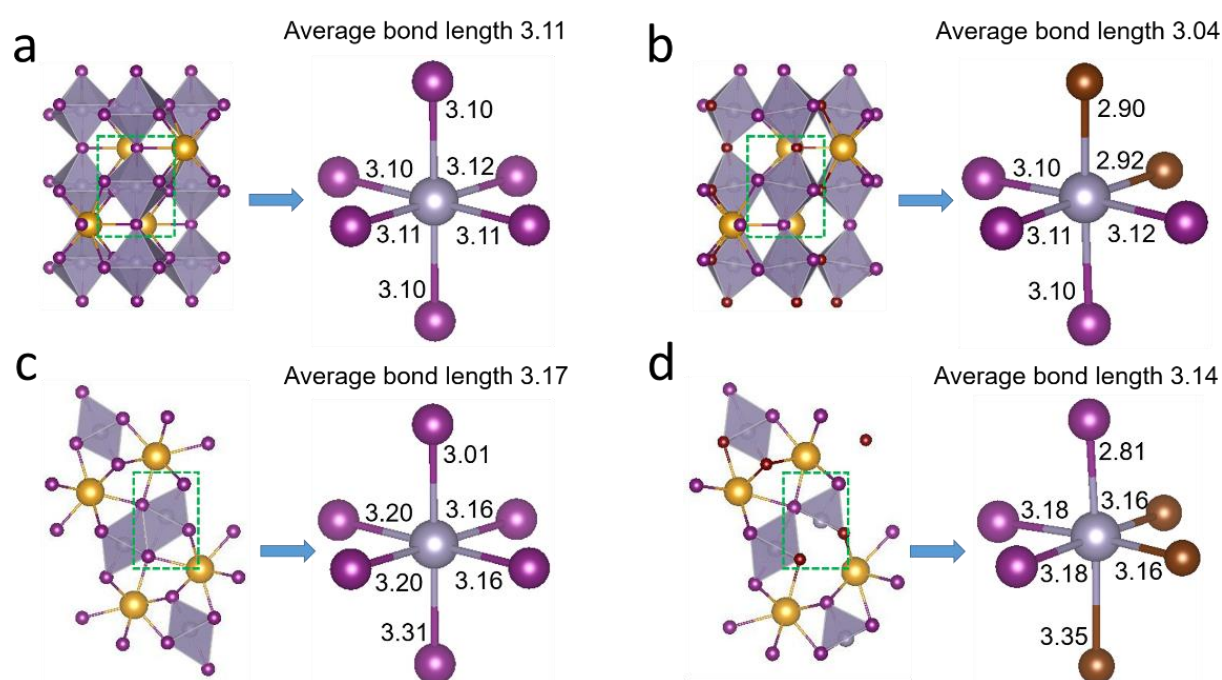


Figure 3.7. Comparison of structural properties of perovskite and nonperovskite $\text{CsSn}(\text{Br}_z\text{I}_{1-z})_3$. Crystal structure and bond lengths of Sn-X bonds (in units of Å) of (a) perovskite CsSnI_3 , (b) perovskite CsSnBrI_2 , (c) nonperovskite CsSnI_3 , and (d) nonperovskite CsSnBrI_2 , respectively.

3.3.3. Experimental observation of the phase transition in $\text{CsSn}_y\text{Pb}_{1-y}\text{I}_3$

While the stabilization effect of mixing A cations (Cs and FA) [13, 164] and X anions (Br and I) [165, 166] of MHPs is widely characterized experimentally, mixing of M cations (e.g., Sn and Pb) is less studied. Herein, we synthesized a group of colloidal $\text{CsSn}_y\text{Pb}_{1-y}\text{I}_3$ quantum dots (QDs). Figure 3.8 shows photographs of solutions of $\text{CsSn}_y\text{Pb}_{1-y}\text{I}_3$ ($y = 0, 0.25, 0.5, 0.75, \text{ and } 1$) QDs taken at different periods of time. By

comparing these images, the stability of the mixed colloidal QDs can be compared to those of pure CsSnI_3 and pure CsPbI_3 QDs. When exposed to air, the reference as-synthesized CsSnI_3 and CsPbI_3 QDs are the ones that are first degraded, evidenced by the change of color from black to yellow or orange; CsSnI_3 has the poorest stability (degraded in 10 min), followed by CsPbI_3 (turned orange before 80 days). A much improved stability was found for all mixed QDs, $\text{CsSn}_y\text{Pb}_{1-y}\text{I}_3$ ($y = 0.25, 0.5, 0.75$), where the $\text{CsSn}_{0.75}\text{Pb}_{0.25}\text{I}_3$ QDs are the most stable, maintaining their black colour throughout 170 days observation period. At this stage, the $\text{CsSn}_{0.25}\text{Pb}_{0.75}\text{I}_3$ QDs already converted into the nonperovskite, and the $\text{CsSn}_{0.5}\text{Pb}_{0.5}\text{I}_3$ QDs also partially transformed into the nonperovskite. To understand the improved phase stability of $\text{CsSn}_y\text{Pb}_{1-y}\text{I}_3$, especially the case of $\text{CsSn}_{0.75}\text{Pb}_{0.25}\text{I}_3$, we perform a series of theoretical analyses as we have done above for mixing A cations and X anions.

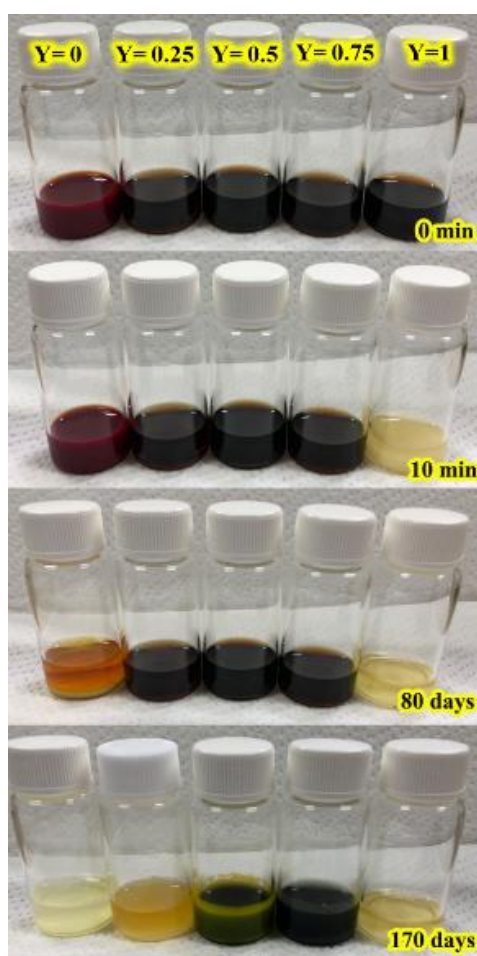


Figure 3.8. Photographs taken at different periods for solutions of the as-synthesized $\text{CsSn}_y\text{Pb}_{1-y}\text{I}_3$ QDs ($y = 0, 0.25, 0.5, 0.75, \text{ and } 1$ from left to right) stored in ambient air. All samples were dispersed in hexane.

3.3.4. Suppression of the phase transition by mixing Sn and Pb in $\text{CsSn}_y\text{Pb}_{1-y}\text{I}_3$

The formation energies of the perovskite are less negative than those of the nonperovskite for both CsPbI_3 and CsSnI_3 (Figure 3.9a), indicating that the perovskite phase is unfavourable. For Sn-Pb mixed compounds, the difference in formation energies of the perovskite and nonperovskite decreases and reaches the minimum difference with 75% Sn. This is a consequence of the faster decrease in the formation energies of the perovskite compared with those of the nonperovskite counterpart with an increasing amount of Sn. The trend in the energies implies that upon mixing Sn with Pb, the perovskite is more favourable with the increasing percentage of Sn.

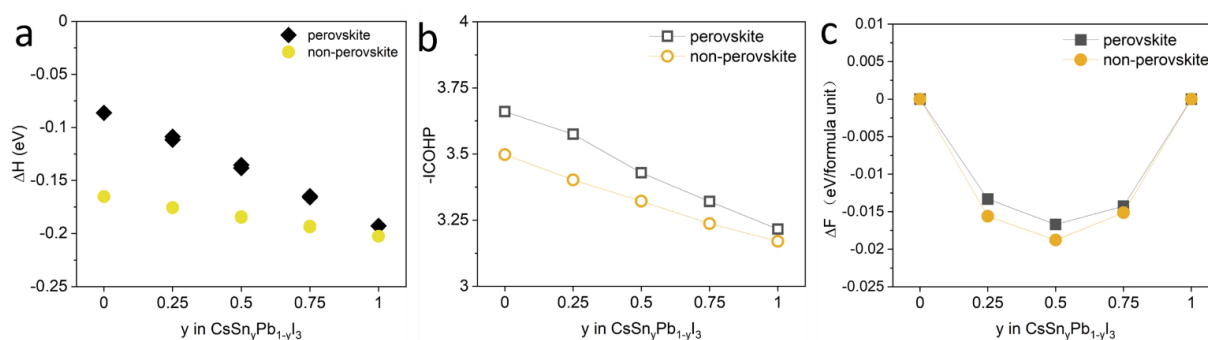


Figure 3.9. (a) Formation energy, (b) -ICOHP, and (c) free energy of mixing for perovskite and nonperovskite $\text{CsSn}_y\text{Pb}_{1-y}\text{I}_3$. The lines are included to guide the eye.

We also compared the atomistic structures of CsPbI_3 and Sn-Pb mixed compounds, using $\text{CsSn}_{0.75}\text{Pb}_{0.25}\text{I}_3$ as an example in Figure 3.10. The average Pb-I bond length of perovskite CsPbI_3 is shorter than that of the nonperovskite (3.18 vs 3.22 Å). Upon mixing 75% Sn with Pb, the average Pb-I bond length of the perovskite decreases while that of the nonperovskite remains the same (3.16 vs 3.22 Å). The trends of the formation energy and bond length are also found in the chemical bonding analysis in Figure 3.9b. With 75% Sn, the difference of -ICOHP is the smallest among all alloys and also smaller than pure CsPbI_3 (Figure 3.8b and Table A.7). From Figure 3.9c, the free energy of mixing is negative upon mixing Sn and Pb for both the perovskite and nonperovskite, thus favouring the mixing.

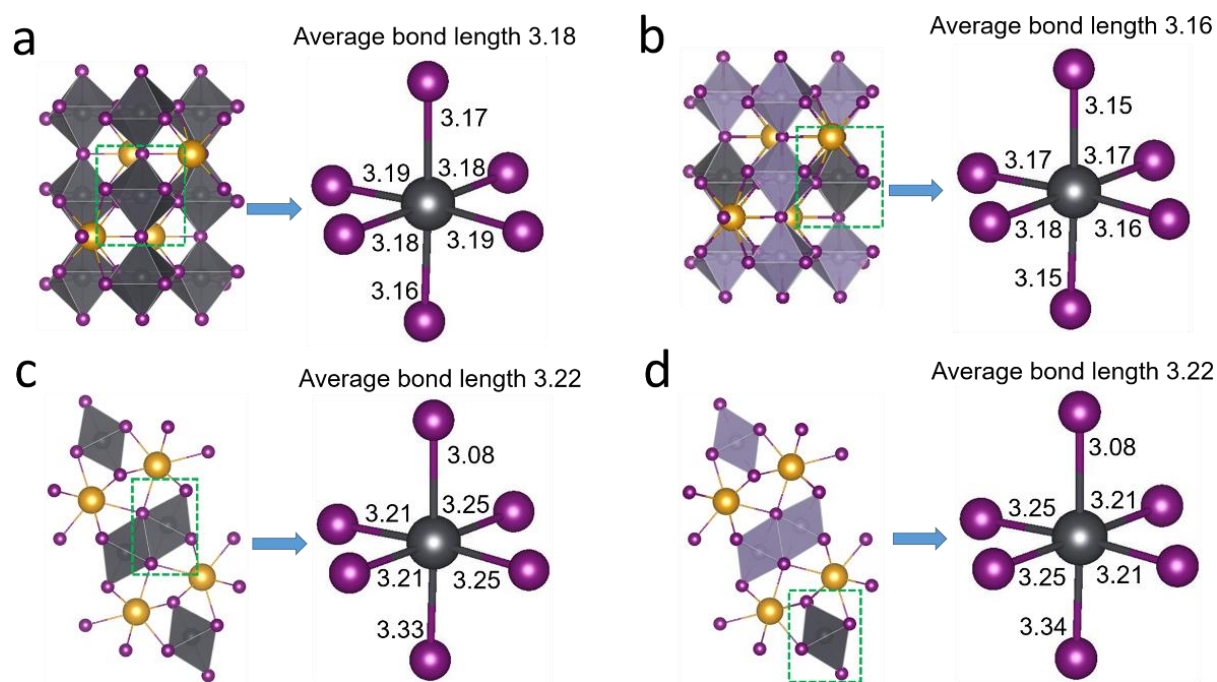


Figure 3.10. Comparison of structures of perovskite and nonperovskite $\text{CsSn}_y\text{Pb}_{1-y}\text{I}_3$. Atomistic structure and bond lengths of Pb-I bonds (in units of Å) of (a) perovskite CsPbI_3 , (b) perovskite $\text{CsSn}_{0.75}\text{Pb}_{0.25}\text{I}_3$, (c) nonperovskite CsPbI_3 , and (d) nonperovskite $\text{CsSn}_{0.75}\text{Pb}_{0.25}\text{I}_3$, respectively.

From above, we found that the increasing Sn concentration tends to stabilize the mixed perovskites, with $\text{CsSn}_{0.75}\text{Pb}_{0.25}\text{I}_3$ being the most stable. However, we are not able to explain the fact that the $\text{CsSn}_{0.75}\text{Pb}_{0.25}\text{I}_3$ is more stable than CsSnI_3 , because the trend in energies we established for other compositions is not applicable here. Considering the unique defect chemistry of Sn perovskites, that is, oxidation of Sn^{2+} to Sn^{4+} spontaneously occurring and often being facilitated by defects [167], we therefore deduce that the Sn vacancy may play an important role in stabilizing the mixed Sn-Pb perovskites. We therefore next calculate the defect formation energies of Sn vacancy (V_{Sn}) in $\text{CsSn}_y\text{Pb}_{1-y}\text{I}_3$ ($y = 1, 0.75, 0.5, \text{ and } 0.25$), as shown in Figure 3.11. We find that the V_{Sn} defect formation energy of Sn-Pb mixed perovskites is significantly higher than that of CsSnI_3 by about 0.3 to 1.0 eV. This means that the formation of V_{Sn} is greatly suppressed upon mixing of Sn and Pb, helping them to maintain the perovskite phase of the mixed compounds.

In summary, both the energy analysis mentioned above for the pristine/mixed Sn-Pb perovskites and the elevated Sn vacancy defect formation energy in their defective

structures point to the same conclusion of the mixed compounds being stabilized, agreeing with our experimental findings. We note that the stability of perovskite QDs can also be affected by the surface ligands [75, 168]. Nevertheless, the agreement of our theoretical validation and experimental tests indicates that the general trends found in the stability of such perovskite QDs are also valid for the bulk perovskites and vice versa.

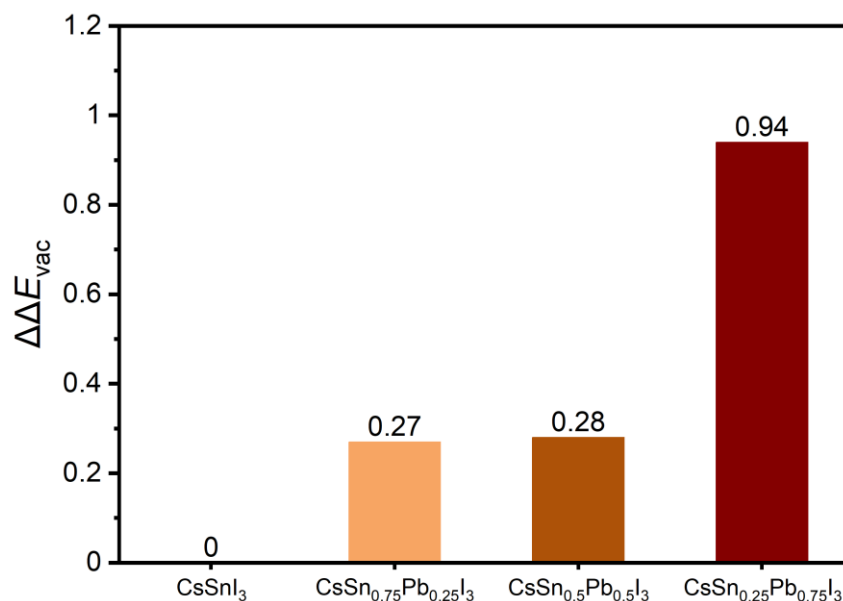


Figure 3.11. Calculated defect formation energies of V_{Sn} in $\text{CsSn}_y\text{Pb}_{1-y}\text{I}_3$ ($y = 1, 0.75, 0.5,$ and 0.25). The value of CsSnI_3 is set to zero for comparison.

3.4. Conclusions

By using DFT calculations, we systematically study the phase stability of several pure and mixed MHPs. We first reveal the atomistic and electronic origin of the phase transition from the perovskite to nonperovskite for some of the pure perovskites using FAPbI_3 , CsPbI_3 , and CsSnI_3 as examples and then investigate why mixing the A or M or X ion can suppress such undesired transitions. We find that the relative bond strength of the perovskite phase compared with their nonperovskite phase is an important parameter, which can be understood by analyzing the bond length, bond strength (-ICOHP), formation energies and/or free energy of mixing, and the Sn vacancy formation energy. By mixing A or M or X ions, the phase stability can be

improved by increasing the stability of the perovskite phase or destabilizing the nonperovskite phase, which will result in a suppressed phase transition from the perovskite phase to the nonperovskite phase.

When mixing Cs and FA in $\text{Cs}_x\text{FA}_{1-x}\text{PbI}_3$, the perovskite phase of the mixed perovskite is slightly more stabilized compared with the nonperovskite phase, leading to an overall better phase stability of the perovskite phases. The composition of 25% Cs (75% FA) is the most stable in the perovskite phase because of a drastic decrease in the hydrogen bond strength in the nonperovskite. Upon mixing Br into CsSnI_3 , the perovskite phase of mixed perovskites become more stable than that of nonperovskites when the Br concentration is larger than 1/3. This is because the introduction of Br makes much stronger Sn-X bonds in the perovskite compared with those in the nonperovskite and therefore suppresses the transition from the perovskite to the nonperovskite. When mixing Sn and Pb in $\text{CsSn}_y\text{Pb}_{1-y}\text{I}_3$, the combination of a stabilization effect found in the perovskite phase and the retarded Sn vacancies suppresses the undesired degradation in the Sn-Pb mixed compositions. We verify that the most stable compound is $\text{CsSn}_{0.75}\text{Pb}_{0.25}\text{I}_3$, in agreement with our experimental findings where $\text{CsSn}_{0.75}\text{Pb}_{0.25}\text{I}_3$ is extremely stable, maintaining its black phase for more than half a year in ambient conditions.

In conclusion, we identify that phase transitions of MHPs from the perovskite to the nonperovskite are correlated with the relative strength of the M-X bonds as well as hydrogen bonds (for hybrid compositions) and with the role of vacancy defects (in the case of Sn-containing perovskites). Using several well-known compositions as examples, we demonstrate that the phase stability of these perovskites can be tuned and optimized by mixing ions, which gives rise to either an increased bond strength of perovskites and/or a decreased bond strength in their nonperovskite counterparts or suppressed defect formation, that is, in the case of Sn-Pb mixed compounds. Insights from this study, therefore, set the fundamental basis for the design of phase-stable mixed perovskites.

Chapter 4

Stabilizing Lead-Free All-Inorganic Tin Halide Perovskites by Ion Exchange

Because of its thermal stability, lead-free composition and nearly ideal optical and electronic properties, the orthorhombic CsSnI₃ perovskite is considered promising as a light absorber for lead-free all-inorganic perovskite solar cells. However, the susceptibility of this three-dimensional perovskite toward oxidation in air has limited the development of solar cells based on this material. Here, we report the findings of a computational study which identifies promising Rb_yCs_{1-y}Sn(Br_xI_{1-x})₃ perovskites for solar cell applications, prepared by substituting cations (Rb for Cs) and anions (Br for I) in CsSnI₃. We show the evolution of the material electronic structure as well as its thermal and structural stabilities upon gradual substitution. Importantly, we demonstrate how the unwanted yellow phase can be suppressed by substituting Br for I in CsSn(Br_xI_{1-x})₃ with $x \geq 1/3$. We predict that substitution of Rb for Cs results in a highly homogeneous solid solution and therefore an improved film quality and applicability in solar cell devices.

This chapter is based on the publication: J Jiang, C K Onwudinanti, R A Hatton, P A Bobbert, S Tao, "Stabilizing Lead-Free All-Inorganic Tin Halide Perovskites by Ion Exchange", Journal of Physical Chemistry C, 2018. 122, 17660-17667.

4.1. Introduction

Organic-inorganic hybrid halide perovskite solar cells (PSCs) have attracted strong attention in the past few years and are becoming one of the most promising types of emerging thin-film solar cells [169-173]. In less than a decade, the power conversion efficiency (PCE) of PSCs has increased from 3.8% in 2009 to more than 25% now [3, 174]. Despite the high efficiency of PSCs, two challenges currently hinder their upscaling toward practical applications [131]. One issue is the long-term instability of PSCs, which is mainly caused by the intrinsic thermal instability of hybrid perovskite materials [175-180]. Encouragingly, it has been demonstrated recently that mixing the cations or replacing the organic cation with an inorganic cation can improve thermal stability and photostability (e.g., substituting FA for MA in MAPbI₃, Rb for Cs in CsSnI₃ and Cs for MA in MAPbI₃; MA stands for CH₃NH₃, and FA stands for NH₂CHNH₂) [131, 164, 181]. The other concern is the well-documented toxicity of lead (Pb), which is particularly problematic because lead halide perovskites decompose into lead compounds that have significant solubility in water [182]. Consequently, an intensive research effort focused on finding air-stable lead-free perovskites suitable as the light-harvesting semiconductor in PSCs is now underway [176, 183-186].

Among the various alternatives to lead, tin (Sn) is regarded as a promising substitute, because Sn-based hybrid perovskites have been shown to exhibit outstanding electrical and optical properties, including high charge carrier mobilities, high absorption coefficients and low exciton binding energies [187-189]. Theoretical predictions by Even *et al.* [155] and Chiarella *et al.* [190] also confirmed the promising properties of Sn perovskites, such as suitable band gaps and favourable effective mass. However, Sn-based perovskites also have drawbacks, which have limited their application in efficient PSCs [169, 189, 191-194]. The primary challenge is the susceptibility of tin toward oxidation from the +2 to the +4 oxidation state upon exposure to ambient air, which, in the case of CsSnI₃, ultimately results in the formation of Cs₂SnI₆, whose relatively weak light absorption across the visible spectrum is undesirable for a photoabsorber [188, 195-198]. Consequently, to date there has been much less research effort directed at the advancement of tin halide PSCs than

their lead analogues, and their PCE has remained below 10% [192, 193]. Recently, a PCE as high as 9.0% in PSCs was achieved using single-crystalline FASnI_3 , made by mixing a small amount of two-dimensional (2D) Sn perovskites with three-dimensional (3D) FASnI_3 in which the organic FA molecules are oriented randomly [199], an approach that promises further improvement.

As compared to hybrid organic-inorganic Sn perovskites, all-inorganic Sn perovskites could have the advantage of improved thermal stability while maintaining favourable optical and electronic properties for photovoltaic (PV) applications [200, 201]. For example, $\gamma\text{-CsSnI}_3$ is a *p*-type semiconductor with a high hole mobility [187, 202], a favourable band gap of ~ 1.3 eV, a low exciton binding energy, and a high optical absorption coefficient [41, 44]. There have been a few attempts to fabricate solar cells using $\gamma\text{-CsSnI}_3$ as a photoactive layer, but their maximum efficiency was still low. In 2012, Chen *et al.* [203] first used CsSnI_3 to fabricate a Schottky contact solar cell which achieved a PCE of 0.9%. In 2014, Kumar *et al.* [204] achieved a PCE of 2.02% by forming the perovskite from solution under Sn-rich conditions, using SnF_2 as the source of excess Sn, an approach that reduces the density of Sn vacancy defects. In 2016, Wang *et al.* [185] achieved a PCE of 3.31%. By removing the electron-blocking layer in a simplified inverted solar cell architecture and using the additive SnCl_2 instead of SnF_2 , Marshall *et al.* [188] achieved the highest PCE to date of 3.56%, together with exceptional device stability under continuous illumination without device encapsulation. However, the PCE of $\gamma\text{-CsSnI}_3$ based solar cells is still significantly lower than those of their hybrid organic-inorganic Sn and Pb perovskite counterparts, primarily because of the lower open-circuit voltage. The most important challenges are therefore to develop ways to increase the open-circuit voltage and to stabilize tin halide perovskites toward oxidation in air. The oxidation instability manifests as a phase transition from the photoactive black orthorhombic (γ) phase to a photoinactive 2D yellow (δ) phase upon exposure to water vapor, which spontaneously converts to the weakly absorbing one-dimensional Cs_2SnI_6 [188], leading to difficulties in controlling the morphology and quality of the perovskite film.

In Pb halide perovskites, the strategy of mixing cations or anions has been widely used to improve the stability and PV performance of PSCs [35, 79, 179, 205-208]. In contrast, explorations of the mixing of cations and anions in all-inorganic Sn-based perovskites are scarce [33, 131, 209, 210]. Recently, the electronic structure variation of γ -CsSnI₃ by mixing A-site cations (e.g., mixing Cs and Rb) has been investigated by Jung *et al.* [131] However, the relative stability of the structures as compared to the δ -phase was not investigated. To our knowledge, the amalgamated effect of exchange of both the A-site metal cation and the halide anion in completely inorganic tin perovskites has not been investigated.

In this paper, we present a theoretical study of the impact of cation and anion mixing (Rb/Cs cation exchange and Br/I anion exchange) in all-organic γ -CsSnI₃ using the DFT-1/2 method (the LDA-1/2 version) [110, 211-213], taking into account the spin-orbit coupling (SOC) effect. We focus on the evolution of the electronic properties as well as the thermal and structural stabilities when substituting Br for I and Rb for Cs in γ -CsSnI₃. We predict that 3D perovskites with the composition Rb_yCs_{1-y}Sn(Br_xI_{1-x})₃, where $0 \leq x, y \leq 1$, are direct band gap semiconductors with band gaps in the range 1.3-2.0 eV. Importantly, our results indicate that substitution of Br for I in CsSnI₃ can prevent the unwanted γ -to- δ phase transition, evidenced by the favourable formation energies of the γ -phase over the δ -phase. In addition, calculations of the free energy of mixing and the prediction of phase diagram demonstrate that further substitution of Rb for Cs in CsSn(Br_xI_{1-x})₃ can improve the mixing thermodynamics, which is expected to improve the film-forming properties. Our predicted trends in the thermodynamic stability and band gaps provide a guideline to develop more efficient and stable lead-free all-inorganic perovskites for PSCs.

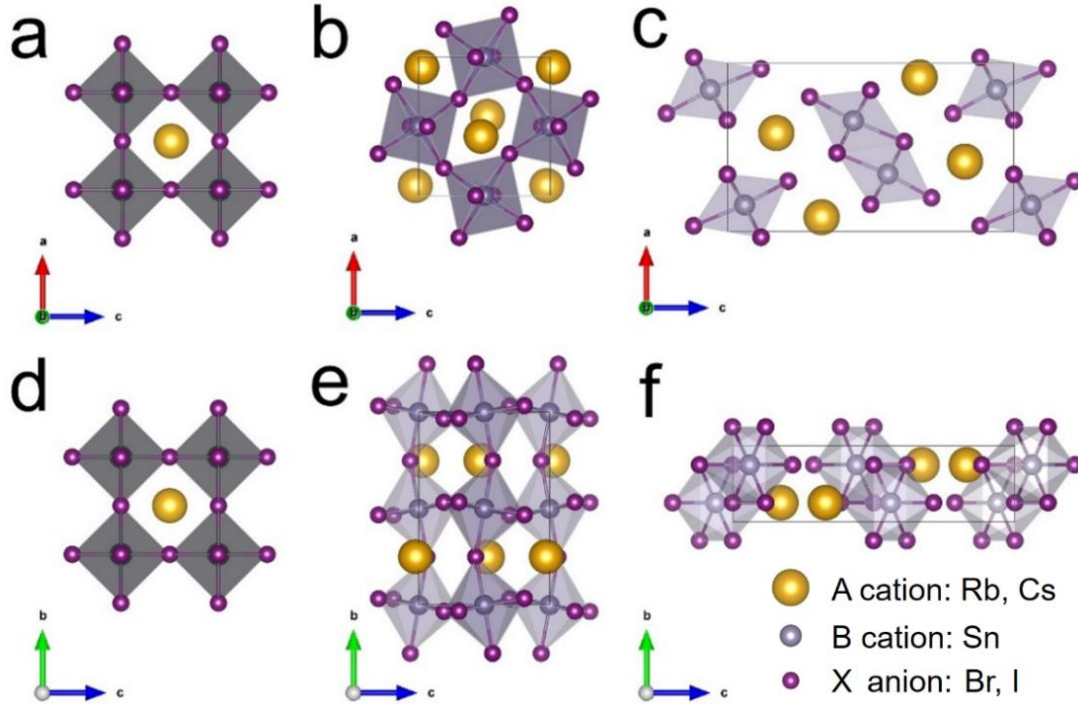


Figure 4.1. Top (a-c) and side (d-f) views of the cubic (α , $Pm\bar{3}m$), orthorhombic (γ , $Pnma$), and yellow phase (δ , $Pnma$) of $ASnX_3$ (A = Cs, Rb and X = Br, I).

4.2. Computational methods and structural models

The initial structure optimizations are performed using DFT as implemented in the Vienna *ab-initio* simulation package (VASP) [137, 214]. The PBE functional within the generalized gradient approximation is used [108]. The outermost *s*, *p*, and *d* (in the case of Sn) electrons are treated as valence electrons, whose interactions with the remaining ions are modeled by pseudopotentials generated within the PAW method [138, 139]. Figure 4.1 shows the crystal structures and cells used in the DFT calculations. Unit cells with 20 atoms (four $ASnX_3$ units) are used for all structures using a $1 \times 1 \times 1$ cell for the γ and δ -phases and $2 \times 2 \times 1$ supercells for the α -phase. In the structural optimization, the positions of the atoms as well as the cell volume and cell shape are all allowed to relax by setting $ISIF = 3$. An energy cutoff of 500 eV and $4 \times 4 \times 8$, $6 \times 4 \times 6$ and, $4 \times 10 \times 2$ *k*-point meshes (α , γ , and δ -phase structures, respectively) are used to achieve an energy and force convergence of 0.1 meV and 2 meV/Å, respectively. The subsequent electronic structure calculations were performed using an efficient approximate quasi-

particle DFT method, namely, the DFT-1/2 method. The DFT-1/2 method stems from Slater's proposal of an approximation for the excitation energy, a transition-state method [111, 215], to reduce the band gap inaccuracy by introducing a half-electron/half-hole occupation. Teles *et al.* [110, 211-213] extended the method to modern DFT and particularly to solid-state systems. Recently, we successfully applied this method in predicting accurate band gaps of metal halide perovskites [156]. The computational effort is the same as for standard DFT, with a straightforward inclusion of SOC when coupled with VASP. In this work, we extend the use of the DFT-1/2 method with the same settings (CUT values of 2.30, 3.34, and 3.76 for Sn, I, and Br, respectively, with half-ionized p orbitals) to alloys of CsSnI₃ when mixing Cs with Rb and I with Br. The physical insights of why Sn p and halide I or Br p orbitals are both half-ionized are demonstrated in Figure B.1.

We calculated the free energy [131, 161] of mixing for each composition according to the expression:

$$\Delta F = \Delta U - T\Delta S \quad (4.1)$$

where ΔU and ΔS are the internal energy and entropy of mixing and T is the absolute temperature. The internal energy of mixing of Rb_xCs_{1-x}SnX₃ is then calculated via the formula:

$$\Delta U = E_{\text{Rb}_x\text{Cs}_{1-x}\text{SnX}_3} - xE_{\text{RbSnX}_3} - (1-x)E_{\text{CsSnX}_3} \quad (4.2)$$

where $E_{\text{Rb}_x\text{Cs}_{1-x}\text{SnX}_3}$, E_{RbSnX_3} , and E_{CsSnX_3} are the total energies of Rb_xCs_{1-x}SnX₃, RbSnX₃, and CsSnX₃, respectively.

The internal energy of mixing of ASn(Br_xI_{1-x})₃ is calculated using the formula

$$\Delta U = E_{\text{ASn}(\text{Br}_x\text{I}_{1-x})_3} - xE_{\text{ASnBr}_3} - (1-x)E_{\text{ASnI}_3} \quad (4.3)$$

where $E_{\text{ASn}(\text{Br}_x\text{I}_{1-x})_3}$, E_{ASnBr_3} , and E_{ASnI_3} are the total energies of ASn(Br_xI_{1-x})₃, ASnBr₃, and ASnI₃, respectively.

The entropy of mixing is calculated in the homogeneous limit according to the formula

$$\Delta S = -k_B[x\ln x + (1-x)\ln(1-x)] \quad (4.4)$$

where k_B is the Boltzmann constant.

We plot the phase diagram by using the generalized quasi-chemical approximation (GQCA) [161, 216] code developed by Walsh *et al.* [161] to further investigate the thermodynamic properties of γ -ASnX₃. The phase diagram offers insight into the critical temperature for mixing and into the stability of the solid solution for typical temperatures at which perovskites are synthesized.

On the basis of the size of the cells for calculations, we have considered seven (ASn(Br_xI_{1-x})₃, $x = 0, 1/6, 1/3, 1/2, 2/3, 5/6,$ and 1) and five (Rb_yCs_{1-y}SnX₃, $y = 0, 1/4, 1/2, 3/4,$ and 1) concentrations of A cations and X anions, respectively. For the γ -phase structures, all possible configurations (2, 4, and 2 for $y = 1/4, 1/2,$ and $3/4,$ respectively) of substituting Rb for Cs were considered. Owing to the large number of possible configurations of substituting Br for I (22, 139, 252, 139, and 22 possible configurations for $x = 1/6, 1/3, 1/2, 2/3,$ and $5/6,$ respectively), we have considered only two possible configurations for each concentration of Br, namely, the two extreme cases with most negative and least negative ΔH . From Figure B.2 and Table B.1, the formation energy of configuration 3 is the most negative, whereas that of configuration 7 is the least negative. This indicates that the Br ions tend to sit as close as possible to each other and to form as many bonds as possible with Sn ions. We use this strategy to select two extreme configurations for all other Br-I alloys considered in this work.

4.3. Results and discussion

Before studying the mixing of A cations and X anions in ASnX₃, we first performed calculations for the four pure compounds: CsSnI₃, CsSnBr₃, RbSnI₃, and RbSnBr₃. The calculated lattice parameters of orthorhombic (γ) ASnX₃ are shown in Table 1. Those of other polymorphs including cubic α , tetragonal β , and δ -phase structures are listed in Table B.2. The optimized lattice parameters are in good agreement with experiments, with a slight overestimation of lattice constants by about 1%, and with other theoretical results (differences within 0.1%) [41, 131, 210, 217-220]. It should be noted here that the predicted lattice parameters of α -CsSnI₃ and γ -CsSnI₃ in our previous work are smaller because of the use of LDA, which slightly underestimates the lattice parameters [156].

In this work, Perdew, Burke, and Ernzerhof (PBE) is used, resulting in a slight overestimation of lattice parameters. Consequently, the predicted band gap of γ -CsSnI₃ (1.36 eV) in this work (will be discussed in the next paragraph) is slightly higher compared to that of previous work (1.34 eV) [156].

The calculated band gaps of γ -CsSnI₃ and γ -CsSnBr₃ are 1.36 eV and 1.72 eV, respectively, in excellent agreement with reported experimental measurements [210] (1.27 eV and 1.75 eV) and GW₀ calculations [220] (1.34 eV and 1.83 eV). There are no experimental reports known to us of the band gap of either RbSnI₃ or RbSnBr₃. Only theoretical results from HSE06 for γ -RbSnI₃ and PBE for α -RbSnBr₃ are found to be 1.41 and 0.57 eV, respectively [131, 221]. Our predicted band gap for γ -RbSnI₃ is 1.55 eV. Substituting Br for I in γ -RbSnI₃ further increases the band gap to 2.01 eV.

It is worth noting that although CsSnBr₃ is reported to have the α structure at room temperature, the actual atomic arrangement at finite temperature (due to the dynamic disorder of the ions in the lattice) [222] resembles that of the γ -phase. Consequently, it is not surprising that predicted band gaps using α structures are always significantly smaller than those measured experimentally [131, 155, 223, 224]. Therefore, in this work we always report band gaps calculated using γ -phases. RbSnI₃ has been reported to exist in a nonperovskite 2D δ -phase structure owing to the small cationic size of Rb⁺ [41, 218]. Nevertheless, for comparison with the alloys Rb_yCs_{1-y}SnI₃, the band gaps of RbSnI₃ in a 3D γ -phase are also predicted. In addition, all band gaps of α structures are also provided in the Supporting Information in Table B.2 and Figure B.3 for comparison. The calculated effective masses of the electrons and holes at G point for γ -ASnX₃ are given in Table B.3.

Table 4.1. Lattice constants (in Å) obtained by DFT, band gap energies E_g (in eV) obtained with the DFT-1/2 method including spin-orbit coupling, compared to experimental data and theoretical predictions based on hybrid and GW methods. a: ref. [41], b: ref. [131], c: ref. [210], d: ref. [220].

Material	Lattice	Lattice	Lattice	E_g	E_g	E_g
	constants (this work)	constants (experimental)	constants (other theoretical work)	DFT-1/2 + SOC	(experi- mental)	+SOC
γ -CsSnI ₃	8.99, 12.52,	8.69, 12.38,	8.94, 12.52,	1.36	1.27 ^c	1.34
	8.63	8.64 ^a	8.69 ^b			
γ -RbSnI ₃	8.91, 12.28,	-	8.93, 12.28,	1.55	-	1.13
	8.47	-	8.47 ^b			
γ -CsSnBr ₃	8.36, 11.79,	-	-	1.72	-	1.83
	8.22	-	-			
γ -RbSnBr ₃	8.38, 11.55,	-	-	2.01	-	-
	7.98	-	-			

Figure 4.2 shows the computed band gaps for the γ -phases of $\text{ASn}(\text{Br}_x\text{I}_{1-x})_3$ and $\text{Rb}_y\text{Cs}_{1-y}\text{SnX}_3$ perovskites, while the band gaps of the other structures are shown in Figure B.4. In general, the band gap increases with increasing percentage of Br in $\text{ASn}(\text{Br}_x\text{I}_{1-x})_3$ and increasing percentage of Rb in $\text{Rb}_y\text{Cs}_{1-y}\text{SnX}_3$. From Figure 4.2a and Table B.4, generally the band gaps change because of the variations in both volume and lattice distortion. However, the changes in cell volume have more pronounced effects on the band gaps than the changes in lattice distortion, that is, octahedral tilting. The reduction of the cell volume is responsible for the widening of the band gap in $\text{ASn}(\text{Br}_x\text{I}_{1-x})_3$ or $\text{Rb}_y\text{Cs}_{1-y}\text{SnX}_3$ solid solutions with an increased Br or Rb percentage. For the band gap variations with the same Br or Rb percentage in $\text{ASn}(\text{Br}_x\text{I}_{1-x})_3$ or $\text{Rb}_y\text{Cs}_{1-y}\text{SnX}_3$ solid solutions, there is no certain relationship found between the degree of lattice distortion (i.e. the degree of octahedral tilting, which is the tilting angle difference $|\Delta\bar{\theta}|$) [172] and band gaps.

It is well-known that for single-junction, the Shockley–Queisser limit suggests optimal band gap ranges of 0.9-1.6 eV for achieving a maximum PCE [189, 225]. The semiconductors with wide band gap (e.g., 1.6-2.0 eV) are ideal in conjunction with narrow band gap semiconductors in forming the multi-junction solar cells [226]. The band gaps of $\text{CsSn}(\text{Br}_x\text{I}_{1-x})_3$ are completely in the optimal range (1.30-1.55 eV) for single-junction PSCs. When substituting Rb for Cs in $\text{CsSn}(\text{Br}_x\text{I}_{1-x})_3$, the band gaps of $\text{RbSn}(\text{Br}_x\text{I}_{1-x})_3$ increase by 0.2-0.3 eV as compared to their Cs counterparts, making $\text{RbSn}(\text{Br}_x\text{I}_{1-x})_3$ ($x > 1/3$) ideal as a wide band gap material for tandem solar cells in conjunction with narrow band gap semiconductors such as Si or $\text{CsSn}(\text{Br}_x\text{I}_{1-x})_3$. The changes in band gap when mixing Rb and Cs cations are much smaller than those when mixing I and Br. This is true for all values $0 \leq y \leq 1$ and also for different structures with a fixed y . The band gaps of $\text{Rb}_y\text{Cs}_{1-y}\text{SnBr}_3$ (1.71 eV to 2.01 eV) are in the ideal range for the conjunction components of tandem solar cells, while the band gaps of $\text{Rb}_y\text{Cs}_{1-y}\text{SnI}_3$ (1.36 eV to 1.55 eV) are in the optimal range for single-junction solar cells, respectively.

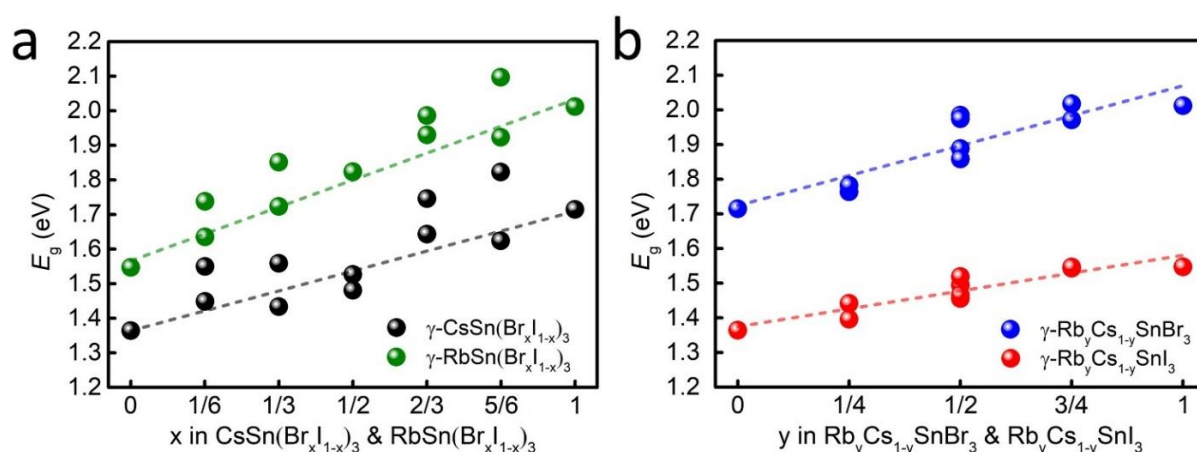


Figure 4.2. Calculated band gaps of (a) $\gamma\text{-ASn}(\text{Br}_x\text{I}_{1-x})_3$ and (b) $\gamma\text{-Rb}_y\text{Cs}_{1-y}\text{SnX}_3$ perovskites. The dashed lines are guides to the eye.

In addition to the band gap, another key property for the application of mixed inorganic perovskites in PSCs is their structural stability. CsSnI_3 has two coexisting polymorphs (the γ and δ -phases) at room temperature, which both belong to the Pnma space group. Although both phases have similar free energies and stable phonon modes, a transition from the black γ phase to the yellow δ -phase has been observed in ambient conditions [40, 41, 131]. Oxidation of Sn^{2+} to Sn^{4+} spontaneously occurs after the transformation of the γ phase to the δ -phase [167].

Because of the different crystal structure and electronic properties of the δ -phase (i.e., a 2D structure and an indirect band gap of 2.6 eV), the unwanted phase transition from γ to δ can considerably decrease the efficiency of a solar cell [43, 164, 167, 188, 227]. In addition, the δ -phase will spontaneously react with O_2 when exposed to air, resulting in Cs_2SnI_6 with a face-centered cubic (FCC) structure [195, 197]. Therefore, we focus here on the evolution of the stability of the γ - and δ -phases upon gradual substitution of Br for I and Rb for Cs. The results of our calculations for other structures are given in Figure B.5.

The formation energy of ASnX_3 is defined as $\Delta H = E_{\text{ASnX}_3} - E_{\text{AX}} - E_{\text{SnX}_2}$, where E_{ASnX_3} , E_{AX} and E_{SnX_2} are the total energies of ASnX_3 , AX and SnX_2 , respectively. Here, a negative value of ΔH represents favourable formation of ASnX_3 perovskites. The more negative ΔH , the more stable the corresponding structure. It can be clearly seen in Figure 4.3 that all perovskites considered exhibit good thermal stability, with large negative ΔH values. Figure 4.3 also shows the effect of ion mixing on the stability of the γ -phase with respect to the δ -phase.

For CsSnI_3 the formation energies of the γ - and δ -phases are the same. However, with the increase of Rb concentration, the structural instability of $\text{Rb}_y\text{Cs}_{1-y}\text{SnI}_3$ becomes an increasingly pronounced. Consequently, upon exposure to air, the rate at which the perovskite oxidizes is predicted to increase with increasing Rb concentration [167]. The substitution of Rb for Cs seems to facilitate the formation of the δ -phase, as now evidenced by the more negative formation energy of the δ -phase than the γ -phase. It should be mentioned that the formation energies are both negative for RbSnI_3 in both γ - and δ -phases. However, the formation energy of the δ -phase is relatively more

negative, indicating that the δ -phase is more favourable than the γ -phase. Indeed, the instability of the γ -phase is in agreement with the experimental observation of RbSnI_3 only existing in a 2D yellow phase [167]. On the contrary, for CsSnBr_3 , the formation energy of the δ -phase is much less negative than that of the γ -phase (by 0.06 eV), indicating that the γ -phase is more stable than the δ -phase. The substitution of Rb for Cs results in a slight decrease (to 0.04 eV) in the energy differences between the two phases, with the γ -phase still being favored.

The formation energies of mixing Cs and Rb in $\text{Rb}_y\text{Cs}_{1-y}\text{SnI}_3$ or $\text{Rb}_y\text{Cs}_{1-y}\text{SnBr}_3$ follow a perfect linear relation (Figure 4.3b), indicating favourable mixing thermodynamics. However, substitution of Br for I (Figure 4.3a) shows an unusual trend as a function of x : the curves show first a decrease and then an increase, with a valley point at $x = 1/3$ in both $\text{CsSn}(\text{Br}_x\text{I}_{1-x})_3$ and $\text{RbSn}(\text{Br}_x\text{I}_{1-x})_3$. When $x < 1/3$, the most negative ΔH of the γ -phase for each concentration is relatively more positive than or nearly equal to the most negative ΔH of the δ -phase, which indicates that the δ -phase is favored over the γ -phase. When $x = 1/3$, the most negative ΔH of the γ -phase is clearly more negative than the most negative ΔH of the δ -phase, whereas the least negative ΔH of the γ -phase is almost equal to the most negative ΔH of the δ -phase. When $x > 1/3$, all ΔH of the γ -phase for each concentration are more negative than those of the δ -phase, which means that the γ -phase is stabilized. For $\text{Rb}_y\text{Cs}_{1-y}\text{SnI}_3$ or $\text{Rb}_y\text{Cs}_{1-y}\text{SnBr}_3$, mixing Cs and Rb does not change the stability of the γ -phase with respect to the δ -phase (Figure 4.3b). For $\text{Rb}_y\text{Cs}_{1-y}\text{SnI}_3$ the δ -phase is always favored when mixing Rb and Cs, whereas for $\text{Rb}_y\text{Cs}_{1-y}\text{SnBr}_3$ the opposite is true. We conclude that the addition of Br to $\text{Rb}_y\text{Cs}_{1-y}\text{SnI}_3$ tends to stabilize the favourable γ -phase and suppress the transformation to the δ -phase. The critical Br concentration is about one-third. This prediction calls for an experimental validation.

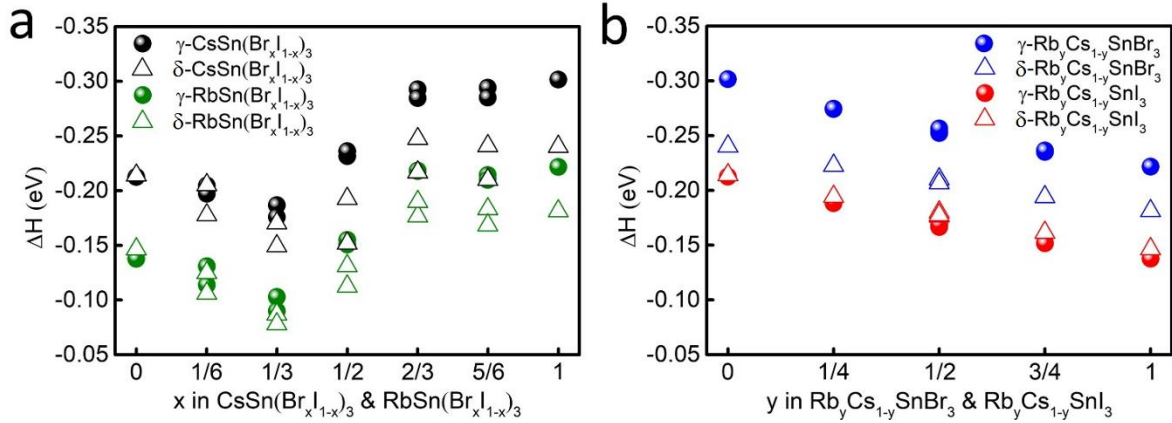


Figure 4.3. Formation energy (ΔH) of (a) $\text{ASn}(\text{Br}_x\text{I}_{1-x})_3$ and (b) $\text{Rb}_y\text{Cs}_{1-y}\text{SnX}_3$ perovskites for the γ - and δ -phases. Because of the large number of possible configurations for each substitution concentration x of Br in $\text{ASn}(\text{Br}_x\text{I}_{1-x})_3$, we only show in (a) the results for the two configurations with the most negative and least negative ΔH .

As shown in Figure 4.3, very different trends are observed for mixing of cations (Rb and Cs) and anions (I and Br) in γ - CsSnI_3 . For a deeper insight, we have investigated the different mixing thermodynamics by calculating the Helmholtz free energy of mixing. Details of the calculations can be found in the Computational methods and structural models section. Results of these calculations are shown in Figure B.6. On the basis of the Helmholtz free energies, we plot the phase diagram for γ - ASnX_3 by using the GQCA [161] code, as shown in Figure 4.4.

For $\text{CsSn}(\text{Br}_x\text{I}_{1-x})_3$, the critical temperature is 291 K (see Figure 4.4a), indicating that the mixing of anions (I and Br) is favourable at room temperature (300 K). However, for $\text{RbSn}(\text{Br}_x\text{I}_{1-x})_3$ at 300 K, a miscibility gap is found in the composition region between $x_1 = 0.33$ and $x_2 = 0.70$ (see Figure 4.4b). The pure compounds RbSnI_3 and RbSnBr_3 are not miscible inside the miscibility gap under equilibrium conditions, leading to the formation of two phases with Br concentrations x_1 and x_2 . Meanwhile, the alloy has spinodal points at the compositions $x'_1 = 0.40$ and $x'_2 = 0.62$ at room temperature. Thus, in the intervals $x_1 < x < x'_1$ and $x'_2 < x < x_2$ a metastable phase can occur, showing small fluctuations in composition. The predicted critical temperature (the temperature above which the solid solution is stable for any composition) is 312 K, which is significantly lower than the critical temperature of 343 K predicted for the $\text{MAPb}(\text{Br}_x\text{I}_{1-x})_3$ perovskite [161]. This indicates that, although mixing of Br and I is not favored slightly below (for

$\text{CsSn}(\text{Br}_x\text{I}_{1-x})_3$) or around (for $\text{RbSn}(\text{Br}_x\text{I}_{1-x})_3$) room temperature, the phase segregation in these alloys is less significant than that in $\text{MAPb}(\text{Br}_x\text{I}_{1-x})_3$ perovskites.

A uniform mixture can be synthesized either through control of the deposition kinetics or by annealing above the critical miscibility temperature. The uniform mixture tends to segregate below the critical temperature, but this segregation is a very slow process [161]. The inclusion of smaller cations often provides an improvement, overcoming kinetic barriers and changing the local critical temperature. For example, smaller cations such as Cs and Rb were introduced in $(\text{FA}/\text{MA})\text{Pb}(\text{I}/\text{Br})_3$, and were shown to have a positive effect on the structural and photostability of state-of-the-art PSCs [175, 177, 180, 228]. Indeed, we predict that mixing of Rb and Cs in $\text{Rb}_y\text{Cs}_{1-y}\text{SnX}_3$ is very favourable at room temperature. For $\text{Rb}_y\text{Cs}_{1-y}\text{SnBr}_3$ and $\text{Rb}_y\text{Cs}_{1-y}\text{SnI}_3$, the phase diagrams show that mixing of cations (Rb and Cs) is favourable at temperatures above 118 K and 137 K, respectively (see Figures 4.4c and d). Our prediction of the critical miscibility temperature of 137 K of $\text{Rb}_y\text{Cs}_{1-y}\text{SnI}_3$ is in good agreement with the result of 140 K calculated by Jung *et al.* [131] The slight difference of the predicted critical temperature could be caused by the small variation in energies per cell due to the differences in computational settings (energy cutoff value, k-point grid, version and implementation of VASP codes) in DFT calculations. The critical temperatures of mixing of Rb and Cs in $\text{Rb}_y\text{Cs}_{1-y}\text{SnX}_3$ are much lower than those of mixing of Br and I in $\text{ASn}(\text{Br}_x\text{I}_{1-x})_3$. Therefore, additional mixing of Cs and Rb in $\text{ASnI}_x\text{Br}_{1-x}$ is predicted to bring down the critical temperature for mixing of Br and I below room temperature, suppressing phase segregation and resulting in better material quality for PV applications.

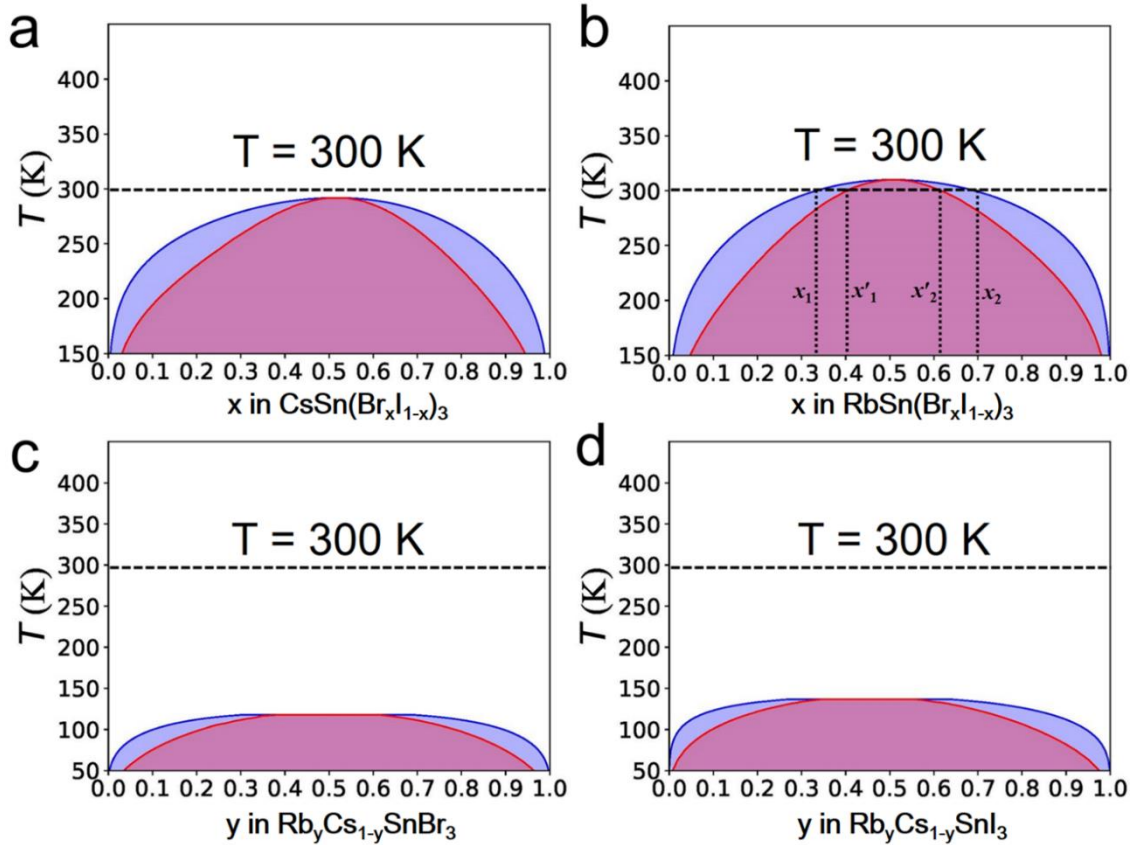


Figure 4.4. Predicted phase diagrams of (a) γ -CsSn(Br_xI_{1-x})₃, (b) γ -RbSn(Br_xI_{1-x})₃, (c) γ -Rb_yCs_{1-y}SnBr₃ and (d) γ -Rb_yCs_{1-y}SnI₃ solid solutions. The purple and pink lines are binodals and spinodals, respectively. The dashed horizontal lines indicate room temperature (300 K). In (b), the gap between the horizontal line and the critical miscibility temperature is the miscibility gap in γ -RbSn(Br_xI_{1-x})₃. A thermodynamically stable solid solution can only be formed in the white region.

4.4. Conclusion

In summary, the effects of cation (Cs and Rb) and anion (I and Br) mixing in all-inorganic tin halide perovskites have been investigated with DFT-based calculations. Using standard DFT for structure optimization and the DFT-1/2 method with SOC for band structure calculations, we studied the evolution of the structural, thermodynamic, and electronic properties as a function of the extent of substitution of Rb for Cs and Br for I. We predict that Cs_yRb_{1-y}Sn(Br_xI_{1-x})₃ perovskites have direct band gaps in the range of 1.3-2.0 eV. The alloys with high I and Cs concentrations are well suited for highly efficient single-junction PSCs, whereas those with high Rb and Br concentrations are suitable as wide band gap materials for tandem PSCs. Importantly,

we found that substitution of Br for I can suppress the unwanted γ -to- δ phase transition. The critical concentration for stabilization of the γ -phase with respect to the δ -phase in $\text{Cs}_y\text{Rb}_{1-y}\text{Sn}(\text{Br}_x\text{I}_{1-x})_3$ is $x = 1/3$. Furthermore, phase diagrams based on the free energy of mixing show that a solid solution of Br and I is thermodynamically possible around and slightly above room temperature for $\text{CsSn}(\text{Br}_x\text{I}_{1-x})_3$ and $\text{RbSn}(\text{Br}_x\text{I}_{1-x})_3$, respectively. Finally, substitution of Rb for Cs to $\text{ASn}(\text{Br}_x\text{I}_{1-x})_3$ is predicted to decrease the critical temperature to well below room temperature, enabling the formation of highly homogeneous solid solutions for improved solar cell performance. Our predictions regarding the stabilization of the γ -phase and the use of five elements in $\text{Rb}_y\text{Cs}_{1-y}\text{Sn}(\text{Br}_x\text{I}_{1-x})_3$ as an efficient and stable light absorber for PSCs call for experimental exploration.

Chapter 5

The Role of Sodium in Stabilizing Tin-Lead (Sn-Pb) Alloyed Perovskite Quantum Dots

Narrow-band gap CsSn_xPb_{1-x}I₃ perovskite quantum dots (QDs) show great promise for optoelectronic applications owing to their reduced use of toxic Pb, improved phase stability, and tunable band gaps in the visible and near-infrared range. The use of small ions has been proven beneficial in enhancing the stability and photoluminescence quantum yield (PLQY) of perovskite QDs. The introduction of sodium (Na) has succeeded in boosting the PLQY of CsSn_{0.6}Pb_{0.4}I₃ QDs. Unfortunately, the initial PLQY of the Na-doped QDs undergoes a fast degradation after one-day storage in solution, hindering its practical applications. Using density functional theory (DFT) calculations and ab-initio molecular dynamics (AIMD) simulations, we study the effect of the Na ion on the strength of surface bonds, defect formation energies, and the interactions between surface ligands and perovskite QDs. Our results suggest Na ion enhances the covalent bonding of the surface tin-iodine bonds and forms strong ionic bonding with the neighboring iodine anions, thus suppresses the formation of I and Sn vacancies. Furthermore, the Na ion also enhances the binding strength of the surface ligands with the perovskite QDs surface. However, according to our AIMD simulations, the enhanced surface ligand binding is only effective on a selected surface configuration. While the position of Na ion remains intact on a CsI-terminated surface but diffuses vigorously on MI₂-terminated surface. As a result, the positive effect of Na vanishes with time, explaining the relatively short lifetime of the experimentally obtained high PLQYs. Our results indicate that engineering the surface termination of the QDs could be the next step to maintain the favourable effect of Na doping for a high and stable PLQY of Sn-Pb QDs.

This chapter is mainly based on the publication: J Jiang, F Liu, Q Shen, S Tao. "The Role of Sodium in Stabilizing Tin-Lead (Sn-Pb) Alloyed Perovskite Quantum Dots", Journal of Materials Chemistry A, 2021, 9, 12087-12098.

5.1. Introduction

Semiconductors with near-infrared absorption and emission attracted tremendous attention for broad applications, including biological labeling, optical communication, and photovoltaics [229-231]. The metal-halide perovskites, as a new class of optoelectronic materials, have been developed rapidly because of their excellent photophysical properties and great success in photovoltaics [126, 232-237]. Among various types of AMX_3 perovskites ($A = Cs^+$, $CH_3NH_3^+$, and $CH_3(NH_2)_2^+$; $M = Pb^{2+}$, Sn^{2+} , Cu^{2+} , Ge^{2+} , and Mn^{2+} ; $X = Cl^-$, Br^- , and I^-), $ASnI_3$ perovskites attracted specific attention owing to their narrower optical band gaps (1.2~1.4 eV), allowing strong response in the near-infrared spectral region [238-240]. The alloying Sn with Pb at M-site leads to the formation of an unusual band gap, which is lower than that of the pure-Sn and -Pb perovskites, making the mixed Sn/Pb perovskites more attractive for the applications in high-efficiency tandem solar cells [232, 241-245]. Additionally, mixing Sn and Pb is beneficial for stabilizing the fragile Sn-perovskite cubic phase and retarding the oxidation of Sn^{2+} to Sn^{4+} [37, 241, 246-249]. As a result, the alloyed Sn-Pb perovskite solar cells already showed enhanced phase stability and improved power conversion efficiency, making them attractive for various optoelectronic applications [250-253].

Reducing crystallite size to the nanometer scale, for example, quantum dot (QD) dimension, further improves their phase stability because of the large contribution of surface energy and the protection by organic passivation ligands [64-70, 254]. Moreover, the increased exciton binding energy of QDs results from geometry and quantum confinement compared with the bulk counterpart. Thus, excitons are more dominant than free carriers in these nano-sized semiconductor crystals, leading to the enhanced radiative recombination and therefore a high theoretical PLQY [71]. The synthesis of pure Sn or Sn-Pb alloyed perovskite QDs with reasonable luminescence efficiency is challenging. Even a slight incorporation of Sn in Pb host would cause dramatic degradation of their radiative recombination, which usually leads to extremely low PLQYs of 0.3~3% [255, 256]. The presence of charge traps and

recombination centers in these Sn-contained QDs are believed to be the reasons for luminescent inefficiency [257, 258]. It is generally accepted that the Sn vacancy defects are held accountable because of their low formation energy [41]. However, previous computational studies suggested that Sn vacancies do not introduce deep-level traps inside the band gap. Hence, they are unlikely to produce such devastating consequences [68, 202, 259]. Another possible contribution to trap states in Sn-Pb alloyed QDs may come from surface halide vacancies, which will create under-coordinated metal ions. This resembles those cases in previous Pb-based perovskites where surface halide vacancies have been identified as the major defects negatively impacting their electronic properties [260-266]. However, from the viewpoint of electronic structure, this is not the primary reason as deep-level states only present in those Cl-based perovskites, while in Br- and I-perovskites, the deficiency in surface halogen atoms will only introduce shallow defect levels [260, 267].

Recent studies suggest that the formation of Sn vacancy and the oxidation of Sn^{2+} to Sn^{4+} are responsible for the overall degradation in Sn-contained perovskite [199, 268]. Namely, the spontaneous oxidation starting from a bond breaking of Sn-I, the under-coordinated Sn^{2+} can be easily oxidized to Sn^{4+} . This accelerates the formation of Sn vacancies and finally converts the perovskite to the nonperovskite phase [65, 141, 246, 258]. This indicates that the optimization of these defect-intolerant nanocrystals would require a significant suppression of the Sn vacancy formation and the oxidation of Sn^{2+} to Sn^{4+} . A high PLQY of CsSnI_3 QDs, 59%, was achieved by using the kinetically controlled ion-exchange method by Yang *et al.* [269] They first synthesized the highly stable CsPbBr_3 QDs and then by introducing SnI_2 precursor obtained the CsSnI_3 QDs with less defect and good structural stability. This demonstrates again the importance of the defect suppression in Sn-containing perovskite QDs. Meanwhile, tailoring the QDs synthesis route (with ion-exchange reaction) [269, 270], co-doping [271, 272], or inducing different ligands [74, 273, 274] has been investigated to improve the stability of perovskite QDs and increase the PLQY. For Sn-contained QDs, the stronger interaction between ligands and the surface has been proven with a stabilization effect [275-278]. Overall, the prerequisite of retrieving near-infrared emission for these Sn-

contained QDs is to enhance the bonding strength between the Sn^{2+} and I^- ions and passivation effect of surface ligands.

Doping of semiconductors has been proven to be a powerful tool to alter structural and optoelectronic properties for both traditional semiconductors and perovskite nanocrystals [50, 52, 279-284]. Encouragingly, the lanthanide series (e.g. Yb^{3+} and Ce^{3+}) was successfully doped into lattices of wide band gap perovskite QDs, which demonstrated enhanced optical and electric properties, leading to remarkably high PLQY above 100% [285-288]. However, such effect seem to be less effective in low band gap perovskite QDs. For instance, mixing Br into CsPbCl_3 QDs caused a rapid drop in PLQY [286]. Very recently, we found that ultra-low Na doping effectively improves optoelectronic properties of the Sn-Pb alloyed QDs, boosting PLQY from $\sim 0.3\%$ to 28% (see Figure 5.1) [173]. The X-ray photoelectron spectroscopy (XPS) analyses suggest that the Na dopant potentially enhances the chemical bonding of Sn^{2+} and I^- with surrounding ions thus suppresses the formation of trapping states. However, the PLQY of the Na-doped QDs undergoes a fast degradation from $\sim 28\%$ to 4% within 24 hours at room temperature. The atomistic origin of the improved luminescence efficiency of the Na doped Sn-Pb alloyed QDs, and their subsequent degradation mechanisms remain unclear.

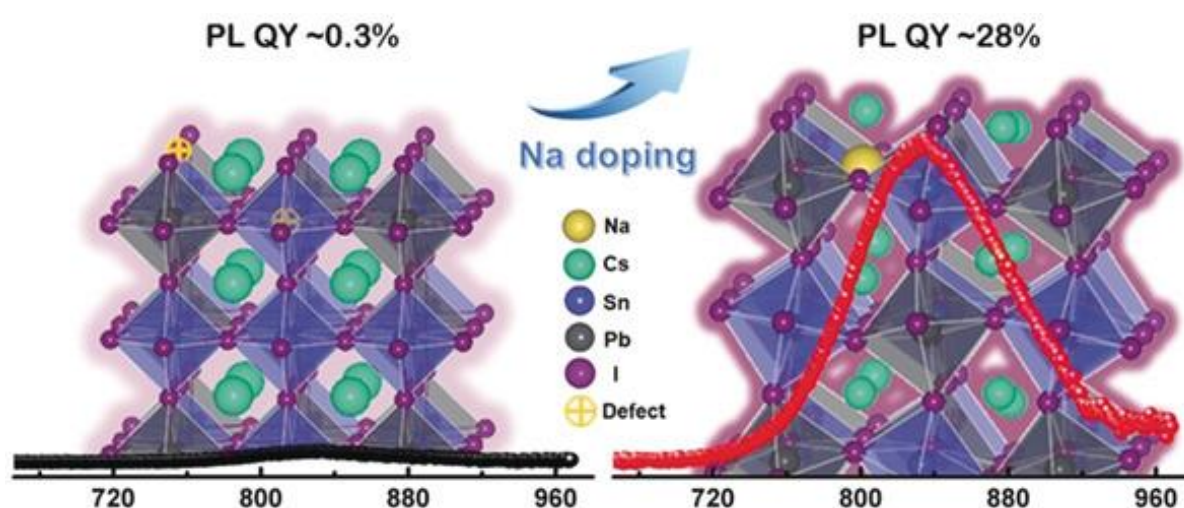


Figure 5.1. Near-infrared emission from Sn-Pb alloyed perovskite QDs was achieved for the first time by Na doping.

In this work, combining DFT calculations and AIMD simulations, we study the effect of the Na ion on the strength of surface bonds, defect formation energies, and the interactions between surface ligands and perovskite QDs. We find that Na dopant preferentially occupies the surface interstitial site, leading to the strengthened ionic bonding of Na with the surrounding I⁻ ions and enhanced covalent bonding of the Sn²⁺ with I⁻ ions in [SnI₆]⁴⁻ octahedra. Both consequences suggest that the incorporation of Na effectively suppresses the formation of I and Sn vacancies. Furthermore, the binding energy of ligands with perovskites increases upon Na doping, resulting in a stronger passivation effect of the ligands and thus stabilizing the Sn-Pb perovskite QDs. The high mobility of exotic Na dopant on MI₂-terminated surface is observed from AIMD simulations, indicating that the Na ion could not stabilize itself in one out of the two surface terminations, causing the rapid decrease of PLQY.

5.2. Methods

5.2.1. Density functional theory calculation

Structural optimizations of all structures were performed using DFT implemented in the Vienna *ab initio* simulation package (VASP) [137]. The Perdew-Burke-Ernzerhof (PBE) functional within the generalized gradient approximation (GGA) was used [108]. The outermost s, p, and d (for Pb and Sn) electrons were treated as valence electrons, whose interactions with the remaining ions were modeled by pseudopotentials generated within the projector-augmented wave (PAW) method [138, 139]. During the structural optimization, all ions were allowed to relax. An energy cutoff of 500 eV and a k-point scheme of $6 \times 6 \times 1$ were used to achieve energy and force convergence of 0.01 meV and 20 meV Å⁻¹, respectively.

5.2.2. *Ab Initio* molecular dynamics simulation

Ab initio molecular dynamics (AIMD) simulations were executed by using a canonical ensemble (NVT) with a Nosé–Hoover thermostat at 300 K [289, 290], as implemented in the VASP code. The PAW method was employed to describe the core-valence interaction, and the PBE exchange-correlation functional was used. The kinetic cutoff

energy of 400 eV was used for plane wave expansion. The energy and force convergence parameters were set at 0.01 meV and 20 meV Å⁻¹, respectively. A single k-point sampled at the Γ only was used to speed up the computations. The total simulation time of each calculation is 6 ps with a time step of 2 fs.

5.2.3. Chemical bonding analysis

An in-depth analysis of the chemical bonding was carried out to understand the chemical bonding for Na-doped perovskites. The main interest of the bond is those between Sn cation and I anion. The strength of the chemical bonding is investigated by analyzing both the covalent and ionic bondings. The covalent contribution can be analyzed by the bond order, which correlates with the electron density value at a bond-critical point (saddle-points of electron density along the bond paths). The larger the bond order value, the stronger a covalent bond. The ionic contribution of a bond can be characterized by net atomic charge, which quantifies the charge transfer between atoms. The positive net atomic charge of an atom indicates losing electrons, and the negative one indicates gaining electrons. The bond order and net atomic charge calculations were carried out by DDEC6 charge partitioning implemented in the Chgemo1 code [291-294].

5.2.4. Structural models

The incorporation of Na⁺ at different locations on the surface and the bulk of QDs was investigated by using CsSn_{0.6}Pb_{0.4}I₃ surface models with the top and bottom surfaces being the [1 0 0] facets terminated by CsI and MI₂ (M = Sn or Pb) layer, respectively (Figure 5.2). The surfaces were modeled using slab models consisting of (2 × 2) cells in the x and y direction and 5 repeating units (20 Cs atoms, 12 Sn atoms, 8 Pb atoms, and 60 I atoms) with a vacuum of 15 Å in the z-direction. The dipole correction along the z-direction is considered. It should be noted that when using a quantum dot model [82, 295, 296], a global view of the morphology of the perovskite QDs surfaces and their interaction with ligands can be obtained. The surface structures, especially the surface bonds show slightly different length and strength due to the quantum confinement effect [297, 298]. However, such QDs models are computationally expensive because

of the need to simulate a large number of atoms. Therefore, slab models are often used as an alternative, which is proven to be effective in correctly capturing the qualitative trends in such confinement effects [299, 300]. The usage of slab models to investigate the properties of perovskite QDs has also led to many successes in previous works [275, 278, 301, 302].

To understand the surface ligand effect to the QDs, the slab model used above were passivated by oleylammonium ($C_{18}H_{35}NH_3^+$: OLA) or oleate ($C_{18}H_{33}O_2^-$: OA) on CsI or MI_2 termination, respectively. To validate our ligand slab model, we also calculated the ligand density and compared it with experiment data (Table C.1) [303]. For DFT and AIMD simulations, atoms away from the ligand side (three repeating MI_6 octahedral layers) have been fixed to mimic the bulk nature. The rest of the atoms, including the OLA and OA on top of the surface were optimized. All structural models are visualized by using VESTA [304].

5.2.5. Vacancy formation energy

For Na doping, we replace one Cs^+ cation with Na^+ . We calculate the formation energies of I and Sn vacancies at the CsI-terminated surface and MI_2 -terminated surface (M: Sn or Pb) of this structure. As references, we also calculate the same formation energy of unmodified CsI- and MI_2 -terminated surfaces. The details of the procedure are as follows. The defect formation energy of an ion (I anion, Sn cation, or Pb cation) is defined as:

$$\Delta E_{vac} [ion] = E_{tot} [ion-vac] - (E_{tot} [surface] - \mu[ion]) + qE_{Fermi} \quad (5.1)$$

where $E_{tot} [ion-vac]$ and $E_{tot} [surface]$ are the total energies of the surfaces with and without ion vacancy, respectively, and E_{Fermi} and $\mu[ion]$ are the Fermi energy and the chemical potential of the ion, respectively. The E_{Fermi} and $\mu[ion]$ is assumed to be the same for all perovskites. This approximation is valid because, in our experiments [173], the important parameters (*e.g.*, precursor concentration, the source of ions, and synthesis temperature) during the synthesis process of these perovskites are kept the same.

We define the suppression of ion vacancy formation [163, 283] due to the introduction of Na^+ , as:

$$\Delta\Delta E_{vac} = \Delta E_{vac} [\text{ion}] [\text{Na}] - \Delta E_{vac} [\text{ion}][\text{ref}] \quad (5.2)$$

where $\Delta E_{vac} [\text{ion}] [\text{Na}]$ is the formation energy of an ion defect in the presence of Na, and $\Delta E_{vac} [\text{ion}][\text{ref}]$ represents one of the unmodified CsI-terminated surfaces or unmodified MI_2 -terminated surfaces.

5.2.6. Ligand binding energy

The binding energy (E_b) of the ligands to the QDs surface is computed as:

$$E_b = (E_{tot} - E_{per} - E_{lig})/S \quad (5.3)$$

where E_{tot} is the energy of the slab model passivated with ligands, E_{per} the energy of the slab model without the ligand, and E_{lig} the energy of the ligand, and S is the surface area of the interfaces. The more negative the E_b , the stronger the binding strength between the ligand and the QDs.

5.2.7. Charge displacement curve

The binding of perovskites and ligands will cause the charge redistribution at the interface. To analyze the charge redistribution, the charge density difference $\Delta\rho$ is calculated by:

$$\Delta\rho = \Delta\rho_{tot} - \Delta\rho_{per} - \Delta\rho_{lig} \quad (5.4)$$

where ρ_{tot} , ρ_{per} , and ρ_{lig} denote the charge density of the optimized perovskite/ligand structure, the separated perovskite slab, and the separated ligand layer, respectively. To investigate the charge redistribution between the ligand and the perovskite, the plane-averaged charge density difference $\Delta\rho_{avg}(z)$ is defined as:

$$\Delta\rho_{avg}(z) = \int_{\Sigma(z)} dx dy \Delta\rho = \sum_{ij} \Delta x_i \Delta y_i \Delta\rho_{i,j} \quad (5.5)$$

the positive and negative signals of $\Delta\rho_{avg}(z)$ represent electron accumulation and depletion along the z -direction, respectively. Then, the charge displacement curve ΔQ ,

which can be used to determine the direction of the charge transfer, is given by integrating $\Delta\rho_{\text{avg}}(z)$ along z -direction as follows:

$$\Delta Q = \int_0^z \Delta\rho_{\text{avg}}(z) dz \quad (5.6)$$

the negative value of ΔQ represents that the electrons are transferred along the positive direction of the z -axis, and the positive value corresponds to the electron transfer along the negative direction of the z -axis.

5.2.8. Diffusion coefficient

The mean square displacement (MSD) function, which increases linearly with time in gaseous or liquid phase system with free motion of atoms, is used to calculate the diffusion coefficient (D):

$$D = \frac{1}{6N} \lim_{t \rightarrow \infty} \frac{d}{dt} \sum_{i=1}^{N_\alpha} \langle [r_i(t) - r_i(0)]^2 \rangle \quad (5.7)$$

where $\langle \cdot \rangle$ represents an average over all the guest molecules, $r_i(t)$ and $r_i(0)$ denote the position vector of the analyte molecule i in space at time t and its initial position, respectively. These calculations are executed by using VASPKIT code [305].

5.2.9. Experiments

We synthesized the undoped and Na-doped $\text{CsSn}_{0.6}\text{Pb}_{0.4}\text{I}_3$ colloidal QDs and executed the X-ray photoelectron spectroscopy (XPS) characterization to analyze the surface environment of QDs. For the colloidal synthesis of undoped and Na-doped $\text{CsSn}_{0.6}\text{Pb}_{0.4}\text{I}_3$ QDs [173], 0.75 g of SnI_2 (99%, Wako Pure Chemicals, Japan) and 0.25 g of PbI_2 (99%, Sigma-Aldrich, USA) were mixed into 2.5 mL of tri-*n*-octylphosphine (TOP, 97%, Sigma-Aldrich, USA). The mixture was vigorously stirred on a hot plate at 90 °C for about 2 h. In a 50 mL three-neck flask, 0.07 g of Cs_2CO_3 (99.9%, Sigma-Aldrich, USA), 0.4 mL of oleic acid ($\geq 65.0\%$, Wako Pure Chemicals, Japan), and 0.4 mL of oleylamine (70%, Sigma-Aldrich, USA) were mixed into 12 mL of octadecene (90%, Sigma-Aldrich, USA). The mixture was heated at 100 °C with vigorous stirring under vacuum for 30 min and then heated to 120 °C under nitrogen until the solution became

clear. For Na doping, after the complete dissolution of Cs_2CO_3 , the solution was first cooled down to room temperature and 0.06~0.13 g of sodium acetate trihydrate was added. The solution was then again heated to 120 °C under nitrogen for 20 min until the Na salt was completely dissolved. For both undoped and Na-doped synthesis, the temperature was raised to 165 °C followed by quick injection of the above prepared TOP-SnI₂-PbI₂ solution. About 5 secs after injection, the reaction was quenched by immediate immersion of the flask into an ice bath. After cooling, the crude solution was transferred to centrifuge tubes and to each tube three volumes of methyl acetate (MeOAc, anhydrous 99.5%, Sigma-Aldrich, USA) were added to precipitate the QDs, followed by centrifugation at 4000 rpm for 2 min. The supernatant was discarded and the QD precipitate was dispersed in hexane. X-ray photoelectron spectroscopy (XPS) data were accumulated on a photoelectron spectrometer, JPS-90MX (JEOL, Ltd., Japan).

5.3. Results and discussion

5.3.1. Enhancing the surface Sn-I bonding strength

We first determine the possible atomistic locations of Na^+ in the QDs. Figure 5.2 depicts the three possible locations of Na in the QDs, where the Na^+ is found to be more stable on surfaces than in bulk by 0.2 to 0.3 eV. On both CsI- and MI_2 -terminated surfaces, Na^+ preferentially occupies the interstitial site, rather than an A site. This is not unexpected considering the large difference in ionic radii of Na^+ and Cs^+ as well as the small size of Na^+ . In fact, previous studies also indicated Na^+ prefers to occupy an interstitial site in hybrid Pb perovskites [135, 163].

Further zooming into the surface modification by Na, we found evident changes in surface atomic structure as well as charge redistribution at the surface layers of $\text{CsSn}_{0.6}\text{Pb}_{0.4}\text{I}_3$ perovskite. We found that the incorporation of Na does not affect the surface Pb-I bond strength because the bond order is kept constant as 0.55. As the Sn^{2+} plays a more important role than Pb^{2+} in the stability of the QDs (see the Introduction section), we thus focus our study on the changes of the bonding state of the surface Sn^{2+} ions (Figure 5.3a, b). We observe that the Sn-I bonds at the surface layer with Na are on average shorter than those without Na (one is shorter by 0.07Å and the other

slightly longer by 0.01Å). Further chemical bonding analysis reveals an overall stronger covalent bonding between the Sn and the surface I atoms upon the incorporation of the Na dopant (Figure 5.3c, Figure C.1, and Table C.2). For example, we see that the bond order of the Sn-11/I-52 bond has been increased from 0.60 to 0.66. Such enhancement is also reflected in the electron localization function (Figure 5.3e, f), where the electron cloud around the Sn^{2+} ion and I ion is more delocalized, a sign of a stronger covalent bonding in the Na-doped perovskite compared to the pristine one. The strengthened chemical bonding between the surface I and the Sn may originate from the newly formed strong Na-I ionic bonding on the subsurface layer, which induces a noticeable decrease in the covalent bond between the subsurface I⁻ and the central Sn^{2+} ions (as evidenced by the decreased bond order in pairs such as Sn-11/I-50 and Sn-11/I-54). Overall, the introduction of Na^+ induces charge redistribution, which is favourable for the formation of stronger covalent bonding of the surface Sn-I bonds.

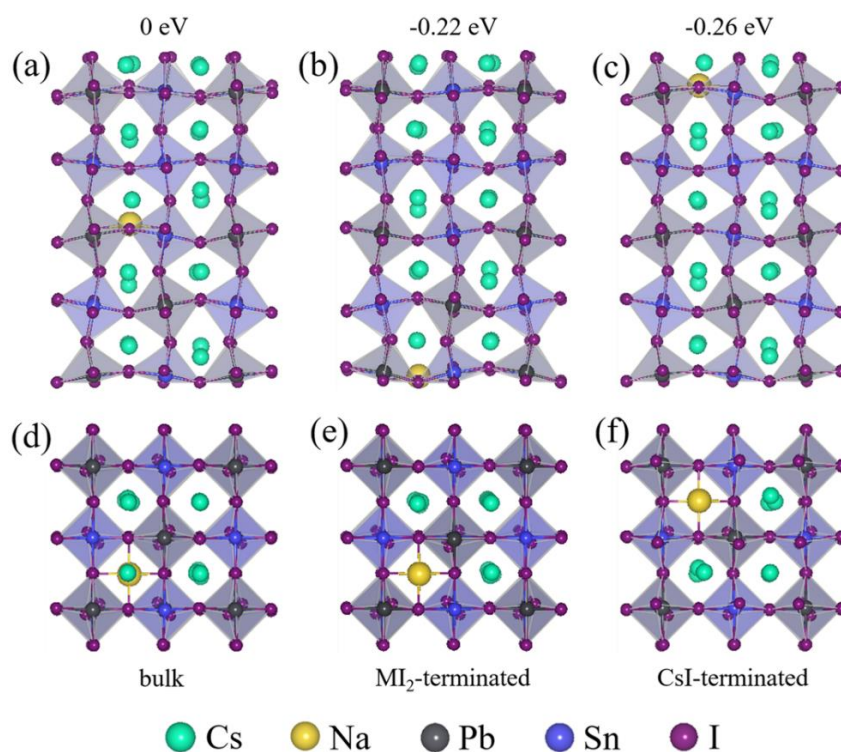


Figure 5.2. DFT optimized structures of Na-doped $\text{CsSn}_{0.6}\text{Pb}_{0.4}\text{I}_3$ perovskite. In all structures, one Na ion (the yellow sphere) substitutes one Cs cation. (a-c) Side views and (d-f) top views of Na in bulk, at MI_2 -terminated surface, and CsI-terminated surface (M: Pb or Sn). The (a) structure gives the highest energy. Using this as a reference, (b) has an energy of -0.22 eV, and (c) has an energy of -0.26 eV. The yellow, purple, grey, and blue spheres denote the Na^+ , I, Pb^{2+} , and Sn^{2+} ions, respectively.

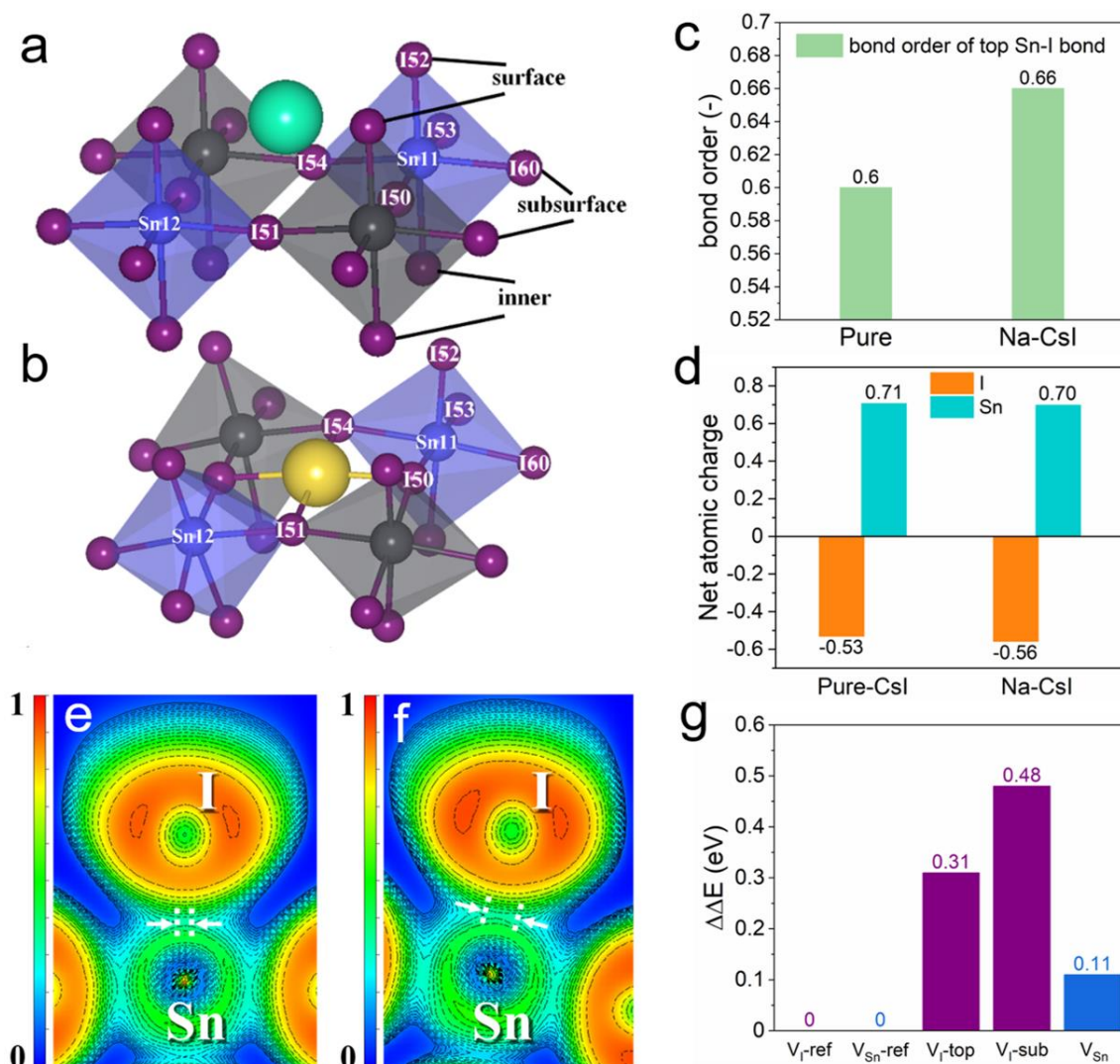


Figure 5.3. Atomistic view of the CsI-terminated surfaces of $\text{CsSn}_{0.6}\text{Pb}_{0.4}\text{I}_3$ perovskite: (a) the clean (pure-CsI) and (b) Na-doped (Na-CsI). The atom numbers are from the visualized model by using VESTA. The structure details with atomic coordinate can be found in Supplemental Information. (c) Average net atomic charges of the surface I and Sn^{2+} ions with and without incorporation of Na. (d) Comparison of the average bond order of surface Sn-I bonds with and without incorporation of Na. Electron localization function of the surface I- and Sn^{2+} ions (e) without and (f) with the incorporation of Na. The arrows and dots indicate the magnitude of the electron delocalization around the Sn^{2+} and I-. (g) Formation energies of the Sn and I vacancies (on top layer) in the pristine and Na-doped $\text{CsSn}_{0.6}\text{Pb}_{0.4}\text{I}_3$ perovskites.

We now analyze the impact of the incorporation of Na on the ionic bonding of the surrounding I⁻ and Sn^{2+} . Overall, the ionic charge of I⁻ ions adjacent to Na dopant has increased, while that of the Sn^{2+} ions remain almost unchanged (see Figure 5.3d). The ionic charge of I-51 is increased from -0.53 to -0.55, and that of I-50 is increased from -0.53 to -0.56. Consequently, a stronger chemical bonding of I⁻ with Na^+ than that with

Cs^+ will be formed. The I^- with more atomic charges will form an enhanced ionic bonding with the neighboring Sn cations, which is expected for retarding the formation of Sn^{4+} . We also observe similar trends for the MI_2 -terminated surface, and the details can be found in Figure C.2 and Table C.3.

To investigate the effect of the chemical bonding change on the behavior of defects, we then calculated the formation energies of I and Sn vacancies. We found that in the presence of Na, formation energies of those nearby I vacancies have increased significantly: by 0.48 eV on the CsI-terminated surface (Figure 5.3g) and by 0.89 eV on the MI_2 -terminated surface. This increased vacancy formation energy of the subsurface I^- ions can be attributed to their stronger interaction with Na dopant, as evidenced by both increased ionic and covalent interactions (the increased ionic charge on I^- ions and the larger bond order of Na-I than that of Cs-I, in Figure C.1 and Table C.2). Such enhanced bonding with neighboring atoms helps to suppress the diffusion of these anions [163]. For those I^- ions sitting at the top layer of CsI-terminated surface, we also found a high vacancy formation energy by 0.31 eV. This observation is also consistent with our earlier conclusion that the surface I^- ions form a stronger covalent bonding with the subsurface Sn^{2+} ions upon incorporating Na dopant. Previous studies showed that iodine vacancy does not create deleterious deep-level trap states within the band gap [260, 306]. However, we consider the suppression of I vacancies can be important for these Sn-containing perovskites. This is because I vacancies would exacerbate the problem of Sn^{4+} by exposing more uncoordinated Sn atoms, which are more susceptible to oxidation. As for Sn vacancy, we found their formation energies are also moderately increased on both CsI- and MI_2 -terminated surfaces by 0.11 eV and 0.44 eV, respectively, indicating that Na doping is also effective in suppressing the formation of these surface Sn vacancies. The increased formation energy of the Sn vacancy is a result of their enhanced chemical bonding with surrounding I^- ions, as discussed above.

To summarize, we have shown that Na dopant enhances the chemical stability of Sn^{2+} and suppresses the formation of I and Sn vacancies. Both effects potentially retard the oxidation of Sn^{2+} to Sn^{4+} and the subsequent degradation of the perovskite

compound, therefore improve the optoelectronic properties of these Sn-containing perovskites.

5.3.2. Enhancing the ligand passivation effect

Surface ligand binding strength is another crucial factor contributing to the overall stability of perovskite QDs. The perovskite compounds will be significantly affected by the ligands due to the highly ionic and environmentally sensitive characters. We therefore speculate the stability of the Sn-Pb alloyed perovskite QDs is related with the strength of chemical bonding between ligands and the surface. To examine this, we calculated the ligand binding energy (E_b) to evaluate the bond strength of ligands and $\text{CsSn}_{0.6}\text{Pb}_{0.4}\text{I}_3$ QD surface, including the CsI and MI_2 -termination. The scheme of these two terminations are shown in Figure 5.4a. The ligand type information is experimentally affirmed in our previous work [173], therefore, we built the $\text{CsSn}_{0.6}\text{Pb}_{0.4}\text{I}_3$ surface models that are capped with positive charged OLA and negatively charged OA, shown in Figure 5.4b. The ligands density of our model is 1.24 ligand/ nm^2 , which is close to the experimental results of Rossini *et al.* obtained by using solid-state NMR spectroscopy [303].

It is necessary to further explore the surface termination of $\text{CsSn}_{0.6}\text{Pb}_{0.4}\text{I}_3$ QDs owing to the different surface elemental compositions. Thus, we checked the surface composition by using XPS, as shown in Table C.4. The surface I/Cs chemical stoichiometric ratio is 2.65, which is smaller than the ratio in chemical formula I/Cs = 3. This implies that the $\text{CsSn}_{0.6}\text{Pb}_{0.4}\text{I}_3$ surface is mixed with both terminated surfaces but more CsI- than MI_2 -termination. Thus, the two major terminations are both considered thereafter, to study the surface ligand binding.

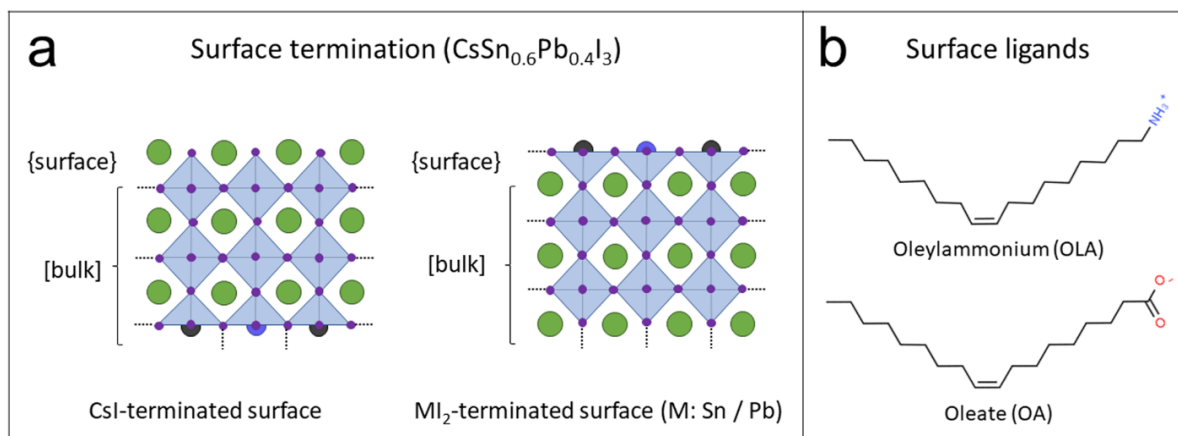


Figure 5.4. (a) Idealized models of the surface termination of the as-synthesized $\text{CsSn}_{0.6}\text{Pb}_{0.4}\text{I}_3$ QDs. Both surfaces are capped by cationic and anionic organic ligands at the outermost layer. (b) The considered cationic OLA and the anionic OA ligands in this study.

To investigate the effect of Na on the ligand binding strength, the E_b were calculated for different binding modes of $\text{CsSn}_{0.6}\text{Pb}_{0.4}\text{I}_3$ surfaces and ligands without and with Na incorporation, which schematically illustrates in Figure 5.5. The ligands are assumed to attach or substitute the exposed Cs, Pb, Sn, or I surface atoms. For CsI-terminated surface, four surface ligand configurations were considered: OLA attaches to I and OA attaches to Cs; OLA substitutes Cs; OA substitutes I; OLA substitutes I and OA substitutes Cs, shown in Figure 5.5a and b from left to right. For MI_2 -terminated surface, four configurations were constructed too, that is: OLA attaches to A cation and OA attaches to Pb; OLA attaches to A cation and OA attaches to Sn; OLA and OA both attach to A cation; OA substitutes I, shown in Figure 5.5c and d from left to right.

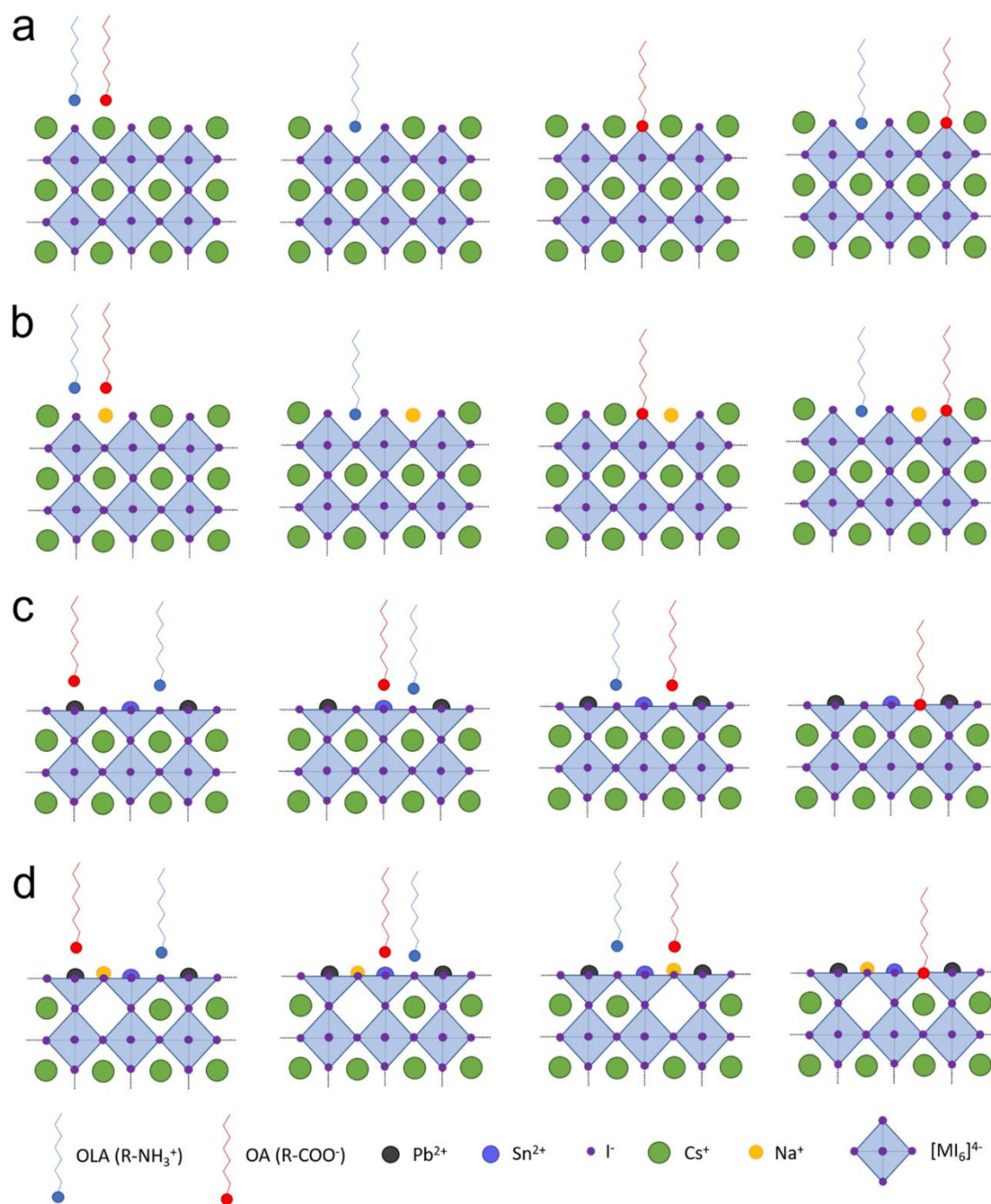


Figure 5.5. Schematic illustration of CsSn_{0.6}Pb_{0.4}I₃ QDs with a CsI-terminated surface (a) without and (b) with Na incorporation; MI₂-terminated surface (c) without and (d) with Na incorporation. Four different passivated configurations for CsI-terminated surface are named as OA-Cs_OLA-I, OLA*, OA*, and OA*_OLA* from left to right. Similarly, four configurations for MI₂-terminated surface are named as OA-Pb_OLA-I, OA-Sn_OLA-I, OLA-Cs_OA-A, and OA* from left to right. The * indicates the substitution of surface ion.

The calculated E_b are all more negative after Na doping, regardless of the surface termination and ligand interaction mode (see Figure 5.6). For the CsI-terminated surface, the OLA attached to I and OA attached to Cs configurations show the smallest

binding strength, while the OLA substituting Cs and OA substituting I show the largest (see Figure 5.6a). This suggests that the ligands prefer to substitute the surface ions rather than (OA substituting I and OLA substituting Cs) being physisorbed on the surface and interacting with the ions with opposite charge. For MI_2 -terminated surface, the interaction mode of OLA attached to A cation and OA attached to Pb configurations show the smallest binding strength, while the OLA attached to A cation and OA attached to Sn configuration being the largest (see Figure 5.6b). Overall, our results show that the binding strength between surface and ligands are highly sensitive to the local atomic structure of the QDs. The incorporation of Na enhances the binding strength of the ligands with the perovskite surface, regardless of surface configurations. To investigate the genericity of alkali doping, we also studied the possible doping site and binding energy of all other alkali cations (see Table C.5 and Figure C.6), and the results show that only Na^+ has such a positive effect. These results further elucidate the unique role of Na^+ in enhancing the stability of the $CsSn_{0.6}Pb_{0.4}I_3$ QDs. We attribute the positive effect of Na^+ to the ionic size. The Na^+ is with an apropos ionic size that could occupy the surface interstitial site and causing the stronger interaction with neighboring ions, enhancing the ligand binding strength.

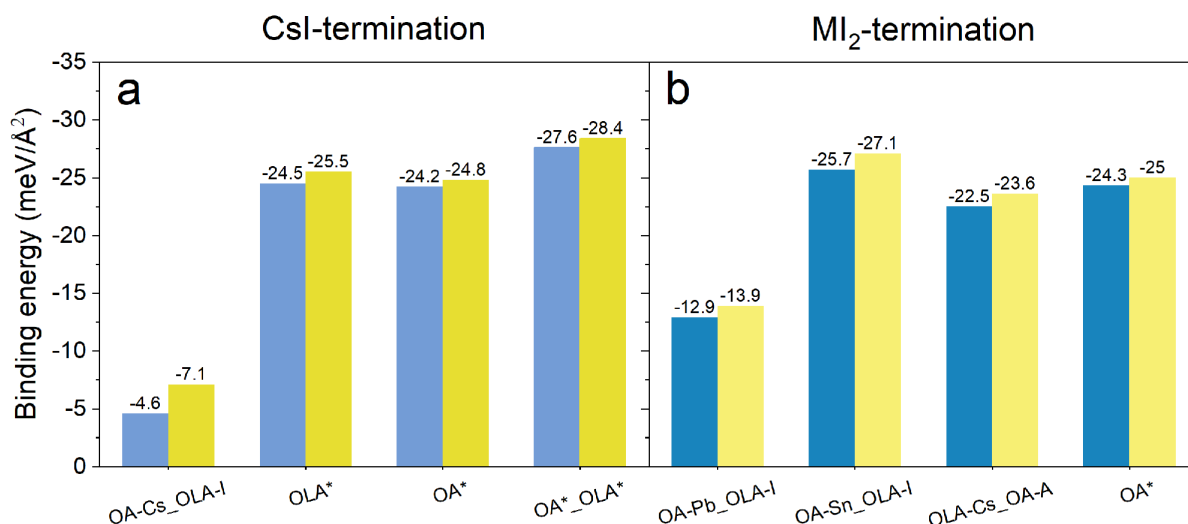


Figure 5.6. Binding energies of all ligand configurations of (a) CsI- and (b) MI_2 -termination, respectively. The blue bar and yellow bar denote the original surface and the Na-incorporated surface, respectively.

To shed light on the enhanced ligand binding strength, we selected the configuration with the largest binding strength in each termination to analyze the charge transfer between ligand and perovskite. We define $\Delta\rho_{\text{avg}}$ as the plane-averaged charge density difference and ΔQ as the charge displacement curve along the z-direction (see Supporting Information for the details). The results of charge transfer at two different terminations are displayed in Figure 5.7. We found that the charge variations mainly occur at the interface region between surface and ligands in both slab models. For the CsI-terminated surface shown in Figure 5.7a, electrons are transferred from the ligand side to the perovskite layer in both undoped and Na-doped systems. The calculated ΔQ presented in Figure 5.7c confirms this charge transfer behavior by the presence of a significant positive peak at the perovskite side but negative peaks at the side of the ligand. Moreover, an enhanced positive peak at the perovskite side and the reduced negative peaks at the ligand side are observed after Na doping. This means a stronger charge transfer occurs at the surface after incorporating the Na, which indicates a stronger interaction between ligand and perovskite. For MI_2 -terminated interface, a similar pattern is observed, where electrons are depleted near the ligands and accumulated at the exposed perovskite surface (see Figure 5.7b). The calculated ΔQ also suggests the electron transfer from the ligands to the perovskite. The reduced negative peak at the interface and enhanced positive peak in the perovskite side after the Na incorporation in Figure 5.7d indicate stronger interaction between ligand and perovskite. Our analysis confirms that incorporating Na at surfaces of perovskites strengthens the interaction of ligand and perovskite by charge transfers from one to the other side.

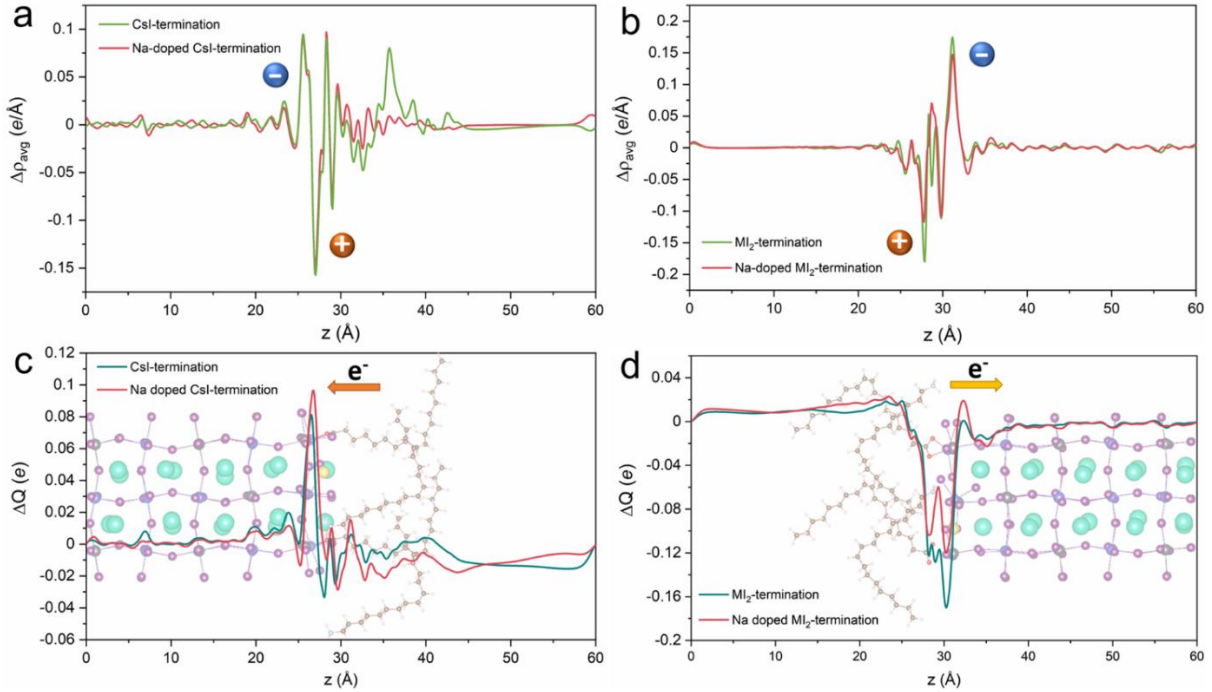


Figure 5.7. Plane-averaged charge density difference $\Delta\rho$ of the ligand-perovskite interfaces on (a) CsI- and (b) MI_2 -terminated surface without and with doping. Charge displacement ΔQ of the ligand-perovskite interface on (c) CsI- and (d) MI_2 -terminated surface without and with doping. The orange (+) and blue (-) spheres represent the depletion and accumulation of charges, respectively. The arrows represent the direction of the electron transfer. The inserted structure diagram is the Na-doped CsI- and MI_2 -terminated surfaces.

5.3.3. Interface dynamics on different terminations

The surface ligands binding is considered to be closely related to the thermal effect [76]. We thus also investigate the dynamics of the ligands on perovskite QD surfaces and the role of Na by using *ab-initio* molecular dynamics (AIMD) simulations at room temperature 300 K. The configurations with the largest binding strength in each termination are used as the starting point for the MD simulations. The temperature evolution during simulation time (see Figure C.3) and the $\log(\text{MSD})$ versus $\log(\text{time})$ (see Figure C.4) indicating the diffusivities of the systems reached equilibrium.

Figure 5.8a and b show the mean square displacement (MSD) of all the diffusive ions in undoped and Na-doped systems. After incorporating the Na, the MSD for CsI-terminated surface is reduced, while slightly increased for MI_2 -terminated surface. This difference suggests the incorporation of Na ions has a different effect on two terminations. Therefore, we zoom into the dynamics of specific ions. By tracking the

dynamic positions of the tail-end N atom in OLA (N_{OLA}), O atom in OA (O_{OA}) and Na, we obtain the diffusion coefficient of these ions (Figure 5.8c and d). On the CsI-terminated surface, the N_{OLA} and O_{OA} have an overall lower diffusion coefficient with Na than without during the simulation and as well as at the end of 6 ps AIMD simulation ($3.47 \times 10^{-5} \text{ cm}^2/\text{s}$ vs. $5.13 \times 10^{-5} \text{ cm}^2/\text{s}$ for N_{OLA} and $4.23 \times 10^{-5} \text{ cm}^2/\text{s}$ vs. $1.12 \times 10^{-4} \text{ cm}^2/\text{s}$ for O_{OA}), see Figure 5.8c. In contrast, at the MI_2 -terminated surface, the N_{OLA} and O_{OA} have an overall higher diffusion coefficient during the AIMD simulation after Na incorporation (Figure 5.8d) as well as at the end of 6 ps AIMD simulation ($1.22 \times 10^{-4} \text{ cm}^2/\text{s}$ vs. $9.38 \times 10^{-5} \text{ cm}^2/\text{s}$ for N_{OLA} and $8.35 \times 10^{-5} \text{ cm}^2/\text{s}$ vs. $6.64 \times 10^{-5} \text{ cm}^2/\text{s}$ for O_{OA}). It is worth noting that a large contrast is found in the diffusion coefficients of Na: that on CsI-terminated is much smaller than that on MI_2 -terminated surface during AIMD simulation. The same is true for the final diffusion coefficient after 6 ps is two magnitudes smaller ($3.34 \times 10^{-6} \text{ cm}^2/\text{s}$ vs. $1.48 \times 10^{-4} \text{ cm}^2/\text{s}$).

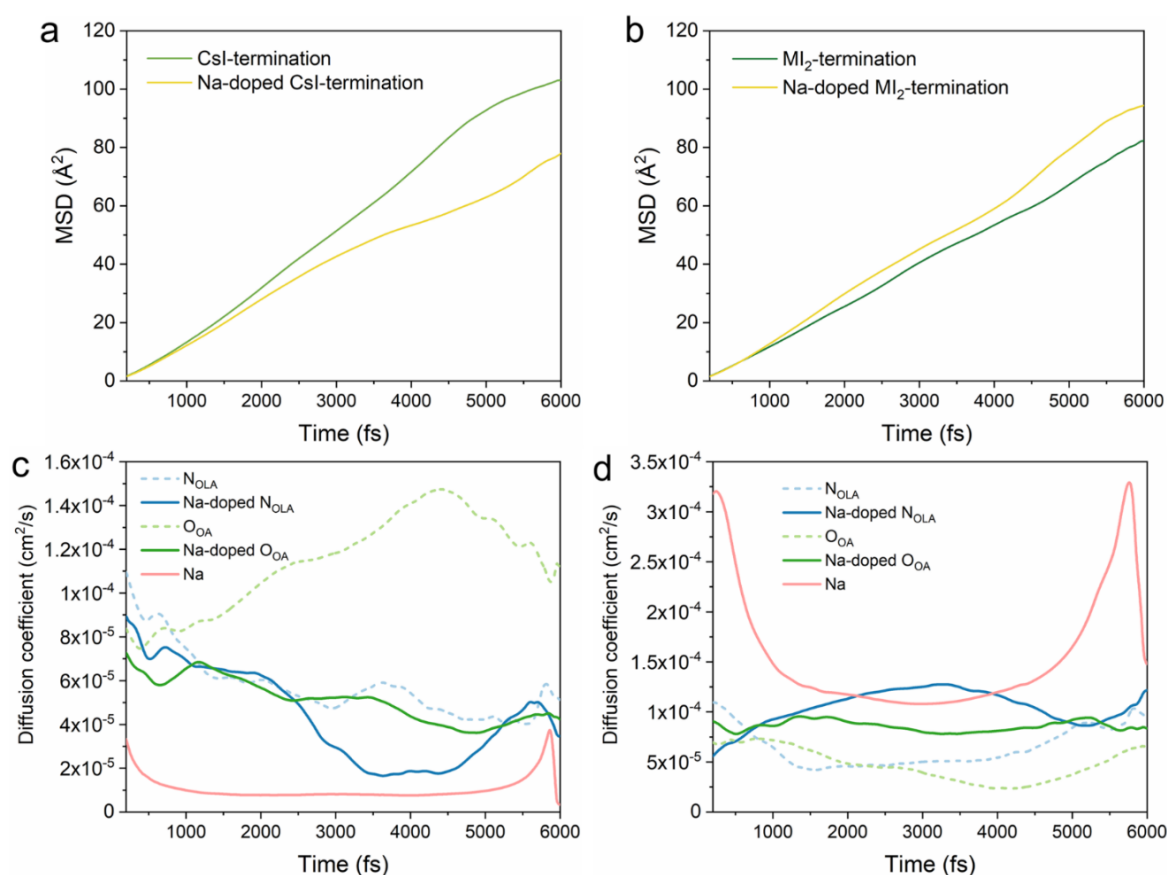


Figure 5.8. Mean-square displacement (MSD) of ligands and surface ions movement in (a) CsI and (b) MI_2 -terminated surface without and with Na doping. Diffusion coefficient of different ions on (c) CsI- and (d) MI_2 -terminated surfaces without and with Na doping.

Figure 5.9 illustrates the snapshots of four models in the AIMD simulations. For the undoped models in Figure 5.9a and b, the ligand and CsI-terminated perovskite have closely interacted while the ligand in MI_2 terminated perovskite pulls the ions away from the surface, indicating the degradation of perovskite. After doping the Na to the surface of perovskite, the CsI-termination maintains a stable binding interaction with ligands, while the degradation in the MI_2 -termination is not mitigated as the Sn and adjacent I ions are pulled up by the OA, leading to the formation of Sn vacancy.

Furthermore, we found that the Na is less mobile in the CsI-terminated model than in MI_2 terminated model. This is evidenced by the time-dependent location distribution density analysis that the Na^+ is almost stationary on the CsI-terminated surface but diffuses violently on the MI_2 -terminated surface (see Figure C.5). The different diffusive behavior of Na^+ on different terminations can be explained by the comparison of net atomic charge of Na^+ and adjacent I ions in two terminations (see Figure C.6). We found that the Na^+ and adjacent I ions contain a larger amount of net charges, indicating the formation of a stronger ionic bond between Na and I ions in CsI-termination than in MI_2 -termination, which manifests the much smaller Na^+ mobility at CsI-termination.

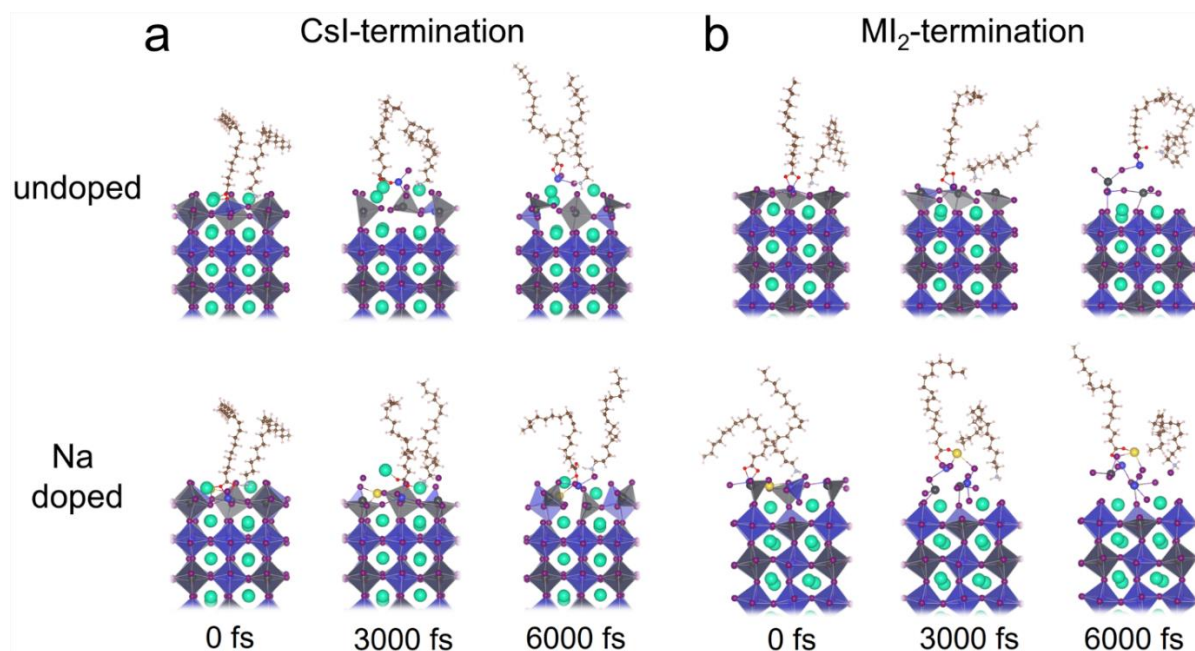


Figure 5.9. Snapshots of the interfaces after 6000 fs AIMD simulation of CsI- and MI_2 -terminated surfaces without and with Na doping.

5.4. Conclusions

To understand the role of Na ion in $\text{CsSn}_{0.6}\text{Pb}_{0.4}\text{I}_3$ perovskite QDs with enhanced photoluminescence and its subsequent photoluminescence degradation, we investigate the strength of surface bonds, defect formation energies, and the interaction of surface ligands and perovskite surfaces by first-principles DFT and MD calculations. Our results indicate that the Na doping has the following effects: First, Na ion prefers to locate at the surface and occupies the interstitial site. This enhances covalent bonding of the surface Sn-I bonds and ionic bonding of Na^+ with the neighboring Sn cations, therefore improves the chemical stability of Sn^{2+} and suppresses the formation of I and Sn vacancies. Second, Na ion strengthens the ligand-QDs surface binding and the two together passivate the surface dangling bonds of the QDs. Finally, AIMD simulations show Na ion on the CsI-terminated surface tends to suppress the diffusion of surface ligands but does the opposite on the MI_2 -terminated surface. The latter leads to the detachment of ligands and the perovskite surface layer, therefore fast degradation of the MI_2 -terminated surface. The above results indicate that the combination of the Na doping and CsI-termination of the QDs may result in the best improvement in maintaining a long lifetime of high photoluminescence efficiency. Therefore, we foresee the surface termination engineering could offer a breakthrough in improving the efficiency and the lifetime of perovskite QDs for near-infrared applications. Moreover, in addition to the detrimental effect of Sn oxidation, the origin of the relative low PLQY in infrared emitting $\text{CsSn}_{0.6}\text{Pb}_{0.4}\text{I}_3$ QDs could also be attributed to the constituents assembled imperfectly during the reaction process, which induced the structural defects and challenging to eradicate only by adjusting the synthetic factors (e.g. reaction temperature and duration, and stoichiometry of reactants). We anticipate that tailoring synthesis route, such as co-doping, or introducing different ligands may improve the stability of the Sn-Pb alloyed perovskite QDs further, meriting further experimental and theoretical study.

Chapter 6

The Role of Solvents in the Formation of Methylammonium Lead Triiodide Perovskite

Metal halide perovskites (MHPs) are gaining increasing attention as low-cost, high-performance semiconductors for optoelectronics. In particular, their solution processing is compatible with the large-scale manufacturing of thin-film devices, including solar cells and light-emitting diodes. Understanding the coordination chemistry in precursor-solvent solution and atomistic mechanisms of film formation is of great importance for optimizing the optoelectronic properties of the final films. Using the methylammonium lead triiodide (MAPbI₃) as an example, we study the complex evolution of the molecular species from the solution to the initial stage of the crystallization by using a combination of density functional theory (DFT) calculations and ab-initio molecular dynamics (AIMD) simulations. We focus on the widely employed solvents DMSO and DMF, analyze the structures and energies of the iodoplumbate complexes in the form of simple complex of [PbI_mL_n]^{2-m} and polymeric iodoplumbates of ([PbI_mL_n]^{2-m})_x. Based on the calculated formation enthalpies, we propose reaction schemes of MAPbI₃ formation in DMSO, DMF and DMSO-DMF binary solvent and explain the advantages of the binary solvent. Our findings indicate unbalanced reaction energies at several elementary reaction steps in either DMF (formation of [PbI₄L_n]²⁻ being highly favourable) or DMSO (formation of PbI₅ being retarded). Mixing a small amount of DMSO in DMF gives rise to a better balance in the energies and, therefore, potentially better equilibria in the overall crystallization process and better quality of the final perovskite films. Our results provide insights into the role of the solvents in tuning the energetics of the first steps of the perovskite formation and an important basis for precursor-solvent engineering for improved perovskite films.

6.1. Introduction

Metal halide perovskites (MHPs) are among the most studied materials in the last decade due to their promising optoelectronic properties, which enable highly efficient solar cells and light-emitting diodes [6, 9, 233, 307]. The impressive progress in achieved power conversion efficiency (PCE) has established the success of MHPs and consolidated their popularity among photovoltaic materials [3]. The MHPs are made by simple solution-processed deposition techniques by mixing a metal-halide precursor with a halide salt in a solution. For instance, methylammonium iodide (MAI) is added to a lead iodide (PbI_2) solution in coordinating solvents. From the mixture, colloidal particles form first and then produce a MHPs film by solvent evaporation. However, in contrast to the simplicity of the synthesis, the physicochemical processes during the synthesis are very complex. The synthesis involves the solvation/desolvation and complexation equilibria of all participating species at solvents-precursors, nucleation, and it evolves through various intermediate phases in the two-step method [90, 92, 94], and/or iodoplumbate complexes in the one-step method [87, 91, 95].

Using MAPbI_3 as an example, various complexes could be formed in a solution, depending on the type and the concentration of ions (MA^+ cations and I^- anions) or solvents (L) near the Pb metal ions. When I^- anions together with MA^+ cations are added to the PbI_2 solution, competition in binding can be observed between I^- and solvent molecules to the Pb^{2+} cation. The I^- anion and solvent will coordinate around the central Pb^{2+} cation, forming iodoplumbate complexes, i.e., $[\text{PbI}_2\text{L}_n]$, $[\text{PbI}_3\text{L}_n]^{1-}$, $[\text{PbI}_4\text{L}_n]^{2-}$, $[\text{PbI}_5\text{L}_n]^{3-}$, and $[\text{PbI}_6\text{L}_n]^{4-}$ [92, 98, 308-311]. During the iodoplumbates formation reaction, a small amount of I^- is adequate to replace the position of solvent molecules, thus induce the formation of iodoplumbate species [98, 309]. Indeed, iodoplumbate complexes, such as $[\text{PbI}_3\text{L}_n]^-$ and $[\text{PbI}_4\text{L}_n]^{2-}$ can be stabilized in the presence of large excess iodide ions [98, 308]. The higher I coordinated iodoplumbate, such as $[\text{PbI}_5\text{L}_n]^{3-}$ and $[\text{PbI}_6\text{L}_n]^{4-}$ are less often directly observed in experiments. However, their presence cannot be excluded, and it is speculated to play an important role in the final steps of the formation of MHPs [92, 309-311].

Besides the simple iodoplumbates discussed above, polymeric iodoplumbates were proposed to be formed using simple iodoplumbates, such as $[\text{PbI}_2\text{L}_n]$, $[\text{PbI}_3\text{L}_n]^{1-}$, or $[\text{PbI}_4\text{L}_n]^{2-}$ monomers as building blocks [98, 312]. The atomistic structure, electronic and optical property of the polymeric species during the MHPs formation has been extensively investigated [87, 98, 312]. Oleksandra and co-workers [98, 312] propose the formation of polynuclear, i.e., formation of $([\text{PbI}_m\text{L}_n]^{2-m})_x$ from $[\text{PbI}_2\text{L}_4]$, is essential in the formation of MHPs. It has been proposed that the polymeric iodoplumbates in the form of $([\text{PbI}_m\text{L}_n]^{2-m})_x$ most likely occur when a high concentration of lead-iodide are used in the precursor solutions [98, 312]. However, an atomistic scale evolution for the molecular complex remains unclear, and the crystallization pathways at various synthesizing conditions remain highly debated.

Another important factor that impacts the coordination chemistry of MHPs is the type of solvents. The most commonly used solvents are dimethylformamide (DMF) [91, 97] and dimethyl sulfoxide (DMSO) [90, 97]. The usage of binary solvent, one as the basic solvent and another as co-solvent, i.e., coordinative additives, is also widely used in the synthesis of MHPs [88, 92, 313-315]. The additives are believed to play an important role in controlling the crystallization process of perovskite films and thus their quality. Among various co-solvents, DMSO is the most used ones in combination with DMF [92, 314, 316]. It has been proposed from experiments that the use of DMSO-DMF binary solvent could retard the crystallization by forming MAI-PbI₂-DMSO complexes, thus slowing down the nucleation rate of MHPs and therefore leads to higher quality final films [84, 316, 317]. However, the atomistic origin of such effects and evolutions relevant complexes involved in the crystallization is challenging to obtain in experiments due to the limitations in the tempo spatial resolutions.

The atomistic simulation is a powerful tool to investigate the fundamental aspects of chemical processes during crystallization at an atomic scale. However, due to the complexity of the species involved, theoretical studies are only emerging. Clancy *et al.* [318] theoretically investigated the relative stability of precursors in solution, and showed that the Mayer bond order could predict the solubility of the lead halide precursors in the solvent. Rothlisberger and colleagues [319] used metadynamics to

investigate the nucleation of MHPs, mimicking a one-step synthesis route. Recently, Angelis *et al.* [308, 310] have studied the formation of high-I-coordinated iodoplumbates. They concluded that a large amount of MAI is needed for the formation of iodine-rich iodoplumbates [308]. This implies the difficulty in the formation of $[\text{PbI}_5\text{L}_n]^{3-}$ and $[\text{PbI}_6\text{L}_n]^{4-}$, which are considered necessary for the formation of high-quality perovskite films [97, 311, 320-324]. To our knowledge, the conversion from the low-I-coordinated iodoplumbates (i.e., PbI_2) to high-I-coordinated iodoplumbates and their conversion to polymeric iodoplumbates is not systematically studied yet. Also, the highly dynamic formation process of the iodoplumbate complexes can be significantly affected by the A-cations as well as the type of solvents, the interplay of which have not been investigated either.

In this work, using MAPbI_3 and two commonly employed solvents (DMF and DMSO) as an example, we investigate the evolution of the iodoplumbates in solutions using a combination of DFT and AIMD simulations. We obtain information on structures and reaction enthalpies of elemental reaction steps from low to high-I-coordinated complexes and investigate how solvents impact the overall reaction pathways. We start the commonly used solvents, DMF and DMSO, and study the impact of the co-solvent DMSO in DMF, by constructing a binary DMF-DMSO model. By analyzing the changes in the structures and energetics of elementary steps, we discuss the advantages of the binary solvent over that of the DMF and DMSO alone. Our work provides an atomistic understanding of the first steps of the crystallization of MHPs and forms a basis for further investigation of more complex perovskite systems or longer time scale simulations to model complete crystallization processes.

6.2. Methods

6.2.1. Density functional theory calculations

All DFT calculations were performed in the Kohn-Sham framework, using the Amsterdam Density Functional package (version ADF 2019.302) [325, 326]. Geometry optimizations were done using the Perdew-Burke-Ernzerhof (PBE) functional [108]. A combination of Herman-Skillman numerical atomic orbitals (NAOs) with Slater type

Triple-zeta (TZP) basis sets were used for heavy atoms (Pb and I), whereas for C, N, H, O, and S atoms, a Double-zeta (DZP) basis sets were used. The cores 1s–4d, 1s–4p, and 1s–2s were kept frozen, respectively, for Pb, I, and S, to speed up the calculations. Vibrational frequencies were obtained with the optimized configurations through numerical differentiation of the analytical gradient. The harmonic level approximation was applied to ensure that the optimized structures are located at global or local minima on the potential energy surface [327-329]. The enthalpies were calculated at 298.15 K and 1 atm from the bond energies and vibrational frequencies by using a standard thermochemistry relation described by Bickelhaupt *et al.* [330, 331]. The solvents were simulated with both implicit solvation models (the COSMO dielectric continuum solvation scheme) [332] and explicit solvent molecules. The use of the hybrid implicit-explicit models were proven to be useful to describe the precursor chemistry of halide perovskites in previous publications [308, 310, 318, 333].

6.2.2. *Ab Initio* molecular dynamics simulation

Ab-initio molecular dynamics (AIMD) simulations were also performed to study the dynamics of precursor-solvent interactions by using the CP2K code [334, 335]. The QUICKSTEP, the electronic structure part of CP2K, uses the combined Gaussian and plane-wave (GPW) method to calculate forces and energies. The GPW method is based on the Kohn-Sham formulation of DFT and employs a hybrid scheme combining Gaussian and plane wave functions. The Born-Oppenheimer molecular dynamics (BOMD) simulations were executed by using a canonical ensemble (NVT) with a Nosé–Hoover thermostat [290] at temperature 353 K (typical temperature for the spin-coating procedure in experiments) [313, 315, 336-338]. All simulations made use of DFT at the PBE level with double-zeta basis sets (DZVP-MOLOPT for Pb, I, S, O, C, N, H) [339] and Goedecker-Teter-Hutter (GTH) pseudopotentials [340] with a 500 Ry density cut-off. A single *k*-point sampled at the Γ was used to speed up the computation. The total simulation time of each calculation is 30 ps with a time step of 1 fs.

6.2.3. Structural models

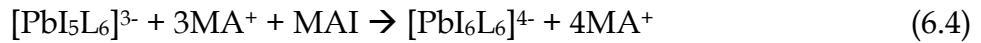
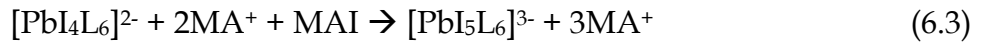
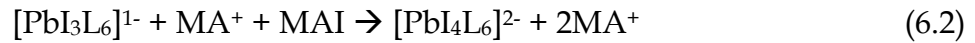
To calculate the formation enthalpy of the iodoplumbates with increased I coordination, models $[\text{PbI}_m\text{L}_n]^{2-m}$ ($m = 2, 3, 4, 5, 6$; $n = 6$) for simple complex and $[(\text{PbI}_m\text{L}_n)^{2-m}]_2$ ($m = 2, 3, 4$; $n = 6-m$) for polymeric iodoplumbates were used, where m is the number of coordinated I, L is the solvent molecules, and n is the number of solvents. We noted that a Pb ion could be fully coordinated with six iodine ions and/or solvent molecular. While for a fully coordinated iodoplumbate complex, more solvent molecular does not directly coordinate with the center Pb ion. The scheme of the formation of both simple and polymeric iodoplumbates are shown in Figure 6.1. In order to ensure charge neutrality, the number of MA^+ cations included in the models equals to the number of the access I^- ions ($m-2$ for simple complex and $2m-4$ for polymeric iodoplumbates). For AIMD simulations, the homogeneous mixture of ions with fixed loading: 6 $[\text{PbI}_3]^-$, 6 MA^+ , and 18 solvents were constructed, with lattice parameters of 14.5 Å to keep the mass concentration of the precursor-solvent at ~2.8 g/mL. The calculated molar concentration of MAI / PbI_2 blend in DMSO or DMF is 2.6M ($M = \text{mol/L}$). The calculated molar concentration of MAI / PbI_2 blend in DMF is equivalent to 1.82 M as a practical concentration, according to the second-order polynomial fitting of the results obtained by Zhang *et al.* [341], which is similar to the experiment concentration of 1.64 M (see Figure D.1). In the DMF-DMSO binary solvents model for DFT calculations, we incorporated 1 DMSO in DMF-DMSO binary solvent models (DMSO:DMF = 1:5) and use DMF as the implicit solvent. While for AIMD simulations of binary solvents model, we induced 2 DMSO, resulting in the ratio of DMSO:DMF = 1:8. The atomic structures and key parameters of DMSO and DMF are shown in Table D.1.

6.3. Results and discussion

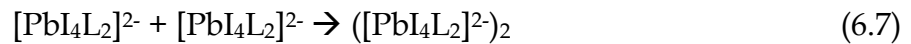
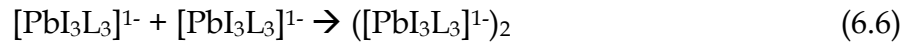
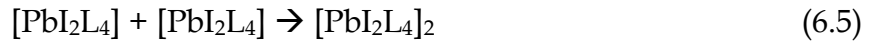
6.3.1. Formation enthalpies of iodoplumbates

To gain insights into the formation of iodoplumbate, we considered from low to high I-coordination, i.e. from $[\text{PbI}_2\text{L}_6]$ to $[\text{PbI}_6\text{L}_6]^{4-}$ in this study. As illustrated in Figure 6.1 (top), the conversion from low I-coordinated iodoplumbate (i.e., $[\text{PbI}_2\text{L}_6]$) to high I-

coordinated iodoplumbate ($[\text{PbI}_3\text{L}_6]^{1-}$, $[\text{PbI}_4\text{L}_6]^{2-}$, $[\text{PbI}_5\text{L}_6]^{3-}$, and $[\text{PbI}_6\text{L}_6]^{4-}$) involves a reaction that requires or releases energy. It should be noted that the negative charge on the coordination sphere due to the access I⁻ is compensated by adding positively charged MA⁺ ions in our simulations. The formation enthalpy of each step is calculated using the Equations 6.1 - 6.4 as following:



To study the formation of polymeric iodoplumbate, we centred on investigating the formation of iodoplumbates dimers $[\text{PbI}_2\text{L}_4]_2$, $([\text{PbI}_3\text{L}_3]^{1-})_2$, and $([\text{PbI}_4\text{L}_2]^{2-})_2$ from the simple iodoplumbates from above, $[\text{PbI}_2\text{L}_6]$, $[\text{PbI}_3\text{L}_3]^{1-}$, and $[\text{PbI}_4\text{L}_2]^{2-}$, respectively, as shown in Figure 6.1 (bottom). The formation enthalpy of the polymeric iodoplumbates is evaluated by using Equations 6.5 – 6.7, as following:



The formation enthalpy for all steps with respect to different solvents are summarized in Figure 6.1. A negative formation enthalpy indicates that the corresponding iodoplumbates formation reaction is favourable. We first look at the step-by-step formation of iodoplumbate from low to high I-coordination. For DMF, the reaction of all steps are favourable, evidenced by the negative formation enthalpies. Especially, the formation enthalpy from $[\text{PbI}_3\text{L}_6]^{1-}$ to $[\text{PbI}_4\text{L}_6]^{2-}$ is -0.72 eV, which is much more negative (about 0.5 eV) than other steps, indicating a rapid formation of $[\text{PbI}_4\text{L}_6]^{2-}$. For DMSO, the formation enthalpies are all negative (in the range of about -0.4 to -0.5 eV), except for the step from $[\text{PbI}_4\text{L}_6]^{2-}$ to $[\text{PbI}_5\text{L}_6]^{3-}$, which is close to 0 (-0.07 eV). This indicates the formation of $[\text{PbI}_5\text{L}_6]^{3-}$ in the solvent-precursor solution become unfavourable. When mixing a small amount of DMSO in DMF, i.e., using a DMF-

DMSO binary solvent, we observe interesting changes in the reaction energetics compared to DMF or DMSO, respectively. While the formation enthalpies of all steps are negative, that from $[\text{PbI}_3\text{L}_6]^{1-}$ to $[\text{PbI}_4\text{L}_6]^{2-}$ become relatively small, being -0.19 eV, compared to -0.72 eV and -0.48 eV for DMF and DMSO, respectively. This indicates that conversion from $[\text{PbI}_3\text{L}_6]^{1-}$ to $[\text{PbI}_4\text{L}_6]^{2-}$ becomes relatively difficult, i.e., relatively slower coordination reactions. It is worth noting that the conversion of $[\text{PbI}_4\text{L}_6]^{2-}$ to $[\text{PbI}_5\text{L}_6]^{3-}$ become more likely, evidenced by the much more negative reaction enthalpy for DMF-DMSO binary compared to DMF or DMSO.

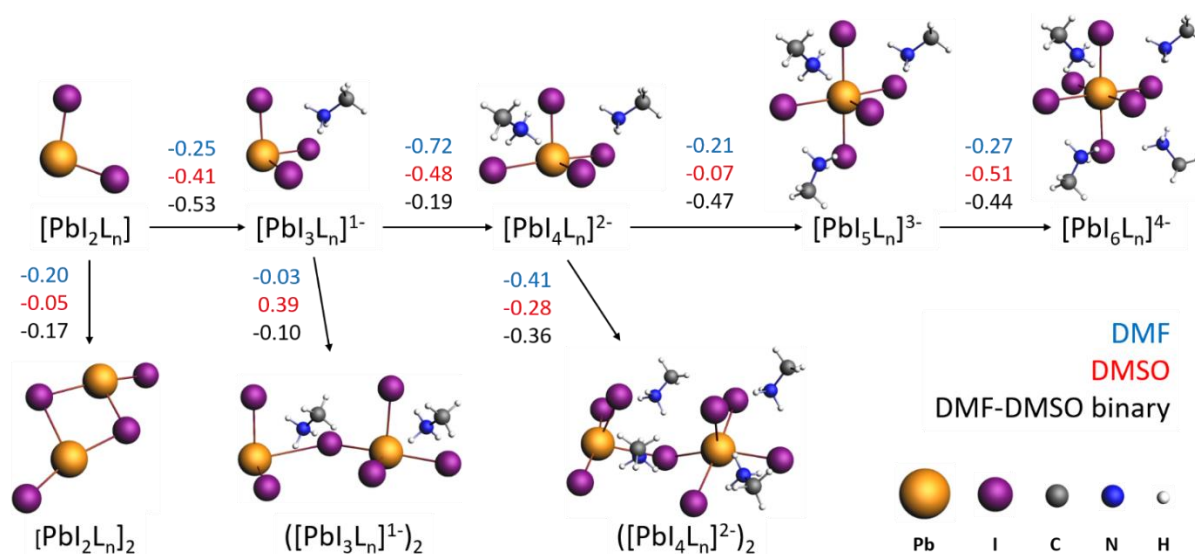


Figure 6.1. Schematic illustration of the iodoplumbate complexes formation: top images are for the simple iodoplumbate complexes, and bottom images are for polymeric iodoplumbate complexes. Formation enthalpy (in eV) of each step using DMF, DMSO, and DMF-DMSO binary as solvents are shown with values in blue, red, and black, respectively. The reaction enthalpies shown in the scheme are calculated by averaging four data points from supporting information in Table D.2, D.3, D.5, D.6, D.8, and D.9. The calculations were done using a hybrid explicit-implicit solvent model using solvent DMF as an example. For clarity, the solvents molecules are not shown in the scheme.

To gain insight into the underlying mechanisms of the significant changes in reaction energies from $[\text{PbI}_3\text{L}_6]^{1-}$ to $[\text{PbI}_4\text{L}_6]^{2-}$ and from $[\text{PbI}_4\text{L}_6]^{2-}$ to $[\text{PbI}_5\text{L}_6]^{3-}$ by using DMF-DMSO binary, we analyze the atomistic structures of the relevant complexes. No significant changes nor general trends in the average Pb-I bond or Pb-O bond were found from $[\text{PbI}_2\text{L}_6]^{1-}$ up to $[\text{PbI}_5\text{L}_6]^{3-}$ (see Figure D.2). We, however, observe an interesting interaction pattern in hydrogen bonds, $\text{NH}\cdots\text{O}$, between N-H bonds of MA^+

cation and the O atom of the solvents in Figure 6.2. The number of NH...O hydrogen bonds in DMF or DMSO increase from $[\text{PbI}_2\text{L}_6]^{1-}$ to $[\text{PbI}_3\text{L}_6]^{1-}$ and to $[\text{PbI}_4\text{L}_6]^{2-}$ but decrease at $[\text{PbI}_5\text{L}_6]^{3-}$. The increase can be explained by the fact more MA^+ are added during the reaction from low to high I-coordinated complexes. Such increase is especially significant with a net increase of 2 from $[\text{PbI}_3\text{L}_6]^{1-}$ to $[\text{PbI}_4\text{L}_6]^{2-}$, explaining the largely negative reaction energies (-0.72/-0.48 eV for DMF/DMSO) compared to the reactions before and after this step. However, the trend is interrupted at $[\text{PbI}_5\text{L}_6]^{3-}$ and the number of NH...O is decreasing instead of increasing. This causes less negative reaction energies (-0.21/-0.07 eV for DMF/DMSO) at this step, because more (weaker) NH...I hydrogen bonds are formed instead of (stronger) NH...O bonds in $[\text{PbI}_5\text{L}_6]^{3-}$ (see Figure D.3). In contrast, for DMF-DMSO binary solvents, the number of NH...O hydrogen bonds does not change from $[\text{PbI}_3\text{L}_6]^{1-}$ to $[\text{PbI}_4\text{L}_6]^{2-}$ and then increases from $[\text{PbI}_4\text{L}_6]^{2-}$ to $[\text{PbI}_5\text{L}_6]^{3-}$. The consequence of this is the formation energy of $[\text{PbI}_4\text{L}_6]^{2-}$ become less negative (-0.19 eV *vs* -0.72/-0.48 eV) and that of $[\text{PbI}_5\text{L}_6]^{3-}$ become more negative (-0.47 eV *vs* -0.21/-0.07 eV). These findings show the importance of A-cation MA^+ and the unique role of NH...O hydrogen bonds in the formation energies of iodoplumbates monomers, a factor that has not been considered in previous studies.

From the energies shown in Figure 6.1 (bottom), most polymeric complexes can be formed in DMF (evidenced by the negative formation enthalpies) with one exception: the formation energy of $([\text{PbI}_3\text{L}_3]^{1-})_2$ being almost zero, -0.03 eV. Another important trend is that the energies of DMSO are all more positive than those in DMF, in particular, the formation energy of $([\text{PbI}_3\text{L}_3]^{1-})_2$ is as high as 0.39 eV. The overall trend can be readily explained by the solvent coordination power of these two solvents with a general trend of DMSO > DMF [310, 322, 342-346]. Indeed, the atomistic structure in Figure D.4 show the two $[\text{PbI}_3\text{L}_3]^{1-}$ monomers cannot or only weakly interact with each other in DMSO because of the strong coordination/interactions of DMSO molecules with Pb^{2+} , giving rise to the largely positive reaction energy of 0.39 eV. A higher likelihood of forming polynuclear complexes can be expected for solvents with weaker coordination ability, such as DMF, because the solvent with weak coordination can be replaced more easily by the I⁻ in the adjacent monomer (see Figure D.4). The DMF-

DMSO binary solvent gives values in between the DMF and DMSO for $[\text{PbI}_2\text{L}_4]_2$ and $([\text{PbI}_4\text{L}_2]^{2-})_2$, but brings down the value for $([\text{PbI}_3\text{L}_3]^{1-})_2$ to below zero (-0.10 eV).

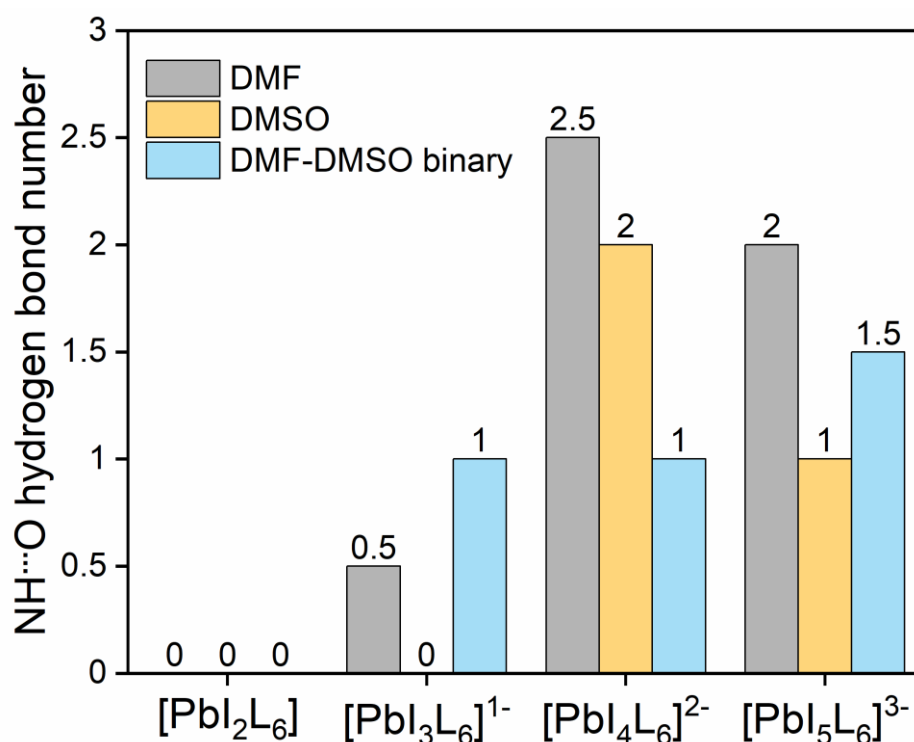


Figure 6.2. The number of $\text{NH}\cdots\text{O}$ hydrogen bonds for $[\text{PbI}_2\text{L}_6]$, $[\text{PbI}_3\text{L}_6]^{1-}$, $[\text{PbI}_4\text{L}_6]^{2-}$, and $[\text{PbI}_5\text{L}_6]^{3-}$ in DMSO and DMF, respectively. Typically, the length of $\text{NH}\cdots\text{O}$ hydrogen bond is shorter than 2.0 \AA [347]. The value shown in the figure is averaged from all $\text{NH}\cdots\text{O}$ hydrogen bonds of two iodoplumbate configurations considered (Table D.4, D.7, and D.10).

From the analysis of the reactions of the simple and polymeric iodoplumbate, we can construct a combined reaction scheme in Figure 6.1 and analyze the effect of the solvents. For DMF, the step-by-step reaction from low to high-I-iodoplumbate are all favourable, especially the formation from $[\text{PbI}_3\text{L}_6]^{1-}$ to $[\text{PbI}_4\text{L}_6]^{2-}$, indicating a rapid formation of $[\text{PbI}_4\text{L}_6]^{2-}$. Polymeric complexes such as $[\text{PbI}_2\text{L}_n]_2$ and $([\text{PbI}_4\text{L}_3]^{2-})_2$ can be formed except for the $([\text{PbI}_3\text{L}_3]^{1-})_2$. The overall energy pathway indicates a rapid conversion from low to high-I-coordinated PbI_x complex. For DMSO, all reaction energies at each step, including the formation of simple and polymeric complex, have become more positive compared to those in DMF. In particular, the step from $[\text{PbI}_4\text{L}_6]^{2-}$ to $[\text{PbI}_5\text{L}_6]^{3-}$ become much more difficult with a reaction energy of close to 0 (-0.07 eV). This indicates the formation of high-I-coordinated complexes, such as $[\text{PbI}_5\text{L}_6]^{3-}$ is

hindered. When mixing a small amount of DMSO in DMF, the reaction energies of all reaction steps fall nicely in a range of -0.50 to -0.10 eV, slowing down the fast conversion from $[\text{PbI}_3\text{L}_6]^-$ to $[\text{PbI}_4\text{L}_6]^{2-}$ in DMF and speeding up the difficult conversion from $[\text{PbI}_4\text{L}_6]^{2-}$ to $[\text{PbI}_4\text{L}_6]^{2-}$ in DMSO. Such balanced energetics can potentially lead to better equilibria among all reaction steps and therefore better final perovskite films. Our analysis is in agreement with several experimental findings that point to the fact when mixing DMSO in DMF, the formation of MAI-PbI₂-DMSO complexes slows down the overall nucleation rate and therefore leads to higher quality final film [84, 316].

6.3.2. Formation dynamics of MHPs with different solvents

The thermodynamics investigation above indicates that the energetics of monomer starting from $[\text{PbI}_3\text{L}_n]^{1-}$ are different from one solvent to another, indicating their importance in determining the overall thermodynamics and as well as the kinetics of the formation of MHPs. We next investigate the dynamical evolution [348-352] of the relevant complexes starting from $[\text{PbI}_3\text{L}_n]^{1-}$ (to reduce computational cost) by using *ab-initio* molecular dynamics (AIMD) simulations. All simulations were done for 30 ps at a typically spin-coating temperature 353 K [313, 315, 336-338]. The trajectory of the initial 5 ps in each simulation is discarded for the data analysis because of the relatively large temperature and energy oscillation (see Figure D.5).

Figure 6.3 illustrates the snapshots of the beginning and the end of the frames in the AIMD simulations. For the DMF, we observe quickly formation of high-I-coordinated iodoplumbate such as $[\text{PbI}_4\text{L}_n]^{2-}$ and $[\text{PbI}_5\text{L}_n]^{3-}$ within only 30 ps, and face sharing polymeric complexes, indicating a relatively fast nucleation rate. In contrast, in DMSO, we only observe a small amount of corner-sharing polymeric complexes, with the majority of the species preserving the feature of starting monomer $[\text{PbI}_3\text{L}_n]^{1-}$. Moving to the DMF-DMSO binary, we find a large block of PbI_x complex that are centred by face-shared and fully-coordinated iodoplumbate and surrounded by some corner-sharing $[\text{PbI}_3\text{L}_n]^{1-}$. We speculate such complex is a starting point for the formation of 3D perovskite structure (fully coordinated PbI_x complexes that are cornered shared with each other). Indeed, Rothlisberger *et al.* [319, 353] demonstrated

a slow transition from edge-sharing octahedra to the corner-sharing octahedra after hundreds of nanoseconds using metadynamics. This explains the reason we do not observe a full transition to 3D perovskites in our simulations (due to the short time scale and the limited size of our simulation cell). The quantitative trends are however well captured in our simulations.

To zoom in to the atomistic details of the simulations from Figure 6.3, we plot in Figure 6.4 the $g(r)$ and cumulative radial distribution functions $\text{int}[g(r)]$ for Pb-I and Pb-O bonds in different solvents. The $g(r)$ of Pb-I shows that the iodine mainly interacts with Pb at the typical Pb-I bond distance of slightly longer than 3.0 Å, which agrees with the results from Angelis *et al.* [354] by using Car-Parrinello molecular dynamics (CPMD) simulations for two-step formation of MAPbI₃. The $\text{int}[g(r)]$ of Pb-I shows that the average coordination number of iodine to the Pb is between 3 and 4 for DMSO and DMF, and larger than 4 for the DMF-DMSO binary solvent. This trend is supported by the trend seen in Pb-O bonds, where the number of the Pb-O coordination, being about 0.2, is the smallest in the binary solvent, with DMF being 1 and DMSO being 0.5, respectively. This analysis supports the findings above that the use of DMF-DMSO binary solvent promotes the growth of high I-coordinated iodoplumbate.

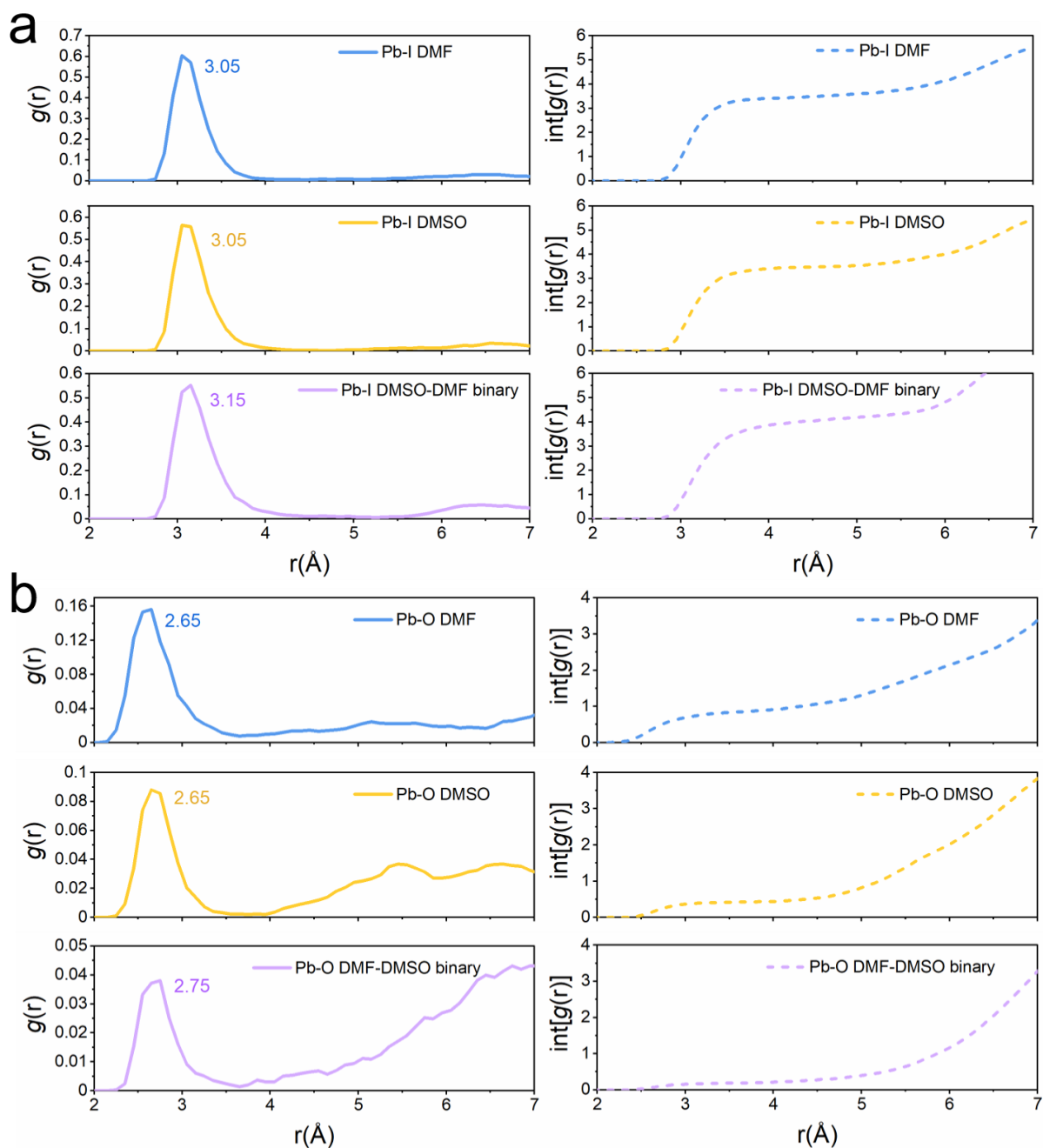


Figure 6.4. Radial distribution function $g(r)$ (left) and cumulative radial distribution functions $\text{int}[g(r)]$ (right) of (a) Pb-I, and (b) Pb-O for DMF, DMSO, and DMF-DMSO binary solvents, respectively.

6.4. Conclusions

In summary, to understand the coordination chemistry in MHPs precursor solutions, we study the interactions of perovskite precursors with solvents by combining DFT and AIMD calculations. We construct a reaction scheme for the crystallization of MAPbI_3 at the early stage by combining reactions that form simple and polymeric PbI_x

complexes and analyze the effect of the commonly used solvents, DMF, DMSO as well as DMF-DMSO binary solvents. For DMF, the step-by-step reaction from low to high I-iodoplumbate are all favourable. In particular, the conversion from $[\text{Pb}_3\text{L}_6]^{1-}$ to $[\text{Pb}_4\text{L}_6]^{2-}$ is highly favourable, indicating a rapid formation of $[\text{Pb}_4\text{L}_6]^{2-}$. Polymeric complexes, for instance, the $[\text{PbI}_2\text{L}_n]_2$ and $([\text{PbI}_4\text{L}_3]^{2-})_2$ can also be formed. The overall energetics of all elementary reaction steps indicates a rapid reaction from low to high I-coordinated PbI_x complex. For DMSO, due to its high ability to coordinate with solvents, all reactions have become less favourable than those in DMF. In particular, the step from $[\text{Pb}_4\text{L}_6]^{2-}$ to $[\text{Pb}_5\text{L}_6]^{3-}$ become difficult. When using DMSO as an additive for DMF, the reaction energies are well balanced, where the reaction from $[\text{Pb}_3\text{L}_6]^-$ to $[\text{Pb}_4\text{L}_6]^{2-}$ is slower compared to the fast conversion in DMF, and the conversion from $[\text{Pb}_4\text{L}_6]^{2-}$ to $[\text{Pb}_4\text{L}_6]^{2-}$ is promoted compared to the difficult conversion in DMSO. The balanced energetics potentially lead to better equilibria among all reaction steps and therefore better final perovskite films.

The results from AIMD simulations confirm our observations obtained from DFT. In DMF, while high-I-coordinated PbI_x complex quickly forms, they exhibit face-sharing configuration. For DMSO, the reaction is much slower, and the majority of the species remain unreacted. The mixture of DMF and DMSO in a binary solvent promotes not only high-I-coordinated iodoplumbate but also PbI_x complex with a corner-sharing feature, which can be served as a nucleation center to form 3D perovskites.

Our results provide insights into the role of precursors and solvents in the thermodynamics and kinetics of perovskite formation. The detailed atomistic analysis offers a unique and experimentally inaccessible insight regarding the early stages of the perovskite crystallization and provide an important basis for future work on more complex perovskite compositions and/or a complete crystallization process.

Chapter 7

Conclusions and Outlook

7.1. Conclusions

This thesis focuses on a computational study of the compositional engineering, including the precursors and solvents, the chemical compositions and dimensionality of the final films with the aim of improving the stability of MHP halide perovskites and their devices.

In Chapter 3, we provide insights into the unwanted phase transition of three pristine perovskites (FAPbI_3 , CsPbI_3 , and CsSnI_3) and reveal the mechanisms of the improved phase stability of the mixed compounds ($\text{Cs}_x\text{FA}_{1-x}\text{PbI}_3$, $\text{CsSn}_y\text{Pb}_{1-y}\text{I}_3$, and $\text{CsSn}(\text{Br}_z\text{I}_{1-z})_3$) by using DFT calculations. We identify that phase transitions of MHPs from the perovskite to the nonperovskite phase are related to the relative strength of the metal-halide bonds as well as hydrogen bonds (for hybrid compositions), and the role of vacancy defects (in the case of Sn-containing perovskites). We demonstrate that the phase stability of several well-known perovskite compositions can be optimized by mixing ions, which gives rise to either increased bond strengths of the perovskites and/or decreased bond strengths in their nonperovskite counterparts or suppressed defect formation, in the case of Sn-Pb mixed compounds. Insights obtained from this study provide a comprehensive understanding of the mechanisms for the phase instability and provide design rules for engineering phase-stable perovskite compositions.

Inspired by the results from Chapter 3, we further design new perovskite compositions. Here, we aim to avoid the toxic element Pb by replacing Pb with Sn. Although Sn is one of the most promising alternatives, the stability of Sn-based perovskites is far from ideal. Here, we identify in Chapter 4 a promising $\text{Rb}_y\text{Cs}_{1-y}$

$y\text{Sn}(\text{Br}_x\text{I}_{1-x})_3$ perovskite for solar cell applications, prepared by mixing cations (Rb for Cs) and anions (Br for I) in CsSnI_3 . We studied the evolution of the structural, thermodynamic, and electronic properties as a function of the percentages of the substitution of Rb for Cs and Br for I. We show that $\text{Cs}_y\text{Rb}_{1-y}\text{Sn}(\text{Br}_x\text{I}_{1-x})_3$ perovskites have direct band gaps in the range of 1.3-2.0 eV. The alloys with high I and Cs concentration are well suited for highly efficient single-junction PSCs, while those with high Rb and Br concentration are suitable as wide band gap materials for tandem PSCs. Importantly, we found that substitution of Br for I can improve the phase stability, suppressing the unwanted phase transition from the perovskite to the nonperovskite structure. $\text{Cs}_y\text{Rb}_{1-y}\text{Sn}(\text{Br}_x\text{I}_{1-x})_3$ prefers the perovskite phase when $x > 1/3$. Moreover, substitution of Rb for Cs enables the formation of highly homogeneous solid solutions for improved solar cell performance.

In Chapter 5, we extend our investigation from bulk perovskites to quantum dots (QDs), using the dimensional engineering strategy. This is motivated by the fact that reducing the 3D perovskite grains down to 0D QDs shows great potential in stabilizing the perovskite phase. Here, using Sn-Pb alloyed QDs as an example, we investigate how additives affect the properties of perovskite QDs and improve the performance and stability of Sn-based QDs. The role of sodium additive in stabilizing $\text{CsSn}_{0.6}\text{Pb}_{0.4}\text{I}_3$ perovskite QDs was studied by calculating the strength of the surface bonds, defect formation energies, and the interaction of surface ligands with perovskite surfaces by DFT and AIMD simulations. The results suggest that Na ions enhance the covalent bonding of the surface tin-iodine bonds and form strong ionic bonding with the neighbouring iodine anions, thus suppressing the formation of I and Sn vacancies. Furthermore, the Na ions also enhance the binding strength of the surface ligands with the perovskite QDs surface. Nevertheless, according to AIMD simulations, the enhanced surface ligand binding is only effective on a specific surface configuration. The Na ions remain fixed on a CsI-terminated surface, but they diffuse vigorously on a MI_2 -terminated surface. Correspondingly, the positive effect of Na vanishes with time, explaining the relatively short lifetime of the experimentally obtained high photoluminescence quantum yield (PLQY). From these results, we propose that the

surface termination engineering of the QDs could be the next step to maintain the favourable effect of Na doping for a high and stable PLQY of Sn-Pb QDs.

Finally, improving the stability of perovskites final film can be done by engineering the growth conditions of MHPs. Therefore, in Chapter 6 we perform a comprehensive investigation to understand the crystallization chemistry and the impact of the precursors and solvents engineering. Here, using MAPbI₃ as an example, we study the complex evolution of the molecular species from the solution to the initial stage of the nucleation and determine the reaction pathways for the formation of polynuclear iodoplumbates in different solvents. For DMF, the step-by-step reactions from low to high-I-iodoplumbate are all favourable, especially the formation from [PbI₃L₆]¹⁻ to [PbI₄L₆]²⁻, indicating a rapid formation of [PbI₄L₆]²⁻. Polymeric complexes including [PbI₂L_n]₂ and ([PbI₄L₃]²⁻)₂ can be formed in DMF but fails for ([PbI₃L₃]¹⁻)₂. The formation path in DMF indicates an overall rapid reaction from a low to a high I-coordinated PbI_x complex. For DMSO, all reactions, including the simple and polymeric complex formation, become more difficult than in DMF. Particularly, the conversion from [PbI₄L₆]²⁻ to [PbI₅L₆]³⁻ becomes much more difficult. This indicates that the formation of the high-I-coordinated complex (e.g. [PbI₅L₆]³⁻) is suppressed. When using a DMF-DMSO binary solvent, the reaction from [PbI₃L₆]⁻ to [PbI₄L₆]²⁻ is slower as compared to the fast conversion in DMF, while the conversion from [PbI₄L₆]²⁻ to [PbI₅L₆]³⁻ is easier as compared to the difficult conversion in DMSO. The balanced energetics gives rise to better equilibrium among all reaction steps and therefore potentially better final perovskite films. The results from AIMD simulations starting from a [PbI₃L_n]¹⁻ monomer further confirmed our observations from DFT calculations. In DMF, while high-I-coordinated PbI_x quickly forms, a face-sharing configuration is exhibited. For DMSO, the reaction is much slower, where the majority of the species remain unreacted. The mixture of DMF and DMSO in a binary solvent promotes not only high-I-coordinated iodoplumbate but also PbI_x complexes with corner-sharing feature, which can serve as a nucleation center to form 3D perovskites. Our work provides an atomistic understanding of the first steps of the crystallization of MHPs

and forms a basis for further investigation of more complex perovskite systems or longer time scale simulations to model complete crystallization processes.

7.2. Outlook

Although several compositional engineering solutions were explored in this thesis, our efforts are in no way exhaustive. Below, some future directions are discussed, including aspects of both materials engineering as well as computational methodology advances.

For the compositional engineering of MHPs, all simulations in this thesis were done for single-crystalline bulk systems. However, experimental absorber layers in perovskite solar cells (PSCs) often have polycrystalline structures, thus involving grain boundaries [355]. These grain boundaries will greatly influence the long-term stability of the PSCs, because they are shown to be sensitive to thermal stress [356-358] and environmental species such as water [359-361]. Additionally, this thesis mainly focused on compositions with binary cations or anions. The extension to ternary ion compositions is very much relevant, as FA-MA-Cs triple cation perovskite show considerably improved stability [43, 362]. Further improvement of the stability of MHPs could also be realized through surface and/or interface post-treatment with chemical modification to alleviate lattice strain and minimize vacancy defects, including dimensional control (e.g. quantum dots or quasi-2D perovskites) and heterojunction control (interface between perovskite and HTL/ETL).

For the Sn-Pb perovskite QDs, the PLQY is still much lower than for other perovskite QDs, because Sn suffers from oxidation, drastically increasing the defect density and decreasing PLQY and stability. Therefore, further investigations for improving both the stability and the PLQY are highly desired. First, ligand engineering by introducing new ligands could be a promising strategy. Second, tailoring the Sn-Pb perovskite QDs by doping with other elements, for instance, rare-earth elements, could be tried. In this thesis, perovskite QDs are studied using the slab model. Although the slab model has been widely accepted for studying QDs, a quantum dot model that considers the surface structures of a 3D QD structure would be useful. There are recent

investigations [82, 363] of perovskite QDs by using the quantum dot model. However, most of these studies rely on AIMD simulations, which are computationally expensive and therefore limit the model size and the timescale.

Regarding the engineering of the precursor solution of MHPs, future efforts could be directed towards the computational screening of novel solvents. These can include the investigation of other binary solvents beyond DMF-DMSO and extending the studies from MAPbI₃ to other perovskites, either organic or inorganic MHPs, such as FAPbI₃, CsPbI₃. Furthermore, investigations of the effect of anti-solvents and the mechanism of the newly developed ionic liquid method [364, 365] are also of great interest.

In this thesis, the compositional engineering of MHPs was investigated using mostly by DFT calculations and sometimes AIMD simulations. However, the MHPs are highly dynamic, and several dynamical processes during the fabrication (nucleation and crystallization), in the final films (lattice vibrations, cation rotations), and during degradation in a working device (ion migration, defect reactions, light-induced segregation) occur at various time scales. All these processes have important implications for the PSC stability. Therefore, future study could benefit from long-time scale Molecular Dynamics simulations, e.g., using Classical MD by making use of ReaxFF, and the Density Functional based Tight Binding (DFTB) method. In particular, the Reactive MD method is powerful in investigating the dynamical and reactive processes (including the various defects and their exchange) for large systems and/or long time scales. This will provide opportunities to study the grain boundaries of polycrystalline MHPs, perovskite QDs with larger size and heavier ligands, and the crystallization process of MHPs.

Appendix A

Supplemental Information for

Chapter 3

Lattice constants (in Å) of nine pure perovskites and nonperovskite phases obtained by PBE, PBEsol, and SCAN-rv010 functionals compared to experimental data; detailed synthetic recipes for obtaining various Pb/Sn ratios for $\text{CsSn}_{1-y}\text{Pb}_y\text{I}_3$; structure model of δ -FAPbI₃ and a -FAPbI₃; structure models for $2 \times 2 \times 2$ a -FAPbI₃ and $1 \times 1 \times 2$ δ -FAPbI₃ with different FA orientations by increasing the degree of FA disorder; structure models for the $2 \times 2 \times 2$ $\text{Cs}_x\text{FA}_{1-x}\text{PbI}_3$ perovskite and $\text{Cs}_x\text{FA}_{1-x}\text{PbI}_3$ nonperovskite with different Cs alignments; $2 \times 2 \times 2$ a -FAPbI₃ perovskite comparison with reference; structure models of CsI, FAI, PbI₂, and SnI₂; pDOS and COHP of CsSnI_3 in the form of perovskite and nonperovskite; ICOHP of metal-halide bonding (also with FA-I bonding for $\text{Cs}_x\text{FA}_{1-x}\text{PbI}_3$) near the Fermi level of perovskite and nonperovskite phases of $\text{CsSn}(\text{Br}_z\text{I}_{1-z})_3$, $\text{Cs}_x\text{FA}_{1-x}\text{PbI}_3$, and $\text{CsSn}_y\text{Pb}_{1-y}\text{I}_3$; and cell volumes of $\text{Cs}_x\text{FA}_{1-x}\text{PbI}_3$, $\text{CsSn}_y\text{Pb}_{1-y}\text{I}_3$, and $\text{CsSn}(\text{Br}_z\text{I}_{1-z})_3$ with different mixing percentages.

Table A.1. Lattice constants (in Å) of ten pure perovskite and nonperovskite phases considered in this work obtained by PBE functional compared to experimental data. a: ref [366], b: ref [367], c: ref. [368], d: ref. [14], e: ref. [41], f: ref. [219]. Lattice parameter mismatch percentage (in %) of this work compared with experimental values.

Material	Lattices constants (this work)	Lattice constants (experimental)	Lattice constant mismatched percentage (%)
α -FAPbI ₃	6.47	6.357 ^a	1.78
δ -FAPbI ₃	8.72, 8.72, 7.95	8.622, 8.622, 7.945 ^b	1.14, 1.14, 0.06
α -CsPbI ₃	6.38	6.2894 ^c	1.44
δ -CsPbI ₃	10.90, 4.88, 18.22	10.462, 4.799, 17.765 ^d	4.19, 1.69, 2.56
γ -CsSnI ₃	8.99, 12.52, 8.63	8.69, 12.38, 8.64 ^e	3.45, 1.13, -0.12
δ -CsSnI ₃	10.94, 4.82, 17.99	10.35, 4.76, 17.68 ^e	5.70, 1.26, 1.75
α -CsSnBr ₃	5.89	5.804 ^f	1.48
γ -CsSnBr ₃	8.36, 11.79, 8.22	-	-
δ -CsSnBr ₃	10.02, 4.59, 17.12	-	-

Table A.2. Lattice constants (in Å) of ten pure perovskite and nonperovskite phases considered in this work obtained by PBEsol functional compared to experimental data. a: ref [366], b: ref [367], c: ref. [368], d: ref. [14], e: ref. [41], f: ref. [219]. Lattice parameter mismatch percentage (in %) of this work compared with experimental values.

Material	Lattices constants (this work)	Lattice constants (experimental)	Lattice constant mismatched percentage (%)
α -FAPbI ₃	6.37	6.357 ^a	0.2
δ -FAPbI ₃	8.66, 8.66, 7.90	8.622, 8.622, 7.945 ^b	0.44, 0.44, -0.57
α -CsPbI ₃	6.23	6.2894 ^c	-0.94
δ -CsPbI ₃	10.42, 4.76, 17.68	10.462, 4.799, 17.765 ^d	-0.40, -0.81, -0.48
γ -CsSnI ₃	8.76, 12.25, 8.38	8.69, 12.38, 8.64 ^e	0.81, -1.05, -3.01
δ -CsSnI ₃	10.40, 4.69, 17.59	10.35, 4.76, 17.68 ^e	0.48, -1.47, -0.51
α -CsSnBr ₃	5.75	5.804 ^f	-0.93
γ -CsSnBr ₃	8.23, 11.53, 7.92	-	-
δ -CsSnBr ₃	9.67, 4.47, 16.62	-	-

Table A.3. Lattice constants (in Å) of ten pure perovskite and nonperovskite phases considered in this work obtained by SCAN-rVV10 functional compared to experimental data. a: ref [366], b: ref [367], c: ref. [368], d: ref. [14], e: ref. [41], f: ref. [219]. Lattice parameter mismatch percentage (in %) of this work compared with experimental values.

Material	Lattices constants (this work)	Lattice constants (experimental)	Lattice constant mismatched percentage (%)
α -FAPbI ₃	6.26	6.357 ^a	-1.53
δ -FAPbI ₃	8.66, 8.66, 7.90	8.622, 8.622, 7.945 ^b	0.44, 0.44, -0.57
α -CsPbI ₃	6.05	6.2894 ^c	-0.38
δ -CsPbI ₃	10.03, 4.61, 17.15	10.462, 4.799, 17.765 ^d	-4.13, -3.94, -3.46
γ -CsSnI ₃	9.17, 11.94, 7.22	8.69, 12.38, 8.64 ^e	5.52, -3.55, -16.44
δ -CsSnI ₃	10.00, 4.52, 17.20	10.35, 4.76, 17.68 ^e	-3.38, -5.04, -2.71
α -CsSnBr ₃	5.60	5.804 ^f	-3.51
γ -CsSnBr ₃	8.65, 11.29, 6.78	-	-
δ -CsSnBr ₃	9.17, 4.13, 16.60	-	-

Table A.4. The detailed synthetic recipes for obtaining various quantum dots (QDs) with compositions of CsSn_{1-y}Pb_yI₃ (y = 0, 0.25, 0.5, 0.75, 1).

QDs	TOP (mL)	SnI ₂ (mmol)	PbI ₂ (mmol)
CsPbI ₃	2.5	/	2
CsSn _{0.25} Pb _{0.75} I ₃	2.5	2	0.9
CsSn _{0.25} Pb _{0.75} I ₃	2.5	2	0.7
CsSn _{0.75} Pb _{0.25} I ₃	2.5	2	0.45
CsSnI ₃	2.5	2	/

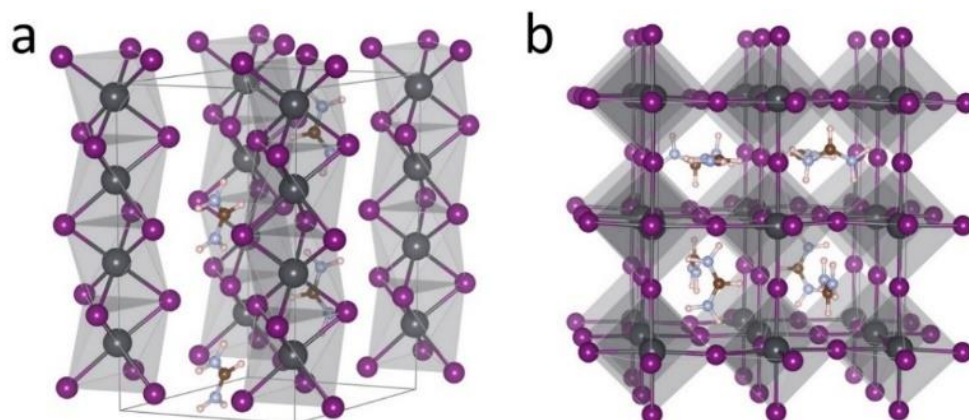


Figure A.1. Structure models of (a) yellow δ -phase FAPbI_3 and (b) black α -phase FAPbI_3 . The $1 \times 1 \times 2$ δ - FAPbI_3 and $2 \times 2 \times 2$ α - FAPbI_3 supercells are used for the calculations presented in the main text. It should be noted that, for $\text{Cs}_x\text{FA}_{1-x}\text{PbI}_3$ perovskites, the nonperovskite structure of FAPbI_3 and CsPbI_3 are different. According to previous study [13, 164], in the range of $0 \leq x \leq 0.5$, the δ phase with hexagonal structure is adopted; for $0.5 \leq x \leq 1$, the δ -phase with orthorhombic structure is chosen. For $x = 0.5$, we calculate the energies of δ -phase with both hexagonal and orthorhombic structures and adopt the one with the most negative energy.

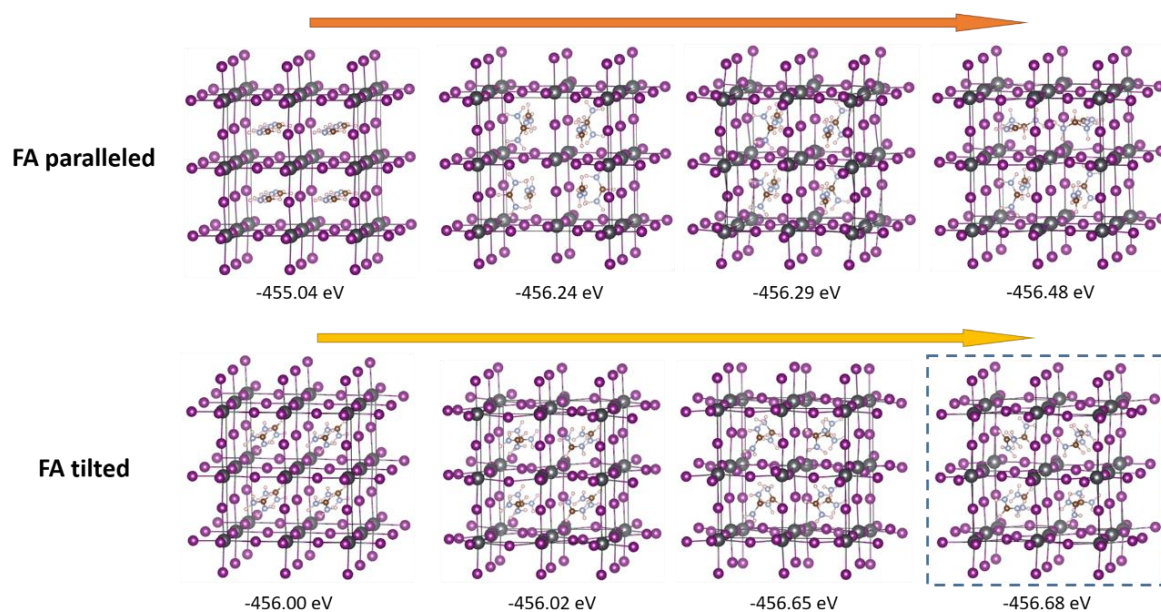


Figure A.2. Structure models for $2 \times 2 \times 2$ α - FAPbI_3 with different FA orientations (paralleled and tilted) by increasing degree of disorder of FA. The configuration with the most disordered distribution of tilted FA cations is the most stable one, highlighted by blue dashed line.

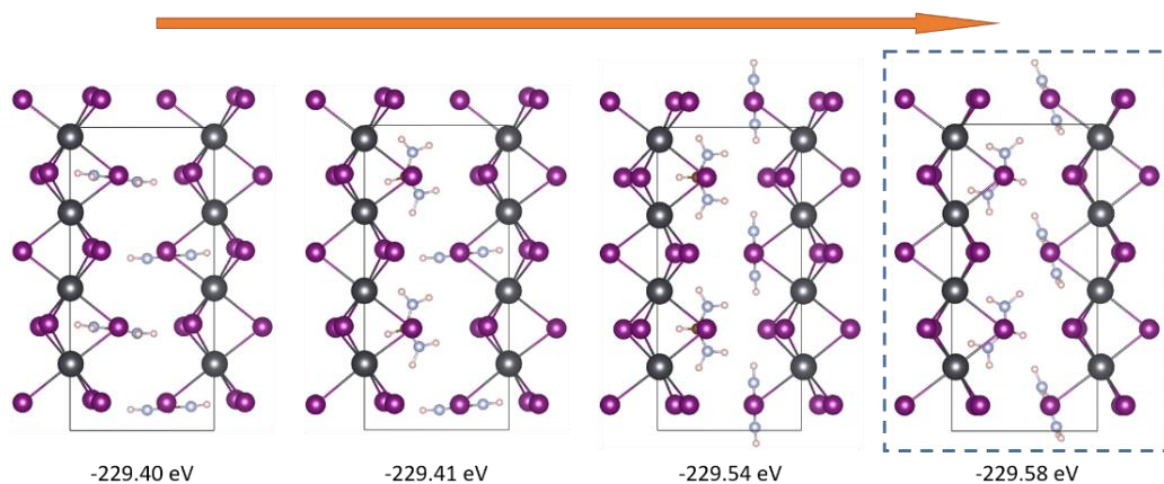


Figure A.3. Structure models for $1 \times 1 \times 2$ hexagonal δ -FAPbI₃ with different FA orientation by increasing degree of FA disorder. The configuration with the most disordered distribution of FA cations is the most stable one, highlighted by blue dashed line.

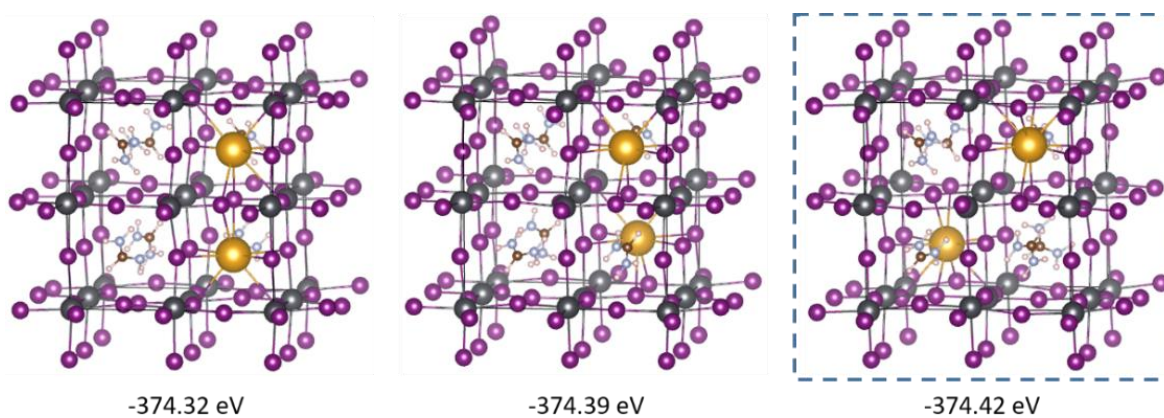


Figure A.4. Structure models for $2 \times 2 \times 2$ Cs_{0.25}FA_{0.75}PbI₃ perovskite with different combination of Cs and FA cations. The most stable configuration is highlighted by blue dashed line.

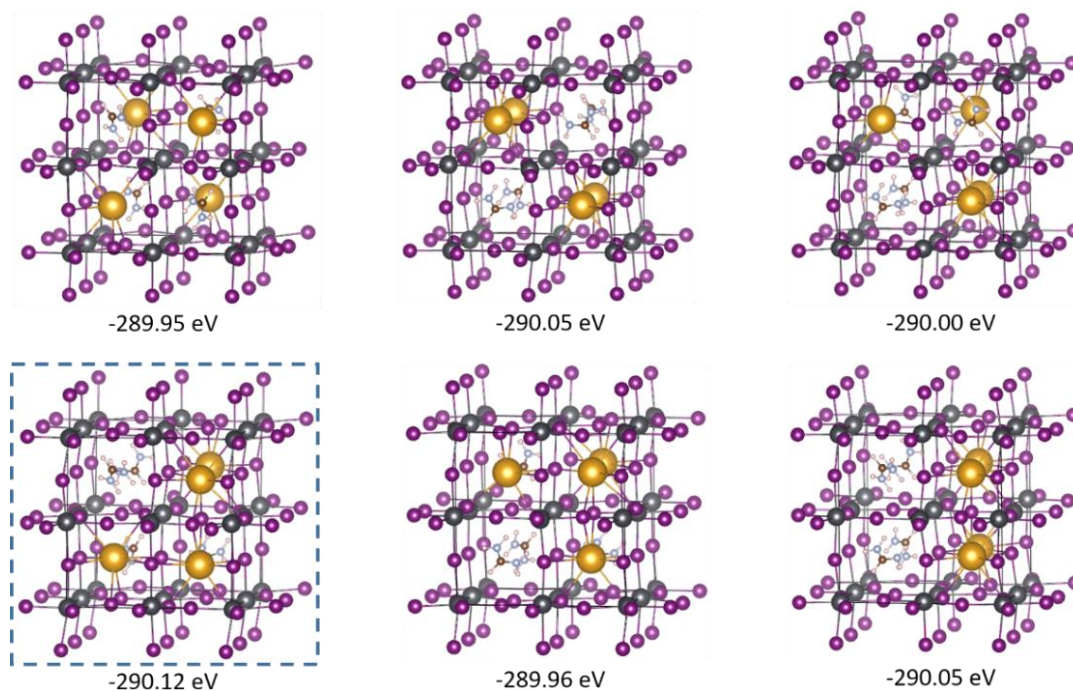


Figure A.5. Structure models for $2 \times 2 \times 2$ $\text{Cs}_{0.5}\text{FA}_{0.5}\text{PbI}_3$ perovskite with different combination of Cs and FA cations. The most stable configuration is highlighted by blue dashed line.

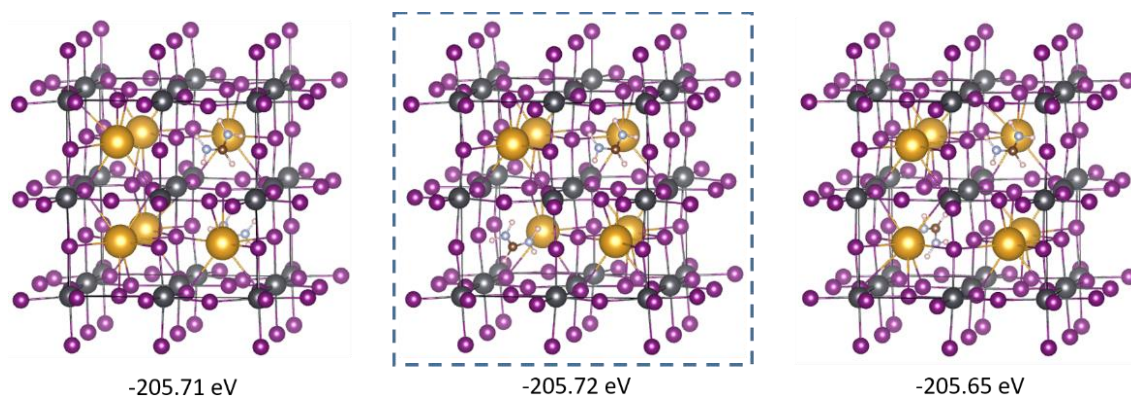


Figure A.6. Structure models for $2 \times 2 \times 2$ $\text{Cs}_{0.75}\text{FA}_{0.25}\text{PbI}_3$ perovskite with different combination of Cs and cations. The most stable configuration is highlighted by blue dashed line.

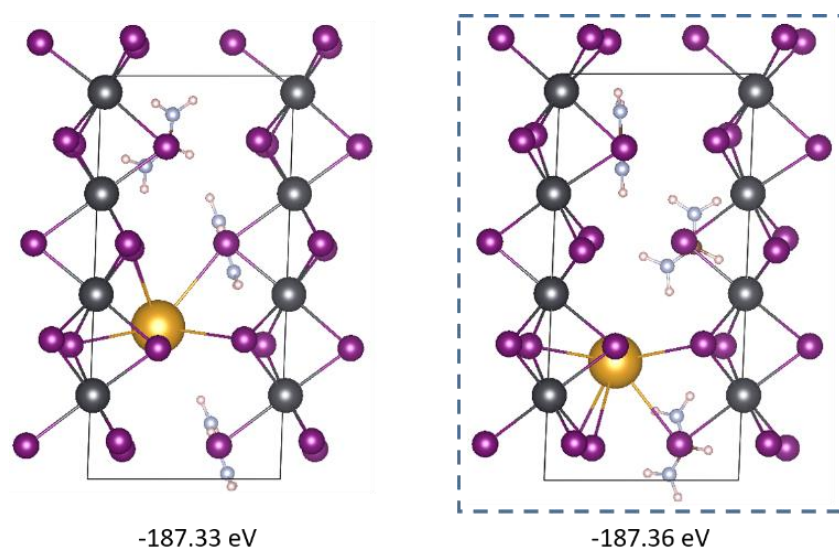


Figure A.7. Structure models for $1 \times 1 \times 2$ hexagonal $\text{Cs}_{0.25}\text{FA}_{0.75}\text{PbI}_3$ nonperovskite with different combination of Cs and FA cations. The most stable configuration is highlighted by blue dashed line.

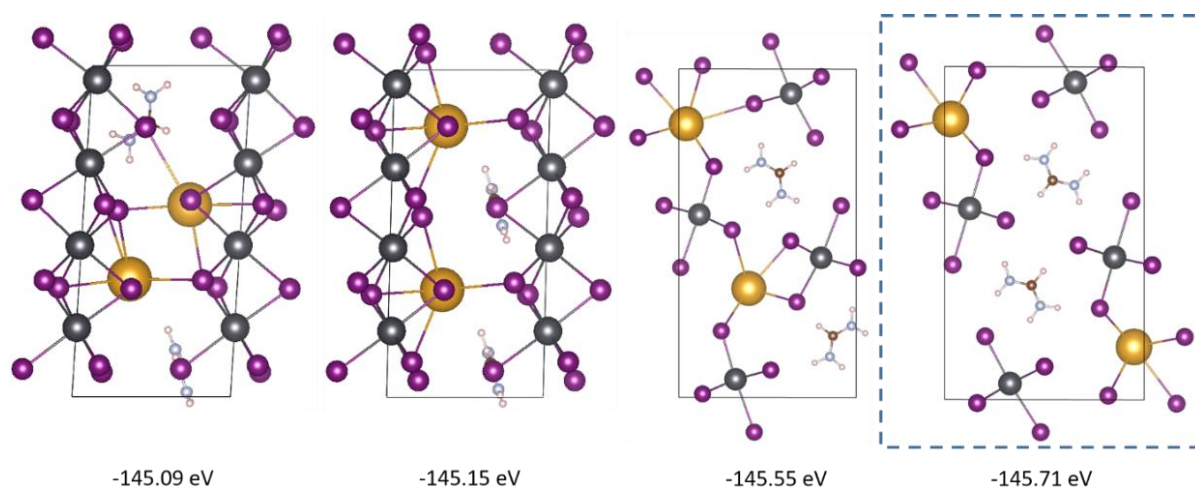


Figure A.8. Structure models for both $1 \times 1 \times 2$ hexagonal $\text{Cs}_{0.5}\text{FA}_{0.5}\text{PbI}_3$ and $1 \times 1 \times 1$ orthorhombic $\text{Cs}_{0.5}\text{FA}_{0.5}\text{PbI}_3$ nonperovskite with different combination of Cs and FA cations. The most stable configuration is highlighted by blue dashed line.

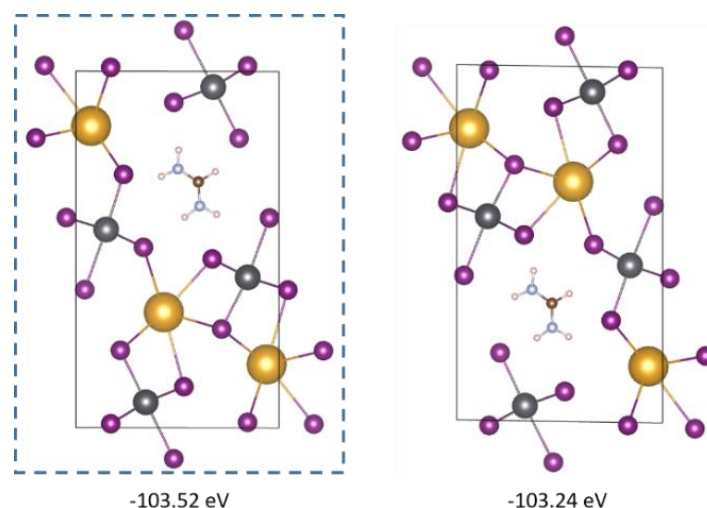


Figure A.9. Structure models for $1\times 1\times 1$ orthorhombic $\text{Cs}_{0.75}\text{FA}_{0.25}\text{PbI}_3$ nonperovskite with different combination of Cs and FA cations. The most stable configuration is highlighted by blue dashed line.

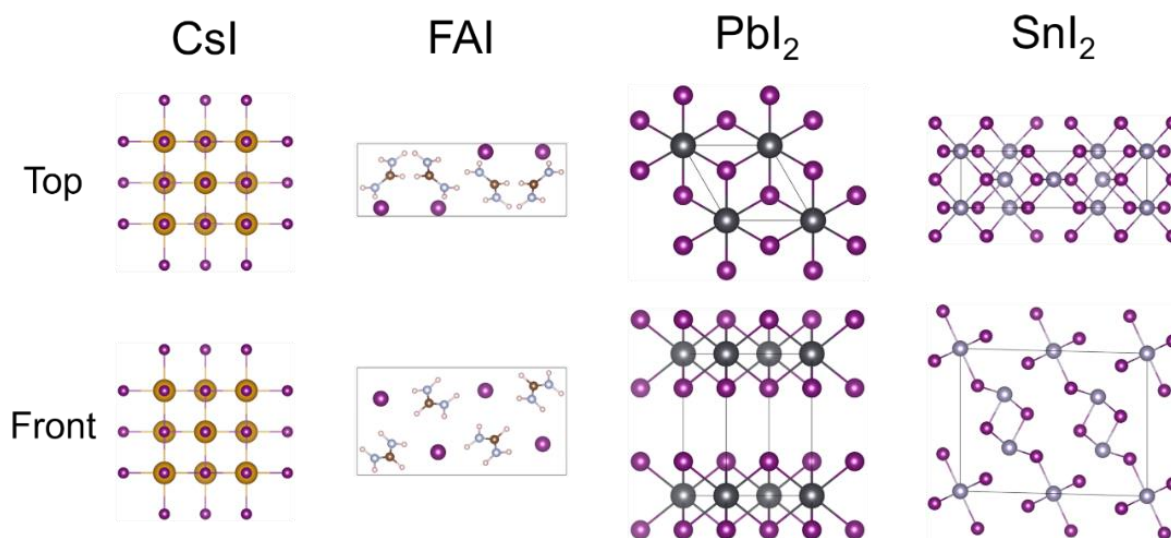


Figure A.10. Structure models of CsI, FAI, PbI_2 , and SnI_2 . The CsI model consists of 4 Cs atoms, and 4 I atoms, respectively. The FAI model consists of 4 C atoms, 8 N atoms, 20 H atoms, and 4 I atoms, respectively. The PbI_2 model consists of 1 Pb atom and 2 I atoms, respectively. The SnI_2 model consists of 6 Sn atoms and 12 I atoms, respectively. To calculate the formation energy of the perovskites, their energies are normalized by each formula unit (AM or MX_2).

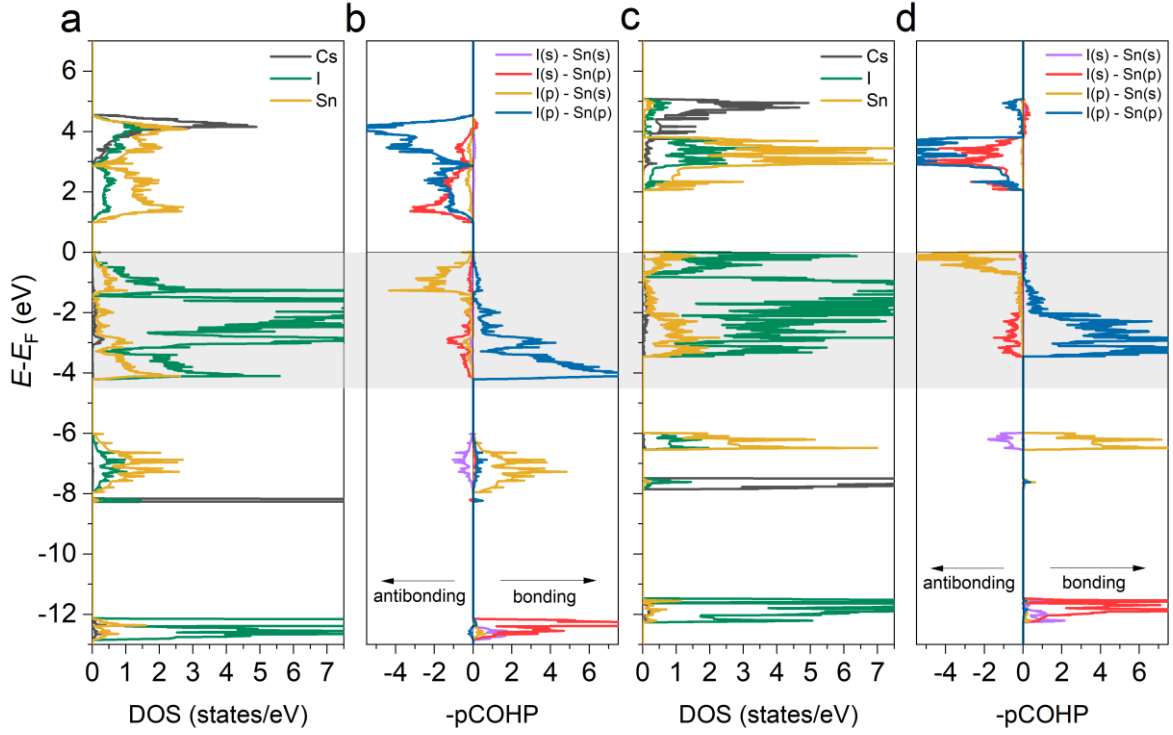


Figure A.11. Comparison of partial Density of State (pDOS) and Crystal Orbital Hamilton Population analysis (-COHP) of CsSnI_3 in the form of perovskite and nonperovskite: (a) and (c) are pDOS, and (b) and (d) are orbital-resolved -COHP. The -COHP plots are normalized by each AMX_3 formula unit.

Table A.5. The -ICOHP of metal-halide bond and FA-I interaction from -4.5 eV to E_F for the perovskite and nonperovskite $\text{Cs}_x\text{FA}_{1-x}\text{PbI}_3$ ($x = 0, 0.25, 0.5, 0.75, 1$). The values are normalized by each AMX_3 formula unit.

$\text{Cs}_x\text{FA}_{1-x}\text{PbI}_3$	0	0.25	0.5	0.75	1
$-\text{ICOHP}_{\text{perovskite I-Pb}}$	3.69	3.67	3.65	3.65	3.52
$-\text{ICOHP}_{\text{perovskite FA-I}}$	1.29	0.89	0.54	0.24	0
$-\text{ICOHP}_{\text{perovskite}}$	4.98	4.56	4.19	3.89	3.52
$-\text{ICOHP}_{\text{nonperovskite I-Pb}}$	3.35	3.34	3.53	3.49	3.50
$-\text{ICOHP}_{\text{nonperovskite FA-I}}$	1.32	0.87	0.56	0.27	0
$-\text{ICOHP}_{\text{nonperovskite}}$	4.67	4.21	4.09	3.76	3.50
$-\text{ICOHP difference}$	0.31	0.35	0.1	0.13	0.02

Table A.6. The -ICOHP of metal-halide bond from -4.5 eV to E_F for the perovskite and nonperovskite $\text{CsSn}(\text{Br}_z\text{I}_{1-z})_3$ ($z = 0, 1/3, 1/2, 2/3, 1$). These values are normalized by each AMX_3 formula unit.

$\text{CsSn}(\text{Br}_z\text{I}_{1-z})_3$	0	1/3	1/2	2/3	1
-ICOHP _{perovskite} X-Sn	3.22	3.10	3.08	3.02	2.98
-ICOHP _{nonperovskite} X-Sn	3.17	2.34	2.34	2.32	2.30
-ICOHP difference X-Sn	0.05	0.76	0.74	0.70	0.68

 Table A.7. The -ICOHP of metal-halide bond from -4.5 eV to E_F for the perovskite and nonperovskite $\text{CsSn}_y\text{Pb}_{1-y}\text{I}_3$ ($y = 0, 0.25, 0.5, 0.75, 1$). These values are normalized by each AMX_3 formula unit.

$\text{CsSn}_y\text{Pb}_{1-y}\text{I}_3$	0	0.25	0.5	0.75	1
-ICOHP _{perovskite} I-M	3.66	3.57	3.43	3.32	3.22
-ICOHP _{nonperovskite} I-M	3.50	3.40	3.32	3.24	3.17
-ICOHP difference I-M	0.16	0.17	0.11	0.08	0.05

 Table A.8. Cell volume of $\text{Cs}_x\text{FA}_{1-x}\text{PbI}_3$, $\text{CsSn}_y\text{Pb}_{1-y}\text{I}_3$, and $\text{CsSn}(\text{Br}_z\text{I}_{1-z})_3$ for both phases of perovskite and nonperovskite. The unit is in \AA^3 and the values are normalized by each AMX_3 formula unit.

Phase x/y/z	$\text{Cs}_x\text{FA}_{1-x}\text{PbI}_3$		$\text{CsSn}(\text{Br}_z\text{I}_{1-z})_3$		$\text{CsSn}_y\text{Pb}_{1-y}\text{I}_3$	
	perovskite	nonperovskite	perovskite	nonperovskite	perovskite	nonperovskite
0	260.44	255.64	224.96	214.25	233.09	218.97
1/6	-	-	219.46	208.56	-	-
1/4	247.62	247.42	-	-	230.80	217.40
1/3	-	-	213.54	202.46	-	-
1/2	242.86	247.75	206.81	197.66	228.65	216.36
2/3	-	-	200.76	190.94	-	-
3/4	238.95	229.79	-	-	226.93	215.05
5/6	-	-	194.45	183.79	-	-
1	241.97	218.97	188.06	179.25	224.96	214.25

Appendix B

Supplemental Information for

Chapter 4

Physical insights of why Sn p and halide I or Br p orbitals are both half-ionized; illustration of the selection strategy of $A\text{Sn}(\text{Br}_x\text{I}_{1-x})_3$ to reduce computational effort; summary of lattice constants and band gaps (E_g) of polymorphs of $A\text{Sn}X_3$ (CsSnI_3 , RbSnI_3 , CsSnBr_3 and RbSnBr_3); band structures for CsSnI_3 , CsSnBr_3 , RbSnI_3 , and RbSnBr_3 with the γ -phase and the α -phase, respectively; effective masses for γ - CsSnI_3 , γ - CsSnBr_3 , γ - RbSnI_3 , and γ - RbSnBr_3 ; average tilting angles and cell volumes of γ - $\text{CsSn}(\text{Br}_x\text{I}_{1-x})_3$, γ - $\text{RbSn}(\text{Br}_x\text{I}_{1-x})_3$, γ - $\text{Rb}_y\text{Cs}_{1-y}\text{SnBr}_3$, and γ - $\text{Rb}_y\text{Cs}_{1-y}\text{SnI}_3$; band gaps and formation energies of $A\text{Sn}(\text{Br}_x\text{I}_{1-x})_3$ and $\text{Rb}_y\text{Cs}_{1-y}\text{SnX}_3$ perovskites, including the α -phase; and Helmholtz free energy of mixing of α and γ polymorphs.

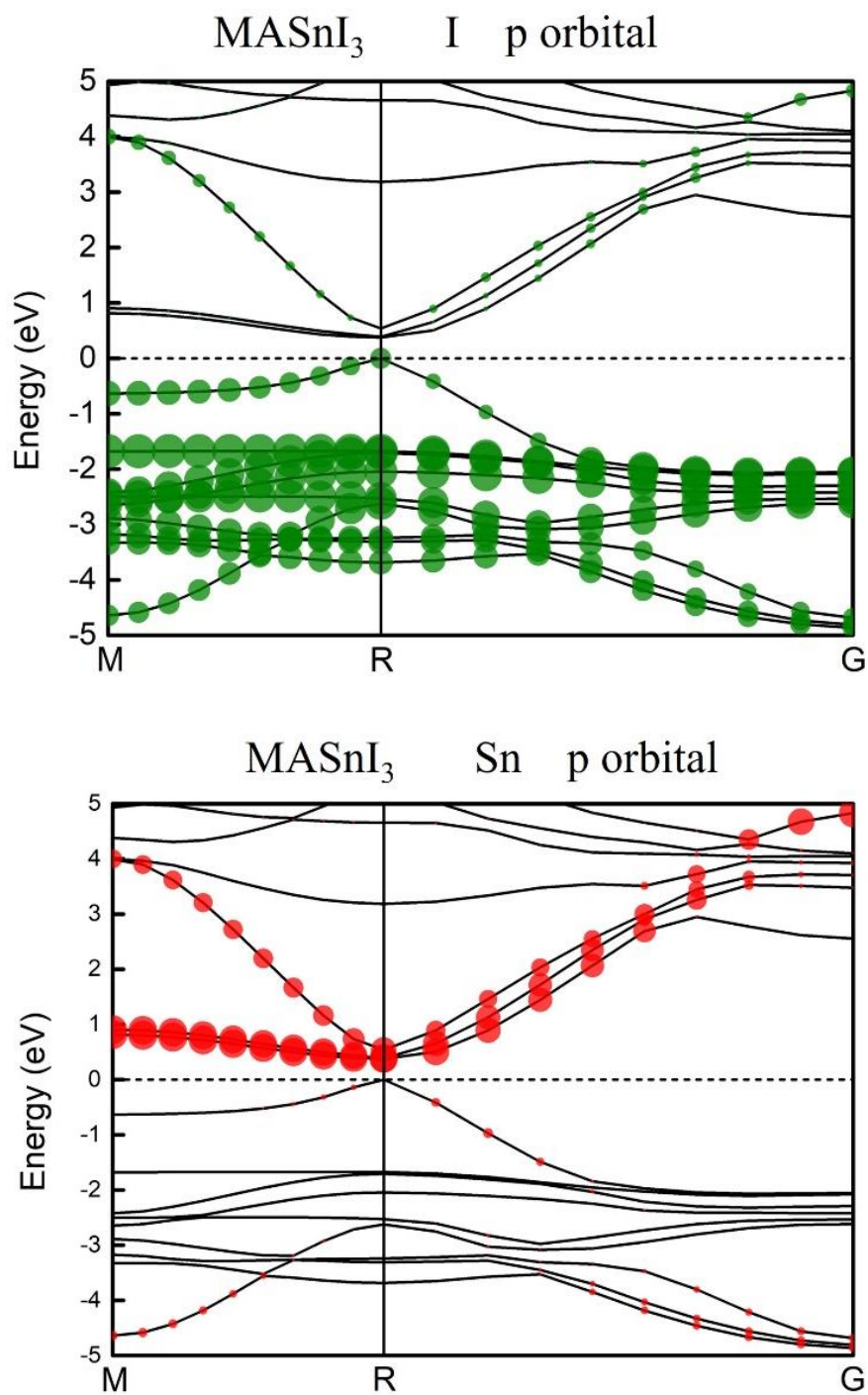


Figure B.1. Projected band structure of MASnI_3 . The potential of p orbital for I and Sn are represented by green and red circles, respectively.

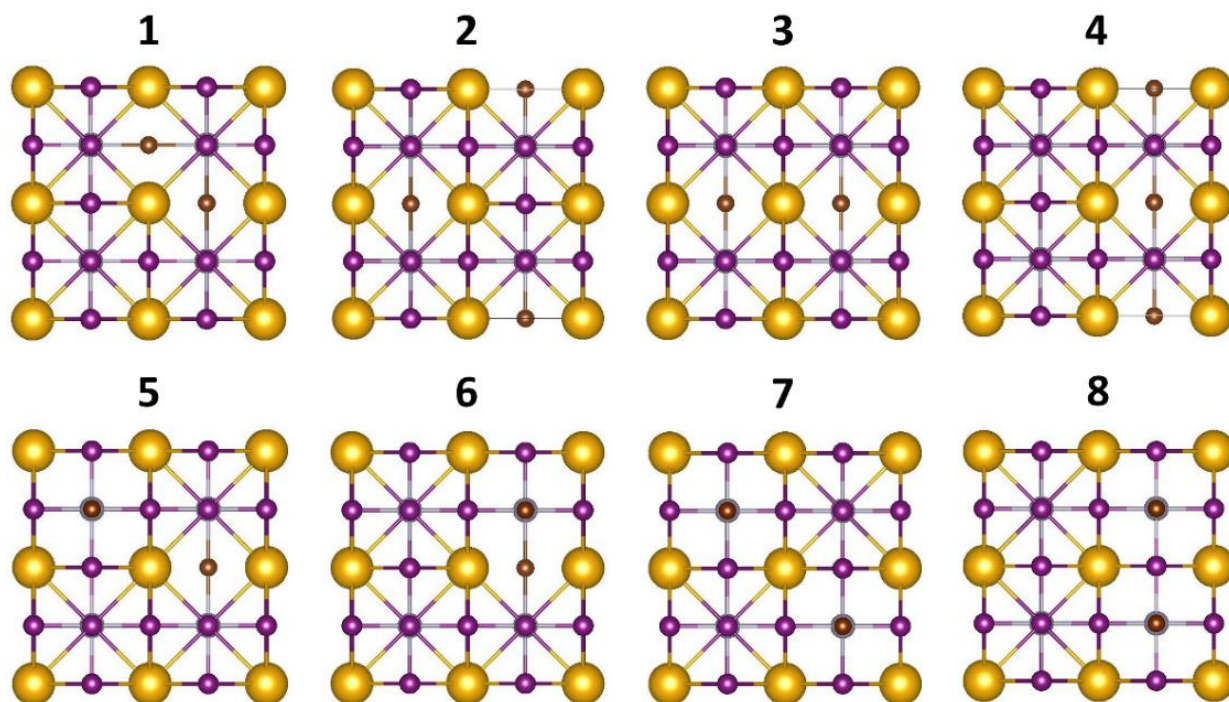


Figure B.2. Eight possible configurations of α -ASn(Br_{1/6}I_{5/6})₃. Dark yellow, purple, brown and grey spheres denote A, I, Br and Sn atom, respectively.

Table B.1. Formation energy (ΔH) of α -ASn(Br_{1/6}I_{5/6})₃.

configuration	1	2	3	4	5	6	7	8
CsSn(Br _x I _{1-x}) ₃ ΔH	-0.147	-0.157	-0.158	-0.131	-0.132	-0.134	-0.130	-0.131

Table B.2. Lattice constants (in Å) obtained by DFT, band gap energies E_g (in eV) obtained with the DFT-1/2 method including spin-orbit coupling, compared to experimental data and theoretical predictions based on hybrid and GW methods. α , β , γ and δ denote cubic, tetragonal, orthorhombic and yellow phase structures of $ASnX_3$, respectively. a: ref. [41], b: ref. [217], c: ref. [131], d: ref. [218], e: ref. [219], f: ref. [210], g: ref. [220]. * The actual atomic arrangement at finite temperature resembles that of the γ -phase [222].

Material	Lattice constants (this work)	Lattice constants (experimental)	Lattice constants (other theoretical work)	E_g DFT-1/2 + SOC	E_g (experimental)	E_g +SOC
α -CsSnI ₃	6.28	6.21 ^a	6.29 ^b	0.96	-	0.96 (GW ₀) ^g
β -CsSnI ₃	8.76, 8.76, 6.35	8.72, 8.72, 6.19 ^a	8.77, 8.77, 6.35 ^c	-	-	-
γ -CsSnI ₃	8.99, 12.52, 8.63	8.69, 12.38, 8.64 ^a	8.94, 12.52, 8.69 ^c	1.36	1.27 ^f	1.34 (GW ₀) ^g
δ -CsSnI ₃	10.94, 4.82, 17.99	10.35, 4.76, 17.68 ^a	10.82, 4.82, 18.12 ^c	-	-	-
α -RbSnI ₃	6.25	-	6.25 ^c	0.73	-	-
β -RbSnI ₃	8.64, 8.64, 6.32	-	8.65, 8.65, 6.32 ^c	-	-	-
γ -RbSnI ₃	8.91, 12.28, 8.47	-	8.93, 12.28, 8.47 ^c	1.55	-	1.13 (HSE06) ^c
δ -RbSnI ₃	10.72, 4.78, 17.54	10.184, 4.747, 17.309 ^d	10.74, 4.78, 17.51 ^c	-	-	-
α -CsSnBr ₃	5.89	5.804 ^e	-	1.27	1.75 ^f	1.41 (GW ₀) ^g
β -CsSnBr ₃	8.24, 8.24, 5.94	8.195, 8.195, 5.805 ^e	-	-	-	-
γ -CsSnBr ₃	8.36, 11.79, 8.22	-	-	1.72	*1.75 ^f	1.83 (GW ₀) ^g
δ -CsSnBr ₃	10.02, 4.59, 17.12	-	-	-	-	-
α -RbSnBr ₃	5.86	-	-	1.28	-	-
β -RbSnBr ₃	8.13, 8.13, 5.92	-	-	-	-	-
γ -RbSnBr ₃	8.38, 11.55, 7.98	-	-	2.01	-	-
δ -RbSnBr ₃	9.83, 4.56, 16.54	-	-	-	-	-

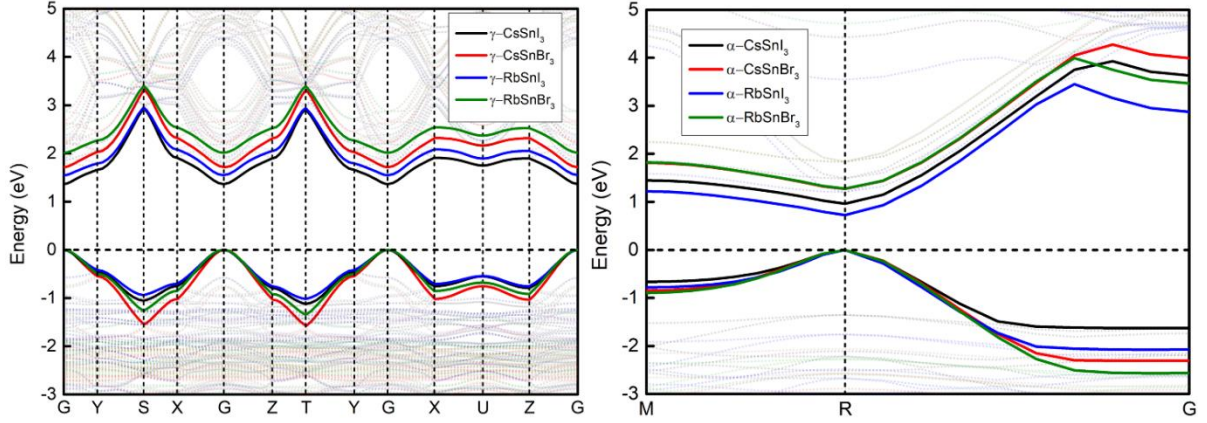


Figure B.3. Calculated band structures for CsSnI_3 , CsSnBr_3 , RbSnI_3 and RbSnBr_3 with γ and α phase, respectively. The energy zero is set in both cases at the highest occupied state. VBM and CBM highlighted as thick solid lines.

Table B.3. Calculated effective masses of the electrons and holes at G point (in units of the free-electron mass, m_0) for $\gamma\text{-CsSnI}_3$, $\gamma\text{-CsSnBr}_3$, $\gamma\text{-RbSnI}_3$, and $\gamma\text{-RbSnBr}_3$, respectively.

	m_e^*	m_h^*	m_e^*	m_h^*	m_e^*	m_h^*
	G-X	G-X	G-Y	G-Y	G-Z	G-Z
CsSnI_3	0.30	-0.26	0.14	-0.11	0.34	-0.28
CsSnBr_3	0.39	-0.30	0.19	-0.14	0.41	-0.30
RbSnI_3	0.33	-0.32	0.20	-0.15	0.37	-0.34
RbSnBr_3	0.47	-0.38	0.27	-0.18	0.54	-0.42

Table B.4. Average tilting angles ($\bar{\theta}_{ab}$ and $\bar{\theta}_c$), tilting angle differences ($|\Delta\bar{\theta}|$), and cell volumes of γ -CsSn(Br_xI_{1-x})₃, γ -RbSn(Br_xI_{1-x})₃, γ -Rb_yCs_{1-y}SnBr₃, and γ -Rb_yCs_{1-y}SnI₃. Average tilting angles and cell volume are in units of degree (°) and Å³, respectively. The θ_{ac} and θ_b are defined by measuring the Sn–X–Sn bonding angles in the SnX₆ octahedral frameworks for each unit cell within the ac-plane and along the b-axis, and then subtracting from 180°.

	γ -CsSn(Br _x I _{1-x}) ₃				γ -RbSn(Br _x I _{1-x}) ₃			
	$\bar{\theta}_{ac}$	$\bar{\theta}_b$	$ \Delta\bar{\theta} $	Cell volume	$\bar{\theta}_{ac}$	$\bar{\theta}_b$	$ \Delta\bar{\theta} $	Cell volume
0	25.428	19.598	5.830	970.979	32.167	30.630	1.537	928.016
1/6	24.796	24.140	0.656	945.451	32.767	32.790	0.023	902.175
1/6	29.536	22.760	6.776	958.758	34.015	33.759	0.256	913.360
1/3	23.303	20.728	2.575	918.412	33.099	31.713	1.386	878.321
1/3	29.686	22.321	7.365	930.934	29.756	31.668	1.912	891.424
1/2	23.129	17.994	5.135	895.255	33.953	28.824	5.129	854.566
1/2	16.741	16.307	0.434	891.517	31.098	25.059	6.039	859.777
2/3	24.812	18.551	6.261	871.471	34.798	30.105	4.693	830.100
2/3	22.408	19.625	2.783	880.063	31.869	30.765	1.104	835.337
5/6	20.526	14.659	5.867	836.809	29.392	25.774	3.618	800.621
5/6	20.687	16.354	4.333	853.814	32.523	30.375	2.148	811.600
1	20.151	16.093	4.058	810.643	29.650	29.379	0.271	772.000
	γ -Rb _y Cs _{1-y} SnBr ₃				γ -Rb _y Cs _{1-y} SnI ₃			
0	20.151	16.093	4.058	810.643	25.428	19.598	5.830	970.979
1/4	22.486	21.699	0.787	798.532	27.180	22.625	4.555	965.663
1/4	22.784	17.764	5.020	801.584	25.703	16.620	9.083	966.851
1/2	28.197	29.308	1.111	796.508	31.486	26.197	5.289	952.113
1/2	28.889	25.230	3.659	792.599	28.963	24.719	4.244	955.349
1/2	24.506	23.788	0.718	791.271	26.028	23.924	2.104	954.854
1/2	25.662	17.847	7.815	796.170	27.774	18.709	9.065	958.224
3/4	30.401	25.352	5.049	782.983	32.457	28.468	3.989	943.157
3/4	26.678	26.165	0.513	783.281	29.723	26.004	3.719	944.904
1	29.650	29.380	0.270	772.000	32.167	30.630	1.537	928.016

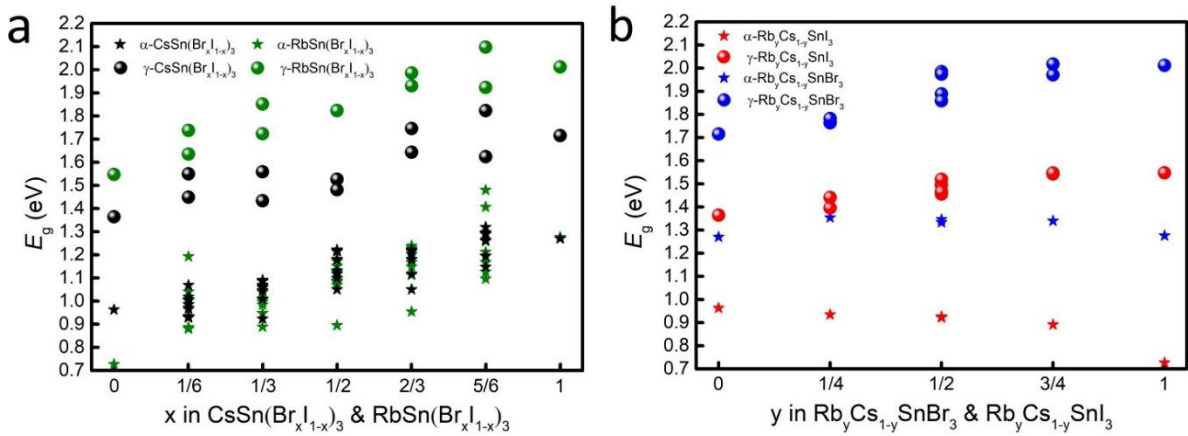


Figure B.4. Calculated band gaps of (a) $\text{ASn}(\text{Br}_x\text{I}_{1-x})_3$ and (b) $\text{Rb}_y\text{Cs}_{1-y}\text{SnX}_3$ perovskites for the α - and γ -phases, and all of them are direct band gap semiconductors.

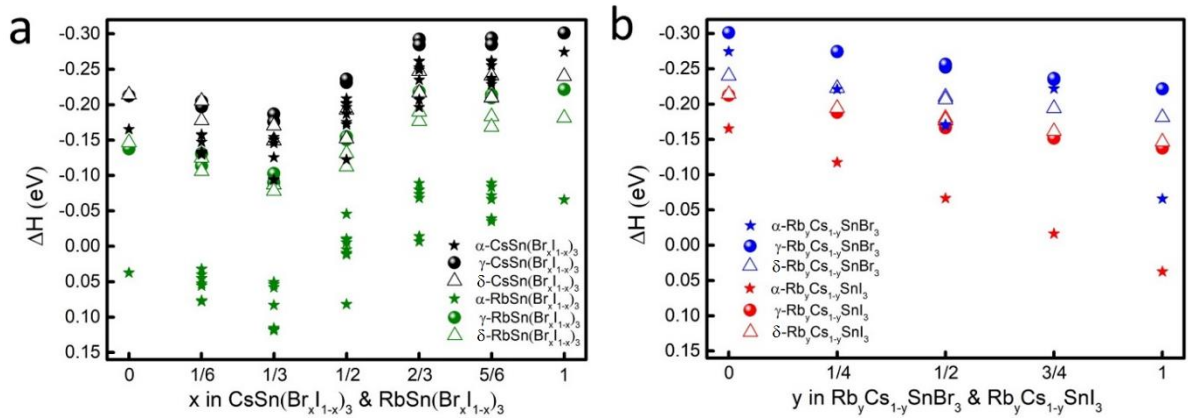


Figure B.5. Formation energy (ΔH) of (a) $\text{ASn}(\text{Br}_x\text{I}_{1-x})_3$ and (b) $\text{Rb}_y\text{Cs}_{1-y}\text{SnX}_3$ perovskites for the α -, γ -, and δ -phases.

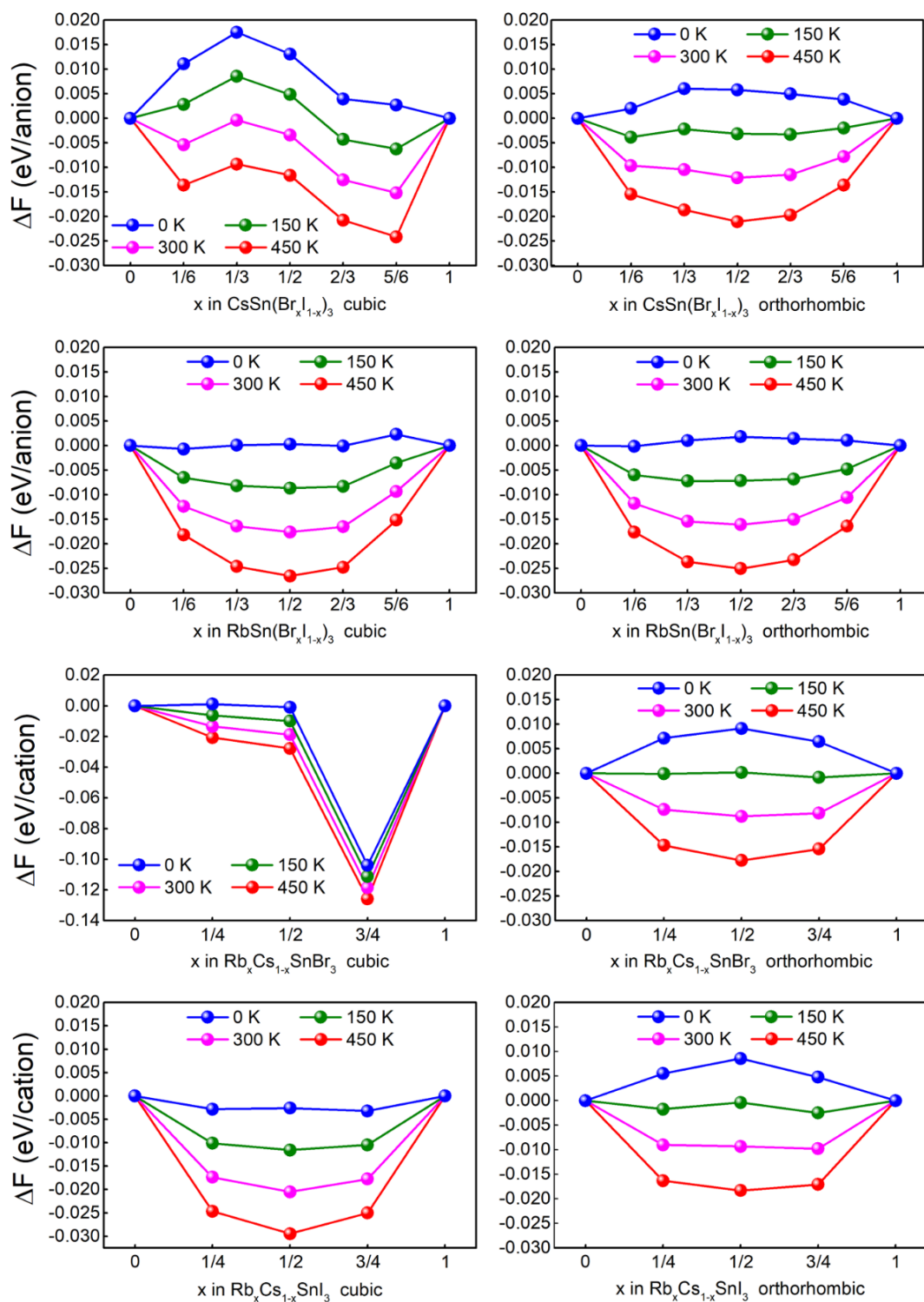


Figure B.6. Helmholtz free energy of mixing (ΔF) of solid solutions (alloys) of $ASnX_3$ with α - and γ -phases. At 0 K, all free energy of γ - $ASnX_3$ are positive, indicating that the solid solutions prefer to separate into the constituent $ASnX_3$. However, as temperature increases, the contribution of entropy become significant and the solid solutions gradually stabilize with a negative free energy of mixing.

Appendix C

Supplemental Information for

Chapter 5

Comparison of ligand density with experimental data; atomistic view, bond length, bond order, and net charge of the CsI-terminated and MI₂-terminated surface; surface atomistic composition from XPS data; temperature evolution, the plot of log (MSD) against log (time) of AIMD simulations; time-dependent location distribution density of Na ion; net atomic charges of the Na and adjacent I for ligand included models; and the comparison of the introduction of alkali cations (Li, Na, K, Rb, and Fr) with doping site and binding energy.

Table C.1. The comparison of ligand density with experimental data.

	¹ H NMR and calculation [303]	Our model
Total ligand density	1.70	1.24
R-NH ₃ ⁺ ligand density ^a	1.00	0.62
Oleate density	0.62	0.62

^a CsPbBr₃ QDs with ammonium ligand dodecylammonium (DDA). The oleate densities are the same.

The R-NH₃⁺ ligand density and the total ligand density is lower than the measurement. The OLA ligand is longer than DDA in the reference paper, which indicates that the lower R-NH₃⁺ ligand density in our work is reasonable. Thus, the feasibility of our model is validated. The unit of the ligand density is in ligand/nm².

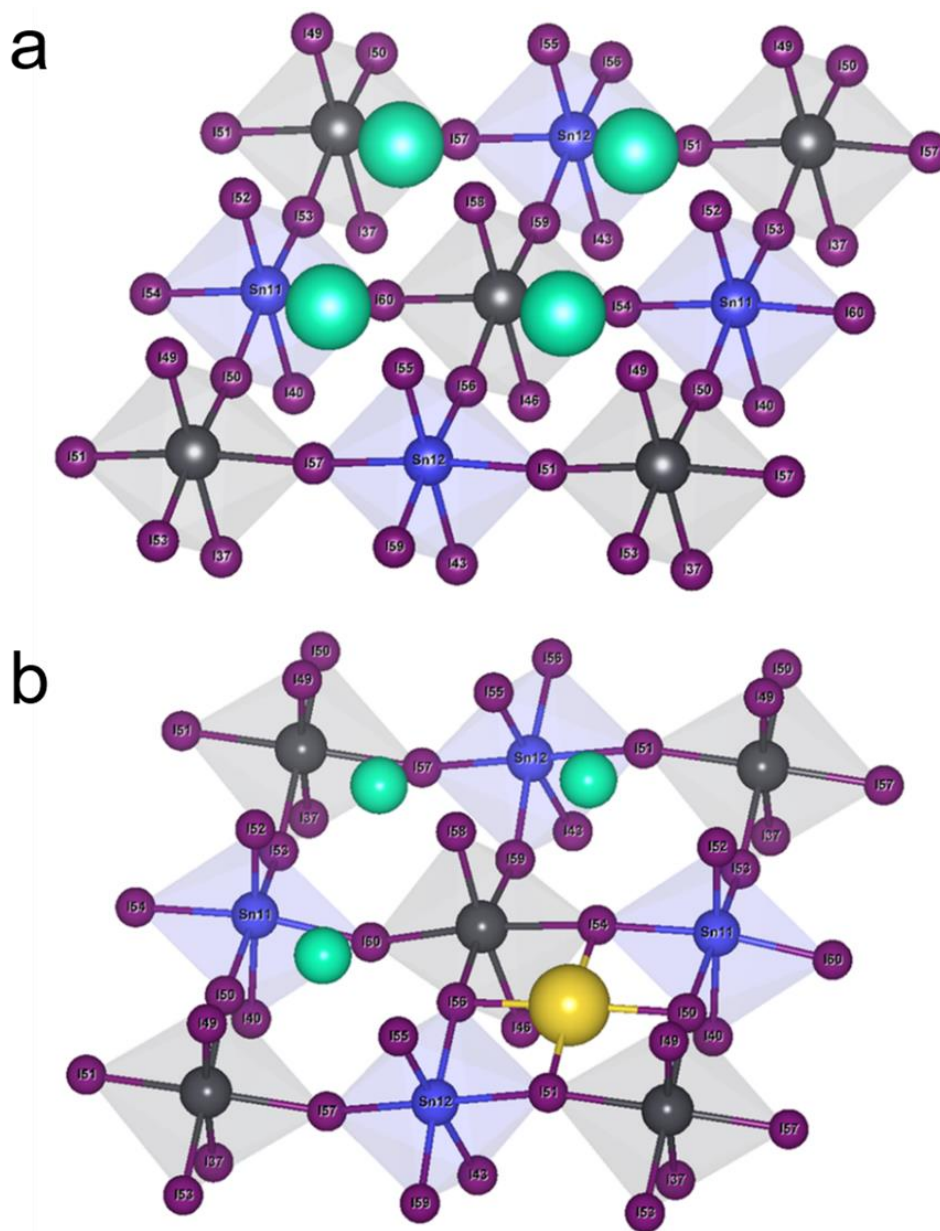


Figure C.1. Atomistic view of the CsI-terminated surface of CsSn_{0.6}Pb_{0.4}I₃ perovskite (a) without and (b) with the incorporation of Na⁺ ions.

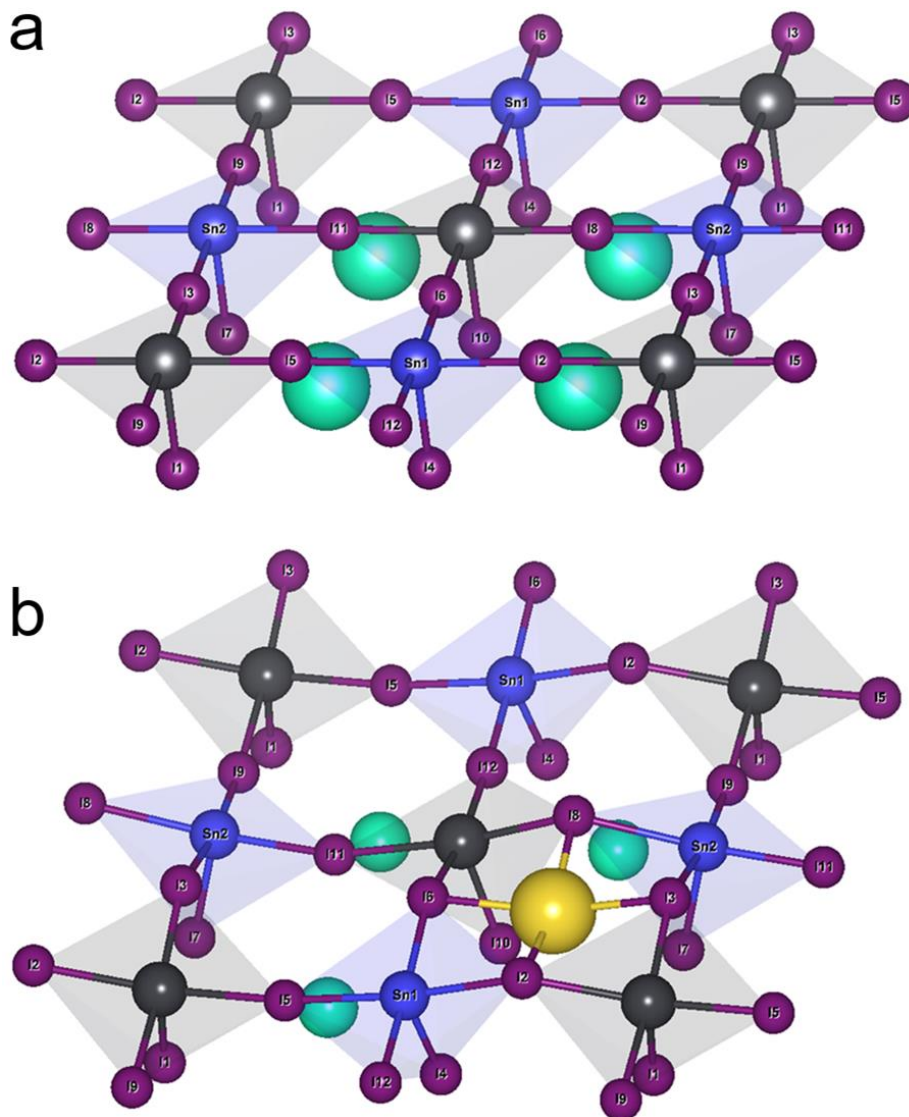


Figure C.2. Atomistic view of the MI_2 -terminated surface of $CsSn_{0.6}Pb_{0.4}I_3$ perovskite (a) without and (b) with incorporation of Na^+ ions.

Table C.2. Detailed information of bond length and bond order between atoms, and net atomic charge of each atom in Figure C.1 (CsI-terminated surface).

Bond Length	Sn11/I50	Sn11/I52	Sn11/I53	Sn11/I54	Sn11/I60	Sn12/I51	
undoped	3.15	3.01	3.15	3.15	3.15	3.14	
Na-doped	3.22	2.94	3.16	3.22	3.16	3.22	
	Sn12/I55	Sn12/I56	Sn12/I57	Sn12/I59	Cs(Na)/I50	Cs(Na)/I51	
undoped	3.01	3.14	3.14	3.14	Cs17/I50: 4.00	Cs17/I51: 4.01	
Na-doped	3.02	3.22	3.16	3.16	Na/I50: 3.18	Na/I51: 3.11	
Bond Order	Sn11/I50	Sn11/I52	Sn11/I53	Sn11/I54	Sn11/I60	Sn12/I51	
undoped	0.44	0.60	0.44	0.44	0.44	0.44	
Na-doped	0.39	0.66	0.44	0.39	0.44	0.40	
	Sn12/I55	Sn12/I56	Sn12/I57	Sn12/I59	Cs(Na)/I50	Cs(Na)/I51	
undoped	0.60	0.44	0.44	0.44	Cs17/I50: 0.10	Cs17/I51: 0.10	
Na-doped	0.58	0.40	0.44	0.44	Na/I50: 0.12	Na/I51: 0.14	
Net Atomic Charge	Sn-11	Sn-12	I-50	I-51	I-52	I-53	I-54
undoped	0.71	0.70	-0.52	-0.53	-0.55	-0.53	-0.53
Na-doped	0.70	0.70	-0.56	-0.55	-0.48	-0.51	-0.56
	I-55	I-56	I-57	I-58	I-59	I-60	
undoped	-0.55	-0.53	-0.53	-0.59	-0.53	-0.53	
Na-doped	-0.53	-0.55	-0.53	-0.56	-0.53	-0.51	

Table C.3. Detailed information of bond length and bond order between atoms, and net atomic charge of each atom in Figure C.2 (MI₂-terminated surface).

Bond Length	Sn1/I2	Sn1/I4	Sn1/I5	Sn1/I6	Sn2/I3	Sn2/I7	
undoped	3.14	2.95	3.14	3.14	3.14	2.96	
Na-doped	3.20	2.92	3.16	3.20	3.35	2.93	
	Sn2/I8	Sn2/I9	Sn2/I11	Cs(Na)/I6	Cs(Na)/I8		
undoped	3.14	3.14	3.14	Cs1/I6: 4.08	Cs1/I8: 4.10		
Na-doped	3.35	3.10	3.10	Na/I6: 3.20	Na/I8: 3.17		
Bond Order	Sn1/I2	Sn1/I4	Sn1/I5	Sn1/I6	Sn2/I3	Sn2/I7	
undoped	0.47	0.61	0.47	0.47	0.46	0.59	
Na-doped	0.43	0.65	0.46	0.43	0.35	0.65	
	Sn2/I8	Sn2/I9	Sn2/I11	Cs(Na)/I6	Cs(Na)/I8		
undoped	0.46	0.46	0.46	Cs1/I6: 0.09	Cs1/I8: 0.08		
Na-doped	0.35	0.51	0.51	Na/I6: 0.12	Na/I8: 0.13		
Net Atomic Charge	Sn-1	Sn-2	I-2	I-3	I-4	I-5	I-6
undoped	0.71	0.72	-0.50	-0.50	-0.46	-0.50	-0.50
Na-doped	0.69	0.69	-0.51	-0.51	-0.41	-0.51	-0.51
	I-7	I-8	I-9	I-10	I-11	I-12	
undoped	-0.48	-0.50	-0.50	-0.49	-0.50	-0.50	
Na-doped	-0.39	-0.51	-0.51	-0.43	-0.51	-0.51	

Table C.4. The surface atomistic composition of CsSn_{0.6}Pb_{0.4}I₃ QDs excludes the ligands, showed by XPS.

Element	Cs	Pb	Sn	I	I/Cs
Atomistic %	21.71	14.64	6.05	57.60	2.65

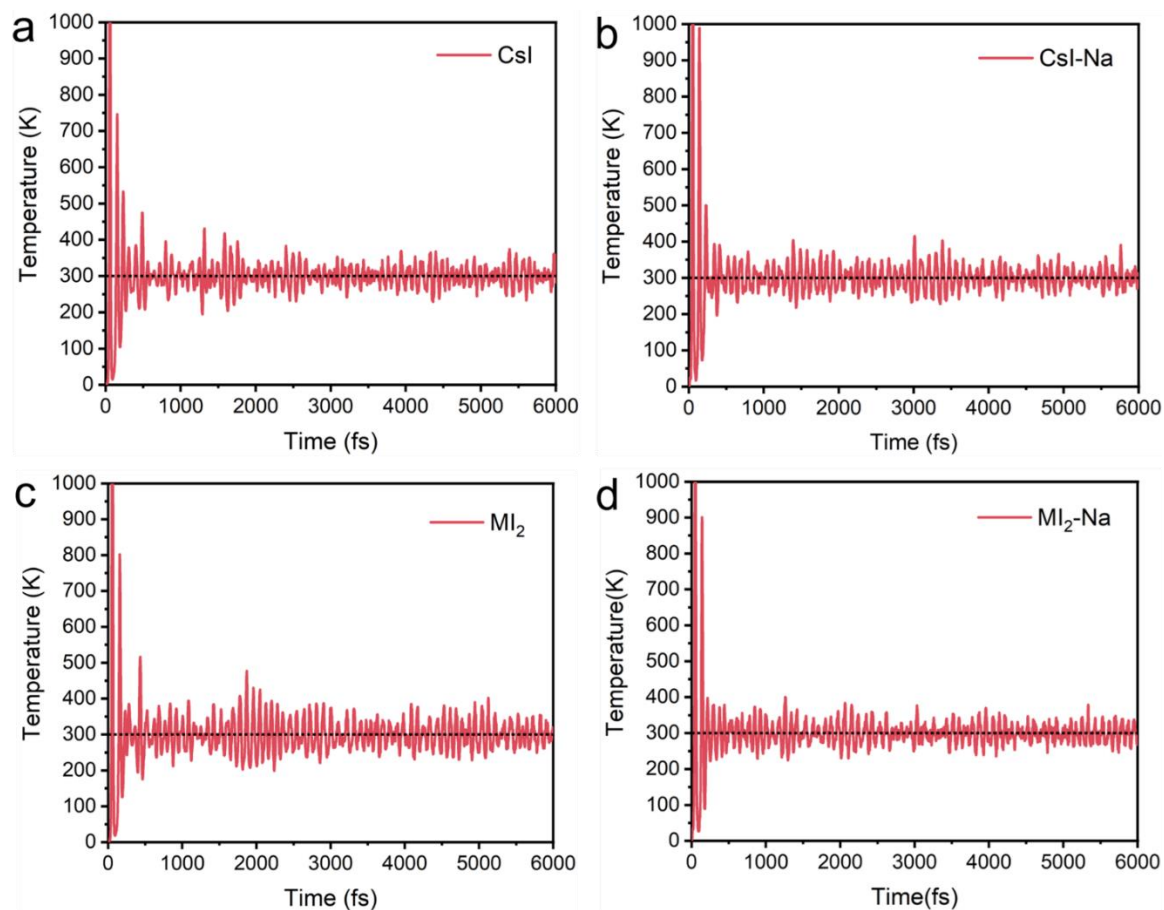


Figure C.3. The simulated temperature of CsI-terminated surface model (a) without and (b) with Na doping, and MI₂-terminated surface model (c) without and (d) with Na doping. These figures show that the simulations reach an equilibrium temperature of 300 K after about 200 fs. Therefore, the trajectory of the first 200 fs in each simulation is depleted for the data analysis.

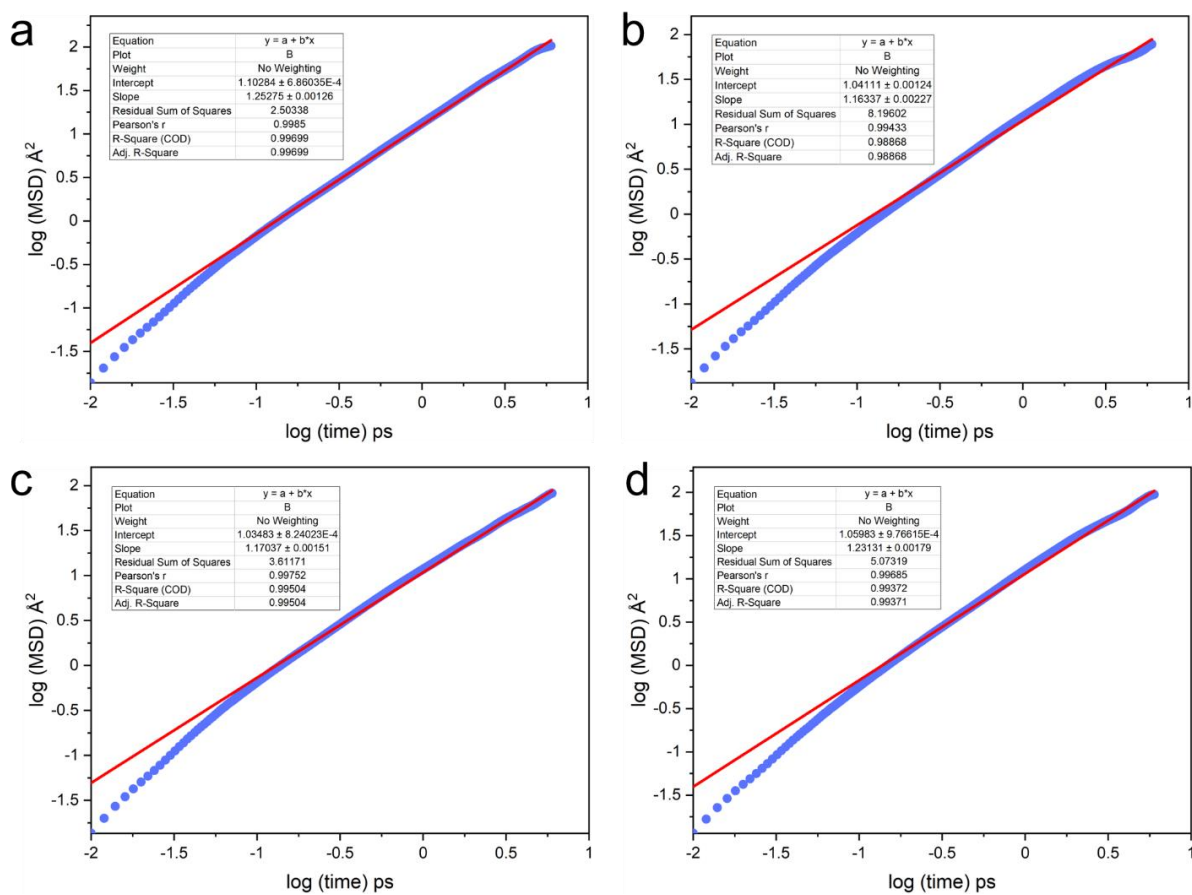


Figure C.4. $\log(\text{MSD})$ as a function of $\log(\text{time})$ of for the diffusive ions in (a) CsI, (b) CsI-Na, (c) MI₂, and (d) MI₂-Na surface models. The red line is the linear fit of the data (blue dots).

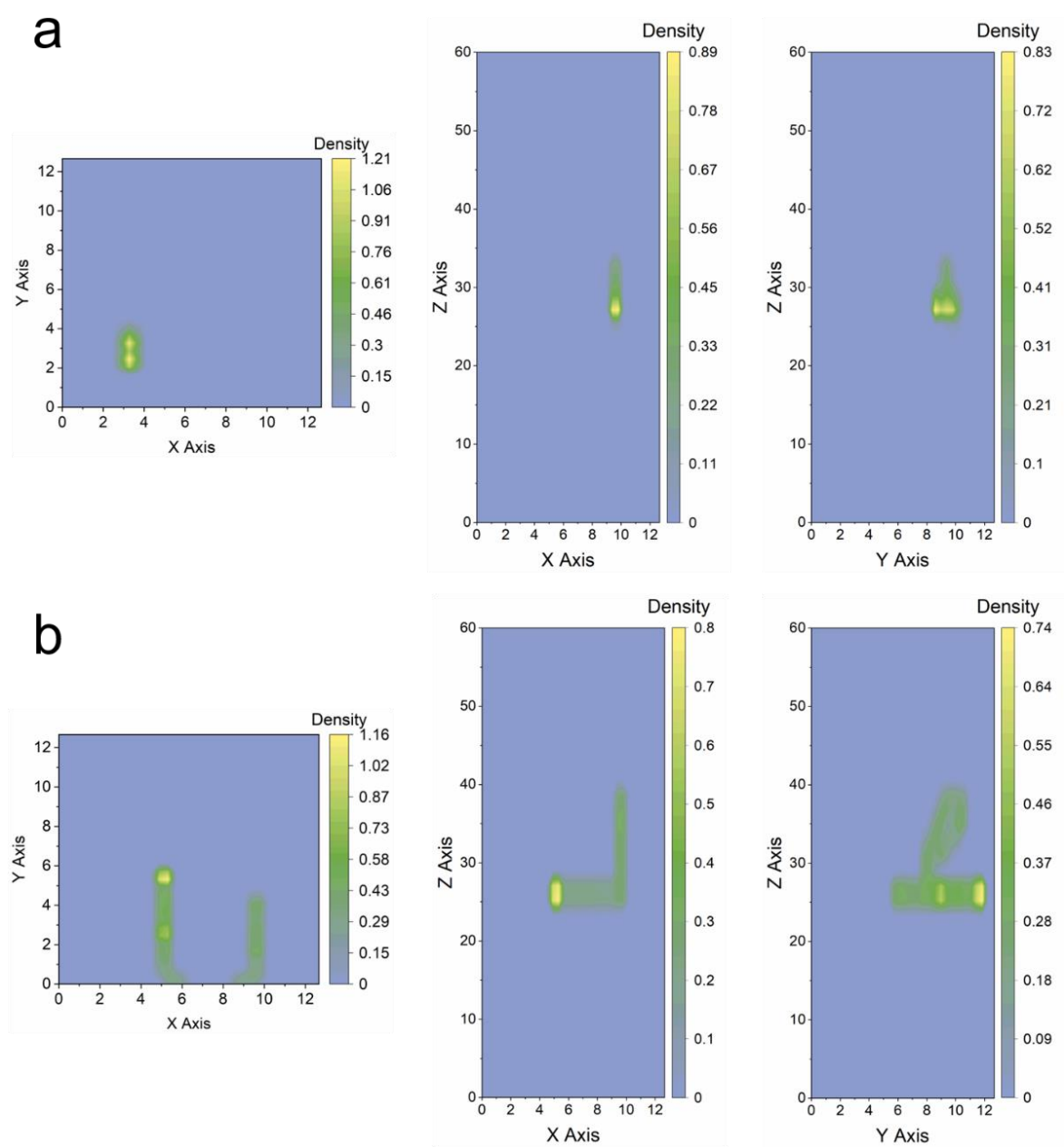


Figure C.5. Location distribution density plot of Na^+ at (a) CsI- and (b) MI_2 -terminated surface during 6 ps AIMD simulation (top view, front view, and side view from left to right).

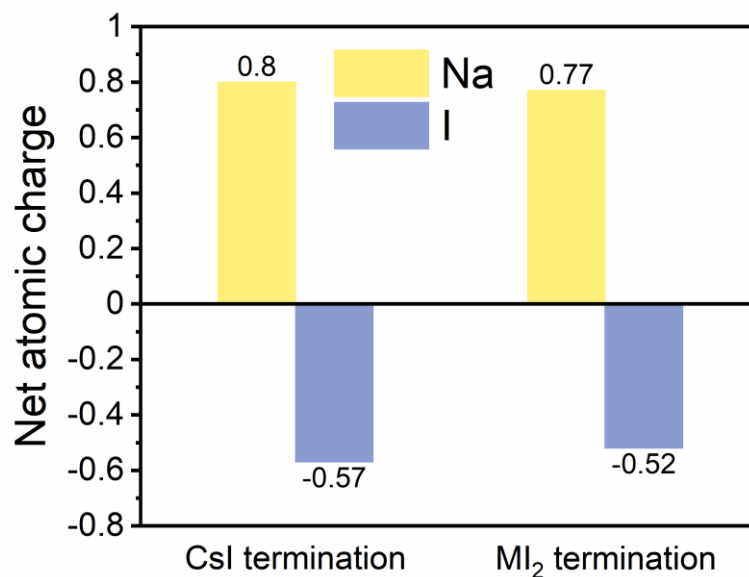


Figure C.6. Net atomic charges of the Na⁺ and adjacent I ion for CsI-terminated surface and MI₂-terminated surface, respectively. The value of I is averaged from 4 adjacent atoms of Na.

Effect of introducing other alkali cations

Encouraged by the positive effect of Na doping, we also investigated the effect of introducing other alkali cations Li, Na, K, Rb, and Fr and made a comparison with Na. We first determined the possible atomistic locations of alkali cations in the QDs. Table C.5 summarizes the three possible locations of different alkali cations in the QDs. Similar to Na⁺, the Li⁺, K⁺, and Rb⁺ are found to be more stable on surfaces (Li⁺ on interstitial site, K⁺ and Rb⁺ on A site), while the Fr⁺ do not show preference of locating on the surface or in the bulk. Generally, the preference of locating on the surface decreases with the increased size of the ions. We then calculated the ligand binding energy with alkali cations doping on both CsI-termination and MI₂-termination, and compared with the undoped configuration, see Figure C.7. The binding energies show that except for the Na⁺, all other alkali cations show a negative effect. The binding energies are significantly reduced on CsI-termination and moderately reduced on MI₂-termination.

Table C.5. The energy comparison of alkali cations doping at various location: in the bulk, on CsI-termination, and on MI_2 -termination, respectively. The energy in the bulk is set to 0 eV for comparison.

Energy (eV) \ Cation type	Bulk	CsI-termination	MI_2 -termination
Li	0	-0.27	-0.29
Na	0	-0.22	-0.26
K	0	-0.22	-0.15
Rb	0	-0.14	-0.07
Fr	0	0	-0.03

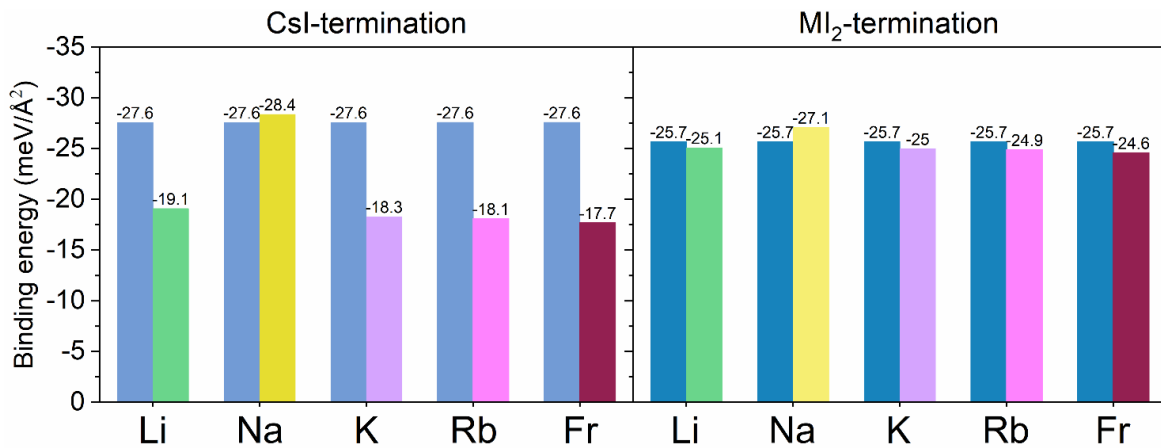


Figure C.7. Binding energies of Li, Na, K, Rb, and Fr doping on (a) CsI- and (b) MI_2 -termination, respectively. The blue bar denotes the original surface. The green, yellow, violet, pink, and wine-red bars denote the Li, Na, K, Rb, and Fr-incorporated surfaces. The binding energies are calculated by using the most favourable ligands binding mode in each termination. For CsI-termination, the OLA substituting Cs and OA substituting I configuration is used, and for MI_2 -termination, the attaching mode of OLA attached to A cation and OA attached to Sn is used.

Appendix D

Supplemental Information for Chapter 6

The correlation between theoretically calculated concentration and practical concentration; atomistic structure, donor number and boiling point of solvents; completed data of all the enthalpies and formation enthalpies for solvents with different configurations; Pb-I and Pb-O bond lengths; the optimized iodoplumbates configurations $[\text{PbI}_5\text{L}_6]^{3-}$ of DMF and DMSO; the optimized polymeric iodoplumbates (dimer) configurations; and temperature and energy oscillations during AIMD simulation.

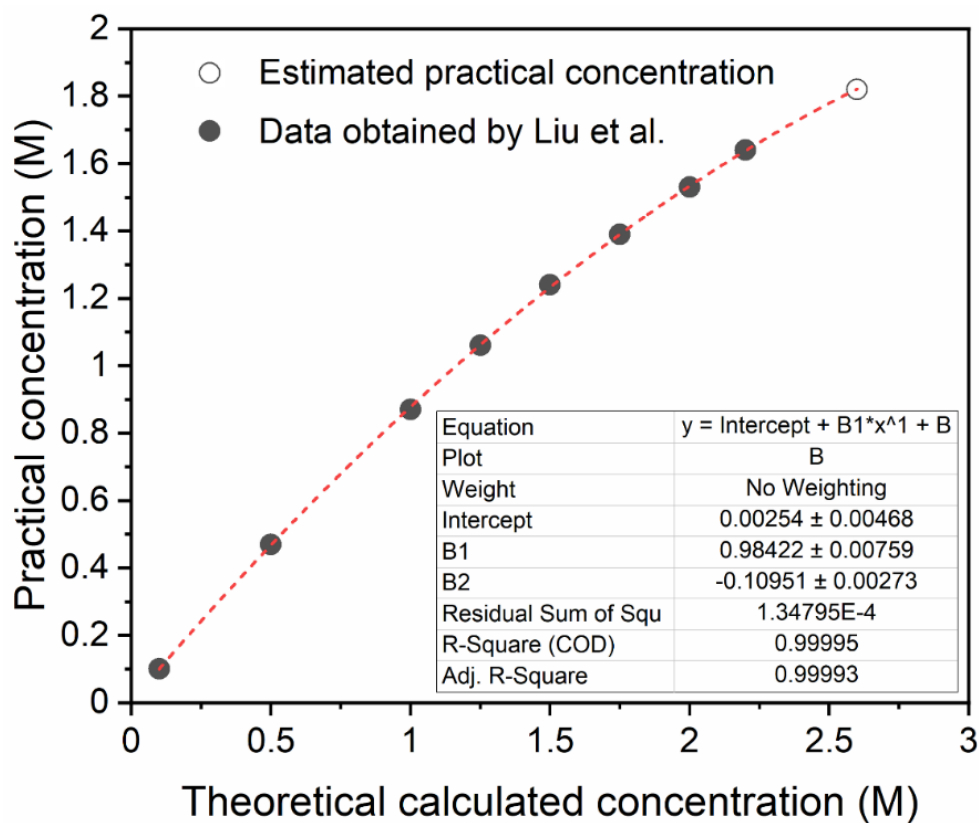


Figure D.1. Correlation between theoretically calculated concentration and practical concentration. The solid dots are obtained from the results measured by Liu, et al.[341] The hollowed dot is the theoretical concentration using in this study for DMF solvent. The practical concentration is estimated as 1.82 M by fitting with the results from Ref. [341].

Table D.1. Donor number and boiling point of DMSO and DMF. Values are obtained from Ref [88].

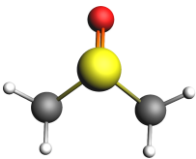
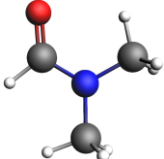
	DMSO	DMF
		
Donor number	29.8	26.6
Boiling point (°C)	189	153

Table D.2. The step-by-step formation enthalpy of different of DMF.

Configurations Reactions	Formation enthalpy (eV)				
	1-1	2-2	1-2	2-1	average
[PbI ₂ L ₆] to [PbI ₃ L ₆] ¹⁻	-0.30	-0.20	-0.37	-0.13	-0.25
[PbI ₃ L ₆] ¹⁻ to [PbI ₄ L ₆] ²⁻	-0.53	-0.91	-0.70	-0.74	-0.72
[PbI ₄ L ₆] ²⁻ to [PbI ₅ L ₆] ³⁻	-0.18	-0.23	0.02	-0.44	-0.21
[PbI ₅ L ₆] ³⁻ to [PbI ₆ L ₆] ⁴⁻	-0.29	-0.24	-0.04	-0.50	-0.27

Table D.3. The formation enthalpy of polymeric iodoplumbates of DMF.

Configurations Reactions	Formation enthalpy (eV)				
	1-1	2-2	1-2	2-1	average
[PbI ₂ L ₄] to [PbI ₂ L ₄] ₂	-0.33	-0.17	-0.24	-0.08	-0.20
[PbI ₃ L ₃] ¹⁻ to ([PbI ₃ L ₃] ¹⁻) ₂	-0.03	0.15	-0.21	-0.03	-0.03
[PbI ₄ L ₂] ²⁻ to ([PbI ₄ L ₂] ²⁻) ₂	-0.46	-0.51	-0.30	-0.35	-0.41

Table D.4. The enthalpy of two considered configurations for DMF.

Configurations Iodoplumbates	Enthalpy (eV)		
	1	2	average
[PbI ₂ L ₆]	-397.27	-397.20	-397.24
[PbI ₃ L ₆] ¹⁻	-436.93	-436.75	-436.84
[PbI ₄ L ₆] ²⁻	-476.81	-477.01	-476.91
[PbI ₅ L ₆] ³⁻	-516.34	-516.59	-516.47
[PbI ₆ L ₆] ⁴⁻	-555.98	-556.18	-556.08

Table D.5. The step-by-step formation enthalpy of different of DMSO.

Configurations Reactions	Formation enthalpy (eV)				
	1-1	2-2	1-2	2-1	average
[PbI ₂ L ₆] to [PbI ₃ L ₆] ¹⁻	-0.36	-0.46	-0.51	-0.31	-0.41
[PbI ₃ L ₆] ¹⁻ to [PbI ₄ L ₆] ²⁻	-0.46	-0.49	-0.51	-0.44	-0.48
[PbI ₄ L ₆] ²⁻ to [PbI ₅ L ₆] ³⁻	-0.10	-0.05	-0.12	-0.03	-0.07
[PbI ₅ L ₆] ³⁻ to [PbI ₆ L ₆] ⁴⁻	-0.71	-0.31	-0.78	-0.24	-0.51

Table D.6. The formation enthalpy of polymeric iodoplumbates of DMSO.

Configurations Reactions	Formation enthalpy (eV)				
	1-1	2-2	1-2	2-1	average
[PbI ₂ L ₄] to [PbI ₂ L ₄] ₂	-0.10	-0.04	-0.07	-0.01	-0.05
[PbI ₃ L ₃] ¹⁻ to ([PbI ₃ L ₃] ¹⁻) ₂	0.50	0.48	0.30	0.28	0.39
[PbI ₄ L ₂] ²⁻ to ([PbI ₄ L ₂] ²⁻) ₂	-0.26	-0.15	-0.40	-0.29	-0.28

Table D.7. The enthalpy of two considered configurations for DMSO.

Configurations Iodoplumbates	Enthalpy (eV)		
	1	2	average
[PbI ₂ L ₆]	-292.98	-292.83	-292.91
[PbI ₃ L ₆] ¹⁻	-332.73	-332.68	-332.70
[PbI ₄ L ₆] ²⁻	-372.57	-372.56	-372.57
[PbI ₅ L ₆] ³⁻	-412.06	-411.99	-412.03
[PbI ₆ L ₆] ⁴⁻	-452.16	-451.69	-451.92

Table D.8. The step-by-step formation enthalpy of different of DMF-DMSO binary.

Configurations Reactions	Formation enthalpy (eV)				
	1-1	2-2	1-2	2-1	average
[PbI ₂ L ₆] to [PbI ₃ L ₆] ¹⁻	-0.60	-0.47	-0.52	-0.55	-0.53
[PbI ₃ L ₆] ¹⁻ to [PbI ₄ L ₆] ²⁻	-0.15	-0.24	-0.20	-0.19	-0.19
[PbI ₄ L ₆] ²⁻ to [PbI ₅ L ₆] ³⁻	-0.69	-0.25	-0.64	-0.29	-0.47
[PbI ₅ L ₆] ³⁻ to [PbI ₆ L ₆] ⁴⁻	-0.21	-0.67	-0.60	-0.28	-0.44

Table D.9. The formation enthalpy of polymeric iodoplumbates of DMF-DMSO binary.

Configurations Reactions	Formation enthalpy (eV)				
	1-1	2-2	1-2	2-1	average
[PbI ₂ L ₆] to [PbI ₂ L ₆] ₂	-0.23	-0.12	-0.22	-0.11	-0.17
[PbI ₃ L ₃] ¹⁻ to ([PbI ₃ L ₃] ¹⁻) ₂	-0.27	-0.09	-0.12	0.06	-0.10
[PbI ₄ L ₂] ²⁻ to ([PbI ₄ L ₂] ²⁻) ₂	-0.25	-0.21	-0.41	-0.36	-0.36

Table D.10. The enthalpy of two considered configurations for DMF-DMSO binary.

Configurations Iodoplumbates	Enthalpy (eV)		
	1	2	average
[PbI ₂ L ₆]	-379.76	-379.84	-379.80
[PbI ₃ L ₆] ¹⁻	-419.71	-419.66	-419.68
[PbI ₄ L ₆] ²⁻	-459.20	-459.25	-459.23
[PbI ₅ L ₆] ³⁻	-499.24	-498.85	-499.04
[PbI ₆ L ₆] ⁴⁻	-538.80	-538.87	-538.83

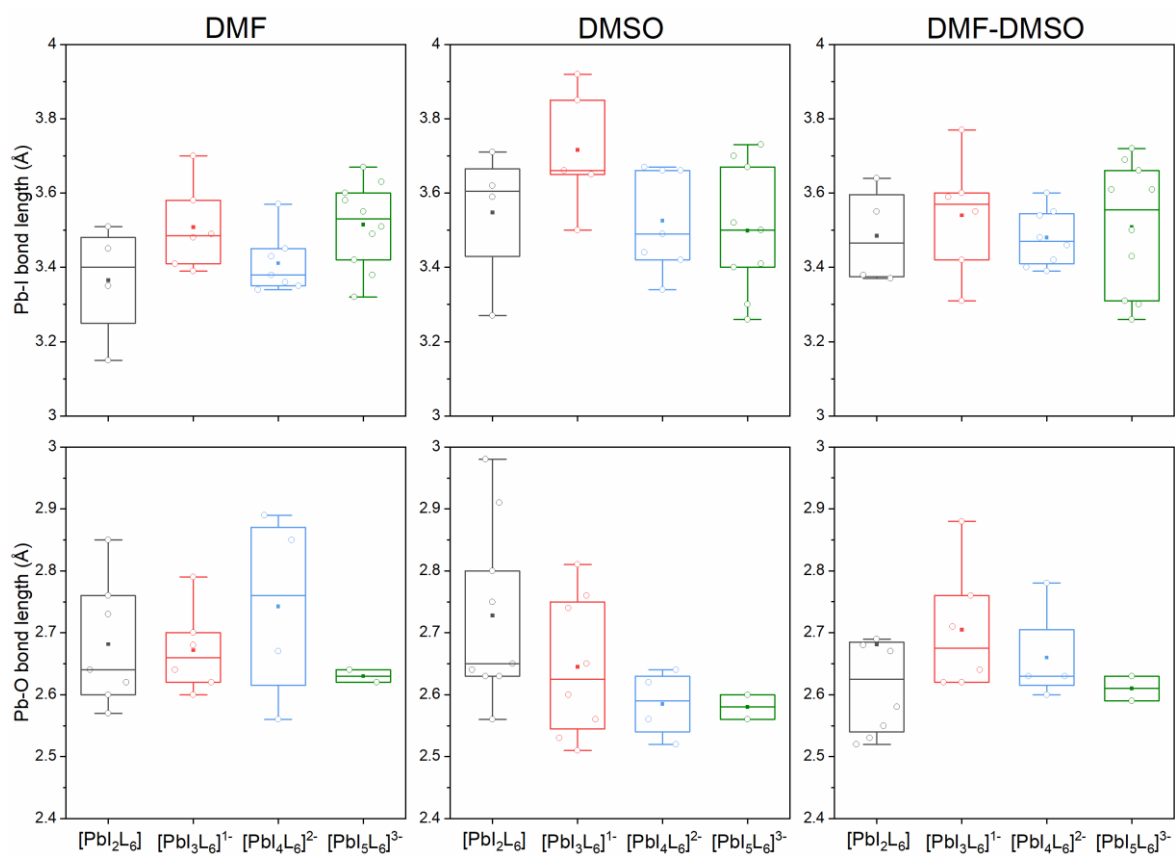


Figure D.2. Pb-I and (b) Pb-O bond lengths of $[PbI_2L_6]$, $[PbI_3L_6]^{1-}$, $[PbI_4L_6]^{2-}$, and $[PbI_5L_6]^{3-}$ of DMF, DMSO, and DMF-DMSO binary, respectively.

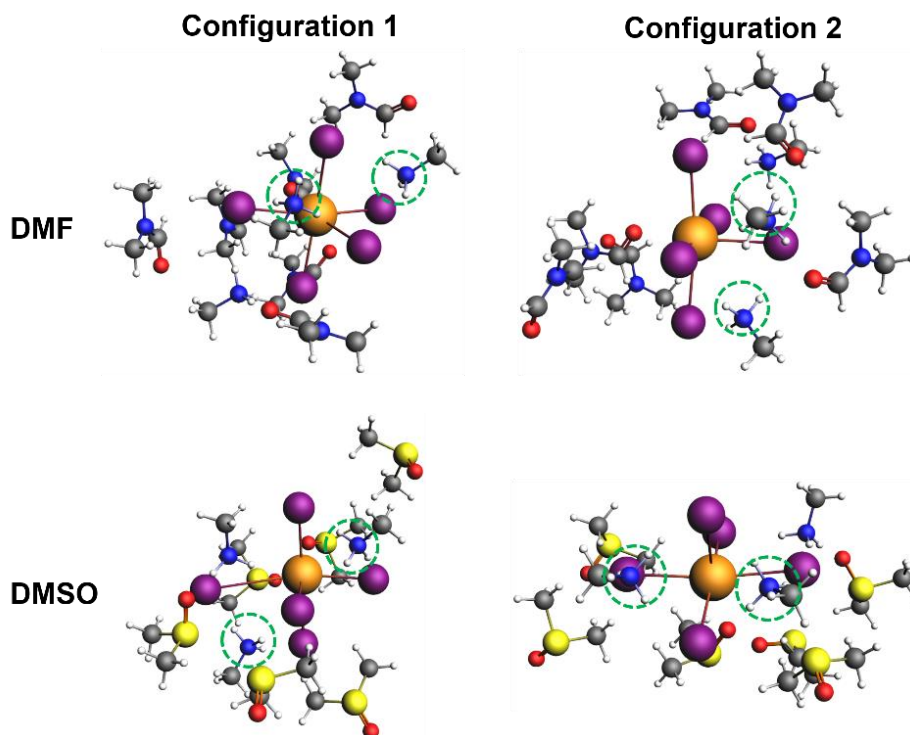


Figure D.3. The optimized iodoplumbates configurations $[\text{Pb}_5\text{I}_6]^{3-}$ of DMF and DMSO, respectively. There are more $\text{NH}\cdots\text{I}$ hydrogen bond formed (indicated by dashed circles).

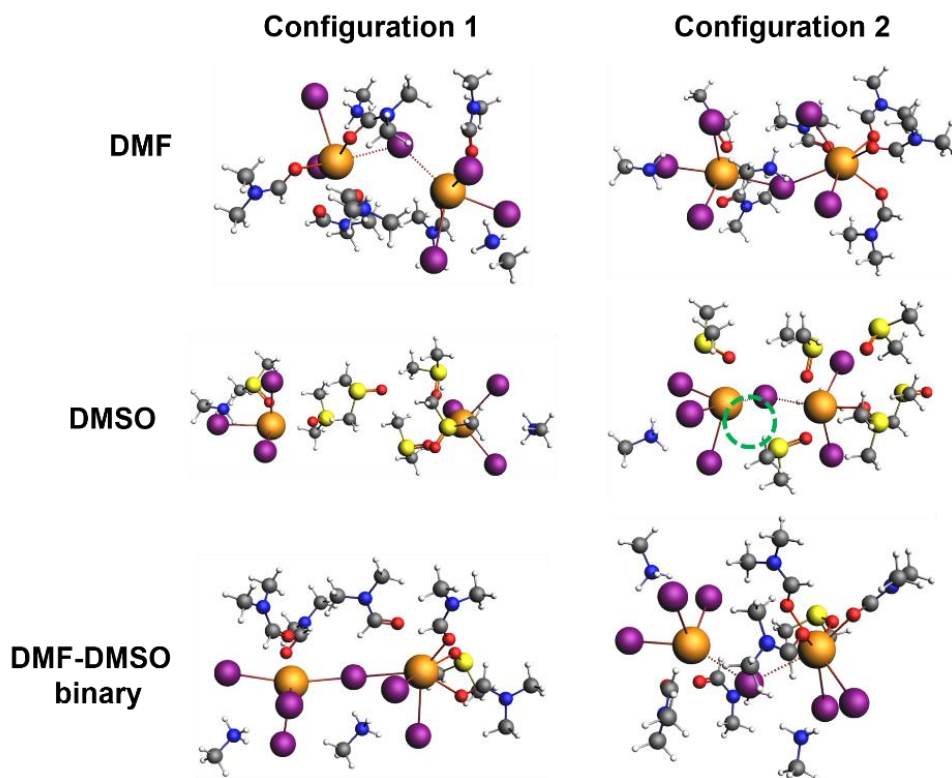


Figure D.4. The optimized polymeric iodoplumbates (dimer) configurations of $[\text{PbI}_2\text{L}_6]$, $[\text{PbI}_3\text{L}_6]^{1-}$, $[\text{PbI}_4\text{L}_6]^{2-}$, and $[\text{PbI}_5\text{L}_6]^{3-}$ of DMF, DMSO, and DMF-DMSO binary, respectively. The $([\text{PbI}_3\text{L}_3]^{1-})_2$ are not formed (left), or not fully bonded with solvents (indicated by a dashed circle).

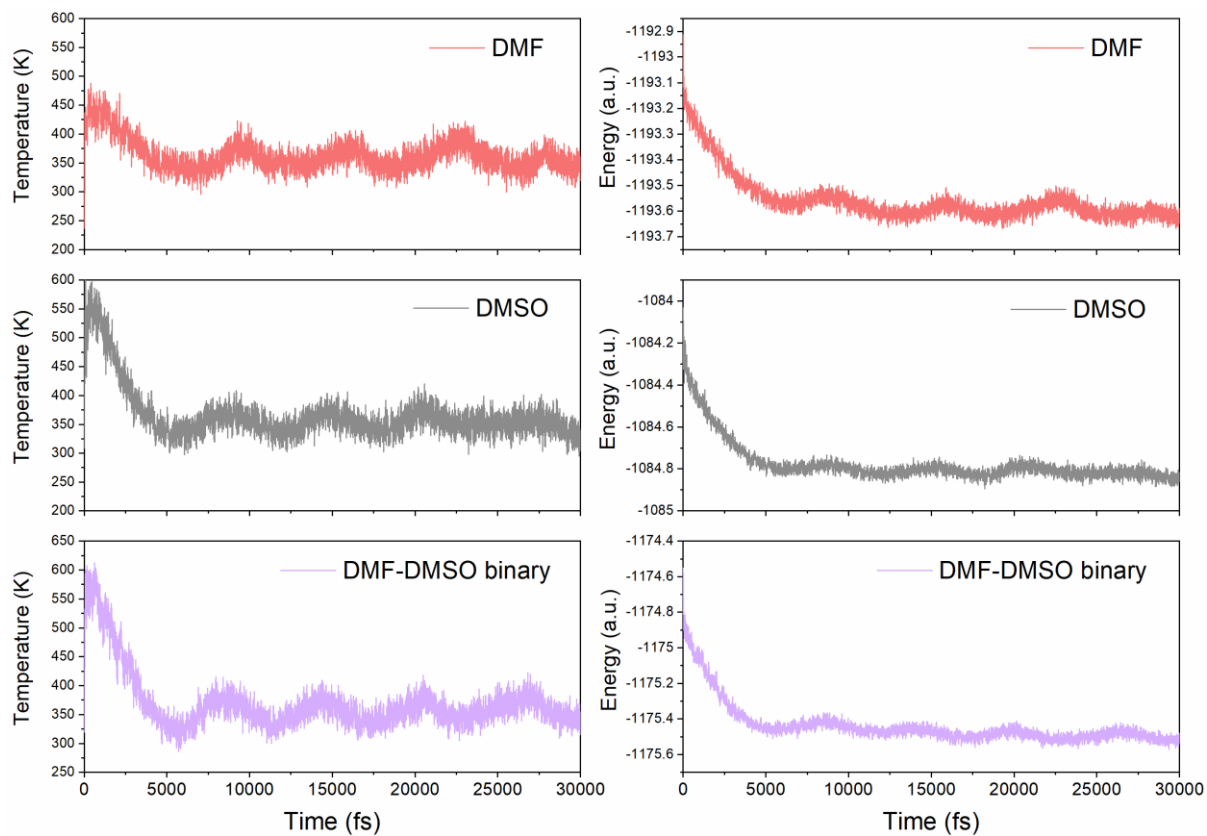


Figure D.5. These temperature and energy oscillations show that the simulations reach an equilibrium after about 5000 fs. Therefore, the trajectory of the first 5000 fs in each simulation is depleted for the data analysis.

Bibliography

- [1] The Newsletter of the IEA Solar Heating and Cooling Programme. SHC solar update. 2015 November.
- [2] Park N-G. Perovskite solar cells: an emerging photovoltaic technology. *Materials Today*, 2015, 18(2):65-72.
- [3] National Renewable Energy Laboratory, Best Research-Cell Efficiencies: Best Research-Cell Efficiencies, <https://www.nrel.gov/pv/cell-efficiency.html>.
- [4] Bao C, Yang J, Bai S, Xu W, Yan Z, Xu Q, et al. High Performance and Stable All-Inorganic Metal Halide Perovskite-Based Photodetectors for Optical Communication Applications. *Advanced Materials*, 2018, 30(38):1803422.
- [5] Chen AZ, Foley BJ, Ma JH, Alpert MR, Niezgoda JS, Choi JJ. Crystallographic orientation propagation in metal halide perovskite thin films. *Journal of Materials Chemistry A*, 2017, 5(17):7796-800.
- [6] Zhang W, Eperon GE, Snaith HJ. Metal halide perovskites for energy applications. *Nature Energy*, 2016, 1(6):16048.
- [7] Sun J, Wu J, Tong X, Lin F, Wang Y, Wang ZM. Organic/Inorganic Metal Halide Perovskite Optoelectronic Devices beyond Solar Cells. *Advanced Science*, 2018, 5(5):1700780.
- [8] Lei L, Dong Q, Gundogdu K, So F. Metal Halide Perovskites for Laser Applications. *Advanced Functional Materials*, 2021, 31(16):2010144.
- [9] Stranks SD, Snaith HJ. Metal-halide perovskites for photovoltaic and light-emitting devices. *Nature Nanotechnology*, 2015, 10(5):391-402.
- [10] Leijtens T, Eperon GE, Barker AJ, Grancini G, Zhang W, Ball JM, et al. Carrier trapping and recombination: the role of defect physics in enhancing the open circuit voltage of metal halide perovskite solar cells. *Energy & Environmental Science*, 2016, 9(11):3472-81.

- [11] Scheidt RA, Kamat PV. Temperature-driven anion migration in gradient halide perovskites. *The Journal of Chemical Physics*, 2019, 151(13):134703.
- [12] Wu M, Haji Ladi N, Yi Z, Li H, Shen Y, Wang M. Stability Issue of Perovskite Solar Cells under Real-World Operating Conditions. *Energy Technology*, 2020, 8(4):1900744.
- [13] Li Z, Yang M, Park J-S, Wei S-H, Berry JJ, Zhu K. Stabilizing Perovskite Structures by Tuning Tolerance Factor: Formation of Formamidinium and Cesium Lead Iodide Solid-State Alloys. *Chemistry of Materials*, 2015, 28(1):284-92.
- [14] Sutton RJ, Filip MR, Haghighirad AA, Sakai N, Wenger B, Giustino F, et al. Cubic or orthorhombic? Revealing the crystal structure of metastable black-phase CsPbI₃ by theory and experiment. *ACS Energy Letters*, 2018, 3(8):1787-94.
- [15] Slotcavage DJ, Karunadasa HI, McGehee MD. Light-Induced Phase Segregation in Halide-Perovskite Absorbers. *ACS Energy Letters*, 2016, 1(6):1199-205.
- [16] Beal RE, Hagström NZ, Barrier J, Gold-Parker A, Prasanna R, Bush KA, et al. Structural Origins of Light-Induced Phase Segregation in Organic-Inorganic Halide Perovskite Photovoltaic Materials. *Matter*, 2020, 2(1):207-19.
- [17] Akbulatov AF, Luchkin SY, Frolova LA, Dremova NN, Gerasimov KL, Zhidkov IS, et al. Probing the Intrinsic Thermal and Photochemical Stability of Hybrid and Inorganic Lead Halide Perovskites. *The Journal of Physical Chemistry Letters*, 2017, 8(6):1211-8.
- [18] Kim GY, Senocrate A, Yang T-Y, Gregori G, Grätzel M, Maier J. Large tunable photoeffect on ion conduction in halide perovskites and implications for photodecomposition. *Nature Materials*, 2018, 17(5):445-9.
- [19] Christians JA, Miranda Herrera PA, Kamat PV. Transformation of the Excited State and Photovoltaic Efficiency of CH₃NH₃PbI₃ Perovskite upon Controlled Exposure to Humidified Air. *Journal of the American Chemical Society*, 2015, 137(4):1530-8.
- [20] Ding X, Cai M, Liu X, Ding Y, Liu X, Wu Y, et al. Enhancing the Phase Stability of Inorganic α -CsPbI₃ by the Bication-Conjugated Organic Molecule for Efficient Perovskite Solar Cells. *ACS Applied Materials & Interfaces*, 2019, 11(41):37720-5.
- [21] Aristidou N, Sanchez-Molina I, Chotchuangchutchaval T, Brown M, Martinez L, Rath T, et al. The Role of Oxygen in the Degradation of Methylammonium Lead Trihalide Perovskite Photoactive Layers. *Angewandte Chemie International Edition*, 2015, 54(28):8208-12.
- [22] Aristidou N, Eames C, Sanchez-Molina I, Bu X, Kosco J, Islam MS, et al. Fast Oxygen Diffusion and Iodide Defects Mediate Oxygen-Induced Degradation of Perovskite Solar Cells. *Nature Communications*, 2017, 8(1):15218.

- [23] Leijtens T, Eperon GE, Noel NK, Habisreutinger SN, Petrozza A, Snaith HJ. Stability of Metal Halide Perovskite Solar Cells. *Advanced Energy Materials*, 2015, 5(20):1500963.
- [24] Xiang W, Liu S, Tress W. A review on the stability of inorganic metal halide perovskites: challenges and opportunities for stable solar cells. *Energy & Environmental Science*, 2021, 14(4):2090-113.
- [25] Liu F, Ding C, Zhang Y, Ripolles TS, Kamisaka T, Toyoda T, et al. Colloidal Synthesis of Air-Stable Alloyed CsSn_{1-x}Pb_xI₃ Perovskite Nanocrystals for Use in Solar Cells. *Journal of the American Chemical Society*, 2017, 139(46):16708-19.
- [26] Jiang Y, Yuan J, Ni Y, Yang J, Wang Y, Jiu T, et al. Reduced-Dimensional α -CsPbX₃ Perovskites for Efficient and Stable Photovoltaics. *Joule*, 2018, 2(7):1356-68.
- [27] Wang J, Zhang J, Zhou Y, Liu H, Xue Q, Li X, et al. Highly efficient all-inorganic perovskite solar cells with suppressed non-radiative recombination by a Lewis base. *Nature Communications*, 2020, 11(1):177.
- [28] Kang D-H, Kim S-Y, Lee J-W, Park N-G. Efficient surface passivation of perovskite films by a post-treatment method with a minimal dose. *Journal of Materials Chemistry A*, 2021, 9(6):3441-50.
- [29] Steele JA, Jin H, Dovgaliuk I, Berger RF, Braeckvelt T, Yuan H, et al. Thermal unequilibrium of strained black CsPbI₃ thin films. *Science*, 2019, 365(6454):679-84.
- [30] Xue D-J, Hou Y, Liu S-C, Wei M, Chen B, Huang Z, et al. Regulating strain in perovskite thin films through charge-transport layers. *Nature Communications*, 2020, 11(1):1514.
- [31] Goldschmidt VM. Die gesetze der krystallochemie. *Naturwissenschaften*, 1926, 14(21):477-85.
- [32] Anaya M, Lozano G, Calvo ME, Míguez H. ABX₃ Perovskites for Tandem Solar Cells. *Joule*, 2017, 1(4):769-93.
- [33] Saliba M, Matsui T, Domanski K, Seo J-Y, Ummadisingu A, Zakeeruddin SM, et al. Incorporation of rubidium cations into perovskite solar cells improves photovoltaic performance. *Science*, 2016, 354(6309):206.
- [34] Correa-Baena J-P, Saliba M, Buonassisi T, Grätzel M, Abate A, Tress W, et al. Promises and Challenges of Perovskite Solar Cells. *Science*, 2017, 358(6364):739-44.
- [35] Ono LK, Juarez-Perez EJ, Qi Y. Progress on Perovskite Materials and Solar Cells with Mixed Cations and Halide Anions. *ACS Applied Materials & Interfaces*, 2017, 9(36):30197-246.

- [36] Onoda-Yamamuro N, Yamamuro O, Matsuo T, Suga H. p-T phase relations of $\text{CH}_3\text{NH}_3\text{PbX}_3$ (X = Cl, Br, I) crystals. *Journal of Physics and Chemistry of Solids*, 1992, 53(2):277-81.
- [37] Stoumpos CC, Malliakas CD, Kanatzidis MG. Semiconducting Tin and Lead Iodide Perovskites with Organic Cations: Phase Transitions, High Mobilities, and Near-Infrared Photoluminescent Properties. *Inorganic Chemistry*, 2013, 52(15):9019-38.
- [38] Marronnier A, Roma G, Boyer-Richard S, Pedesseau L, Jancu J-M, Bonnassieux Y, et al. Anharmonicity and Disorder in the Black Phases of Cesium Lead Iodide Used for Stable Inorganic Perovskite Solar Cells. *ACS Nano*, 2018, 12(4):3477-86.
- [39] Shum K, Chen Z, Qureshi J, Yu C, Wang JJ, Pfenninger W, et al. Synthesis and characterization of CsSnI_3 thin films. *Applied Physics Letters*, 2010, 96(22):221903.
- [40] Da Silva EL, Skelton JM, Parker SC, Walsh A. Phase Stability and Transformations in the Halide Perovskite CsSnI_3 . *Physical Review B*, 2015, 91(14):144107.
- [41] Chung I, Song J-H, Im J, Androulakis J, Malliakas CD, Li H, et al. CsSnI_3 : Semiconductor or Metal? High Electrical Conductivity and Strong Near-Infrared Photoluminescence from a Single Material. High Hole Mobility and Phase-Transitions. *Journal of the American Chemical Society*, 2012, 134(20):8579-87.
- [42] Koji Y, Shinya F, Hiromi H, Takashi M, Tsutomu O, Sumio I. Structural Phase Transitions of the Polymorphs of CsSnI_3 by Means of Rietveld Analysis of the X-Ray Diffraction. *Chemistry Letters*, 1991, 20(5):801-4.
- [43] Saliba M, Matsui T, Seo J-Y, Domanski K, Correa-Baena J-P, Nazeeruddin MK, et al. Cesium-Containing Triple Cation Perovskite Solar Cells: Improved Stability, Reproducibility and High Efficiency. *Energy & Environmental Science*, 2016, 9(6):1989-97.
- [44] Huang L-y, Lambrecht WRL. Electronic Band Structure, Phonons, and Exciton Binding Energies of Halide Perovskites CsSnCl_3 , CsSnBr_3 , and CsSnI_3 . *Physical Review B*, 2013, 88(16).
- [45] Ma F, Li J, Li W, Lin N, Wang L, Qiao J. Stable α/δ phase junction of formamidinium lead iodide perovskites for enhanced near-infrared emission. *Chemical science*, 2017, 8(1):800-5.
- [46] Sharma S, Weiden N, Weiss A. Phase diagrams of quasibinary systems of the type: $\text{ABX}_3 - \text{A}'\text{BX}_3$; $\text{ABX}_3 - \text{AB}'\text{X}_3$, and $\text{ABX}_3 - \text{ABX}'_3$; X = halogen. *Zeitschrift für Physikalische Chemie*, 1992, 175(1):63-80.
- [47] Hu Y, Bai F, Liu X, Ji Q, Miao X, Qiu T, et al. Bismuth incorporation stabilized α - CsPbI_3 for fully inorganic perovskite solar cells. *ACS Energy Letters*, 2017, 2(10):2219-27.

- [48] Chen J, Xu J, Xiao L, Zhang B, Dai S, Yao J. Mixed-Organic-Cation (FA) \times (MA) $1-x$ PbI₃ Planar Perovskite Solar Cells with 16.48% Efficiency via a Low-Pressure Vapor-Assisted Solution Process. *ACS applied materials & interfaces*, 2017, 9(3):2449-58.
- [49] Zhang Y, Grancini G, Feng Y, Asiri AM, Nazeeruddin MK. Optimization of Stable Quasi-Cubic FA \times MA $1-x$ PbI₃ Perovskite Structure for Solar Cells with Efficiency beyond 20%. *ACS Energy Letters*, 2017, 2(4):802-6.
- [50] Swarnkar A, Mir WJ, Nag A. Can B-Site Doping or Alloying Improve Thermal- and Phase-Stability of All-Inorganic CsPbX₃ (X = Cl, Br, I) Perovskites? *ACS Energy Letters*, 2018, 3(2):286-9.
- [51] Jia X, Zuo C, Tao S, Sun K, Zhao Y, Yang S, et al. CsPb(I_xBr $_{1-x}$)₃ solar cells. *Science Bulletin*, 2019, 64(20):1532-9.
- [52] Zou S, Liu Y, Li J, Liu C, Feng R, Jiang F, et al. Stabilizing Cesium Lead Halide Perovskite Lattice through Mn(II) Substitution for Air-Stable Light-Emitting Diodes. *Journal of the American Chemical Society*, 2017, 139(33):11443-50.
- [53] Sutton RJ, Eperon GE, Miranda L, Parrott ES, Kamino BA, Patel JB, et al. Bandgap - tunable cesium lead halide perovskites with high thermal stability for efficient solar cells. *Advanced Energy Materials*, 2016, 6(8).
- [54] Beal RE, Slotcavage DJ, Leijtens T, Bowring AR, Belisle RA, Nguyen WH, et al. Cesium lead halide perovskites with improved stability for tandem solar cells. *The journal of physical chemistry letters*, 2016, 7(5):746-51.
- [55] Dou L, Wong AB, Yu Y, Lai M, Kornienko N, Eaton SW, et al. Atomically thin two-dimensional organic-inorganic hybrid perovskites. *Science*, 2015, 349(6255):1518-21.
- [56] Yu Y, Zhang D, Yang P. Ruddlesden-Popper Phase in Two-Dimensional Inorganic Halide Perovskites: A Plausible Model and the Supporting Observations. *Nano Letters*, 2017, 17(9):5489-94.
- [57] Mao L, Ke W, Pedesseau L, Wu Y, Katan C, Even J, et al. Hybrid Dion-Jacobson 2D Lead Iodide Perovskites. *Journal of the American Chemical Society*, 2018, 140(10):3775-83.
- [58] Soe CMM, Stoumpos CC, Kepenekian M, Traoré B, Tsai H, Nie W, et al. New Type of 2D Perovskites with Alternating Cations in the Interlayer Space, (C(NH₂)₃)(CH₃NH₃)_nPb_nI_{3n+1}: Structure, Properties, and Photovoltaic Performance. *Journal of the American Chemical Society*, 2017, 139(45):16297-309.
- [59] Stoumpos CC, Cao DH, Clark DJ, Young J, Rondinelli JM, Jang JJ, et al. Ruddlesden-Popper Hybrid Lead Iodide Perovskite 2D Homologous Semiconductors. *Chemistry of Materials*, 2016, 28(8):2852-67.

- [60] Chen Y, Sun Y, Peng J, Tang J, Zheng K, Liang Z. 2D Ruddlesden–Popper Perovskites for Optoelectronics. *Advanced Materials*, 2018, 30(2):1703487.
- [61] Kepenekian M, Traore B, Blancon J-C, Pedesseau L, Tsai H, Nie W, et al. Concept of Lattice Mismatch and Emergence of Surface States in Two-dimensional Hybrid Perovskite Quantum Wells. *Nano Letters*, 2018, 18(9):5603-9.
- [62] Blancon J-C, Even J, Stoumpos CC, Kanatzidis MG, Mohite AD. Semiconductor physics of organic–inorganic 2D halide perovskites. *Nature Nanotechnology*, 2020, 15(12):969-85.
- [63] Li X, Hoffman JM, Kanatzidis MG. The 2D Halide Perovskite Rulebook: How the Spacer Influences Everything from the Structure to Optoelectronic Device Efficiency. *Chemical Reviews*, 2021, 121(4):2230-91.
- [64] Protesescu L, Yakunin S, Bodnarchuk MI, Krieg F, Caputo R, Hendon CH, et al. Nanocrystals of Cesium Lead Halide Perovskites (CsPbX₃, X = Cl, Br, and I): Novel Optoelectronic Materials Showing Bright Emission with Wide Color Gamut. *Nano Letters*, 2015, 15(6):3692-6.
- [65] Swarnkar A, Marshall AR, Sanhira EM, Chernomordik BD, Moore DT, Christians JA, et al. Quantum Dot–Induced Phase Stabilization of α -CsPbI₃ Perovskite for High-Efficiency Photovoltaics. *Science*, 2016, 354(6308):92-5.
- [66] Xue J, Lee J-W, Dai Z, Wang R, Nuryyeva S, Liao ME, et al. Surface Ligand Management for Stable FAPbI₃ Perovskite Quantum Dot Solar Cells. *Joule*, 2018, 2(9):1866-78.
- [67] Huang J, Lai M, Lin J, Yang P. Rich Chemistry in Inorganic Halide Perovskite Nanostructures. *Advanced Materials*, 2018, 30(48):1802856.
- [68] Wong AB, Bekenstein Y, Kang J, Kley CS, Kim D, Gibson NA, et al. Strongly Quantum Confined Colloidal Cesium Tin Iodide Perovskite Nanoplates: Lessons for Reducing Defect Density and Improving Stability. *Nano Letters*, 2018, 18(3):2060-6.
- [69] Wang Z, Ganose Alex M, Niu C, Scanlon DO. First-Principles Insights into Tin-Based Two-Dimensional Hybrid Halide Perovskites for Photovoltaics. *Journal of Materials Chemistry A*, 2018, 6(14):5652-60.
- [70] Lin J-T, Liao C-C, Hsu C-S, Chen D-G, Chen H-M, Tsai M-K, et al. Harnessing Dielectric Confinement on Tin Perovskites to Achieve Emission Quantum Yield up to 21%. *Journal of the American Chemical Society*, 2019, 141(26):10324-30.
- [71] Shirasaki Y, Supran GJ, Bawendi MG, Bulovic V. Emergence of Colloidal Quantum-Dot Light-Emitting Technologies. *Nature Photonics*, 2013, 7(1):13-23.

- [72] Smock SR, Williams TJ, Brutchey RL. Quantifying the Thermodynamics of Ligand Binding to CsPbBr₃ Quantum Dots. *Angewandte Chemie International Edition*, 2018, 57(36):11711-5.
- [73] Xue J, Wang R, Yang Y. The surface of halide perovskites from nano to bulk. *Nature Reviews Materials*, 2020, 5(11):809-27.
- [74] Wang Y, Yuan J, Zhang X, Ling X, Larson BW, Zhao Q, et al. Surface Ligand Management Aided by a Secondary Amine Enables Increased Synthesis Yield of CsPbI₃ Perovskite Quantum Dots and High Photovoltaic Performance. *Advanced Materials*, 2020, 32(32):2000449.
- [75] Park SM, Abtahi A, Boehm AM, Graham KR. Surface Ligands for Methylammonium Lead Iodide Films: Surface Coverage, Energetics, and Photovoltaic Performance. *ACS Energy Letters*, 2020, 5(3):799-806.
- [76] De Roo J, Ibáñez M, Geiregat P, Nedelcu G, Walravens W, Maes J, et al. Highly Dynamic Ligand Binding and Light Absorption Coefficient of Cesium Lead Bromide Perovskite Nanocrystals. *ACS Nano*, 2016, 10(2):2071-81.
- [77] Ravi VK, Santra PK, Joshi N, Chugh J, Singh SK, Rensmo H, et al. Origin of the Substitution Mechanism for the Binding of Organic Ligands on the Surface of CsPbBr₃ Perovskite Nanocubes. *The Journal of Physical Chemistry Letters*, 2017, 8(20):4988-94.
- [78] Almeida G, Goldoni L, Akkerman Q, Dang Z, Khan AH, Marras S, et al. Role of Acid-Base Equilibria in the Size, Shape, and Phase Control of Cesium Lead Bromide Nanocrystals. *ACS Nano*, 2018, 12(2):1704-11.
- [79] Akkerman QA, D'Innocenzo V, Accornero S, Scarpellini A, Petrozza A, Prato M, et al. Tuning the Optical Properties of Cesium Lead Halide Perovskite Nanocrystals by Anion Exchange Reactions. *Journal of the American Chemical Society*, 2015, 137(32):10276-81.
- [80] Nedelcu G, Protesescu L, Yakunin S, Bodnarchuk MI, Grotevent MJ, Kovalenko MV. Fast Anion-Exchange in Highly Luminescent Nanocrystals of Cesium Lead Halide Perovskites (CsPbX₃, X = Cl, Br, I). *Nano Letters*, 2015, 15(8):5635-40.
- [81] Li J, Xu L, Wang T, Song J, Chen J, Xue J, et al. 50-Fold EQE Improvement up to 6.27% of Solution-Processed All-Inorganic Perovskite CsPbBr₃ QLEDs via Surface Ligand Density Control. *Advanced Materials*, 2017, 29(5):1603885.
- [82] ten Brinck S, Infante I. Surface Termination, Morphology, and Bright Photoluminescence of Cesium Lead Halide Perovskite Nanocrystals. *ACS Energy Letters*, 2016, 1(6):1266-72.
- [83] Zito J, Infante I. The Future of Ligand Engineering in Colloidal Semiconductor Nanocrystals. *Accounts of Chemical Research*, 2021.

- [84] Ahn N, Son D-Y, Jang I-H, Kang SM, Choi M, Park N-G. Highly Reproducible Perovskite Solar Cells with Average Efficiency of 18.3% and Best Efficiency of 19.7% Fabricated via Lewis Base Adduct of Lead(II) Iodide. *Journal of the American Chemical Society*, 2015, 137(27):8696-9.
- [85] Hwang K, Jung Y-S, Heo Y-J, Scholes FH, Watkins SE, Subbiah J, et al. Toward Large Scale Roll-to-Roll Production of Fully Printed Perovskite Solar Cells. *Advanced Materials*, 2015, 27(7):1241-7.
- [86] Seok SI, Grätzel M, Park N-G. Methodologies toward Highly Efficient Perovskite Solar Cells. *Small*, 2018, 14(20):1704177.
- [87] Li B, Dai Q, Yun S, Tian J. Insights into iodoplumbate complex evolution of precursor solutions for perovskite solar cells: from aging to degradation. *Journal of Materials Chemistry A*, 2021, 9(11):6732-48.
- [88] Li B, Binks D, Cao G, Tian J. Engineering Halide Perovskite Crystals through Precursor Chemistry. *Small*, 2019, 15(47):e1903613.
- [89] Jung M, Ji SG, Kim G, Seok SI. Perovskite precursor solution chemistry: from fundamentals to photovoltaic applications. *Chemical Society Reviews*, 2019, 48(7):2011-38.
- [90] Cao J, Jing X, Yan J, Hu C, Chen R, Yin J, et al. Identifying the Molecular Structures of Intermediates for Optimizing the Fabrication of High-Quality Perovskite Films. *Journal of the American Chemical Society*, 2016, 138(31):9919-26.
- [91] Petrov AA, Sokolova IP, Belich NA, Peters GS, Dorovatovskii PV, Zubavichus YV, et al. Crystal Structure of DMF-Intermediate Phases Uncovers the Link Between $\text{CH}_3\text{NH}_3\text{PbI}_3$ Morphology and Precursor Stoichiometry. *The Journal of Physical Chemistry C*, 2017, 121(38):20739-43.
- [92] Shargaieva O, Näsström H, Smith JA, Töbrens D, Munir R, Unger E. Hybrid perovskite crystallization from binary solvent mixtures: interplay of evaporation rate and binding strength of solvents. *Materials Advances*, 2020, 1(9):3314-21.
- [93] Szostak R, Sanchez S, Marchezi PE, Marques AS, Silva JC, Holanda MS, et al. Revealing the Perovskite Film Formation Using the Gas Quenching Method by In Situ GIWAXS: Morphology, Properties, and Device Performance. *Advanced Functional Materials*, 2020, 31(4):2007473.
- [94] Ortoll-Bloch AG, Herbol HC, Sorenson BA, Poloczek M, Estroff LA, Clancy P. Bypassing Solid-State Intermediates by Solvent Engineering the Crystallization Pathway in Hybrid Organic-Inorganic Perovskites. *Crystal Growth & Design*, 2019, 20(2):1162-71.

- [95] Manser JS, Reid B, Kamat PV. Evolution of Organic-Inorganic Lead Halide Perovskite from Solid-State Iodoplumbate Complexes. *The Journal of Physical Chemistry C*, 2015, 119(30):17065-73.
- [96] Borghesi C, Radicchi E, Belpassi L, Meggiolaro D, De Angelis F, Nunzi F. The nature of the lead-iodine bond in PbI_2 : A case study for the modelling of lead halide perovskites. *Computational and Theoretical Chemistry*, 2019, 1164:112558.
- [97] Kim J, Park B-w, Baek J, Yun JS, Kwon H-W, Seidel J, et al. Unveiling the Relationship between the Perovskite Precursor Solution and the Resulting Device Performance. *Journal of the American Chemical Society*, 2020, 142(13):6251-60.
- [98] Shargaieva O, Kuske L, Rappich J, Unger E, Nickel NH. Building Blocks of Hybrid Perovskites: A Photoluminescence Study of Lead-Iodide Solution Species. *ChemPhysChem*, 2020, 21(20):2327-33.
- [99] Schrödinger E. Quantisierung als eigenwertproblem. *Annalen der physik*, 1926, 385(13):437-90.
- [100] Born M, Oppenheimer R. Zur Quantentheorie der Molekeln. *Annalen der Physik*, 1927, 389(20):457-84.
- [101] Hohenberg P, Kohn W. Inhomogeneous Electron Gas. *Physical Review*, 1964, 136(3B):B864-B71.
- [102] Jones RO. Density functional theory: Its origins, rise to prominence, and future. *Reviews of Modern Physics*, 2015, 87(3):897-923.
- [103] Kohn W, Sham LJ. Self-Consistent Equations Including Exchange and Correlation Effects. *Physical Review*, 1965, 140(4A):A1133-A8.
- [104] Tsuneda T. Density functional theory in quantum chemistry. 2014.
- [105] Kohn W. Nobel Lecture: Electronic structure of matter---wave functions and density functionals. *Reviews of Modern Physics*, 1999, 71(5):1253-66.
- [106] Hybertsen MS, Louie SG. Electron correlation in semiconductors and insulators: Band gaps and quasiparticle energies. *Physical Review B*, 1986, 34(8):5390-413.
- [107] Perdew JP, Chevary JA, Vosko SH, Jackson KA, Pederson MR, Singh DJ, et al. Atoms, molecules, solids, and surfaces: Applications of the generalized gradient approximation for exchange and correlation. *Physical Review B*, 1992, 46(11):6671-87.
- [108] Perdew JP, Burke K, Ernzerhof M. Generalized Gradient Approximation Made Simple. *Physical Review Letters*, 1996, 77(18):3865-8.

- [109] Perdew JP, Ruzsinszky A, Csonka GI, Vydrov OA, Scuseria GE, Constantin LA, et al. Restoring the density-gradient expansion for exchange in solids and surfaces. *Physical review letters*, 2008, 100(13):136406.
- [110] Ferreira LG, Marques M, Teles LK. Approximation to density functional theory for the calculation of band gaps of semiconductors. *Physical Review B*, 2008, 78(12):125116.
- [111] Slater JC, Johnson KH. Self-Consistent-Field X α Cluster Method for Polyatomic Molecules and Solids. *Physical Review B*, 1972, 5(3):844.
- [112] Marx D, Hutter J. Ab initio molecular dynamics: basic theory and advanced methods: Cambridge University Press; 2009.
- [113] Andrade X, Castro A, Zueco D, Alonso J, Echenique P, Falceto F, et al. Modified Ehrenfest formalism for efficient large-scale ab initio molecular dynamics. *Journal of chemical theory and computation*, 2009, 5(4):728-42.
- [114] Vacher M, Mendive-Tapia D, Bearpark MJ, Robb MA. The second-order Ehrenfest method. *Theoretical Chemistry Accounts*, 2014, 133(7):1-12.
- [115] Ding F, Goings JJ, Liu H, Lingerfelt DB, Li X. Ab initio two-component Ehrenfest dynamics. *The Journal of chemical physics*, 2015, 143(11):114105.
- [116] Paquet E, Viktor HL. Computational methods for Ab initio molecular dynamics. *Advances in Chemistry*, 2018, 2018:9839641.
- [117] Car R, Parrinello M. Unified Approach for Molecular Dynamics and Density-Functional Theory. *Physical Review Letters*, 1985, 55(22):2471-4.
- [118] Tuckerman M. Statistical mechanics: theory and molecular simulation: Oxford university press; 2010.
- [119] Nosé S. A molecular dynamics method for simulations in the canonical ensemble. *Molecular Physics*, 1984, 52(2):255-68.
- [120] Hoover WG. Canonical dynamics: Equilibrium phase-space distributions. *Physical Review A*, 1985, 31(3):1695-7.
- [121] Xing G, Mathews N, Sun S, Lim SS, Lam YM, Grätzel M, et al. Long-range balanced electron-and hole-transport lengths in organic-inorganic $\text{CH}_3\text{NH}_3\text{PbI}_3$. *Science*, 2013, 342(6156):344-7.
- [122] Yang Y, Yan Y, Yang M, Choi S, Zhu K, Luther JM, et al. Low surface recombination velocity in solution-grown $\text{CH}_3\text{NH}_3\text{PbBr}_3$ perovskite single crystal. *Nature Communications*, 2015, 6(1):7961.

- [123] Burschka J, Pellet N, Moon S-J, Humphry-Baker R, Gao P, Nazeeruddin MK, et al. Sequential deposition as a route to high-performance perovskite-sensitized solar cells. *Nature*, 2013, 499:316.
- [124] Lee MM, Teuscher J, Miyasaka T, Murakami TN, Snaith HJ. Efficient hybrid solar cells based on meso-superstructured organometal halide perovskites. *Science*, 2012, 338(6107):643-7.
- [125] Tan Z-K, Moghaddam RS, Lai ML, Docampo P, Higler R, Deschler F, et al. Bright light-emitting diodes based on organometal halide perovskite. *Nature nanotechnology*, 2014, 9(9):687.
- [126] Dou L, Yang YM, You J, Hong Z, Chang W-H, Li G, et al. Solution-Processed Hybrid Perovskite Photodetectors with High Detectivity. *Nature communications*, 2014, 5:5404.
- [127] Saidaminov MI, Adinolfi V, Comin R, Abdelhady AL, Peng W, Dursun I, et al. Planar-integrated single-crystalline perovskite photodetectors. *Nature communications*, 2015, 6:8724.
- [128] Xing G, Mathews N, Lim SS, Yantara N, Liu X, Sabba D, et al. Low-temperature solution-processed wavelength-tunable perovskites for lasing. *Nature materials*, 2014, 13(5):476.
- [129] Zhu H, Fu Y, Meng F, Wu X, Gong Z, Ding Q, et al. Lead halide perovskite nanowire lasers with low lasing thresholds and high quality factors. *Nature materials*, 2015, 14(6):636.
- [130] Kojima AT, Kenjiro; Shirai, Yasuo; Miyasaka. Sensitizers for Photovoltaic Cells as Visible-Light, Organometal Halide Perovskites. *Journal of the American Chemical Society*, 2009, 131(17):6050-1.
- [131] Jung Y-K, Lee J-H, Walsh A, Soon A. Influence of Rb/Cs Cation-Exchange on Inorganic Sn Halide Perovskites: From Chemical Structure to Physical Properties. *Chemistry of Materials*, 2017, 29(7):3181-8.
- [132] Binek A, Hanusch FC, Docampo P, Bein T. Stabilization of the Trigonal High-Temperature Phase of Formamidinium Lead Iodide. *The Journal of Physical Chemistry Letters*, 2015, 6(7):1249-53.
- [133] Syzgantseva OA, Saliba M, Grätzel M, Rothlisberger U. Stabilization of the perovskite phase of formamidinium lead triiodide by methylammonium, Cs, and/or Rb doping. *The journal of physical chemistry letters*, 2017, 8(6):1191-6.
- [134] Weller MT, Weber OJ, Frost JM, Walsh A. Cubic Perovskite Structure of Black Formamidinium Lead Iodide, α -[HC(NH₂)₂]PbI₃, at 298K. *The Journal of Physical Chemistry Letters*, 2015, 6(16):3209-12.

- [135] Cao J, Tao SX, Bobbert PA, Wong C-P, Zhao N. Interstitial Occupancy by Extrinsic Alkali Cations in Perovskites and Its Impact on Ion Migration. *Advanced Materials*, 2018, 30(26):1707350.
- [136] Kanno S, Imamura Y, Hada M. Theoretical Study on Rotational Controllability of Organic Cations in Organic-Inorganic Hybrid Perovskites: Hydrogen Bonds and Halogen Substitution. *The Journal of Physical Chemistry C*, 2017, 121(47):26188-95.
- [137] Kresse G, Furthmüller J. Efficiency of ab-initio total energy calculations for metals and semiconductors using a plane-wave basis set. *Computational materials science*, 1996, 6(1):15-50.
- [138] Blöchl PE. Projector augmented-wave method. *Physical review B*, 1994, 50(24):17953.
- [139] Kresse G, Joubert D. From ultrasoft pseudopotentials to the projector augmented-wave method. *Physical review B*, 1999, 59(3):1758.
- [140] Peng H, Yang Z-H, Sun J, Perdew JPA. SCAN+rVV10: A promising van der Waals density functional. 2015.
- [141] Jiang J, Onwudinanti CK, Hatton RA, Bobbert PA, Tao S. Stabilizing Lead-Free All-Inorganic Tin Halide Perovskites by Ion Exchange. *Journal of Physical Chemistry C*, 2018, 122(31):17660-7.
- [142] Chen T, Foley BJ, Park C, Brown CM, Harriger LW, Lee J, et al. Entropy-driven structural transition and kinetic trapping in formamidinium lead iodide perovskite. *Science advances*, 2016, 2(10):e1601650.
- [143] Pan Y, Su Y, Hsu C, Huang L, Dou K, Kaun C. First-principles study on electronic structures of FAPbX₃ (X = Cl, Br, I) hybrid perovskites. *J Adv Nanomater*, 2016, 1:33-8.
- [144] Oranskaia A, Schwingenschlögl U. Suppressing X-Migrations and Enhancing the Phase Stability of Cubic FAPbX₃ (X = Br, I). *Advanced Energy Materials*, 2019, 9(32):1901411.
- [145] Dronskowski R, Blöchl PE. Crystal orbital Hamilton populations (COHP): energy-resolved visualization of chemical bonding in solids based on density-functional calculations. *The Journal of Physical Chemistry*, 1993, 97(33):8617-24.
- [146] Deringer VL, Tchougréeff AL, Dronskowski R. Crystal orbital Hamilton population (COHP) analysis as projected from plane-wave basis sets. *The journal of physical chemistry A*, 2011, 115(21):5461-6.
- [147] Maintz S, Deringer VL, Tchougréeff AL, Dronskowski R. Analytic projection from plane - wave and PAW wavefunctions and application to chemical - bonding analysis in solids. *Journal of computational chemistry*, 2013, 34(29):2557-67.

- [148] Maintz S, Deringer VL, Tchougréeff AL, Dronskowski R. LOBSTER: A tool to extract chemical bonding from plane - wave based DFT. *Journal of computational chemistry*, 2016, 37(11):1030-5.
- [149] Wuttig M, Lüsebrink D, Wamwangi D, Welnic W, Gilleßen M, Dronskowski R. The role of vacancies and local distortions in the design of new phase-change materials. *Nature materials*, 2007, 6(2):122.
- [150] Landrum GA, Dronskowski R. The orbital origins of magnetism: from atoms to molecules to ferromagnetic alloys. *Angewandte Chemie International Edition*, 2000, 39(9):1560-85.
- [151] van Santen RA, Tranca I, Hensen EJ. Theory of surface chemistry and reactivity of reducible oxides. *Catalysis Today*, 2015, 244:63-84.
- [152] Rohling RY, Tranca IC, Hensen EJ, Pidko EA. Mechanistic Insight into the [4+2] Diels–Alder Cycloaddition over First Row d-Block Cation-Exchanged Faujasites. *ACS Catalysis*, 2018, 9(1):376-91.
- [153] Rohling RY, Tranca IC, Hensen EJM, Pidko EA. Electronic Structure Analysis of the Diels–Alder Cycloaddition Catalyzed by Alkali-Exchanged Faujasites. *The Journal of Physical Chemistry C*, 2018, 122(26):14733-43.
- [154] Decker A, Landrum GA, Dronskowski R. Structural and electronic peierls distortions in the elements (A): The crystal structure of tellurium. *Zeitschrift für anorganische und allgemeine Chemie*, 2002, 628(1):295-302.
- [155] Even J, Pedesseau L, Jancu J-M, Katan C. DFT and k p Modelling of the Phase Transitions of Lead and Tin Halide Perovskites for Photovoltaic Cells. *physica status solidi (RRL) - Rapid Research Letters*, 2014, 8(1):31-5.
- [156] Tao SX, Cao X, Bobbert PA. Accurate and efficient band gap predictions of metal halide perovskites using the DFT-1/2 method: GW accuracy with DFT expense. *Scientific Reports*, 2017, 7(1):14386.
- [157] Goesten MG, Hoffmann R. Mirrors of Bonding in Metal Halide Perovskites. *Journal of the American Chemical Society*, 2018, 140(40):12996-3010.
- [158] Tao S, Schmidt I, Brocks G, Jiang J, Tranca I, Meerholz K, et al. Absolute energy level positions in tin- and lead-based halide perovskites. *Nature Communications*, 2019, 10(1):2560.
- [159] Quarti C, Mosconi E, Ball JM, D'Innocenzo V, Tao C, Pathak S, et al. Structural and optical properties of methylammonium lead iodide across the tetragonal to cubic phase transition: implications for perovskite solar cells. *Energy & Environmental Science*, 2016, 9(1):155-63.

- [160] Ye M, Kimura A, Miura Y, Shirai M, Cui Y, Shimada K, et al. Role of electronic structure in the martensitic phase transition of $\text{Ni}_2\text{Mn}_{1+x}\text{Sn}_{1-x}$ studied by hard-X-ray photoelectron spectroscopy and ab initio calculation. *Physical review letters*, 2010, 104(17):176401.
- [161] Brivio F, Caetano C, Walsh A. Thermodynamic Origin of Photoinstability in the $\text{CH}_3\text{NH}_3\text{Pb}(\text{I}_{1-x}\text{Br}_x)_3$ Hybrid Halide Perovskite Alloy. *The journal of physical chemistry letters*, 2016, 7(6):1083-7.
- [162] Schelhas LT, Li Z, Christians JA, Goyal A, Kairys P, Harvey SP, et al. Insights into operational stability and processing of halide perovskite active layers. *Energy & Environmental Science*, 2019, 12(4):1341-8.
- [163] Li N, Tao S, Chen Y, Niu X, Onwudinanti CK, Hu C, et al. Cation and anion immobilization through chemical bonding enhancement with fluorides for stable halide perovskite solar cells. *Nature Energy*, 2019, 4(5):408-15.
- [164] Yi C, Luo J, Meloni S, Boziki A, Ashari-Astani N, Grätzel C, et al. Entropic Stabilization of Mixed A-Cation ABX_3 Metal Halide Perovskites for High Performance Perovskite Solar Cells. *Energy & Environmental Science*, 2016, 9(2):656-62.
- [165] Moghe D, Wang L, Traverse CJ, Redoute A, Sponseller M, Brown PR, et al. All vapor-deposited lead-free doped CsSnBr_3 planar solar cells. *Nano Energy*, 2016, 28:469-74.
- [166] Xu H, Duan J, Zhao Y, Jiao Z, He B, Tang Q. 9.13%-Efficiency and stable inorganic CsPbBr_3 solar cells. Lead-free $\text{CsSnBr}_{3-x}\text{I}_x$ quantum dots promote charge extraction. *Journal of Power Sources*, 2018, 399:76-82.
- [167] Marshall KP, Tao S, Walker M, Cook DS, Hughes JL, Varagnolo S, et al. $\text{Cs}_{1-x}\text{Rb}_x\text{SnI}_3$ Light Harvesting Semiconductors for Perovskite Photovoltaics. *Mater Chem Front*, 2018.
- [168] Liu F, Ding C, Zhang Y, Kamisaka T, Zhao Q, Luther JM, et al. GeI_2 Additive for High Optoelectronic Quality CsPbI_3 Quantum Dots and Their Application in Photovoltaic Devices. *Chemistry of Materials*, 2019, 31(3):798-807.
- [169] Yablonovitch E. Lead Halides Join the Top Optoelectronic League. *Science*, 2016, 351(6280):1401-.
- [170] Green MA, Ho-Baillie A, Snaith HJ. The Emergence of Perovskite Solar Cells. *Nature Photonics*, 2014, 8(7):506-14.
- [171] Kadro JM, Pellet N, Giordano F, Ulianov A, Müntener O, Maier J, et al. Proof-of-Concept for Facile Perovskite Solar Cell Recycling. *Energy & Environmental Science*, 2016, 9(10):3172-9.

- [172] Pedesseau L, Saponi D, Traore B, Robles R, Fang HH, Loi MA, et al. Advances and Promises of Layered Halide Hybrid Perovskite Semiconductors. *ACS Nano*, 2016, 10(11):9776-86.
- [173] Liu F, Jiang J, Zhang Y, Ding C, Toyoda T, Hayase S, et al. Near-Infrared Emission from Tin-Lead (Sn-Pb) Alloyed Perovskite Quantum Dots by Sodium Doping. *Angewandte Chemie International Edition*, 2020, 59(22):8421-4.
- [174] Kojima A, Teshima K, Shirai Y, Miyasaka T. Organometal halide perovskites as visible-light sensitizers for photovoltaic cells. *Journal of the American Chemical Society*, 2009, 131(17):6050-1.
- [175] Liang L, Gao P. Lead-Free Hybrid Perovskite Absorbers for Viable Application: Can We Eat the Cake and Have It too? *Advanced Science*, 2017:1700331.
- [176] Wang A, Guo Y, Muhammad F, Deng Z. Controlled Synthesis of Lead-Free Cesium Tin Halide Perovskite Cubic Nanocages with High Stability. *Chemistry of Materials*, 2017, 29(15):6493-501.
- [177] Whalley LD, Frost JM, Jung YK, Walsh A. Perspective: Theory and Simulation of Hybrid Halide Perovskites. *J Chem Phys*, 2017, 146(22):220901.
- [178] Sun Q, Yin WJ. Thermodynamic Stability Trend of Cubic Perovskites. *Journal of the American Chemical Society*, 2017, 139(42):14905-8.
- [179] Gratia P, Grancini G, Audinot JN, Jeanbourquin X, Mosconi E, Zimmermann I, et al. Intrinsic Halide Segregation at Nanometer Scale Determines the High Efficiency of Mixed Cation/Mixed Halide Perovskite Solar Cells. *Journal of the American Chemical Society*, 2016, 138(49):15821-4.
- [180] Correa-Baena J-P, Abate A, Saliba M, Tress W, Jesper Jacobsson T, Grätzel M, et al. The Rapid Evolution of Highly Efficient Perovskite Solar Cells. *Energy & Environmental Science*, 2017, 10(3):710-27.
- [181] Niemann RG, Gouda L, Hu J, Tirosh S, Gottesman R, Cameron PJ, et al. Cs⁺ Incorporation into CH₃NH₃PbI₃ Perovskite: Substitution Limit and Stability Enhancement. *Journal of Materials Chemistry A*, 2016, 4(45):17819-27.
- [182] Babayigit A, Ethirajan A, Muller M, Conings B. Toxicity of Organometal Halide Perovskite Solar Cells. *Nature materials*, 2016, 15(3):247.
- [183] Ju M-G, Chen M, Zhou Y, Garces HF, Dai J, Ma L, et al. Earth-Abundant Nontoxic Titanium(IV)-based Vacancy-Ordered Double Perovskite Halides with Tunable 1.0 to 1.8 eV Bandgaps for Photovoltaic Applications. *ACS Energy Letters*, 2018:297-304.

- [184] Shi Z, Guo J, Chen Y, Li Q, Pan Y, Zhang H, et al. Lead-Free Organic-Inorganic Hybrid Perovskites for Photovoltaic Applications: Recent Advances and Perspectives. *Advanced Materials*, 2017, 29(16):1605005.
- [185] Wang N, Zhou Y, Ju M-G, Garces HF, Ding T, Pang S, et al. Heterojunction-Depleted Lead-Free Perovskite Solar Cells with Coarse-Grained B- γ -CsSnI₃ Thin Films. *Advanced Energy Materials*, 2016, 6(24):1601130.
- [186] Harikesh PC, Mulmudi HK, Ghosh B, Goh TW, Teng YT, Thirumal K, et al. Rb as an Alternative Cation for Templating Inorganic Lead-Free Perovskites for Solution Processed Photovoltaics. *Chemistry of Materials*, 2016, 28(20):7496-504.
- [187] Chung I, Lee B, He J, Chang RP, Kanatzidis MG. All-Solid-State Dye-Sensitized Solar Cells with High Efficiency. *Nature*, 2012, 485(7399):486.
- [188] Marshall KP, Walker M, Walton RI, Hatton RA. Enhanced stability and efficiency in hole-transport-layer-free CsSnI₃ perovskite photovoltaics. *Nature Energy*, 2016, 1(12):16178.
- [189] Konstantakou M, Stergiopoulos T. A Critical Review on Tin Halide Perovskite Solar Cells. *Journal of Materials Chemistry A*, 2017, 5(23):11518-49.
- [190] Chiarella F, Zappettini A, Licci F, Borriello I, Cantele G, Ninno D, et al. Combined Experimental and Theoretical Investigation of Optical, Structural, and Electronic Properties of CH₃NH₃SnX₃ Thin Films (X= Cl, Br). *Physical Review B*, 2008, 77(4):045129.
- [191] Abate A. Perovskite Solar Cells Go Lead Free. *Joule*, 2017, 1(4):659-64.
- [192] Noel NK, Stranks SD, Abate A, Wehrenfennig C, Guarnera S, Haghighirad A-A, et al. Lead-Free Organic-Inorganic Tin Halide Perovskites for Photovoltaic Applications. *Energy & Environmental Science*, 2014, 7(9):3061-8.
- [193] Hao F, Stoumpos CC, Cao DH, Chang RP, Kanatzidis MG. Lead-Free Solid-State Organic-Inorganic Halide Perovskite Solar Cells. *Nature Photonics*, 2014, 8(6):489-94.
- [194] Sun YY, Shi J, Lian J, Gao W, Agiorgousis ML, Zhang P, et al. Discovering Lead-free Perovskite Solar Materials with a Split-Anion Approach. *Nanoscale*, 2016, 8(12):6284-9.
- [195] Lee B, Stoumpos CC, Zhou N, Hao F, Malliakas C, Yeh C-Y, et al. Air-Stable Molecular Semiconducting Iodosalts for Solar Cell Applications: Cs₂SnI₆ as a Hole Conductor. *Journal of the American Chemical Society*, 2014, 136(43):15379-85.
- [196] Xiao Z, Zhou Y, Hosono H, Kamiya T. Intrinsic Defects in a Photovoltaic Perovskite Variant Cs₂SnI₆. *Physical Chemistry Chemical Physics*, 2015, 17(29):18900-3.

- [197] Saparov B, Sun J-P, Meng W, Xiao Z, Duan H-S, Gunawan O, et al. Thin-film deposition and characterization of a Sn-deficient perovskite derivative Cs_2SnI_6 . *Chemistry of Materials*, 2016, 28(7):2315-22.
- [198] Qiu X, Cao B, Yuan S, Chen X, Qiu Z, Jiang Y, et al. From Unstable CsSnI_3 to Air-Stable Cs_2SnI_6 : A Lead-Free Perovskite Solar Cell Light Absorber with Bandgap of 1.48 eV and High Absorption Coefficient. *Solar Energy Materials and Solar Cells*, 2017, 159:227-34.
- [199] Shao S, Liu J, Portale G, Fang H-H, Blake GR, ten Brink GH, et al. Highly Reproducible Sn-Based Hybrid Perovskite Solar Cells with 9% Efficiency. *Advanced Energy Materials*, 2018, 8(4):1702019.
- [200] Gupta S, Bendikov T, Hodes G, Cahen D. CsSnBr_3 , A Lead-Free Halide Perovskite for Long-Term Solar Cell Application: Insights on SnF_2 Addition. *ACS Energy Letters*, 2016, 1(5):1028-33.
- [201] Kontos AG, Kaltzoglou A, Siranidi E, Palles D, Angeli GK, Arfanis MK, et al. Structural Stability, Vibrational Properties, and Photoluminescence in CsSnI_3 Perovskite upon the Addition of SnF_2 . *Inorganic Chemistry*, 2017, 56(1):84-91.
- [202] Xu P, Chen S, Xiang H-J, Gong X-G, Wei S-H. Influence of Defects and Synthesis Conditions on the Photovoltaic Performance of Perovskite Semiconductor CsSnI_3 . *Chemistry of Materials*, 2014, 26(20):6068-72.
- [203] Chen Z, Wang JJ, Ren Y, Yu C, Shum K. Schottky Solar Cells Based on CsSnI_3 Thin-Films. *Applied Physics Letters*, 2012, 101(9):093901.
- [204] Kumar MH, Dharani S, Leong WL, Boix PP, Prabhakar RR, Baikie T, et al. Lead-Free Halide Perovskite Solar Cells with High Photocurrents Realized Through Vacancy Modulation. *Advanced Materials*, 2014, 26(41):7122-7.
- [205] Wang Z, McMeekin DP, Sakai N, van Reenen S, Wojciechowski K, Patel JB, et al. Efficient and Air - Stable Mixed - Cation Lead Mixed - Halide Perovskite Solar Cells with n - Doped Organic Electron Extraction Layers. *Advanced Materials*, 2017, 29(5):1604186.
- [206] Bi D, Tress W, Dar MI, Gao P, Luo J, Renevier C, et al. Efficient Luminescent Solar Cells Based on Tailored Mixed-Cation Perovskites. *Science advances*, 2016, 2(1):e1501170.
- [207] Pellet N, Gao P, Gregori G, Yang TY, Nazeeruddin MK, Maier J, et al. Mixed - Organic - Cation Perovskite Photovoltaics for Enhanced Solar - Light Harvesting. *Angewandte Chemie International Edition*, 2014, 53(12):3151-7.
- [208] McMeekin DP, Sadoughi G, Rehman W, Eperon GE, Saliba M, Hörantner MT, et al. A mixed-cation lead mixed-halide perovskite absorber for tandem solar cells. *Science*, 2016, 351(6269):151-5.

- [209] Li W, Li J, Li J, Fan J, Mai Y, Wang L. Addictive-Assisted Construction of All-Inorganic CsSnIBr₂ Mesoscopic Perovskite Solar Cells with Superior Thermal Stability up to 473 K. *Journal of Materials Chemistry A*, 2016, 4(43):17104-10.
- [210] Sabba D, Mulmudi HK, Prabhakar RR, Krishnamoorthy T, Baikie T, Boix PP, et al. Impact of Anionic Br-Substitution on Open Circuit Voltage in Lead Free Perovskite (CsSnI_{3-x}Br_x) Solar Cells. *The Journal of Physical Chemistry C*, 2015, 119(4):1763-7.
- [211] Pelá R, Caetano C, Marques M, Ferreira L, Furthmüller J, Teles L. Accurate Band Gaps of AlGaN, InGaN, and AlInN Alloys Calculations Based on LDA-1/2 Approach. *Applied Physics Letters*, 2011, 98(15):151907.
- [212] Ferreira LG, Marques M, Teles LK. Slater Half-Occupation Technique Revisited: the LDA-1/2 and GGA-1/2 Approaches for Atomic Ionization Energies and Band Gaps in Semiconductors. *AIP Advances*, 2011, 1(3):032119.
- [213] Pela R, Marques M, Teles L. Comparing LDA-1/2, HSE03, HSE06 and G₀W₀ Approaches for Band Gap Calculations of Alloys. *Journal of Physics: Condensed Matter*, 2015, 27(50):505502.
- [214] Kresse G, Furthmüller J. Efficient iterative schemes for ab initio total-energy calculations using a plane-wave basis set. *Physical review B*, 1996, 54(16):11169.
- [215] Slater JC. Statistical Exchange-Correlation in the Self-Consistent Field. *Advances in Quantum Chemistry*, 1972, 6:1-92.
- [216] Sher A, van Schilfgaarde M, Chen A-B, Chen W. Quasichemical Approximation in Binary Alloys. *Physical Review B*, 1987, 36(8):4279.
- [217] Grote C, Berger RF. Strain Tuning of Tin-Halide and Lead-Halide Perovskites: a First-Principles Atomic and Electronic Structure Study. *The Journal of Physical Chemistry C*, 2015, 119(40):22832-7.
- [218] Thiele G, Serr B. Crystal Structure of Rubidium Triiodostannate (II), RbSnI₃. *Zeitschrift für Kristallographie - Crystalline Materials*, 1995, 210(1):64-.
- [219] Scaife DE, Weller PF, Fisher WG. Crystal preparation and properties of cesium tin(II) trihalides. *Journal of Solid State Chemistry*, 1974, 9(3):308-14.
- [220] Lang L, Zhang Y-Y, Xu P, Chen S, Xiang H, Gong X. Three-Step Approach for Computing Band Offsets and Its Application to Inorganic ABX₃ Halide Perovskites. *Physical Review B*, 2015, 92(7):075102.
- [221] Krishnamoorthy T, Ding H, Yan C, Leong WL, Baikie T, Zhang Z, et al. Lead-Free Germanium Iodide Perovskite Materials for Photovoltaic Applications. *Journal of Materials Chemistry A*, 2015, 3(47):23829-32.

- [222] Carignano MA, Aravindh SA, Roqan IS, Even J, Katan C. Critical Fluctuations and Anharmonicity in Lead Iodide Perovskites from Molecular Dynamics Supercell Simulations. *The Journal of Physical Chemistry C*, 2017, 121(38):20729-38.
- [223] Zhou X, Jankowska J, Dong H, Prezhdov OV. Recent Theoretical Progress in the Development of Perovskite Photovoltaic Materials. *Journal of Energy Chemistry*, 2017.
- [224] Ma CG, Krasnenko V, Brik MG. First-Principles Calculations of Different (001) Surface Terminations of Three Cubic Perovskites CsCaBr₃, CsGeBr₃, and CsSnBr₃. *Journal of Physics and Chemistry of Solids*, 2018, 115:289-99.
- [225] Ju MG, Dai J, Ma L, Zeng XC. Lead-Free Mixed Tin and Germanium Perovskites for Photovoltaic Application. *Journal of the American Chemical Society*, 2017, 139(23):8038-43.
- [226] Mailoa JP, Bailie CD, Johlin EC, Hoke ET, Akey AJ, Nguyen WH, et al. A 2-terminal perovskite/silicon multijunction solar cell enabled by a silicon tunnel junction. *Applied Physics Letters*, 2015, 106(12):121105.
- [227] Marshall K, Walker M, Walton R, Hatton R. Elucidating the Role of the Hole-Extracting Electrode on the Stability and Efficiency of Inverted CsSnI₃/C₆₀ Perovskite Photovoltaics. *Journal of Materials Chemistry A*, 2017, 5(41):21836-45.
- [228] Unger EL, Kegelmann L, Suchan K, Sörell D, Korte L, Albrecht S. Roadmap and Roadblocks for the Band Gap Tunability of Metal Halide Perovskites. *Journal of Materials Chemistry A*, 2017, 5(23):11401-9.
- [229] Barone PW, Baik S, Heller DA, Strano MS. Near-Infrared Optical Sensors Based on Single-Walled Carbon Nanotubes. *Nature Materials*, 2005, 4(1):86-92.
- [230] Sargent EH. Infrared Photovoltaics Made by Solution Processing. *Nature Photonics*, 2009, 3(6):325-31.
- [231] Noda S, Tomoda K, Yamamoto N, Chutinan A. Full Three-Dimensional Photonic Bandgap Crystals at Near-Infrared Wavelengths. *Science*, 2000, 289(5479):604-6.
- [232] Eperon GE, Leijtens T, Bush KA, Prasanna R, Green T, Wang JTW, et al. Perovskite-Perovskite Tandem Photovoltaics with Optimized Band Gaps. *Science*, 2016, 354(6314):861-5.
- [233] Jena AK, Kulkarni A, Miyasaka T. Halide Perovskite Photovoltaics: Background, Status, and Future Prospects. *Chemical Reviews*, 2019, 119(5):3036-103.
- [234] Zhang J, Hodes G, Jin Z, Liu S. All-Inorganic CsPbX₃ Perovskite Solar Cells: Progress and Prospects. *Angewandte Chemie International Edition*, 2019, 58(44):15596-618.

- [235] Yakunin S, Benin BM, Shynkarenko Y, Nazarenko O, Bodnarchuk MI, Dirin DN, et al. High-Resolution Remote Thermometry and Thermography using Luminescent Low-Dimensional Tin-Halide Perovskites. *Nature Materials*, 2019, 18:846-52.
- [236] Zhang D, Yang Y, Bekenstein Y, Yu Y, Gibson NA, Wong AB, et al. Synthesis of Composition Tunable and Highly Luminescent Cesium Lead Halide Nanowires through Anion-Exchange Reactions. *Journal of the American Chemical Society*, 2016, 138(23):7236-9.
- [237] Xiao Z, Song Z, Yan Y. From Lead Halide Perovskites to Lead-Free Metal Halide Perovskites and Perovskite Derivatives. *Advanced Materials*, 2019:1803792.
- [238] Ke W, Stoumpos CC, Kanatzidis MG. "Unleaded" Perovskites: Status Quo and Future Prospects of Tin-Based Perovskite Solar Cells. *Advanced Materials*, 2018:1803230.
- [239] Xing G, Kumar MH, Chong WK, Liu X, Cai Y, Ding H, et al. Solution-Processed Tin-Based Perovskite for Near-Infrared Lasing. *Advanced Materials*, 2016, 28(37):8191-6.
- [240] Jokar E, Chien C-H, Tsai C-M, Fathi A, Diao EW-G. Robust Tin-Based Perovskite Solar Cells with Hybrid Organic Cations to Attain Efficiency Approaching 10%. *Advanced Materials*, 2019, 31(2):1804835.
- [241] Hao F, Stoumpos CC, Chang RPH, Kanatzidis MG. Anomalous Band Gap Behavior in Mixed Sn and Pb Perovskites Enables Broadening of Absorption Spectrum in Solar Cells. *Journal of the American Chemical Society*, 2014, 136(22):8094-9.
- [242] Ogomi Y, Morita A, Tsukamoto S, Saitho T, Fujikawa N, Shen Q, et al. $\text{CH}_3\text{NH}_3\text{Sn}_x\text{Pb}_{(1-x)}\text{I}_3$ Perovskite Solar Cells Covering up to 1060 nm. *Journal of Physical Chemistry Letters*, 2014, 5(6):1004-11.
- [243] Anaya M, Correa-Baena JP, Lozano G, Saliba M, Anguita P, Roose B, et al. Optical Analysis of $\text{CH}_3\text{NH}_3\text{Sn}_x\text{Pb}_{1-x}\text{I}_3$ Absorbers: a Roadmap for Perovskite-on-Perovskite Tandem Solar Cells. *Journal of Materials Chemistry A*, 2016, 4(29):11214-21.
- [244] Liao WQ, Zhao DW, Yu Y, Shrestha N, Ghimire K, Grice CR, et al. Fabrication of Efficient Low-Bandgap Perovskite Solar Cells by Combining Formamidinium Tin Iodide with Methylammonium Lead Iodide. *Journal of the American Chemical Society*, 2016, 138(38):12360-3.
- [245] Tong J, Song Z, Kim DH, Chen X, Chen C, Palmstrom AF, et al. Carrier Lifetimes of $>1 \mu\text{s}$ in Sn-Pb Perovskites Enable Efficient All-Perovskite Tandem Solar Cells. *Science*, 2019, 364(6439):475-9.
- [246] Leijtens T, Prasanna R, Gold-Parker A, Toney MF, McGehee MD. Mechanism of Tin Oxidation and Stabilization by Lead Substitution in Tin Halide Perovskites. *ACS Energy Letters*, 2017, 2(9):2159-65.

- [247] Yamamoto K, Iikubo S, Yamasaki J, Ogomi Y, Hayase S. Structural Stability of Iodide Perovskite: A Combined Cluster Expansion Method and First-Principles Study. *The Journal of Physical Chemistry C*, 2017, 121(50):27797-804.
- [248] Guedes-Sobrinho D, Guilhon I, Marques M, Teles LK. Thermodynamic Stability and Structural Insights for $\text{CH}_3\text{NH}_3\text{Pb}_{1-x}\text{Si}_x\text{I}_3$, $\text{CH}_3\text{NH}_3\text{Pb}_{1-x}\text{Ge}_x\text{I}_3$, and $\text{CH}_3\text{NH}_3\text{Pb}_{1-x}\text{Sn}_x\text{I}_3$ Hybrid Perovskite Alloys: A Statistical Approach from First Principles Calculations. *Scientific Reports*, 2019, 9(1):11061.
- [249] Jiang J, Liu F, Tranca I, Shen Q, Tao S. Atomistic and Electronic Origin of Phase Instability of Metal Halide Perovskites. *ACS Applied Energy Materials*, 2020, 3(12):11548-58.
- [250] Zong Y, Zhou Z, Chen M, Padture NP, Zhou Y. Lewis-Adduct Mediated Grain-Boundary Functionalization for Efficient Ideal-Bandgap Perovskite Solar Cells with Superior Stability. *Advanced Energy Materials*, 2018, 8(27):1800997.
- [251] Shao S, Cui Y, Duim H, Qiu X, Dong J, ten Brink GH, et al. Enhancing the Performance of the Half Tin and Half Lead Perovskite Solar Cells by Suppression of the Bulk and Interfacial Charge Recombination. *Advanced Materials*, 2018, 30(35):1803703.
- [252] Lin R, Xiao K, Qin Z, Han Q, Zhang C, Wei M, et al. Monolithic all-perovskite tandem solar cells with 24.8% efficiency exploiting comproportionation to suppress Sn(ii) oxidation in precursor ink. *Nature Energy*, 2019, 4(10):864-73.
- [253] Hu M, Chen M, Guo P, Zhou H, Deng J, Yao Y, et al. Sub-1.4eV bandgap inorganic perovskite solar cells with long-term stability. *Nature Communications*, 2020, 11(1):151.
- [254] Zhao Q, Hazarika A, Schelhas LT, Liu J, Gauld EA, Li G, et al. Size-Dependent Lattice Structure and Confinement Properties in CsPbI_3 Perovskite Nanocrystals: Negative Surface Energy for Stabilization. *ACS Energy Letters*, 2020, 5(1):238-47.
- [255] Liao Y, Liu H, Zhou W, Yang D, Shang Y, Shi Z, et al. Highly Oriented Low-Dimensional Tin Halide Perovskites with Enhanced Stability and Photovoltaic Performance. *Journal of the American Chemical Society*, 2017, 139(19):6693-9.
- [256] Jellicoe TC, Richter JM, Glass HFJ, Tabachnyk M, Brady R, Dutton SE, et al. Synthesis and Optical Properties of Lead-Free Cesium Tin Halide Perovskite Nanocrystals. *Journal of the American Chemical Society*, 2016, 138(9):2941-4.
- [257] Liu F, Zhang Y, Ding C, Kawabata K, Yoshihara Y, Toyoda T, et al. Trioctylphosphine Oxide Acts as Alkahest for $\text{SnX}_2/\text{PbX}_2$: A General Synthetic Route to Perovskite $\text{ASn}_x\text{Pb}_{1-x}\text{X}_3$ (A = Cs, FA, MA; X = Cl, Br, I) Quantum Dots. *Chemistry of Materials*, 2020, 32(3):1089-100.

- [258] Yan Y, Pullerits T, Zheng K, Liang Z. Advancing Tin Halide Perovskites: Strategies toward the ASnX_3 Paradigm for Efficient and Durable Optoelectronics. *ACS Energy Letters*, 2020, 5(6):2052-86.
- [259] Xiao Z, Yan Y. Progress in Theoretical Study of Metal Halide Perovskite Solar Cell Materials. *Advanced Energy Materials*, 2017, 7(22):1701136.
- [260] Nenon DP, Pressler K, Kang J, Koscher BA, Olshansky JH, Osowiecki WT, et al. Design Principles for Trap-Free CsPbX_3 Nanocrystals: Enumerating and Eliminating Surface Halide Vacancies with Softer Lewis Bases. *Journal of the American Chemical Society*, 2018, 140(50):17760-72.
- [261] Walsh A. Principles of Chemical Bonding and Band Gap Engineering in Hybrid Organic-Inorganic Halide Perovskites. *Journal of Physical Chemistry C*, 2015, 119(11):5755-60.
- [262] Li F, Zhang C, Huang J-H, Fan H, Wang H, Wang P, et al. A Cation-Exchange Approach for the Fabrication of Efficient Methylammonium Tin Iodide Perovskite Solar Cells. *Angewandte Chemie International Edition*, 2019, 58(20):6688-92.
- [263] Walsh A, Scanlon DO, Chen SY, Gong XG, Wei SH. Self-Regulation Mechanism for Charged Point Defects in Hybrid Halide Perovskites. *Angew Chem Int Edit*, 2015, 54(6):1791-4.
- [264] Ball JM, Petrozza A. Defects in Perovskite-Halides and Their Effects in Solar Cells. *Nature Energy*, 2016, 1:16149.
- [265] Yang D, Ming W, Shi H, Zhang L, Du M-H. Fast Diffusion of Native Defects and Impurities in Perovskite Solar Cell Material $\text{CH}_3\text{NH}_3\text{PbI}_3$. *Chemistry of Materials*, 2016, 28(12):4349-57.
- [266] Ono LK, Liu S, Qi Y. Reducing Detrimental Defects for High-Performance Metal Halide Perovskite Solar Cells. *Angewandte Chemie International Edition*, 2020, 59(17):6676-98.
- [267] Yong Z-J, Guo S-Q, Ma J-P, Zhang J-Y, Li Z-Y, Chen Y-M, et al. Doping-Enhanced Short-Range Order of Perovskite Nanocrystals for Near-Unity Violet Luminescence Quantum Yield. *Journal of the American Chemical Society*, 2018, 140(31):9942-51.
- [268] Li J, Hu P, Chen Y, Li Y, Wei M. Enhanced Performance of Sn-Based Perovskite Solar Cells by Two-Dimensional Perovskite Doping. *ACS Sustainable Chemistry & Engineering*, 2020, 8(23):8624-8.
- [269] Li M, Zhang X, Matras-Postolek K, Chen H-S, Yang P. An anion-driven Sn^{2+} exchange reaction in CsPbBr_3 nanocrystals towards tunable and high photoluminescence. *Journal of Materials Chemistry C*, 2018, 6(20):5506-13.

- [270] Imran M, Ramade J, Di Stasio F, De Franco M, Buha J, Van Aert S, et al. Alloy CsCd_xPb_{1-x}Br₃ Perovskite Nanocrystals: The Role of Surface Passivation in Preserving Composition and Blue Emission. *Chemistry of Materials*, 2020, 32(24):10641-52.
- [271] Cheng Y, Shen C, Shen L, Xiang W, Liang X. Tb³⁺, Eu³⁺ Co-doped CsPbBr₃ QDs Glass with Highly Stable and Luminous Adjustable for White LEDs. *ACS Applied Materials & Interfaces*, 2018, 10(25):21434-44.
- [272] Zhai Y, Bai X, Pan G, Zhu J, Shao H, Dong B, et al. Effective blue-violet photoluminescence through lanthanum and fluorine ions co-doping for CsPbCl₃ perovskite quantum dots. *Nanoscale*, 2019, 11(5):2484-91.
- [273] Wu T, Wang Y, Dai Z, Cui D, Wang T, Meng X, et al. Efficient and Stable CsPbI₃ Solar Cells via Regulating Lattice Distortion with Surface Organic Terminal Groups. *Advanced Materials*, 2019, 31(24):1900605.
- [274] Hassan Y, Park JH, Crawford ML, Sadhanala A, Lee J, Sadighian JC, et al. Ligand-engineered bandgap stability in mixed-halide perovskite LEDs. *Nature*, 2021, 591(7848):72-7.
- [275] Yan D, Shi T, Zang Z, Zhou T, Liu Z, Zhang Z, et al. Ultrastable CsPbBr₃ Perovskite Quantum Dot and Their Enhanced Amplified Spontaneous Emission by Surface Ligand Modification. *Small*, 2019, 15(23):1901173.
- [276] Jia D, Chen J, Yu M, Liu J, Johansson EMJ, Hagfeldt A, et al. Dual Passivation of CsPbI₃ Perovskite Nanocrystals with Amino Acid Ligands for Efficient Quantum Dot Solar Cells. *Small*, 2020, 16(24):2001772.
- [277] Shamsi J, Kubicki D, Anaya M, Liu Y, Ji K, Frohna K, et al. Stable Hexylphosphonate-Capped Blue-Emitting Quantum-Confined CsPbBr₃ Nanoplatelets. *ACS Energy Letters*, 2020, 5(6):1900-7.
- [278] Shi J, Li F, Jin Y, Liu C, Cohen-Kleinstein B, Yuan S, et al. In Situ Ligand Bonding Management of CsPbI₃ Perovskite Quantum Dots Enables High-Performance Photovoltaics and Red Light-Emitting Diodes. *Angewandte Chemie International Edition*, 2020, 59(49):22230-7.
- [279] Kumawat NK, Yuan Z, Bai S, Gao F. Metal Doping/Alloying of Cesium Lead Halide Perovskite Nanocrystals and their Applications in Light-emitting Diodes with Enhanced Efficiency and Stability. *Israel Journal of Chemistry*, 2019:doi:10.1002/ijch.201900031.
- [280] Gauld EA, Hao J, Kang HS, Miller EM, Habisreutinger SN, Zhao Q, et al. Conductivity Tuning via Doping with Electron Donating and Withdrawing Molecules in Perovskite CsPbI₃ Nanocrystal Films. *Advanced Materials*, 2019, 31:1902250.

- [281] Wang K, Subhani WS, Wang Y, Zuo X, Wang H, Duan L, et al. Metal Cations in Efficient Perovskite Solar Cells: Progress and Perspective. *Advanced Materials*, 2019, 31(50):1902037.
- [282] Das Adhikari S, Dutta SK, Dutta A, Guria AK, Pradhan N. Chemically Tailoring the Dopant Emission in Manganese-Doped CsPbCl₃ Perovskite Nanocrystals. *Angewandte Chemie International Edition*, 2017, 56(30):8746-50.
- [283] Saidaminov MI, Kim J, Jain A, Quintero-Bermudez R, Tan H, Long G, et al. Suppression of Atomic Vacancies via Incorporation of Isovalent Small Ions to Increase the Stability of Halide Perovskite Solar Cells in Ambient Air. *Nature Energy*, 2018, 3(8):648-54.
- [284] Luo J, Wang X, Li S, Liu J, Guo Y, Niu G, et al. Efficient and Stable Emission of Warm-White Light From Lead-Free Halide Double Perovskites. *Nature*, 2018, 563(7732):541-5.
- [285] Zhou D, Liu D, Pan G, Chen X, Li D, Xu W, et al. Cerium and Ytterbium Codoped Halide Perovskite Quantum Dots: A Novel and Efficient Downconverter for Improving the Performance of Silicon Solar Cells. *Advanced Materials*, 2017, 29(42):1704149.
- [286] Milstein TJ, Kluherz KT, Kroupa DM, Erickson CS, De Yoreo JJ, Gamelin DR. Anion Exchange and the Quantum-Cutting Energy Threshold in Ytterbium-Doped CsPb(Cl_{1-x}Br_x)₃ Perovskite Nanocrystals. *Nano Letters*, 2019, 19(3):1931-7.
- [287] Zhou D, Sun R, Xu W, Ding N, Li D, Chen X, et al. Impact of Host Composition, Codoping, or Tridoping on Quantum-Cutting Emission of Ytterbium in Halide Perovskite Quantum Dots and Solar Cell Applications. *Nano Letters*, 2019, 19(10):6904-13.
- [288] Hu Q, Li Z, Tan Z, Song H, Ge C, Niu G, et al. Rare Earth Ion-Doped CsPbBr₃ Nanocrystals. *Advanced Optical Materials*, 2018, 6(2):1700864.
- [289] Nosé S. A unified formulation of the constant temperature molecular dynamics methods. *The Journal of Chemical Physics*, 1984, 81(1):511-9.
- [290] Martyna GJ, Klein ML, Tuckerman M. Nosé-Hoover chains: The canonical ensemble via continuous dynamics. *The Journal of Chemical Physics*, 1992, 97(4):2635-43.
- [291] Manz TA, Limas NG. Introducing DDEC6 atomic population analysis: part 1. Charge partitioning theory and methodology. *RSC Advances*, 2016, 6(53):47771-801.
- [292] Limas NG, Manz TA. Introducing DDEC6 atomic population analysis: part 2. Computed results for a wide range of periodic and nonperiodic materials. *RSC Advances*, 2016, 6(51):45727-47.

- [293] Manz TA. Introducing DDEC6 atomic population analysis: part 3. Comprehensive method to compute bond orders. *RSC Advances*, 2017, 7(72):45552-81.
- [294] Manz T, Limas NG. Chagemol program for performing DDEC analysis. See the following: <http://ddecsourcesforgenet>, 2016.
- [295] Giansante C, Infante I. Surface Traps in Colloidal Quantum Dots: A Combined Experimental and Theoretical Perspective. *Journal of Physical Chemistry Letters*, 2017, 8(20):5209-15.
- [296] Bodnarchuk MI, Boehme SC, ten Brinck S, Bernasconi C, Shynkarenko Y, Krieg F, et al. Rationalizing and Controlling the Surface Structure and Electronic Passivation of Cesium Lead Halide Nanocrystals. *ACS Energy Letters*, 2019, 4(1):63-74.
- [297] Gao F. Effects of quantum confinement and shape on band gap of core/shell quantum dots and nanowires. *Applied Physics Letters*, 2011, 98(19):193105.
- [298] Lin Z, Li H, Franceschetti A, Lusk MT. Efficient Exciton Transport between Strongly Quantum-Confined Silicon Quantum Dots. *ACS Nano*, 2012, 6(5):4029-38.
- [299] Yu H, Li J, Loomis RA, Wang L-W, Buhro WE. Two- versus three-dimensional quantum confinement in indium phosphide wires and dots. *Nature Materials*, 2003, 2(8):517-20.
- [300] Cipriano LA, Di Liberto G, Tosoni S, Pacchioni G. Quantum confinement in group III-V semiconductor 2D nanostructures. *Nanoscale*, 2020, 12(33):17494-501.
- [301] Zheng Y, Fang Z, Shang M-H, Du Z, Yang Z, Chou K-C, et al. Enhancing the Stability of Orthorhombic CsSnI₃ Perovskite via Oriented π -Conjugated Ligand Passivation. *ACS Applied Materials & Interfaces*, 2020, 12(30):34462-9.
- [302] Binyamin T, Pedesseau L, Remennik S, Sawahreh A, Even J, Etgar L. Fully Inorganic Mixed Cation Lead Halide Perovskite Nanoparticles: A Study at the Atomic Level. *Chemistry of Materials*, 2020, 32(4):1467-74.
- [303] Chen Y, Smock SR, Flintgruber AH, Perras FA, Brutchey RL, Rossini AJ. Surface Termination of CsPbBr₃ Perovskite Quantum Dots Determined by Solid-State NMR Spectroscopy. *Journal of the American Chemical Society*, 2020, 142(13):6117-27.
- [304] Momma K, Izumi F. VESTA 3 for three-dimensional visualization of crystal, volumetric and morphology data. *Journal of applied crystallography*, 2011, 44(6):1272-6.
- [305] Wang V, Xu N, Liu J-C, Tang G, Geng W-T. VASPKIT: A user-friendly interface facilitating high-throughput computing and analysis using VASP code. *Computer Physics Communications*, 2021, 267:108033.

[306] Tan S, Yavuz I, Weber MH, Huang T, Chen C-H, Wang R, et al. Shallow Iodine Defects Accelerate the Degradation of α -Phase Formamidinium Perovskite. *Joule*, 2020, 4(11):2426-42.

[307] Snaith HJ. Perovskites: The Emergence of a New Era for Low-Cost, High-Efficiency Solar Cells. *The Journal of Physical Chemistry Letters*, 2013, 4(21):3623-30.

[308] Radicchi E, Ambrosio F, Mosconi E, Alasmari AA, Alasmary FAS, De Angelis F. Combined Computational and Experimental Investigation on the Nature of Hydrated Iodoplumbate Complexes: Insights into the Dual Role of Water in Perovskite Precursor Solutions. *The Journal of Physical Chemistry B*, 2020, 124(50):11481-90.

[309] Stampelcoskie KG, Manser JS, Kamat PV. Dual nature of the excited state in organic-inorganic lead halide perovskites. *Energy & Environmental Science*, 2015, 8(1):208-15.

[310] Radicchi E, Mosconi E, Elisei F, Nunzi F, De Angelis F. Understanding the Solution Chemistry of Lead Halide Perovskites Precursors. *ACS Applied Energy Materials*, 2019, 2(5):3400-9.

[311] Rahimnejad S, Kovalenko A, Forés SM, Aranda C, Guerrero A. Coordination Chemistry Dictates the Structural Defects in Lead Halide Perovskites. *ChemPhysChem*, 2016, 17(18):2795-8.

[312] Valencia AM, Shargaieva O, Schier R, Unger E, Cocchi C. Optical Fingerprints of Polynuclear Complexes in Lead Halide Perovskite Precursor Solutions. *The Journal of Physical Chemistry Letters*, 2021, 12(9):2299-305.

[313] Cheng F, Jing X, Chen R, Cao J, Yan J, Wu Y, et al. N-Methyl-2-pyrrolidone as an excellent coordinative additive with a wide operating range for fabricating high-quality perovskite films. *Inorganic Chemistry Frontiers*, 2019, 6(9):2458-63.

[314] Zhang J, Zhang L, Li X, Zhu X, Yu J, Fan K. Binary Solvent Engineering for High-Performance Two-Dimensional Perovskite Solar Cells. *ACS Sustainable Chemistry & Engineering*, 2019, 7(3):3487-95.

[315] Chen S, Xiao X, Chen B, Kelly LL, Zhao J, Lin Y, et al. Crystallization in one-step solution deposition of perovskite films: Upward or downward? *Science Advances*, 2021, 7(4):eabb2412.

[316] Chen J, Xiong Y, Rong Y, Mei A, Sheng Y, Jiang P, et al. Solvent effect on the hole-conductor-free fully printable perovskite solar cells. *Nano Energy*, 2016, 27:130-7.

[317] Arain Z, Liu C, Yang Y, Mateen M, Ren Y, Ding Y, et al. Elucidating the dynamics of solvent engineering for perovskite solar cells. *Science China Materials*, 2019, 62(2):161-72.

- [318] Stevenson J, Sorenson B, Subramaniam VH, Raiford J, Khlyabich PP, Loo Y-L, et al. Mayer Bond Order as a Metric of Complexation Effectiveness in Lead Halide Perovskite Solutions. *Chemistry of Materials*, 2016, 29(6):2435-44.
- [319] Ahlawat P, Dar MI, Piaggi P, Grätzel M, Parrinello M, Rothlisberger U. Atomistic Mechanism of the Nucleation of Methylammonium Lead Iodide Perovskite from Solution. *Chemistry of Materials*, 2020, 32(1):529-36.
- [320] Krieg F, Ochsenbein ST, Yakunin S, ten Brinck S, Aellen P, Süess A, et al. Colloidal CsPbX₃ (X = Cl, Br, I) Nanocrystals 2.0: Zwitterionic Capping Ligands for Improved Durability and Stability. *ACS Energy Letters*, 2018, 3(3):641-6.
- [321] Yan K, Long M, Zhang T, Wei Z, Chen H, Yang S, et al. Hybrid Halide Perovskite Solar Cell Precursors: Colloidal Chemistry and Coordination Engineering behind Device Processing for High Efficiency. *Journal of the American Chemical Society*, 2015, 137(13):4460-8.
- [322] Hamill JC, Schwartz J, Loo Y-L. Influence of Solvent Coordination on Hybrid Organic-Inorganic Perovskite Formation. *ACS Energy Letters*, 2017, 3(1):92-7.
- [323] Sharenko A, Mackeen C, Jewell L, Bridges F, Toney MF. Evolution of Iodoplumbate Complexes in Methylammonium Lead Iodide Perovskite Precursor Solutions. *Chemistry of Materials*, 2017, 29(3):1315-20.
- [324] Hu Q, Zhao L, Wu J, Gao K, Luo D, Jiang Y, et al. In situ dynamic observations of perovskite crystallisation and microstructure evolution intermediated from [PbI₆]⁴⁻ cage nanoparticles. *Nature Communications*, 2017, 8:15688.
- [325] te Velde G, Bickelhaupt FM, Baerends EJ, Fonseca Guerra C, van Gisbergen SJA, Snijders JG, et al. Chemistry with ADF. *Journal of Computational Chemistry*, 2001, 22(9):931-67.
- [326] ADF 2019 S, Theoretical Chemistry, Vrije Universiteit, Amsterdam, The Netherlands, <http://www.scm.com>.
- [327] Bérces A, Dickson RM, Fan L, Jacobsen H, Swerhone D, Ziegler T. An implementation of the coupled perturbed Kohn-Sham equations: perturbation due to nuclear displacements. *Computer Physics Communications*, 1997, 100(3):247-62.
- [328] Jacobsen H, Bérces A, Swerhone DP, Ziegler T. Analytic second derivatives of molecular energies: a density functional implementation. *Computer Physics Communications*, 1997, 100(3):263-76.
- [329] Wolff SK. Analytical second derivatives in the Amsterdam density functional package. *International Journal of Quantum Chemistry*, 2005, 104(5):645-59.

- [330] Swart M, Bickelhaupt FM. Proton Affinities of Anionic Bases: Trends Across the Periodic Table, Structural Effects, and DFT Validation. *Journal of Chemical Theory and Computation*, 2006, 2(2):281-7.
- [331] Swart M, Rösler E, Bickelhaupt FM. Proton affinities of main-group-element hydrides and noble gases: Trends across the periodic table, structural effects, and DFT validation. *Journal of Computational Chemistry*, 2006, 27(13):1486-93.
- [332] Pye CC, Ziegler T. An implementation of the conductor-like screening model of solvation within the Amsterdam density functional package. *Theoretical Chemistry Accounts*, 1999, 101(6):396-408.
- [333] Radicchi E, Kachmar A, Mosconi E, Bizzarri B, Nunzi F, De Angelis F. Structural and Optical Properties of Solvated PbI_2 in gamma-Butyrolactone: Insight into the Solution Chemistry of Lead Halide Perovskite Precursors. *The Journal of Physical Chemistry Letters*, 2020, 11(15):6139-45.
- [334] Hutter J, Iannuzzi M, Schiffmann F, VandeVondele J. cp2k: atomistic simulations of condensed matter systems. *WIREs Computational Molecular Science*, 2014, 4(1):15-25.
- [335] VandeVondele J, Krack M, Mohamed F, Parrinello M, Chassaing T, Hutter J. Quickstep: Fast and accurate density functional calculations using a mixed Gaussian and plane waves approach. *Computer Physics Communications*, 2005, 167(2):103-28.
- [336] Chauhan M, Zhong Y, Schötz K, Tripathi B, Köhler A, Huettner S, et al. Investigating two-step MAPbI_3 thin film formation during spin coating by simultaneous in situ absorption and photoluminescence spectroscopy. *Journal of Materials Chemistry A*, 2020, 8(10):5086-94.
- [337] Chouhan L, Ghimire S, Subrahmanyam C, Miyasaka T, Biju V. Synthesis, optoelectronic properties and applications of halide perovskites. *Chemical Society Reviews*, 2020, 49(10):2869-85.
- [338] Kim MK, Lee HS, Pae SR, Kim D-J, Lee J-Y, Gereige I, et al. Effects of temperature and coating speed on the morphology of solution-sheared halide perovskite thin-films. *Journal of Materials Chemistry A*, 2018, 6(48):24911-9.
- [339] VandeVondele J, Hutter J. Gaussian basis sets for accurate calculations on molecular systems in gas and condensed phases. *The Journal of Chemical Physics*, 2007, 127(11):114105.
- [340] Goedecker S, Teter M, Hutter J. Separable dual-space Gaussian pseudopotentials. *Physical Review B*, 1996, 54(3):1703-10.
- [341] Liu Q, Fan L, Huang X, Zhao Y, Fan C, Bai H, et al. High-Quality Concentrated Precursor Solution in N,N-Dimethylformamide for Thick Methylammonium Triiodoplumbate Layer in Solar Cells. *ACS Appl Mater Interfaces*, 2020, 12(23):25972-9.

- [342] Gutmann V. Coordination Chemistry of Certain Transition Metal Ions in Donor Solvents. *Coordination Chemistry in Non-Aqueous Solutions*. Vienna: Springer Vienna; 1968. p. 161-8.
- [343] Munakata M, Kitagawa S, Miyazima M. Classification of solvents based on their coordination power to nickel(II) ion. A new measure for solvent donor ability. *Inorganic Chemistry*, 1985, 24(11):1638-43.
- [344] Persson I, Sandström M, Goggin PL. On the coordinating properties of some solvents. A vibrational spectroscopic study of mercury(II) halides and antimony(V) chloride in solution; new concepts for Lewis basicity scales of solvents. *Inorganica Chimica Acta*, 1987, 129(2):183-97.
- [345] Munakata M, Kitagawa S. Coordination power series of solvents: 2. The solvent effects on complex formations, half-wave potentials, ^{113}Cd NMR resonances and Gibbs free energy changes of transfer. *Inorganica Chimica Acta*, 1990, 169(2):225-34.
- [346] Gritzner G. A critical view on the Lewis-donor (nucleophilic) properties of solvents. *Journal of Molecular Liquids*, 1997, 73-74:487-500.
- [347] Scheiner S. Relative Strengths of $\text{NH}\cdot\text{O}$ and $\text{CH}\cdot\text{O}$ Hydrogen Bonds between Polypeptide Chain Segments. *The Journal of Physical Chemistry B*, 2005, 109(33):16132-41.
- [348] Song T-B, Chen Q, Zhou H, Jiang C, Wang H-H, Yang Y, et al. Perovskite solar cells: film formation and properties. *Journal of Materials Chemistry A*, 2015, 3(17):9032-50.
- [349] Khlyabich PP, Loo Y-L. Crystalline Intermediates and Their Transformation Kinetics during the Formation of Methylammonium Lead Halide Perovskite Thin Films. *Chemistry of Materials*, 2016, 28(24):9041-8.
- [350] Park SJ, Kim AR, Hong JT, Park JY, Lee S, Ahn YH. Crystallization Kinetics of Lead Halide Perovskite Film Monitored by In Situ Terahertz Spectroscopy. *The Journal of Physical Chemistry Letters*, 2017, 8(2):401-6.
- [351] Liao K, Li C, Xie L, Yuan Y, Wang S, Cao Z, et al. Hot-Casting Large-Grain Perovskite Film for Efficient Solar Cells: Film Formation and Device Performance. *Nano-Micro Letters*, 2020, 12(1):156.
- [352] Moser T, Artuk K, Jiang Y, Feurer T, Gilshtein E, Tiwari AN, et al. Revealing the perovskite formation kinetics during chemical vapour deposition. *Journal of Materials Chemistry A*, 2020, 8(42):21973-82.
- [353] Ahlawat P, Hinderhofer A, Alharbi EA, Lu H, Ummadisingu A, Niu H, et al. A combined molecular dynamics and experimental study of two-step process enabling

low-temperature formation of phase-pure α -FAPbI₃. *Science Advances*, 2021, 7(17):eabe3326.

[354] Kaiser W, Mosconi E, Althman AA, Meggiolaro D, Gagliardi A, De Angelis F. Halide-driven formation of lead halide perovskites: insight from ab initio molecular dynamics simulations. *Materials Advances*, 2021.

[355] Castro-Méndez A-F, Hidalgo J, Correa-Baena J-P. The Role of Grain Boundaries in Perovskite Solar Cells. *Advanced Energy Materials*, 2019, 9(38):1901489.

[356] Conings B, Drijkoningen J, Gauquelin N, Babayigit A, D'Haen J, D'Olieslaeger L, et al. Intrinsic Thermal Instability of Methylammonium Lead Trihalide Perovskite. *Advanced Energy Materials*, 2015, 5(15):1500477.

[357] Wang Q, Chen B, Liu Y, Deng Y, Bai Y, Dong Q, et al. Scaling behavior of moisture-induced grain degradation in polycrystalline hybrid perovskite thin films. *Energy & Environmental Science*, 2017, 10(2):516-22.

[358] Yin W-J, Chen H, Shi T, Wei S-H, Yan Y. Origin of High Electronic Quality in Structurally Disordered CH₃NH₃PbI₃ and the Passivation Effect of Cl and O at Grain Boundaries. *Advanced Electronic Materials*, 2015, 1(6):1500044.

[359] Ji F, Pang S, Zhang L, Zong Y, Cui G, Padture NP, et al. Simultaneous Evolution of Uniaxially Oriented Grains and Ultralow-Density Grain-Boundary Network in CH₃NH₃PbI₃ Perovskite Thin Films Mediated by Precursor Phase Metastability. *ACS Energy Letters*, 2017, 2(12):2727-33.

[360] Chu Z, Yang M, Schulz P, Wu D, Ma X, Seifert E, et al. Impact of grain boundaries on efficiency and stability of organic-inorganic trihalide perovskites. *Nature Communications*, 2017, 8(1):2230.

[361] Huang J, Tan S, Lund PD, Zhou H. Impact of H₂O on organic-inorganic hybrid perovskite solar cells. *Energy & Environmental Science*, 2017, 10(11):2284-311.

[362] Wu X, Jiang Y, Chen C, Guo J, Kong X, Feng Y, et al. Stable Triple Cation Perovskite Precursor for Highly Efficient Perovskite Solar Cells Enabled by Interaction with 18C6 Stabilizer. *Advanced Functional Materials*, 2020, 30(6):1908613.

[363] ten Brinck S, Zaccaria F, Infante I. Defects in Lead Halide Perovskite Nanocrystals: Analogies and (Many) Differences with the Bulk. *ACS Energy Letters*, 2019, 4(11):2739-47.

[364] Hui W, Chao L, Lu H, Xia F, Wei Q, Su Z, et al. Stabilizing black-phase formamidinium perovskite formation at room temperature and high humidity. *Science*, 2021, 371(6536):1359-64.

[365] Li G, Su Z, Li M, Yang F, Aldamasy MH, Pascual J, et al. Ionic Liquid Stabilizing High-Efficiency Tin Halide Perovskite Solar Cells. *Advanced Energy Materials*, n/a(n/a):2101539.

[366] Zhumekenov AA, Saidaminov MI, Haque MA, Alarousu E, Sarmah SP, Murali B, et al. Formamidinium Lead Halide Perovskite Crystals with Unprecedented Long Carrier Dynamics and Diffusion Length. *ACS Energy Letters*, 2016, 1(1):32-7.

[367] Prathapani S, Choudhary D, Mallick S, Bhargava P, Yella A. Experimental evaluation of room temperature crystallization and phase evolution of hybrid perovskite materials. *CrystEngComm*, 2017, 19(27):3834-43.

[368] Trots DM, Myagkota SV. High-temperature structural evolution of caesium and rubidium triiodoplumbates. *Journal of Physics and Chemistry of Solids*, 2008, 69(10):2520-6.

Summary

Stabilizing Metal Halide Perovskites by Computational Compositional Engineering

Metal-halide perovskites (MHPs) have attracted substantial attention in the past decade and have become one of the most promising candidates for photovoltaic technologies. Despite the extraordinarily high efficiency of perovskite devices, the race towards a viable photovoltaic technology is continuing because their stability issues remain the main obstacle to practical large-scale applications. Compositional engineering in both the final films and the precursors has been shown to be an effective way to improve their stability, as has been demonstrated by numerous experiments. Therefore, it is vital to gain a fundamental understanding of the underlying mechanisms. Atomistic and molecular simulations are ideal tools to study atomistic and molecular levels of details that often cannot straightforwardly be reached in experiments. This thesis aims to provide insights into the stabilizing effect of the compositional engineering on MHPs from a computational perspective. Several computational techniques are employed to achieve this goal, i.e., Density Functional Theory (DFT) and *ab-initio* Molecular Dynamics (AIMD) simulations. We demonstrate how computational tools can help to better understand the atomistic structure, electronic structure, phase stability, and the precursor chemistry of various halide perovskites.

This thesis starts with a general introduction in Chapter 1, followed by an introduction of the used theoretical and computational methods in Chapter 2. Then in Chapter 3, we start tackling the challenge of phase instability of MHPs. We explain the atomistic origins of the phase instability of some primary perovskites, like CsSnI₃,

CsPbI₃, and FAPbI₃. Furthermore, we reveal the underlying mechanisms for the improved phase stability of MHPs by computational engineering of the mixed compounds (Cs_xFA_{1-x}PbI₃, CsSn_yPb_{1-y}I₃, and CsSn(Br_zI_{1-z})₃). We investigate the electronic properties and relative bond strengths in the different phases to explain how mixing ions affects phase stability. Four correlated factors, namely, the average metal-halide bond length, the overall bonding strength (including metal halide bonds and hydrogen bonds), the formation energies, and the Sn vacancy formation energy are identified to be responsible for the phase transition. We demonstrate phase stability of several well-known compositions of perovskites could be adjusted and optimised by mixing ions, which gives rise to either increased bond strength of perovskite perovskites and/or decreased bond strength in their nonperovskite counterparts or suppressed defect formation, i. e. in the case of Sn-Pb mixed compounds.

In Chapter 4, based on the insights on the origin of the phase instability obtained in Chapter 3, we identify the mixed-cation and mixed-anion Rb_yCs_{1-y}Sn(Br_xI_{1-x})₃ perovskites, and suggest them as promising candidates for solar cell applications. We studied the evolution of the structural, thermodynamic, and electronic properties as a function of the extent of substitution of Rb for Cs and Br for I. We predict that Cs_yRb_{1-y}Sn(Br_xI_{1-x})₃ perovskites have direct bandgaps in the range of 1.3-2.0 eV. The alloys with high I and Cs concentration are well suited for highly efficient single-junction PSCs, while those with high Rb and Br concentration are suitable as wide bandgap materials for tandem PSCs. Importantly, we found that substitution of Br for I can improve the phase stability, with suppression of the unwanted phase transition from perovskite to nonperovskite structure. The stabilization of Cs_yRb_{1-y}Sn(Br_xI_{1-x})₃ prefer the perovskite phase with the concentration $x > 1/3$. In addition, by using binary alloying theory, we predict that mixing both anions and cations is beneficial for a highly homogeneous solid solution and improved film quality. Thus, the Rb_yCs_{1-y}Sn(Br_xI_{1-x})₃ is predicted as an efficient and stable light absorber for PSCs call for experimental exploration.

Furthermore, we extend our investigation from bulk perovskites to quantum dots (QDs). Here, we investigate the role of additives in improving the performance and stability of Sn-based QDs. We then extend our investigation from bulk perovskites to

QDs, as the dimensional engineering will further improve the stability of alloyed and Sn-based perovskites. In Chapter 5, we investigate how additives affect the properties of perovskite QDs and improving the performance and stability of Sn-based QDs. We reveal the role of sodium additive doping in $\text{CsSn}_{0.6}\text{Pb}_{0.4}\text{I}_3$ perovskite QDs by study the strength of surface bonds, defect formation energies, and the interaction of surface ligands and perovskite surfaces by DFT and AIMD simulations. We explain the mechanism for the enhanced photoluminescence of Sn-Pb perovskite QDs and propose strategies to further enhance their stability. These results suggest Na ion enhances the covalent bonding of the surface tin-iodine bonds and forms strong ionic bonding with the neighbouring iodine anions, thus suppresses the formation of I and Sn vacancies. Furthermore, the Na ion also enhances the binding strength of the surface ligands with the perovskite QDs surface. According to the results from AIMD simulations, the enhanced surface ligand binding is only effective on a specific surface configuration. The position of Na ion remains intact on a CsI-terminated surface but diffuses vigorously on MI_2 -terminated surface. The latter leads to the detachment of ligands and the perovskite surface layer, therefore fast degradation of the MI_2 -terminated surface. The above results indicate that the combination of the Na doping and CsI-termination of the QDs may result in the best improvement in maintaining a long lifetime of high photoluminescence efficiency. Therefore, we foresee the surface termination engineering could offer a breakthrough in improving the efficiency and the lifetime of perovskite QDs for near-infrared applications.

Next, to understand the effect of the compositional tuning of precursors solutions in affecting the perovskite crystallization process, in Chapter 6, we make a comprehensive investigation to understand the crystallization chemistry. Here, using MAPbI_3 as an example, we study the complex evolution of the molecular species from the solution to the initial stage of the nucleation and determine the reaction pathways for the formation of a polynuclear iodoplumbate in different solvents environments. The advantage of the usage of DMF-DMSO binary solvents in the experiment is explained. The results obtained for formation enthalpies indicate that the formation of $[\text{PbI}_3\text{L}_n]^{1-}$ iodoplumbate and its further coordination should be one of the key steps

which determine the final crystallinity of MAPbI₃. The DMF-DMSO binary solvent shows slower formation of high-I coordinated iodoplumbates as compared to DMF, which benefits the crystallization of MAPbI₃ with better crystallinity.

Finally, in Chapter 7, we summarize our main conclusions and discuss directions for future research directions.

List of Publications

Publications related to the thesis:

Equal contribution

1. **J Jiang**, F Liu, I Tranca, Q Shen, S Tao, "Atomistic and Electronic Origin of Phase Instability of Metal Halide Perovskites", *ACS Applied Energy Materials*, 2020, 3, 11548-11558. (Chapter 3)
2. **J Jiang**, C K Onwudinanti, R A Hatton, P A Bobbert, S Tao, "Stabilizing Lead-Free All-Inorganic Tin Halide Perovskites by Ion Exchange", *Journal of Physical Chemistry C*, 2018. 122, 17660-17667. (Chapter 4)
3. **J Jiang**[#], F Liu[#], Q Shen, S Tao. "The Role of Sodium in Stabilizing Tin-Lead (Sn-Pb) Alloyed Perovskite Quantum Dots", *Journal of Materials Chemistry A*, 2021, 9, 12087-12098. (Chapter 5)
4. F Liu[#], **J Jiang**[#], Y Zhang, C Ding, T Toyoda, S Hayase, R Wang, S Tao, Q Shen, "Near - Infrared Emission from Tin - Lead (Sn - Pb) Alloyed Perovskite Quantum Dots by Sodium Doping", *Angewandte Chemie - International Edition*, 2020, 59, 8421-8424. (Chapter 5)
5. **J Jiang**, J M Vicent-Luna, S Tao, "The Role of Solvents in the Formation of Methylammonium Lead Triiodide Perovskite", to be submitted. (Chapter 6)

Other publications

6. F Liu[#], **J Jiang**[#], T Toyoda, A Kamarudin, S Hayase, R Wang, S Tao, Q Shen, "Ultra-Halide-Rich Syntheses Stabilize the Pure Tin-Based Halide Perovskite Quantum Dots", *ACS Applied Nano Materials*, 2021, 4, 3958-3968.
7. J Cao[#], **J Jiang**[#], N Li[#], Y Dong, Y Jia, S Tao, N Zhao, "Alkali-Cation-Enhanced Benzylammonium Passivation for Efficient and Stable Perovskite Solar Cells Fabricated Through Sequential Deposition", *Journal of Materials Chemistry A*, 2020, 8, 19357-19366.
8. Y H R Chang, **J Jiang**, HY Khong, I Saad, S S Chai, M M Mahat, S Tao, "Rational design of stretchable AgX (X = Se, Te) for photovoltaic-thermoelectric coupling system and biomedical implant application", *ACS Applied Materials & Interfaces*, 2021, 13, 25121-25136.
9. D Bartesaghi, A Ray, **J Jiang**, R K M Bouwer, S Tao, T J Savenije, "Partially Replacing Pb by Mn in Hybrid Metal Halide Perovskites: Structural and Electronic Properties", *APL Materials*, 2018, 6, 121106.
10. S Tao, I Schmidt, G Brocks, **J Jiang**, I Tranca, K Meerholz, S Olthof, "Absolute Energy Level Positions in Tin-and Lead-Based Halide Perovskites", *Nature communications*, 2019, 10, 2560.
11. N Li, Y Luo, Z Chen, X Niu, X Zhang, J Lu, R Kumar, **J Jiang**, H Liu, X Guo, B Lai, G Brocks, Q Chen, S Tao, DP Fenning, H Zhou et al. "Microscopic Degradation in Formamidinium-Cesium Lead Iodide Perovskite Solar Cells under Operational Stressors", *Joule*, 2020, 4, 1743.
12. F Liu, C Ding, Y Zhang, T Kamisaka, Q Zhao, J M Luther, T Toyoda, S Hayase, T Minemoto, K Yoshino, B Zhang, S Dai, **J Jiang**, S Tao, Q Shen, GeI₂ Additive for High Optoelectronic Quality CsPbI₃ Quantum Dots and Their Application in Photovoltaic Devices. *Chemistry of Materials*, 2019, 31, 798-807.

-
13. J Zhang, R Li, S Apergi, P Wang, B Shia, **J Jiang**, N Ren, W Han, Q Huang, G Brocks, Y Zhao, S Tao, X Zhang, "Multifunctional Molecule Engineered SnO₂ for Perovskite Solar Cells with High Efficiency and Reduced Lead Leakage", *Solar RRL*, 2021, 2100464, DOI: 10.1002/solr.202100464
 14. A Caiazzo, K Datta, **J Jiang**, M C Gélvez-Rueda, J Li, R Olleiro, J M Vicent-Luna, S Tao, F C Grozema, M M Wienk, R A J Janssen, "Effect of co-solvents on the crystallization and phase distribution of mixed-dimensional perovskites", *Advanced Energy Materials*, accepted.
 15. Y H R Chang, **J Jiang**, K H Yeoh, H Y Khong, M M Mahat, S S Chai, I Saad, P Klaver, "Improving the thermoelectric and optical performance of Ag₂Se via halogenation", in preparation.
 16. X Wang, T Bai, B Yang, R Zhang, D Zheng, **J Jiang**, S Tao, F Liu, K Han, "Germanium Halides as Ideal Precursors for Green Synthesis of High Optoelectronic Quality Metal Halide Perovskite Nanocrystals", submitted.

List of Presentations

1. Oral talk at the Physics@Veldhoven, 2021
2. Oral talk at the Internet Conference on Theory and Computation of Halide Perovskites, 2020
3. Oral talk at the nanoGe Fall Meeting, 2020
4. Poster presentation at the MRS Spring/Fall Meeting & Exhibit, 2020
5. Poster presentation at the Applied Computational Science (ACOS) Symposium, 2020
6. Poster presentation at the International Conference on Hybrid and Organic Photovoltaics, 2020
7. Poster presentation at the Applied Computational Science (ACOS) Symposium, 2019
8. Poster presentation at the Next-Gen IV PV Materials, Groningen, 2019
9. Poster presentation at the Applied Computational Science (ACOS) Symposium, 2018
10. Poster presentation at the E-MRS Fall Meeting, Warsaw, 2018
11. Poster presentation at the 4th Dutch Perovskite Workshop, Eindhoven, 2018
12. Poster presentation at the International Conference on Perovskite Thin Film Photovoltaics, Photonics and Optoelectronics, Rennes, 2018

Acknowledgement

I would like to take this opportunity to express my sincere gratitude to all the people who have contributed to this thesis and my incredible PhD journey in Eindhoven.

First and foremost, I would like to thank my supervisor *Shuxia Tao*. Your guidance and support were constant during my PhD journey, which was filled with ups and downs. I still remember my first day in Eindhoven. I had taken the train from Schiphol to Eindhoven, you had greeted me (and my wife) at the station with a warm welcome, and we had drinks at a coffee bar closed to the Eindhoven station. On my first working day, you were waiting for me outside the building and then guided me to get familiar with the working environments, and gave me a nice TU/e map and some scientific articles to read. And you warmly help me with daily life-related things. With your help and support, I could easier get familiar with the life 9000 km from my hometown. From the first day till now, you have always given your valuable time and made yourself available. I would like to thank you for your critical feedback on every manuscript and my thesis. Without your comments, suggestions, and revisions, it will not reach the high scientific level. I am grateful to you for pointing out my shortcomings, suggesting approaches, and encouraging me to overcome them. Since early 2020, with the unexpected pandemic of the coronavirus, we all have to work from home. Luckily, we regularly have meetings and talks online, which helped me approach every milestone of my PhD research on time. You are a hardworking, energetic, enthusiastic, and professional person who inspired me to become a more mature researcher. Thank you for all things throughout these years, without which I would not have been able to finish my PhD.

Next, I would like to thank my promoter *Peter Bobbert* for his guidance and support. I still remember when I was a new bird working as a PhD candidate for the first week, you warmly welcomed me, and we had a nice talk on the first Thursday of my working days. After that, our discussions at the meetings and symposiums and later for the

lead-free perovskite paper have greatly helped me understand computational energy-related research. You keep your concerns and track my research progress for the rest of the years and greatly support my PhD graduation phase. I admire your diligence, meticulousness, and professionalism, and I like to believe that some of it also has rubbed off on me.

I would also like to thank the members of the defence committee, *Laurent Pedesseau, Jan Anton Koster, Adriana Creatore, René Janssen, and Geert Brocks*, for taking the time to read my thesis and for providing valuable comments.

The works presented in this thesis have been received great help from many colleagues and collaborators. *Dozie and Ross*, thank you for your helpful comments and suggestions and polish my first manuscript about lead-free perovskite. I would like to thank *Ionut* for guiding me to learn the COHP and net atomic charge calculations and for all our academic discussions about calculations, methods, and the manuscript. My sincere gratitude to *Vicent* for all your helpful suggestions and discussions for the computational methods, especially on molecular dynamics. You are a warm-hearted and professional researcher. I enjoyed our talks and learned many things from it. Hey *Zehua*, thank you for your helpful suggestions for the DFT calculations. You are a smart, gentle, generous person, and we discussed a lot about all things, not only focus on the research but also on all topics we were interested in. I will remember our gathering for some funny activities. I would like to thank *Sofia Apergi* for the help with proofreading and suggestions for the manuscript. You are always kind and available when I need your help, which I will remember in my heart. Moreover, I would like to express my great appreciation for the excellent collaborator, *Feng*. Even though we have not met each other physically until now, this does not affect our efficient discussion and collaboration. Together, we have investigated many interesting topics on the perovskite QDs and achieved great scientific results. I hope your works will going well at Shandong University, and hopefully, we can meet physically in the near future.

Next, I would like to thank Computational Materials Physics Group (CMPG). I want to thank *Haibo* for the valuable discussion about the defect-related calculations

and the selection of the functional. I will remember our talks, lunch, outing, and your marathon. *Robin*, thank you for the talks about the prediction of the new material and our good collaboration. I wish you much success with your upcoming stay in Eindhoven and all the best for your future career and life. I want to thank some of the current and former group members. *Mike, Sander, Qihua, Min, Lei*, thank you for the discussions at the CMPG group meetings, coffee breaks, and lunchtime. They were precious inspirations for my work.

Next, I would like to thank the Center for Computational Energy Research (CCER). *Vianney, Peter, and Paul*: thank you for organizing all the colloquiums, seminars, CCER corner, and the annual group outings, which not only give me more inspiration but also let me exchange knowledge and have more discussions with the excellent researchers within CCER for different computational aspect. *Geert*, thank you for your comments and input for some collaborated papers and agree to be my defense committee, and give me suggestions on the thesis. *Subash*, I remember the early first year of my PhD, we sat next to each other in the CCER office. I enjoyed all the talks with you and appreciated your help when I just arrived. It is my pleasure as a member of CCER, and wishing you all much success in the future. Being at DIFFER, the conversations at the lunch table and the coffee corner are memorable. I want to thank: *Anja, Kiran, Rochan, Matthijs, Usman, Yu, Qin, Shaojun, Juehan, Xueqing, Zhiyang, Yanliang, Jun*.

Next, I would like to thank the Materials Simulations & Modeling (MSM) group. *Sofia Calero*: thank you for having me as a member started last year. Our group started at a special duration, forcing us to work from home for one year. But organizing all the meetings online helped us to connect to each other. It was beneficial for my research works. Next, I want to express my gratitude to our group secretary *Marjan*. I appreciate your help with all the bureaucratic and administrative procedures. On all things I inquired about, you always gave me quick feedback. I also would like to thank other members of the MSM group. *Xiucheng, Dominika, Esteban, Botagoz, Bipasa, Bram, Ake, Jesse, Victor, and Hans*, I am appreciated for your presentations at the MSM group meetings and wishing you much success in your study, work, and future career.

I would like to thank all the wonderful collaborators for those results not included in this thesis. *Jun*, thanks for all the helpful discussions, wishing you all the best in your new position at Xi'an Jiaotong University. *Alessandro*, thank you for all the scientific discussions about the solvent-precursor interaction of perovskite. Our collaboration helps me with further understanding of the crystalization process of MHPs. To *Jie, Nan*, and *David*, I appreciate our collaboration and wishing you good luck and success in your future career and life.

Life in the Netherlands will not be that colourful without friends. *Ruishen* and *Chunying*, we get to know each other for many years, and we keep the friendship from Guilin to Netherlands and Belgium. It is lucky to have friends like you, and wishing you all the best. I am looking forward to our next gathering and journeys. Here I would like to give my special thanks to some friends that I had the pleasure to meet in Eindhoven: *Yihui, Qi, Xuan, Wei, Huatian, Yaoge, Yatong, Cheng*. You all are very talented and hard-working researchers. I will remember all our discussions, outings, dinners, activities together, hoping you succeed in your career and life. *Xi*, thank you for your welcome when I arrived at the Eindhoven station and help me settled. I wish you much success with your future career. *Qinyi* and *Yizhou*, thank you for the dinners, games, and ping-pong we played together, wishing you all the best in the future.

Finally, I would like to thank my family. To my beloved wife *Qiuhua*, thank you for all your support for the past ten years. It is more than greatest to meet you in my life. You are a wonderful wife, great researcher, and golden partner. You shed light on my life, and I can not imagine that I could achieve all things without your constant support and love. I will continuously express my sincere love to you, and I am looking forward to our new journey when we finish our PhD research. 我要感谢我的父母，感谢你们二十几年来对我的无限的爱与支持，你们的鼓励和支持是我前进的动力，希望我能让你们感到骄傲。祝爸妈身体健康，事事顺意。感谢众多亲友们一直以来对我的关心。

Junke Jiang

蒋琚柯

Eindhoven, September 2021

Curriculum Vitae

Junke Jiang was born on November 21st, 1992, in Hengyang, China. After finishing high school in 2010 at the Yueyun Middle School in Hengyang, he studied microelectronics manufacturing engineering at the Guilin University of Electronic Technology (GUET), Guilin, China. Following graduation in 2014, he studied mechatronics engineering at the same university. His Master's thesis was focused on investigating the sensing mechanism of two-dimensional materials through molecular modelling. In 2016, he was selected to pursue a PhD in computational energy research at TU Eindhoven, the Netherlands. After graduating with first-class honours from GUET in 2017, he was enrolled as a doctoral candidate supported by NWO Shell CSER tenure track program and started his PhD research at the Department of Applied Physics, Eindhoven University of Technology, the Netherlands. The results obtained during his PhD research are presented in this dissertation.

